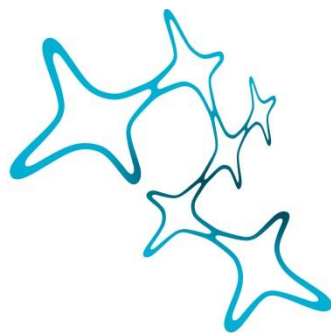# EXPANDING THE SCOPE OF ADENO-ASSOCIATED-VIRUS VECTORS

FROM RETINAL GENE THERAPY TO NEXT GENERATION VACCINATION PLATFORM

Sabrina Babutzka

Graduate School of Systemic Neurosciences

LMU Munich

Dissertation at the
Graduate School of Systemic Neurosciences
Ludwig-Maximilians-Universität München

August, 2023

Table of contents

List of Abbreviations

Abbreviation	Definition
aa	amino acid
AAP	assembly-activating protein
AAV	adeno-associated virus
AB	antibody
AC	affinity chromatography
ACE2	angiotensin-converting enzyme 2
ACHM	achromatopsia
Ad	adenovirus
AEX	anion exchange chromatography
AG	antigen
AH	aqueous humor
ANOVA	analysis of variance
Anti/Anti	antibiotic/antimycotic
APC	antigen-presenting cell
Arg	arginine
Arr3	cone arrestin 3
ATP	adenosine triphosphate
AUC	area under the curve
BBB	blood-brain-barrier
BF	brightfield
bp	base pair
BRB	blood-retina-barrier
CC	connecting cilium
CD	cluster of differentiation
CEX	cation exchange chromatography
cGMP	cyclic guanosine monophosphate
CH	central helix
CMV	cytomegalovirus
CNG	cyclic nucleotide gated ion channel
CNS	central nervous system
CoV	coronavirus
COVID-19	COrona VIrus Disease 2019
cp	capsid protein
cSLO	confocal scanning laser ophthalmoscopy
CT	cytoplasmic tail
CTD	C-terminal domain
CV	column volume
DAPI	4',6-diamidino-2-phenylindole

DC	dendritic cell
ddH$_2$O	double-deionized water
DLG	dorsal lateral geniculate
DLS	dynamic light scattering
DMEM	Dulbecco's Modified Eagle Medium
DNA	desoxyribonucleic acid
dsDNA	double-stranded DNA
EDTA	ethylenediaminetetraacetic acid
eGFP	enhanced green fluorescent protein
ELISA	enzyme-linked immunosorbent assay
EMA	european medicines agency
FBS	fetal bovine serum
FD	fast digest
FDA	Food and Drug Administration
FP	fusion peptide
FPPR	fusion peptide proximal region
GAL	galactose
GC	guanylyl cyclase
GCL	ganglion cell layer
GDP	guanosine diphosphate
GFAP	glial fibrillary acidic protein
GMP	Good Manufacturing Practice
GOI	gene of interested
GTP	guanosine triphosphate
HEK	human embryonal kidney
HeLa	Henrietta Lacks
HIV	human immunodeficiency virus
HPLC	high performance liquid chromatography
HPV	human papillomavirus
HR	heptad repeat domain
hRO	human retinal organoid
HRP	horseradish peroxidase
HS	heparan sulfate
HSPG	heparan-sulfate proteoglycan
HSV	herpes simplex virus
i.v.	intravenous
iDSF	intrinsic differential scanning fluorimetry
IHC	immunohistochemistry
ILM	inner limiting membrane
INL	inner nuclear layer
IOP	intraocular pressure

IPL	inner plexiform layer
iPSC	induced pluripotent stem cell
IRD	inherited retinal dystrophies
IS	inner segment
ITR	inverted terminal repeat
IVT	intravitreal
LamR	laminin receptor
LCA	Leber congenital amaurosis
LPL	lipoprotein lipase deficiency
MAAP	membrane-associated accessory protein
MCS	multiple cloning site
MHC	major histocompatibility complex
MOI	multiplicity of infection
NAb	neutralization antibody
NCPE	non-pigmented ciliary epithelium
NFL	nerve fiber layer
NHP	non-human primate
NIM	neuronal induction medium
NTC	non-transfected control
NTD	N-terminal domain
OCT	optical coherence tomography
ONL	outer nuclear layer
OPL	outer plexiform layer
ORF	open reading frame
OS	outer segment
OV	optic vesicle
pA	polyadenylation
PACG	primary angle-closure glaucoma
PAMP	pathogen-associated molecular pattern
PB	phosphate buffer
PBS	phosphate-buffered saline
PCE	pigmented ciliary epithelium
PCR	polymerase chain reaction
PDE	phosphodiesterase
PECAM	platelet endothelial cell adhesion molecule
PEG	polyethylene glycol
PEI	polyethyleneimine
PFA	paraformaldehyde
PLA	phospholipase
POAG	primary open-angle glaucoma
PRR	pattern recognition receptor

PTM	post-translational modification
PVDF	polyvinylidene difluoride
qRT-PCR	quantitative real-time PCR
rAAV	recombinant AAV
RBD	receptor-binding domain
RDM	retinal differentiation medium
Rho	rhodopsin
RMM	retinal maturation medium
RMPM	rounds per minute
RNA	ribonucleic acid
RP	retinitis pigmentosa
RPE	retinal pigment epithelium
RT	room temperature
SARS-CoV-2	severe acute respiratory syndrome coronavirus 2
scDNA	self-complementary DNA
SEM	standard error of the mean
SIA	sialic acid
SLS	static light scattering
SMA	spinal muscular atrophy
SMN	survival motor neuron
SR	subretinal
ssDNA	single-stranded DNA
SUMO	small ubiquitin related modifier
TBS	tris-buffered saline
T_c	cytotoxic T-cell
T_h	T-helper cell
T_m	melting temperature
vg	viral genomes
VLP	virus-like particle
VP	viral protein
WHO	world health organization
WPI	weeks post injection
WT	wildtype

List of Tables

List of Figures

1 Abstract

Gene therapy of inherited retinal dystrophies (IRDs) using vectors based on adeno-associated viruses (AAVs) has been widely explored to intervene in the progression of retinal degeneration. However, AAVs are further investigated outside the field of gene supplementation approaches allowing for unconventional platforms of use.

Here, we introduce novel AAV9-based capsid variants displaying small peptide insertions attempting to alter the natural tropism for effective transduction of retinal cells after less invasive intravitreal (IVT) administration. Previously heparan-sulfate proteoglycan (HSPG) binding has been shown to significantly contribute to retinal cell tropism. Therefore, we introduced an artificial HSPG-binding site with peptide insertions to investigate how this affects penetration of retinal cell layers after IVT administration. A total of ten different AAV9-based variants were characterized on technical aspects as well as *in vitro, ex vivo* and *in vivo* tropism and transduction properties in mouse retina. AAV9.NNR and AAV9.GLR outperformed AAV9 wildtype as well as previous AAV9 variants lacking a HSPG motif *in vitro* and showed strong eGFP expression *in vivo*. Moreover, AAV9.NNR, AAV9.GLR and AAV9.RAAK mediated efficient transduction of the non-pigmented epithelium (NPCE) of the ciliary body in C57BL/6 mice.

Further, we explore the potential of a novel vaccination platform which uses AAV capsids as scaffolds for large immunogenic epitopes to induce strong and specific immune responses using COVID-19 as a model disease to evaluate this approach. To this end, we introduced large immunogenic peptide insertions of approximately 200 amino acids on the surface exposed loop IV of AAV2 and AAV9. Empty, virus-like particles (VLPs) without vector genome were produced and administered subcutaneously in adult rabbits showing potent IgG and IgM responses specific to the presented antigen. Additionally, vector incubation with blood plasma of mRNA-vaccinated human donors resulted in antigen-specific neutralization effects *in vitro*.

In summary, we introduce novel AAV9-based capsid variants with artificial HSPG-binding motifs that show superior transduction efficiency for retinal cells and additional tropism for ciliary body cells. Furthermore, we present a novel platform that expands the toolbox of AAVs as immunogenic scaffolds for the development of next-generation vaccines in the context of diseases where traditional vaccination approaches have so far not succeeded.

2 Introduction

2.1 Adeno-associated viruses (AAVs) - a powerful tool

When Adeno-associated viruses (AAVs) were first discovered and characterized in 1965 [1], [2] probably no one could have imagined the impact these small viruses will one day have as gene therapy vectors. AAVs were discovered and described as "virus-like" particles (VLPs) and contaminant in the context of simian Adenoviruses (Ad) preparations and further classified as members of the *Parvoviridae* family in the *Dependoparvovirus* genus. Despite only low replication rates in the absence of Adenoviruses the substantial difference of AAVs regarding their immunogenic potential was immediately noticed [1]. From then on AAVs have been extensively characterized as potential therapeutic vectors [3]. Because of their low pathogenic potential for humans combined with a broad serotype dependent tissue tropism [4] and the capability for stable, long-term gene delivery [5], [6] AAVs have become a valuable tool in various gene supplementation approaches as well as unconventional vaccination strategies [7], [8].

2.1.1 Structure and characteristics of AAVs

AAVs are small, non-enveloped viruses carrying a single-stranded DNA (ssDNA) genome of 4.7 kb [9], [10]. The genome is flanked by self-priming origin of replication sequences [11] referred to as inverted terminal repeats (ITRs) [12]. The wildtype (WT) AAV genome contains two open reading frames (ORFs): *Rep* and *Cap* (Figure 1). The *Rep* ORF encodes for four non-structural Rep proteins (Rep78, Rep68, Rep52, and Rep40) derived from individual mRNA sequences. The Rep proteins play an essential role in viral genome transcription, replication and shuttling into assembled AAV capsids [13]. The larger proteins Rep78 and Rep68 are driven by the p5 promoter and harbor site-specific endonuclease, ATPase and DNA helicase activities while the two smaller proteins Rep52 and Rep40 are derived from the p19 promoter via splicing and are essential for genome packaging [14], [15]. The *Cap* ORF is controlled by the p40 promoter and encodes for three structural viral proteins (VPs) namely VP1, VP2 and VP3 with the respective molecular masses of 87, 72 and 62 kDa. These structural VPs form the AAVs characteristic icosahedral capsid comprising of 60 subunits considerably in a 1:1:10 ratio across VPs. The resulting capsid has a diameter of approximately 25 nm or 260 Å [16]. The structural viral proteins share the same C-terminal region within the Cap ORF but have a shifted N-terminal

region truncated by 65 amino acids for VP2 and 138 amino acids for VP3 compared to the full length VP1 [17].
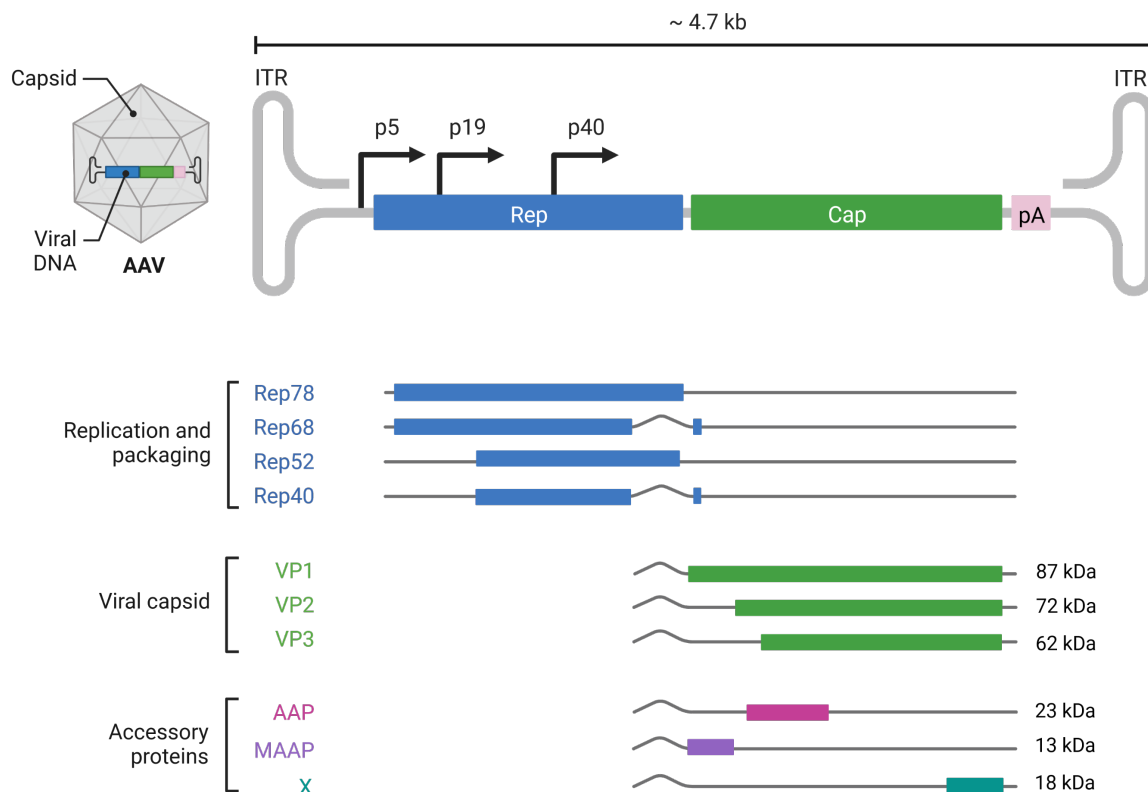
Figure 1 Structure of the AAV genome Schematic depiction of the *Rep* (blue) and *Cap* (green) ORF flanked by inverted terminal repeats (ITRs), AAP assembly-activating protein, MAAP membrane-associated accessory protein, ORF open reading frame, pA polyadenylated tail, X protein X

The AAV capsid can be viewed from three different symmetry axes: The twofold, threefold, and fivefold axis (Figure 2). The fivefold axis is characterized by an 8.5 Å pore which allows for the AAV genome to be shuttled into the assembled viral capsid. Mutations in this region have shown to strongly alter genome packaging efficiency [18]. Further, the N-terminal region of VP1 encodes for the phospholipase A2 (PLA2) which proved to be crucial for the infectivity of AAVs [19], [20].

The *Cap* gene also encodes for three additional proteins, originated from alternative start codons or reading frames [21], namely the assembly activating protein (AAP), the membrane-associated accessory protein (MAAP) and protein X. The AAP results from an alternative reading frame within the VP2/VP3 N-terminal region. This approximately 23 kDa protein is expressed in the nucleolus of the infected host cell and mediates effective capsid assembly by coordinating the subunits for correct interaction and maturation of a functional AAV capsid [22]. Furthermore, the MAAP (13 kDa) was initially discovered to limit efficiency of AAV

production but is today known to play an essential role in viral secretion from host cells [23], [24]. Only little is known about the protein X but it has shown that this 18 kDa protein is involved in upregulation of DNA replication in the presence of Adenoviruses but also promoting autonomous DNA replication in keratinocytes [25].
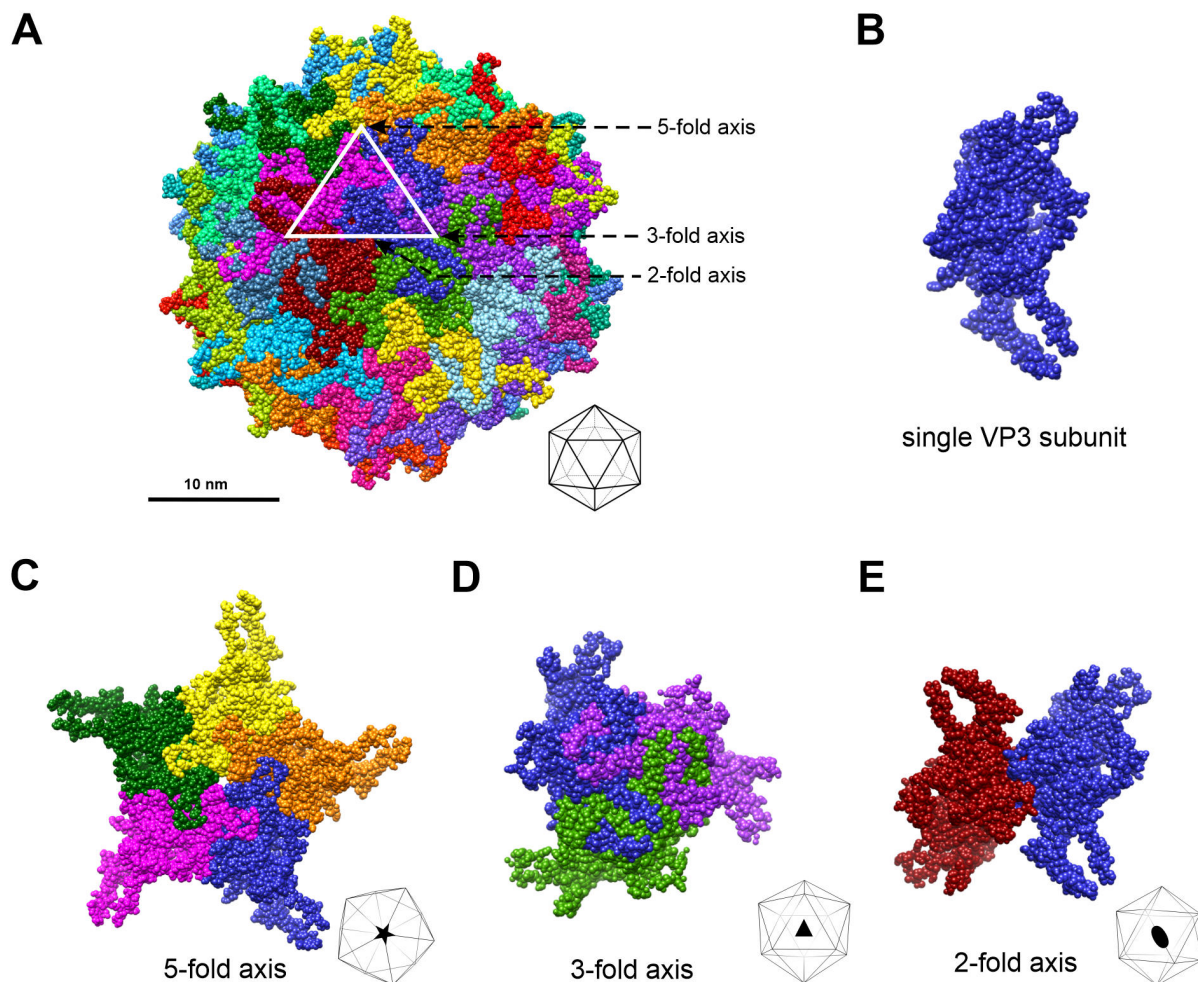
Figure 2 AAV9 capsid orientation (A) Biological assembly of the AAV9 capsid (PDB: 3ux1) created with UCSF Chimera. Triangle (white) marks the symmetry axes (B) Single AAV9 VP3 monomer (C) 5-fold symmetry axis view with the central pore as genomic entry point (D) 3-fold axis view (E) 2-fold axis view [adapted from [26], [27]]

2.1.2 Infectious cycle of AAVs

AAVs are known to interact with specific surface-exposed receptors presented on the host cells. The primary binding receptor varies between AAV serotypes and defines the specific cell tropism [28], [29]. Attachment of AAVs to their respective primary receptor on the cell surface can be increased by co-receptors such as integrins or growth factor receptors [30], [31]. Upon binding, the AAV/receptor-complex gets internalized into the host cell by endocytosis and is rapidly shuttled in clathrin-coated vesicles [32] along the intracellular microtubule network [33] towards the nucleus, where the virus eventually escapes endosomal encapsulation by

acidification of the vesicle [32], [34]. AAVs enter the nucleus through nuclear pore complexes (NPCs) embedded in the membranes of the nuclear envelope (NE) [35]. In the nucleus the viral genome is uncoated followed by ssDNA conversion into dsDNA [36]. The dsDNA persists at an episomal state in the nucleus [37] and eventually gets transcribed into mRNA which is shuttled into the cytosol and translated into a protein (Figure 3). As with other members of the *Dependoparvoviridae* genus, AAV requires co-infection of the cell with a helper virus such as herpes simplex virus 1 (HSV-1) or adenovirus 5 (AdV5) to enable AAV replication [38], [39].
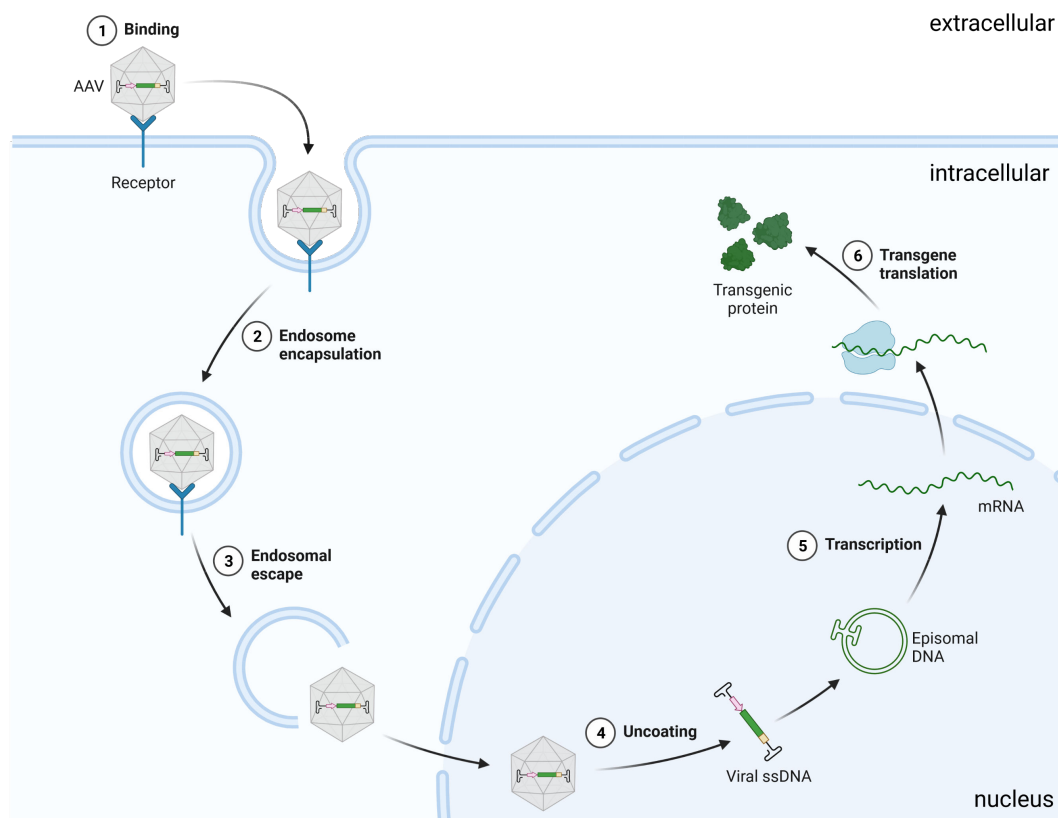
Figure 3 Infectious cycle of AAVs Schematic shows AAV binding to a surface exposed receptor (1) followed by viral uptake into the cell (2) and intracellular endosomal escape (3) prior to entering the nucleus. Subsequently, the AAV is uncoated (4) releasing its ssDNA genome which is converted into double-stranded DNA (dsDNA) in an episomal state. After transcription into mRNA (5) the transgene is shuttled into the cytosol following protein biosynthesis (6) [adapted from Biorender.com].

To date, a variety of naturally occurring AAV serotypes have been identified and isolated from different species. So far 13 maternal serotypes have been found not counting subtypes with only minor amino acid changes [40]. AAV1-10 have been widely characterized focusing on factors like tissue or cell-type specific tropism, general infection capabilities, immunogenic potential or capsid structure [41]–[43]. Extensive characterization of AAV serotypes allowed for mapping of preferred tissue tropism and interaction partners such as primary cell entry receptors (Table 1).

Table 1: Tissue tropism of natural AAV serotypes 1-10 Note that not every tissue specificity was shown across species, [adapted from [3]] CNS central nervous system, SM skeletal muscle

Serotype	Origin	Primary receptor	Secondary receptor	Tissue tropism
AAV1	primate	N-linked sialic acid	AAVR, GPR108, TM9SF2	SM, CNS, lung, retina, pancreas, heart, liver
AAV2	human	heparan-sulfate proteoglycan	AAVR, GPR108, TM9SF2, LamR, αVβ5 integrin, α5β1 integrin, FGRF1, CD9, HGFR	SM, CNS, liver, kidney, retina, lung
AAV3	human	heparan-sulfate proteoglycan	AAVR, GPR108, HGFR TM9SF2, LamR, FGRF1,	Liver, SM, CNS
AAV4	NHP	O-linked sialic acid	GRP108	CNS, retina, lung, kidney, heart
AAV5	human	N-linked sialic acid	AAVR, PDGFR, TM9SF2	SM, CNS, lung, retina, liver
AAV6	human	N-linked sialic acid, heparan-sulfate proteoglycan	AAVR, GPR108, TM9SF2, EGFR	SM, heart, lung, liver, CNS, retina
AAV7	rhesus macaque	-	GPR108, TM9SF2	SM, retina, CNS, liver
AAV8	rhesus macaque	-	AAVR, GPR108, TM9SF2, LamR	Liver, SM, CNS, retina, pancreas, heart, kidney
AAV9	human	terminal N-linked galactose of sialic acid	AAVR, GPR108, TM9SF2, LamR	Liver, heart, SM, lung, pancreas, CNS, retina, kidney
AAVrh.10	rhesus macaque	-	GRP108, LamR	Liver, heart, SM, lung, pancreas, CNS, retina, kidney

2.1.2.1 Glycan binding of AAVs

Various studies have shown that primary receptors of natural AAV serotypes mostly involve binding to glycan residues, however there are differences across serotypes [34], [44]. Overall AAVs can be divided into three major groups based on their glycan receptor binding: Heparan sulfate proteoglycan (HSPG) which is used by AAV2, AAV3, AAV6 and AAV13. Different sialic acid (SIA) residues are used amongst AAV1, AAV4, AAV5 and AAV6 while AAV9 exclusively uses galactose (GAL) as a primary receptor (Figure 4). However, primary receptors for some AAV serotypes, such as AAV7, AAV8 and AAVrh.10 remain unknown so far [28], [45].

HSPG are glycoproteins composed of negatively charged heparan sulfate (HS) polysaccharide chains which function as potent receptors on many cell surfaces or extracellular matrices [46]. Based on their location they can be divided into membrane HSPGs such as syndecan 1-4, extracellular matrix HSPGs as agrins and lastly secretory vesicle proteoglycans such as serglycin [47]. HSPGs have been found to be involved in many biological processes such as angiogenesis [48], cell homeostasis [49], immune reactions [50] and regulation of protease activity [51], [52].
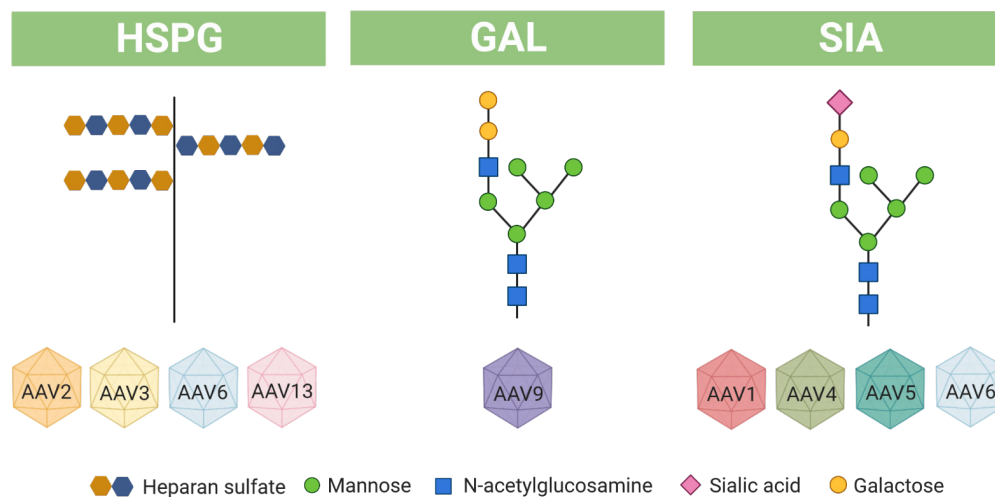
Figure 4 Overview of typical primary receptors of AAVs HSPG heparan-sulfate proteoglycan, GAL galactose, SIA sialic acid (simplified).

Moreover, HSPGs were found to be highly involved in AAV2 cell entry [53]. Due to their highly negative charge, positively charged amino acids such as arginine und lysine in close proximity to one another were found to mediate efficient HSPG-binding in AAV2, namely R585 and R588 [54]. Other AAV2 capsid residues have been shown to participate in HSPG-binding, such as R484, R487, and K532 [55]–[57].

So far, AAV9 is the only natural AAV serotype that has been found to bind to N-linked galactose (GAL) residues [28]. In 2012 Bell et al. discovered the exact GAL binding pocket on the AAV9 capsid which is located next to the protrusions around the 3-fold symmetry axis [58]. The binding of GAL was shown to depend on N470, D271, N272, Y446 and W503 which either forms strong hydrogen bonds or interacts with their aromatic residues with the sugar. In line with this, subretinal (SR) injection of AAV9 in non-human primates (NHPs) results in efficient transduction of cone photoreceptors, which show high levels of galactose on their cell surface [59]. However, AAV9 binding seems to involve additional mechanisms, e.g. interaction with surface exposed laminin receptors (LamR) [60].

AAV1, AAV4, AAV5 and AAV6 attachment to cell surfaces was shown to involve binding to N- or O-linked sialic acid (SIA) [61]. For AAV5 the three major binding positions have been identified to be M569, L587 and Y585 which are responsible for activation and binding specificity [62].

2.2 Ocular gene therapy approaches using AAVs

2.2.1 Anatomy of the mammalian retina

The mammalian retina is a sensory tissue with an average thickness of 100-200 μm located in the back of the eyes. It is a complex neuronal network of inverted structure which allows for detection and initial processing of light stimuli [63], [64]. The retina is comprised of five neuronal cell types: the photoreceptors, bipolar cells, horizontal cells, amacrine cells and ganglion cells which are organized within the retina in different cell layers (Figure 5) [65]. Moreover, Müller glia cells, microglia cells and astrocytes support metabolic, homeostatic and immunological functions within the retina [65], [66]. The photoreceptors can be divided into rods, which are responsible for highly sensitive dim light vision, and cones, which provide high-focus color vision in daylight [67]. The photoreceptors are highly compartmentalized cells with outer and inner segments, cell bodies, an axon, and a ribbon synapse. The photoreceptor synapses form the outer plexiform layer (OPL), whereas cell bodies and axons are forming the outer nuclear layer (ONL). The inner and outer segments extend out of the ONL towards the retinal pigment epithelium (RPE). RPE cells form a tight monolayer that constitutes the outer blood-retina-barrier (BRB) playing an essential role in maintaining the privileged immune status of the eye [68]. As highly pigmented cells, they absorb scattered photons after high intervals of light stimuli. Moreover, RPE cells maintain the recycling of photoreceptors as well as their metabolic processes [69], [70]. After stimulation the photoreceptors transfer the signal via chemical synapses and the neurotransmitter glutamate to the bipolar cells at the OPL. Bipolar cells are classified into two subclasses: ON-bipolar cells, which receive input from rods and/or cones and hyperpolarize upon stimulation and OFF-bipolar cells, which are depolarizing and only synapse with cone photoreceptors [71].

Additionally, synapses of horizontal cells located at the OPL help in modulating signals between bipolar cells and photoreceptors. At the inner nuclear layer (INL) cell bodies of bipolar, amacrine and horizonal cells are located. Signals from photoreceptors are transferred to the ganglion cells via bipolar cells. Horizontal cells function as feedback provider for the photoreceptors [72]. The axons of the bipolar cells communicate with the ganglion cells at the IPL. Here the amacrine cells modulate between both cell types to prevent potentiation of the electrical signal [73]. The ganglion cell layer (GCL) subsequently holds somata of displaced amacrine cells as well as the cell bodies of the ganglion cells. The nerve fiber layer (NFL)

consists of the axons of ganglion cells, which form the optic nerve as well as Müller glia processes and astrocytes [74].
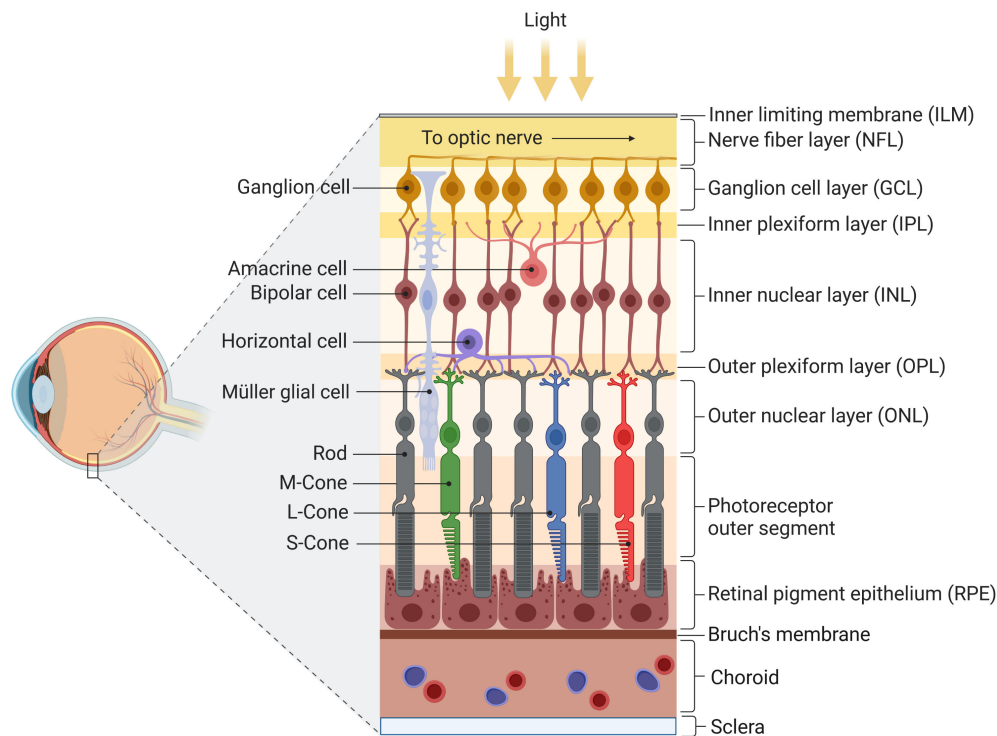
Figure 5 Anatomy of the mammalian retina Schematic illustrates the inverted structure of the mammalian retina and the cell layers to be passed by light stimuli during phototransduction [adapted from Biorender.com].

Lastly, the inner limiting membrane (ILM) as the innermost part of the retina shields it from the vitreous humor. Müller glia cells, which maintain the retinal homeostasis, reach into this thin monolayer with their endfeet. Furthermore, the ILM is also a critical point during ocular gene therapy due to its widely exposed HSPG residues [75].

2.2.1.1 Anatomy of the ciliary body

The ciliary body is a ring-shaped structure within the eyes of mammals responsible for accommodation of the lens as well as production of ocular fluids and maintenance of the intraocular pressure (IOP) [76]. It is located in the periphery of the neural retinal behind the iris and connects the lens and sclera. It can be divided into the ciliary muscle, ciliary processes, and ciliary epithelium. The ciliary muscle is a ring-shaped smooth muscle extending from the *ora serrata* (Figure 6A, blue dashed line) which separates retina from ciliary body. The ciliary muscle is responsible for the accommodation of the eyes focusing objects onto the retina [77]. The ciliary processes are radially folded protrusions with epithelial cells responsible for the production and secretion of aqueous humor (AH) into the posterior chamber [78]. The ciliary epithelium is a two-layered structure which can be divided into the outer layer, the non-

pigmented ciliary epithelium (NCPE) and the inner layer, the pigmented ciliary epithelium (PCE) (Figure 6).
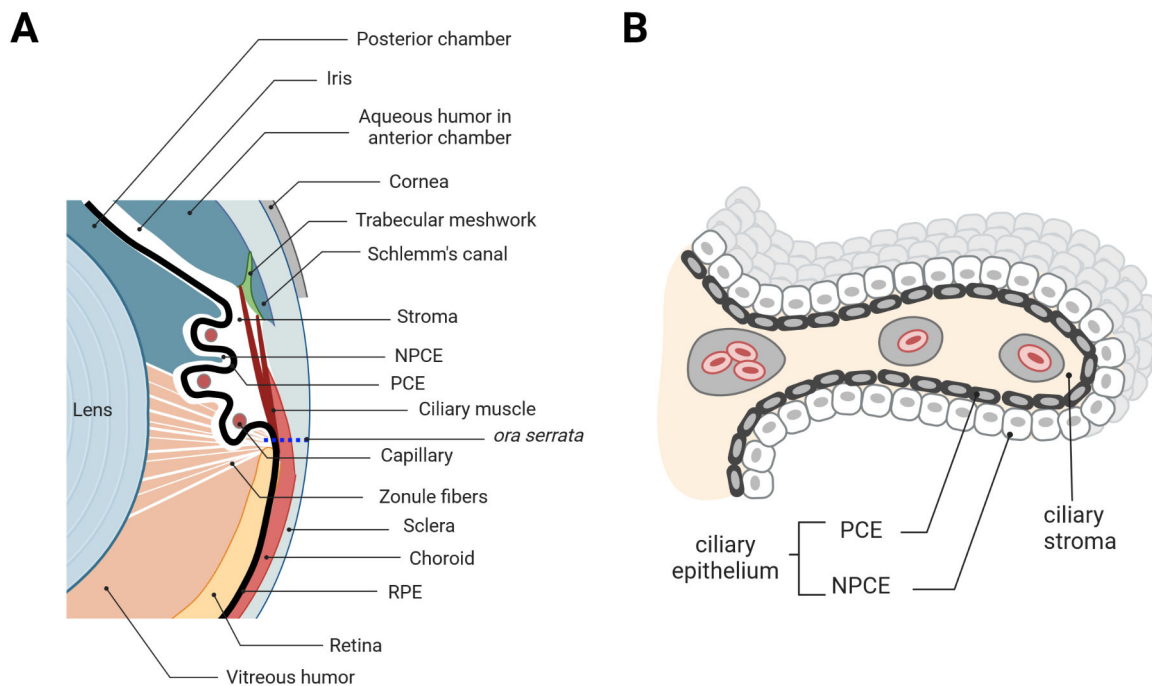
Figure 6 Anatomy of the ciliary body (A) radial view of the ciliary body (B) close-up on the ciliary processes and the ciliary epithelium, PCE pigmented ciliary epithelium, NPCE non-pigmented ciliary epithelium, RPE retinal pigment epithelium [adapted from [79], [80]].

The NPCE is responsible for the production and secretion of AH which provides the lens with nutrients but is also crucial for the maintenance of the IOP, and thus, the shape of the eyeball [81], [82]. The PCE provides the ciliary body with nutrients [83] and also plays an important role in the synthesis of the zonule fibers which center the lens [84], [85]. The ciliary body is supplied with blood from the major ciliary arteries derived from the ophthalmic artery. Tight-junctions between NPCE and the blood vessels build the blood-aqueous barrier [86], [87]. Under physiological conditions, there is a dynamic balance between secretion of the AH from the NPCE into the vitreous and drainage of fluids through the trabecular meshwork into the Schlemm's canal [81], [88]. Imbalances in the production and recycling of ocular fluids can lead to increased IOP and subsequently glaucoma [89], [90].

2.2.1.2 Comparison of human and mouse eye

Due to the ease of genetic manipulation, mice are the most commonly used animal model for investigation of inherited retinal dystrophies (IRDs) and testing experimental gene therapeutic approaches [91], [92]. Often knock-out mouse lines carrying genetic modifications to have a specific gene deletion or non-functional alteration to evaluate supplementation or gene

editing strategies [93], [94]. However, when transferring the results from mice to humans, some anatomical differences must be considered (Figure 7).
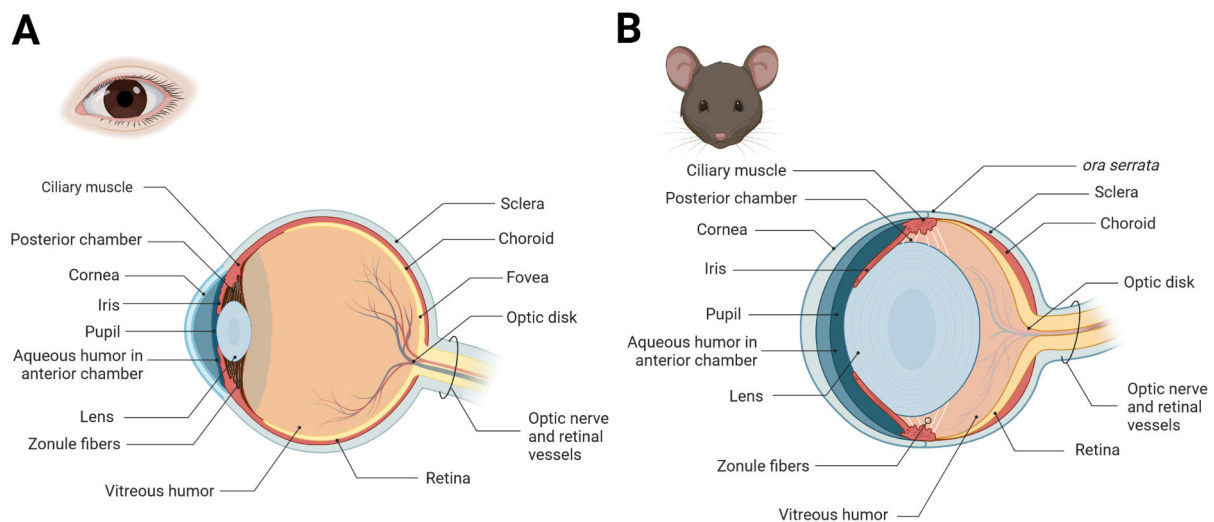
Figure 7 Anatomy of human and mouse eye in comparison Schematic illustrates the anatomic differences between human (A) and mouse (B) eye. Especially the lens and the vitreous differ in size. Additionally, the *fovea centralis* is only present in human eyes.

Firstly, the mouse eye is significantly smaller, which is why many therapeutic approaches after initial evaluation in the mouse model need to be tested in large animals for dose finding studies [95]. Additionally, mice are known to show lower immunogenic reactions compared to observations from clinical trials [96]. Furthermore, the size of the lens is enlarged in mice, which poses an increased risk of lens injury, causing opacification after injection [97]. Due to the increased lens, the vitreous of mice is notably smaller and bears a lower volume of fluids compared to humans [98]. The human retina has a unique cone-rich macula with a cone-only foveal pit (*fovea centralis*), which mediates high acuity vision [99], [100]. The mouse retina lacks a fovea, is rod dominated and shows similar relative cone and rod photoreceptor ratio across the entire retinal area [101].

2.2.2 Photoreceptors and phototransduction

Photoreceptors are highly specialized, light-sensitive neurons that play an essential role in the process of phototransduction and hereby in the process of vision [102]. They are located in the outer parts of the retina and their outer segments are engulfed by microvilli or RPE cells, which support recycling of visual pigments and provide the photoreceptors with nutrients [103]. In general, photoreceptors consist of five major compartments: The inner segment (IS)

and outer segments (OS) which are joined by a connecting cilium (CC), the cell body containing the nucleus and the synaptic terminal [102]. Rod photoreceptors are characterized by their cylindrical OS which consists of a plasma membrane containing a high density compartment of closely stacked phospholipid bilayer discs [104]. In the conical structure of the cone photoreceptor OS these discs were found to be a continuation of the plasma membrane [105]. The inner segments (IS) contain the metabolic machinery which consists of several subcellular organelles but mostly mitochondria, providing the photoreceptors with the appropriate amount of energy during phototransduction [106]. The single axon of photoreceptors concludes with the synaptic terminal region where the signals get chemically transmitted by the neurotransmitter glutamate in synaptic vesicles to the adjacent bipolar cells. During this process the CC allows for protein shuttling between IS and OS [107].

The fundamental difference between vision in mice and humans is their perception of colors (Figure 8): Humans are trichromats, meaning they have typically three types of cones expressing the photopigment opsin with absorption peaks at different wavelengths for color vision: The S-cone (blue, 430 nm), the M-cone (green, 531 nm), and the L-cone (red, 561 nm) which allow for visualizing of color and contrasts at different wavelengths [108], [109]. Mice on the other hand are nocturnal animals and dichromats. They are missing the L-cones and show a more blue-shifted vision spectrum [110]. Their range of detection for green and blue signals also differs in wavelength compared to humans with maximum absorbance at 360 nm for blue (S-cones) and 508 nm for green (M-cone) [111]. However, most cones in mice were found to express both pigments simultaneously (S/M-cone) [112].
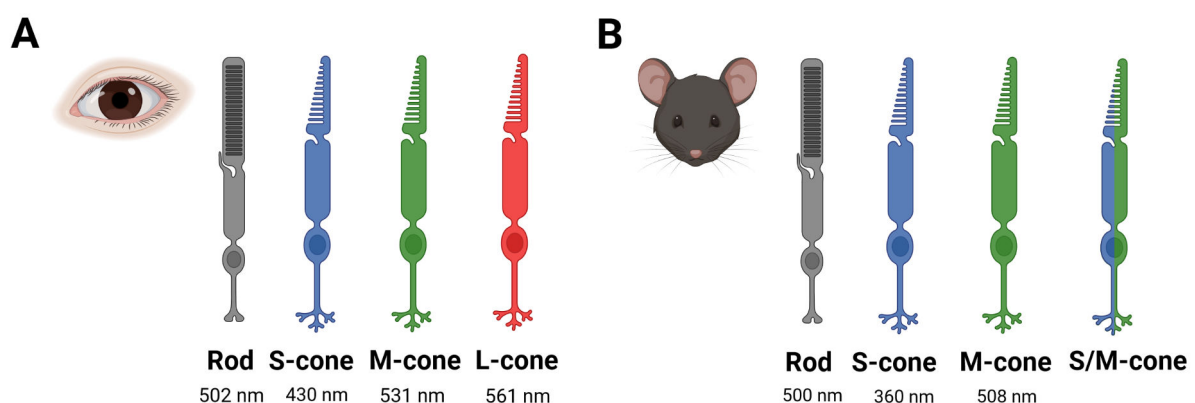
Figure 8 Spectrum of color vision in human vs. mouse Humans are trichromats showing three different types of cones: S-cones, M-cones, and L-cones (A) expressing the photopigment opsin with absorption peaking at different wavelengths (B) Mice as dichromats have two types of cones: S-cones and M-cones, although most cones express both photopigments simultaneously (S/M-cone).

The process of converting light stimuli into a chemical and subsequently an electrical signal in the retina is called phototransduction (Figure 9). Under dark conditions the guanylyl cyclase (GC) continuously produces cyclic guanosine monophosphate (cGMP) which keeps the cyclic nucleotide-gated ion channels (CNG) open and results in an Na^+ and Ca^{2+} Influx increasing the membrane potential (-30 mV) [113]. Without light stimuli the photoreceptors are depolarized and continuously release glutamate at the synaptic terminal [114]. After light stimulus a G-protein-coupled cascade is initiated: Illumination results in isomerization of the photopigment rhodopsin from its 11-*cis*-retinal into the all-*trans*-retinal state [115]. This causes a conformational change of rhodopsin into its active form. Activated rhodopsin now exchanges the transducin-bound guanosine diphosphate (GDP) with guanosine triphosphate (GTP) which ultimately results in the α-subunit of the transducin-complex to be released and trigger the phosphodiesterase (PDE) to hydrolyze cGMP into GMP. The decreasing cGMP-level causes the CNG channel to close preventing Na^+ and Ca^{2+} influx which subsequently leads to hyperpolarization of the membrane (-70 mV). The low membrane potential prevents further glutamate release at the synaptic terminal of photoreceptors [116].
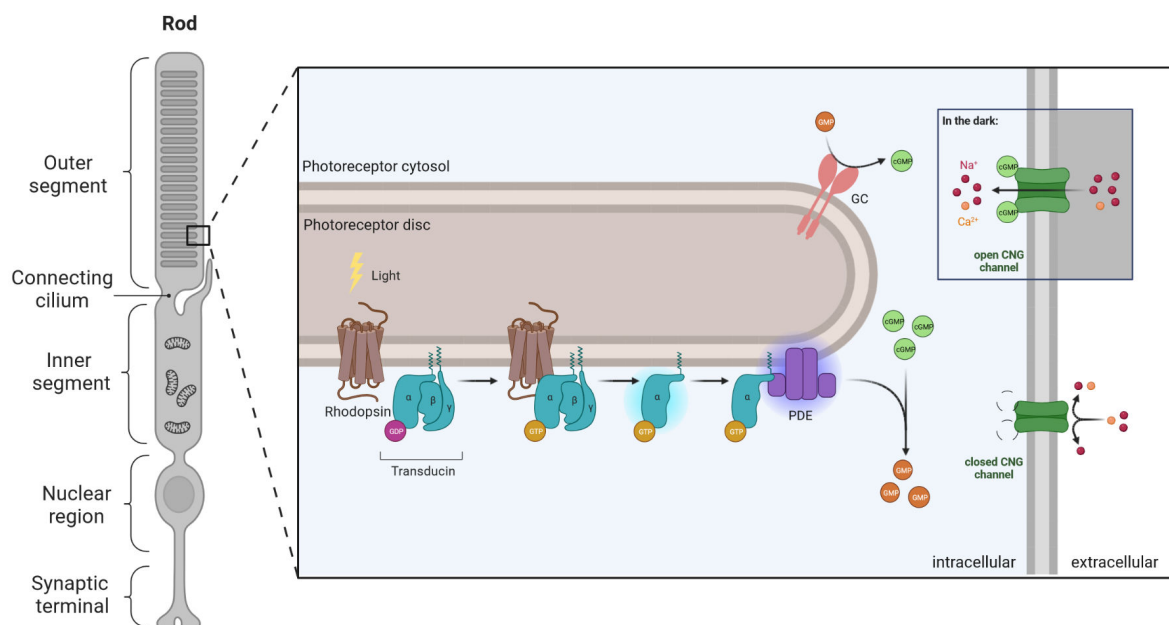
Figure 9 Phototransduction in rod photoreceptors Schematic illustrates the G-protein coupled cascade initiated after light stimuli in the outer segment of a rod photoreceptor. cGMP cyclic guanosine monophosphate, CNG cyclic nucleotide-gated ion channels, GC guanylyl cyclase, GDP guanosine diphosphate, GTP guanosine triphosphate, PDE phosphodiesterase [adapted from Biorender.com].

2.2.3 Inherited retinal dystrophies (IRDs)

The eyes are without doubt one of our most valuable sensory organs. They allow us to perceive our surroundings, process enormous amounts of stimuli and appreciate the world and the people we see. Slowly losing the visual sense due to disease progression is a cruel process for patients as well as for their loved ones to witness [117]. However, treatment possibilities for intervening in retinal degeneration are rare, expensive, and mostly rely on individualized therapeutic strategies on a genomic level [118].

IRDs are a heterogenous group of monogenetic disorders characterized by retinal degeneration over time and subsequently loss of vision which affects nearly 6 Mio people worldwide [119]. Until today, nearly 300 retinopathy genes have been identified [1]. Disease onset and progression vary strongly between IRDs. In addition, the attempted treatment strategies differ in preclinical and clinical studies.

The most common IRD is retinitis pigmentosa (RP) which is characterized by primary loss of rod function, followed by rod degeneration and secondary cone degeneration. Patients initially develop a night blindness followed by progressive loss of peripheral vision. RP can manifest either as an autosomal dominant form or with an autosomal recessive or x-linked recessive genotype. Genes found to be involved in RP include *CNGA1, CNGB1* and *PDE6A* among others [120]–[122]. In contrast, achromatopsia (ACHM) is the most common cone dysfunction syndrome which is characterized by congenital lack of cone function that manifest in color blindness, low visual acuity, nystagmus and photophobia [123]. More than 90% of ACHM cases are due to mutations in *CNGA3* or *CNGB3* [124]. Lastly, Leber congenital amaurosis (LCA) also belongs to the group of early onset diseases with severe visual impairment. The speed of progression of LCA is dependent on the involved genes. In this context *RPE65*-linked LCA is widely discussed because of the first FDA-approved AAV-based ocular gene therapy Luxturna® (voretigene neparvovec-rzyl) [125].

2.2.4 Principle of *in vivo* gene therapy - AAVs as vectors

Gene therapy is a widely used method generally referring to the introduction of genetic material *ex vivo* into cells or tissues as well as *in vivo* into a living organism [126]. For diseases originating in defective genes therapeutic intervention can be attempted by (1) gene

supplementation of a functional copy into the target cells [127], (2) gene editing tools such as CRISPR/Cas9 or Zinc finger nucleases to correct single bases *in vivo* [128], (3) symptomatic therapy by supplementation of proteins or antibodies to improve the phenotype of the disease [129], [130] or (4) nucleic acid-based knock-down of incorrect or non-functional proteins via siRNAs [131].

AAVs have become increasingly popular as a tool for targeted gene therapy due to their ability to efficiently infect a broad spectrum of cells and tissue types [132] and their potential to induce long-term gene expression in non-dividing cells [5], [6]. Additionally, AAVs are replication deficient without the presence of an AdHelper virus [39]. Moreover, recombinant adeno-associated viruses (rAAVs) have been engineered to only express the gene of interest (GOI) driven by a previously selected promotor allowing for a pre-calculated amount of DNA that can be precisely administered [133].

Gene supplementation therapies for IRDs as mentioned above are currently widely investigated. The eyes as a target organ for gene therapy offer many advantages due to their highly compartmentalized location [134], which is easily accessible from outside. AAV vectors can be administered locally in a minimal invasive way, which also allows for lower vector doses to be applied [135]. Post-surgery monitoring of the treated area and the overall retinal condition can be conducted via the pupils by optical coherence tomography angiography (OCT-A) or confocal scanning laser ophthalmoscopy (cSLO). Moreover, the eye is considered immune privileged and mostly not affected by systemic immune reactions due to the blood-retina-barrier and the blood-aqueous-barrier [68], [86], [136]. Potentially occurring local immune reactions can be monitored and treated comparably well with topical anti-inflammatory regimens [137].

For ocular gene supplementation approaches an ITR-flanked transgene cassette containing the GOI, for example, a healthy copy of the affected gene in an IRD patient, under the control of a tissue- or cell type-specific promotor and a polyadenylation (pA) signal is vectorized into an AAV and administered into the eye (Figure 10A). Ideally the transgene is expressed at a level sufficient to compensate the missing function and prevent further progression of the disease.
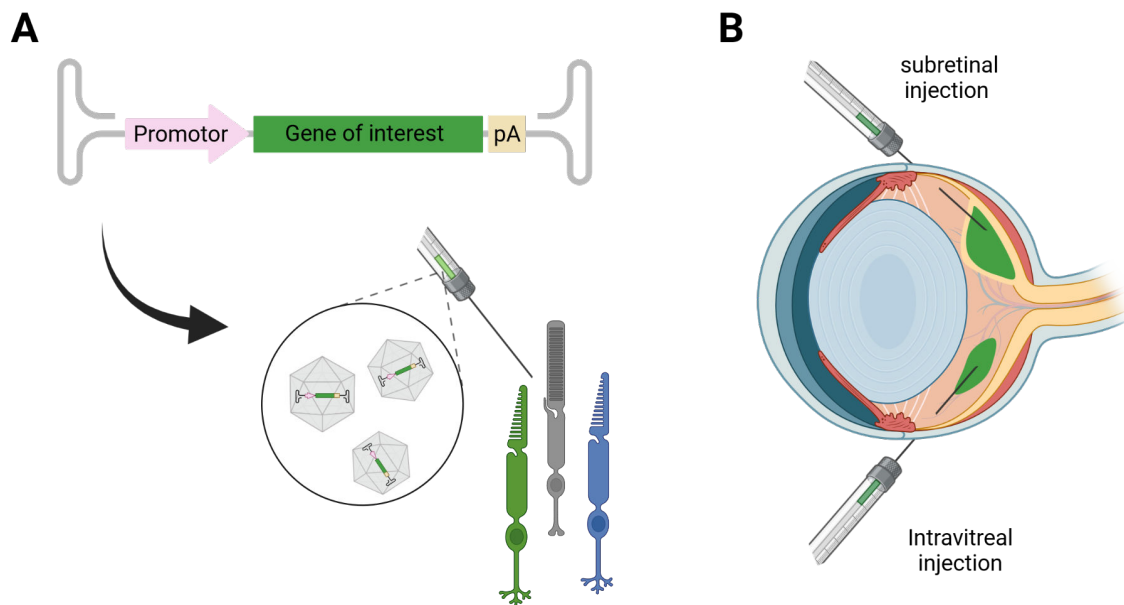
Figure 10 Overview of retinal gene therapy (A) Schematic shows a transgene expression cassette for retinal gene therapy (B) Illustration of the intravitreal vs. subretinal AAV vector delivery into a mouse eye.

The current gold standard in retinal gene therapy is the AAV administration via subretinal injection (SR). Here, the vector is directly applied near the desired target cells between the photoreceptors and the RPE for efficient transduction rates (Figure 10B). This route of delivery however relies on retinal detachment and can cause tissue damage at the injection site [138]. Moreover, the therapeutic effect is often limited to the subretinal bleb and larger areas need to be treated with multiple injections [139]. An alternative administration route is provided by the intravitreal injection (IVT). IVT delivery does not require retinal detachment. The vector is released into the vitreous fluid which allows for broader diffusion and exposure to a larger retinal area [140]. However, this application route poses many challenges for the vectors, as the inverted retinal anatomy requires for many cell layers of the retina to be passed before reaching the main target cells: the photoreceptors and RPE. Moreover, many AAV vectors cannot efficiently surpass the ILM separating retina and vitreous fluid, and thus, cannot support transduction of outer retinal cells [141].

2.2.5 History of AAV-based gene therapy - chances and limitations

Since their discovery, AAVs have been explored in clinical applications with over 150 ongoing studies in Phase III (http://www.genetherapynet.com/clinical-trials.html). Especially gene supplementation strategies for various inherited diseases are tested. To fulfill the unmet need

for sufficient treatment of mostly rare disorders a variety of single or dual vector delivery systems are currently investigated in preclinical approaches.

The first ever AAV-based drug Glybera® (alipogene tiparvovec) to treat lipoprotein lipase deficiency (LPL) was approved in 2012 by the European Medicines Agency (EMA). This gene therapy product was based on AAV1 and supplements the coding sequence of the human lipoprotein lipase which is absent or non-functional in patients leading to accumulation of lipoproteins in the plasma with the risk of causing severe pancreatitis [142], [143]. However, the drug was removed from the market in 2017 since worldwide only 31 people were treated due to low demand, high costs and challenges with reimbursement [144].

In 2017 Luxturna® (voretigene neparvovec-rzyl) an AAV2-based gene therapy approach for treating *RPE65*-linked Leber congenital amaurosis (LCA) was approved by the Food and Drug Administration (FDA) following market access in the EU in 2018 and in Australia and Canada in 2020. This was the first FDA-approved gene therapy for IRDs by delivering a functional copy of the human *RPE65* gene which causes progressive vision loss if mutated [145], [146].

Only two years later, in 2019, the first AAV9-based gene therapy Zolgensma® (onasemnogene abeparvovec-xioi) was granted market access after FDA-approval. This gene supplementation therapy delivers the survival motor neuron 1 (*SMN1*) gene in patients with mutations in both alleles of the same gene that causes spinal muscular atrophy (SMA) [147], which is the leading cause for infant mortality in genetic disorders [148], [149].

In June 2022 Elevidys® (delandistrogene moxeparvovec-rokl) was approved by the FDA as the first gene therapy for treatment of pediatric patients suffering from Duchenne muscular dystrophy (DMD). The vector capsid AAVrh74 is packaged with a ssDNA transgene cassette encoding for the micro-dystrophin protein [150].

Only one month later, in July 2022, Upstaza® (eladocagene exuparvovec) a gene therapy for patients with inherited severe aromatic L-amino acid decarboxylase (AADC) deficiency received EU approval. This gene therapy based on AAV2 delivers the dopa decarboxylase (*DDC*) gene which encodes for an enzyme crucial for dopamine production in the CNS [151], [152].

In November 2022 the first gene therapy for Haemophilia B Hemgenix® (etranacogene dezaparvovec-drlb) based on AAV5 was approved by the FDA. In February 2023, it received the EMA approval for conditional medical use within the EU. Hemgenix® is indicated for patients with congenital Factor IX deficiency resulting in severe bleeding. The AAV5 capsid is packaged with a functional factor IX expressing cassette which proved to normalize coagulation in patients [153].

Just recently, in late June 2023 the first gene therapy for severe Hemophilia A Roctavian® (valoctocogene roxaparvovec-rvox) received full FDA-approval. This AAV5-based gene therapy is indicated for patients suffering from congenital factor VIII deficiency with no pre-existing neutralizing anti-AAV5 antibodies [154].

Although engineering AAVs for gene therapy has become a highly rewarding strategy there are also limitations and recurring challenges. While natural AAV serotypes have been investigated intensively, tailoring novel AAV capsids more specialized to the desired cell or tissue type is the current most viable strategy to improve efficacy and overcome problems such as off-target effects [155]. In combination with cell type-specific promotors [156] this allows for increased safety in regards to possible clinical applications. Many directed evolution approaches based on peptide display or genome shuffling libraries have resulted in capsid variants superior to the intended need than natural serotypes [157]. Since we continue to further understand the capsid structure and its interactions with cell receptors and the immune system, many rational design approaches are currently conducted [158], [159]. However, novel capsid variants that have proven superior in *in vitro* or *in vivo* animal models often fail to translate to human applications [160]. Even more, effects of novel capsids remain only successful in the model they were discovered and do not translate to other species [161]. This has been seen especially in immune reactions which vary between rodents and large animals such as NHP [162]. Another recurring issue is the genome capacity of AAVs of approximately 4.7 kb, which limits it applicability to deliver only small genes [163], [164]. Moreover, the yield of AAV production is comparably low, and scaling up the manufacturing process involves high costs and labor [165].

2.3 A novel platform for engineered AAV-based vaccines

2.3.1 Our immune system - a remarkable defense mechanism

The human immune system is a highly evolved network to protect from infections. It is divided into the innate and the adaptive immune system. The first is an unspecific and immediate reaction to foreign pathogens, while the adaptive immune response is much slower but allows for precise, targeted responses tailored to the pathogen.

Upon first contact with a pathogen its antigens are recognized by antigen-presenting cells (APCs) of the innate immune system (Figure 11). This highly heterogenous group of immune cells counts macrophages, dendritic cells (DC), monocytes but also B-lymphocytes (B-cells) which belong to the adaptive immune system [166]. The recognition of antigens is mediated by pattern recognition receptors (PRRs) which detect specific conserved structures, namely pathogen-associated molecular patterns (PAMPs) on pathogens and present them on the cell surface or directly in the cytosol of APCs [167]. After pathogen-recognition by the APCs, a signaling cascade is triggered which leads to the secretion of various pro-inflammatory cytokines and chemokines [168]. The fragmented antigens are presented on the cell surface by the major histocompatibility complex (MHC). The antigen-presentation is the connection point between innate and adaptive immune system. MHC-I presents antigens from the cytoplasm that entered the host cell through the endogenous pathway (e.g. live attenuated viruses). The MHC-I presentation is recognized by CD8$^+$ T-cells or cytotoxic T-cells (T$_c$) while MHC-II presents antigens entering the cell through the exogenous route via phagocytosis (e.g. inactivated pathogens, recombinant proteins). MHC-II is recognized by CD4$^+$ T-cells or T-helper cells (T$_h$) [169], [170]. The APCs migrate further to the lymph nodes where T-cells are activated and further differentiated [171]. CD4$^+$ T$_h$ present the antigen via MHC-II to B-cells and further release cytokines, which subsequently activate B-cells to differentiate into plasma cells and produce antibodies specifically targeting the presented antigen [172]. After each infection some B- and T-cells remain as memory cells, which allows for a more specific and fast reaction upon next contact with the same pathogen [173]. Immunization strategies like vaccinations aim to trigger a mild version of this cascade without causing a full symptomatic outcome. The goal of successful vaccination is to achieve a long-term protection from infectious diseases by antigen-specific immune memory.
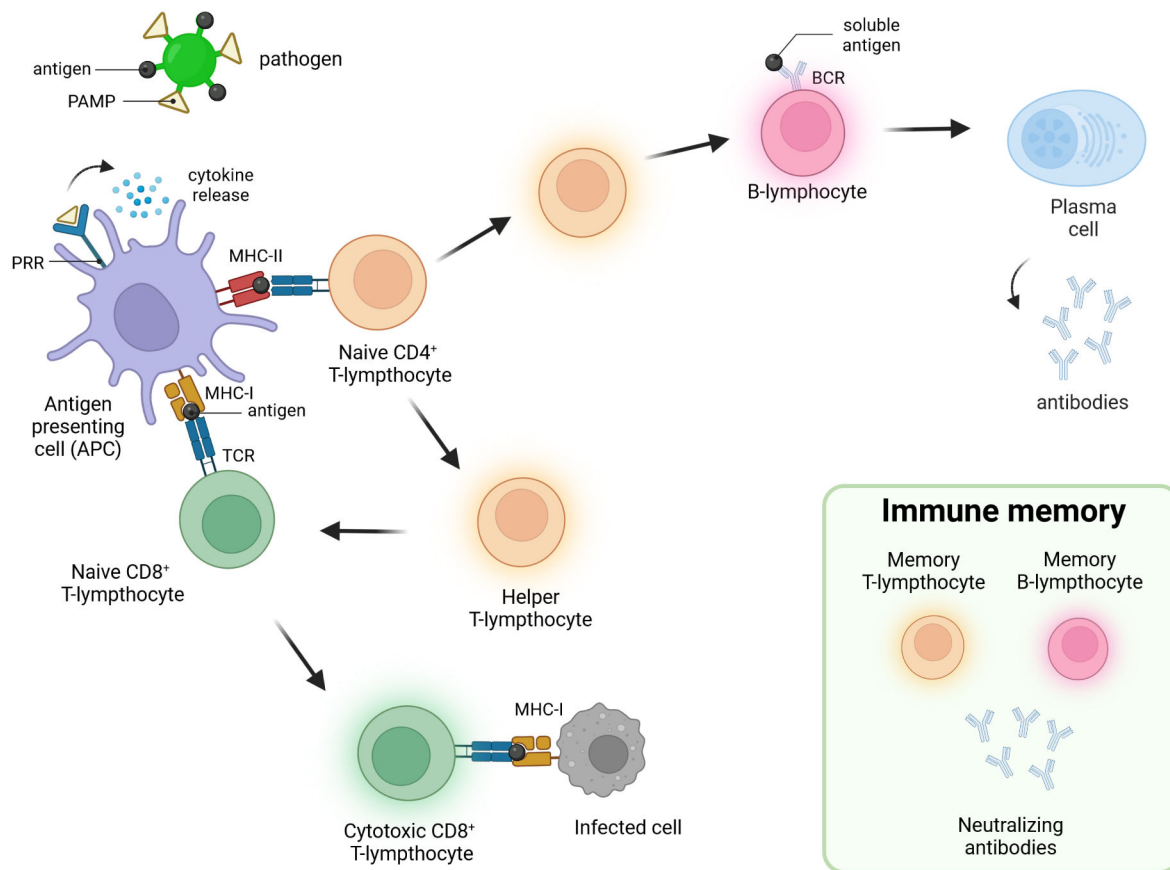
Figure 11 Innate and adaptive immune response Schematic shows the immune responses to an unknown pathogen including B-cell maturation and activation of T-cells; APC antigen presenting cell, BCR B-cell receptor, MHC major histocompatibility complex, PAMP pathogen-associated molecular patterns, PRR pattern recognition receptors, TCR T-cell receptor [adapted from [174]]

2.3.2 Evolution of vaccines - Immunization strategies

Vaccines are without doubt one of the most effective medical tools to protect from infectious diseases or to prevent severe complications hereby reducing morbidity and mortality [175], [176]. During the COVID-19 pandemic the world learned about the importance of fast and effective large scale vaccine development and manufacturing.

It started over 200 years ago, when Edward Jenner in 1796 attempted the first vaccination approach with fresh matter from cowpox wounds to protect from the more severe and at that time deadly smallpox infection [177]. The technology of vaccination spread around the world and ultimately led to the full eradication of smallpox in 1977 [178], [179]. Since then, vaccination strategies and technologies have evolved to overcome challenges and provide the best possible protection from threats to human health. Vaccines are considered biological therapeutics containing modified disease-specific pathogens that utilize and activate the highly evolved mammalian immune system to recognize, effectively target and remember

34

pathogenic antigens for an effective and fast immune reaction upon next contact [169]. So, vaccines serve as a tool for safely inducing mild immune responses aiming to protect from an actual infection. Vaccines can be divided into two basic forms of application: prophylactic vaccines to provoke a pathogen-specific immune reaction in healthy organisms or therapeutic vaccines containing antibodies (immunoglobulins) to fight a current infection or infection risk after direct exposure to a pathogen. While immunoglobulins help to efficiently fight disease outbreaks they do not protect from future infections by activating B- or T-cell memory [170].

Prophylactic vaccines traditionally consist of either live or non-live pathogens. Within the past decade, various next-generation technologies have been explored that differ from conventional vaccination and rely on nucleic acids, viral vectors, or virus-like particles (VLPs) (Figure 12). Vaccination with attenuated live pathogens induces a potent immune response to the weakened but still replication competent pathogen ideally without provoking a symptomatic infection e.g. measles [180]. As a result live attenuated vaccines for some diseases only need a one-time treatment to result in a live long protection e.g. yellow fever [181].
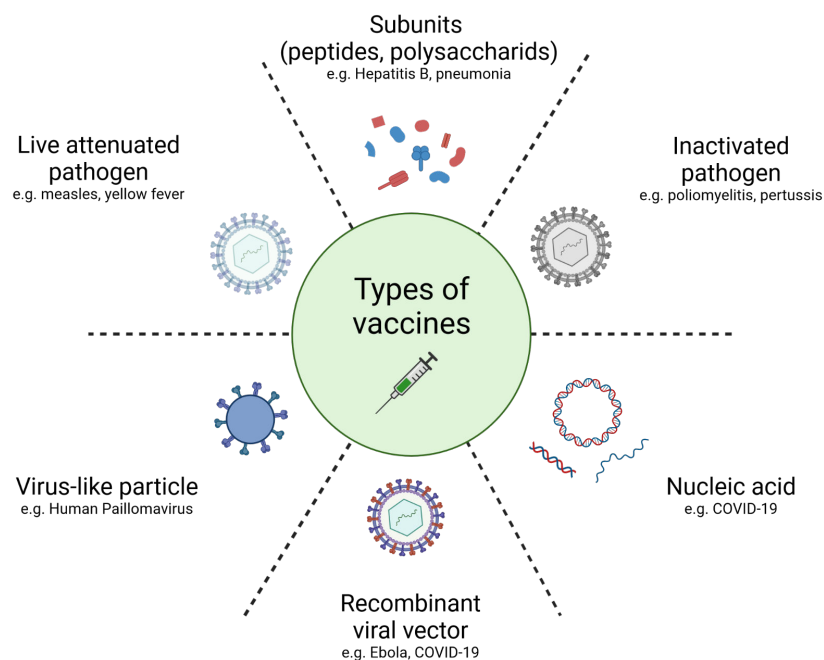
Figure 12 Overview of selected vaccination strategies Schematic depiction of different immunization approaches including conventional vaccination with live attenuated or inactivated pathogens as well as viral vector-based strategies [adapted from [170]].

In contrast, non-live vaccines are either inactivated whole organisms e.g. poliomyelitis and pertussis [182] but also purified or synthetic proteins e.g. Hepatitis B [183] or polysaccharides from the initial pathogen e.g. *streptococcus pneumonia* [184]. Fully inactivated vaccines are considered saver than live attenuated vaccines since they contain pathogens incapable of replication, but also bear the risk of immune reactions too mild for a long-term protection [170]. To keep antibody titers at a protective threshold some vaccines require several booster applications which are usually done in early childhood and have shown to deliver live long protection e.g. tetanus and diphtheria [185], [186].

In the last decades more unconventional vaccination technologies have been explored. First and foremost, viral vector-based vaccines which allow for the combination of presenting an antigen hereby mimicking a natural infection and additionally an expression cassette encoding for the desired antigen. Challenges to overcome in this context are the pre-existing immunity across the population [187] and the rapid development of neutralizing antibodies which could lead to a problem for eventual booster vaccinations with the same capsid [169]. Moreover, virus-like particles (VLPs) as replication defective viral capsids without a transgene cassette have been explored in this context. Their immunogenicity is dependent on the proteins presented on the capsid surface which allows for modulation of tropism and repurposing by switching surface exposed epitopes [188], [189]. This vaccination strategy was also utilized in the context of SARS-CoV-2 and FDA-approved for human papillomavirus vaccinations [190], [191].

Lastly, nucleic acids-based vaccines delivering either DNA or mRNA were explored since quite some time but had their breakthrough during COVID-19. The flexibility of adjusting genomic sequences based on the current infectious SARS-CoV-2 variants allows for time and cost saving vaccine platforms [192]. Nucleic acid-based strategies however rely on either direct cell administration or potent shuttle molecules which bears the risk of eliciting immunologic potential and furthermore relies on continuous cooling during storage due to its limited stability [193].

Overall, many novel approaches are currently under development including but not limited to antigen delivery via liposomes or nanoparticles. These novel strategies hold promising capabilities for future applications for diseases where traditional vaccination has failed so far [194], [195].

2.3.3 Exploring novel vaccination platforms - COVID-19

In 2019 the world was hit by an unexpected pandemic which spread at unprecedented speed around the globe causing a worldwide question of security of public health, treatment availability and emergency plans. By June 2023 over 760 million infections have been reported. Until this day the COVID-19 pandemic has caused over 6.9 Mio confirmed deaths and many patients suffering from post-infectious Long Covid syndrome [2]. Traditionally vaccination development takes more than 10 years, but as COVID-19 has shown, there are possibilities for faster development strategies, production and upscaling [196], [197]. Furthermore, the increasing knowledge in structural immunology and genomics allows for rational design approaches in the context of vaccines [198]. During COVID-19 vaccination platforms including above mentioned "conventional" strategies, such as live attenuated [199], [200] or inactivated viruses [201], [202], followed by vectorized adenoviruses [203], [204] and novel mRNA-based delivery platforms via lipid nanoparticles [205], [206] have been explored. Due to fast mutations and subsequently viral escape the pandemic has highlighted the unmet medical need for innovative and rapidly adaptable next-generation vaccination platforms that allow for fast upscaling and tailoring of immune responses to control emerging pathogens.

2.3.4 Structure and characteristics of SARS-CoV-2

COVID-19 is caused by the severe acute respiratory syndrome coronavirus 2 (SARS-CoV-2) which belongs to the family of *Coronaviridae* and further to the *Betacoronavirus* genus. SARS-CoV-2 is an enveloped positive-strand ssRNA virus with a diameter of approximately 100 nm [207] inducing severe infections of the respiratory tract [208]. Typical symptoms reach from chronic fatigue, fever, cough and shortness of breath to rather unexpected loss of smell and taste which in some cases manifests weeks after the infection [209]. The SARS-CoV-2 genome of the original Wuhan-Hu-1 strain encodes for 9860 amino acids including 16 nonstructural proteins and a total of four structural proteins, namely the spike-glycoprotein (S), the membrane (M), the nucleocapsid (N) and the envelope protein (E) [210], [211].
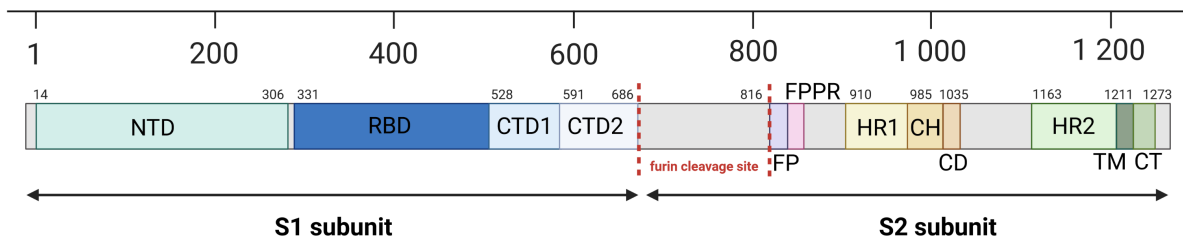
Figure 13 Overview of the spike protein encoding part of the SARS-CoV-2 genome NTD N-terminal domain, RBD receptor-binding domain, CTD1/CTD2 C-terminal domains; FP fusion peptide, FPPR fusion peptide proximal region, HR1/2 heptad repeat domains, CH central helix, CD connector domain, CT cytoplasmic tail.

The S-protein is exposed on the capsid surface and was found to mediate viral cell entry of SARS-CoV-2 [212]. Structurally the S-protein is composed of 1273 amino acids (Figure 13) and can be divided into two subunits, namely S1 and S2 which are cleaved by proprotein convertases like furin during capsid assembly [213]. The S1 subunit holds the receptor-binding domain (RBD) flanked by an N-terminal domain (NTD) and two C-terminal domains (CTD1, CTD2). The S2 protein is composed of a fusion peptide (FP) and its proximal region (FPPR), two heptad repeat domains (HR1, HR2) flanking the central helix (CH) and its connector domain (CD) and concluding with a transmembrane segment and a cytoplasmic tail (CT) [214]. During viral entry the RBD of the S1 subunit interacts with the angiotensin-converting enzyme 2 (ACE2) receptor on the hosts cell surface (Figure 14) while the S2 subunit carries the fusion between virus and host cell membrane following clathrin-mediated endocytosis of SARS-CoV-2 [215]–[217].
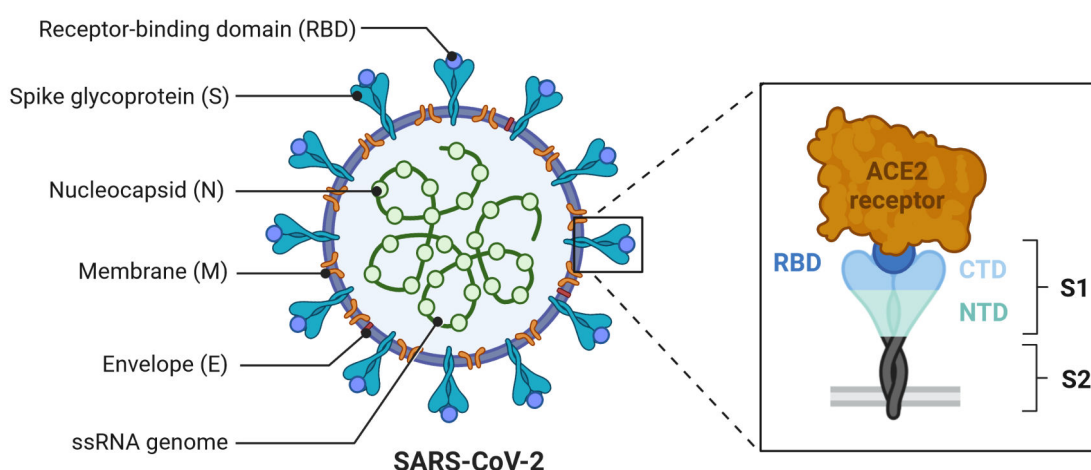
Figure 14 SARS-CoV-2 capsid structure Schematic shows the SARS-CoV-2 capsid with a close-up on the full spike glycoprotein (S) and its primary receptor ACE2; ACE2 angiotensin-converting enzyme 2 receptor, CTD C-terminal domain, NTD N-terminal domain, RBD receptor-binding domain [adapted from Biorender.com].

The RBD is usually hidden by facing downwards in the closed conformation of the spike glycoprotein (Figure 15A) which subsequently leads to immunogenic escape [214]. Before fusion, the spike protein switches into the open prefusion state exposing the RBD in an upwards facing position to interact with the ACE2-receptor (Figure 15B, C) [214]. During the fusion process the immunogenic RBD was found to not only mediate effective cell entry, but moreover plays a crucial role in eliciting production of neutralizing antibodies (NAbs) [218], [219].
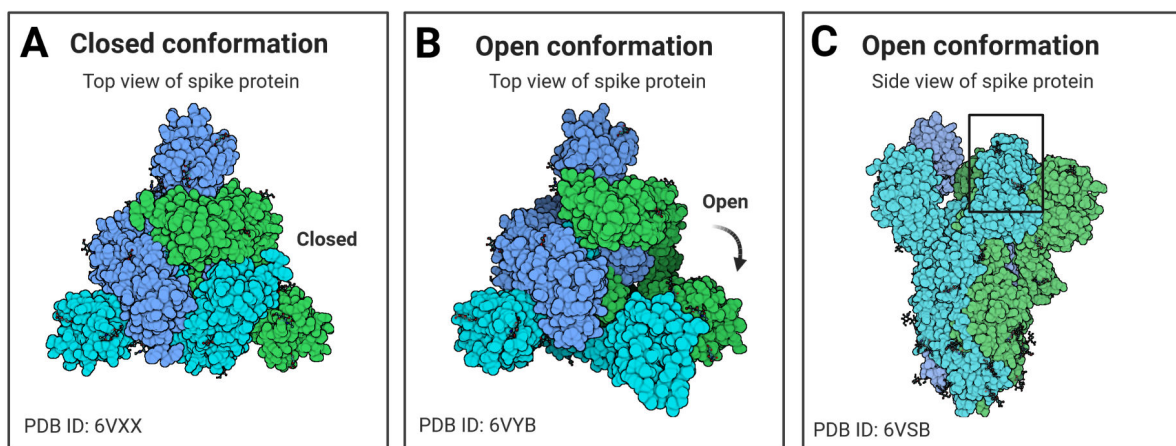
Figure 15 SARS-CoV-2 conformational changes during pre-/post-fusion-state (A) Closed top view on the spike glycoprotein. RBD epitopes are hidden. (B) Top view of the open prefusion conformation of the S1 subunit. RBD epitopes are exposed for ACE2-receptor interaction. (C) Side view of the spike protein in prefusion conformation. RBD (marked in black) is facing upwards [adapted from Biorender.com].

3 Aim of the Study

Adeno-associated viruses (AAVs) have become an important tool for long-term gene delivery: From initial discovery as "contaminant" in adenovirus preparations to FDA-approved gene therapy products. In the context of inherited retinal dystrophies (IRDs) many ongoing studies rely on vectors based on AAV2, the most characterized AAV serotype. However, AAV2 is known to have limitations especially due to high pre-existing immunity across the population.

The first part of this thesis aims to explore AAV9 as alternative serotype for potent gene delivery and high neuronal tropism in ocular gene delivery after less invasive intravitreal (IVT) administration in C57BL6/J mice. To tailor this serotype for retinal tropism ten novel AAV9-based capsids were rationally designed to optimize transduction properties by adapting a strategy which was conducted in AAV2 to improve retinal transduction and vector spreading. Small peptide insertions from AAV2.NN and AAV2.GL were transposed and adapted to alter the natural tropism of AAV9 tailored towards improved retinal transduction. Those novel capsid mutants were extensively characterized *in vitro* and *ex vivo* on various human cell and tissue models and *in vivo* in C57BL6/J mice.

The second part of this thesis aimed to expand the scope of AAVs beyond conventional gene therapy. A novel model platform for engineered AAV-based vaccines was established and evaluated in the context of COVID-19 as a model disease. Therefore, novel AAV2- and AAV9-based capsids were engineered displaying large immunogenic peptide insertions, namely the RBD of SARS-CoV-2 exposed on the capsid surface. This study aimed to mediate natural receptor-ligand-coupled viral cell entry of virus-like particles (VLPs) and subsequently trigger immune responses without necessarily relying on transgene expression. *In vivo* evaluation was conducted in rabbits to assess IgM and IgG production and further compared with blood plasma of human donors immunized with mRNA-based vaccines.

4 Materials & Methods

4.1 Materials

All chemicals used for this study had the quality level "pro analysi" or "for molecular biological use". If not stated otherwise all consumables were obtained from VWR, Roth, Merck, Sigma-Aldrich, or Thermo Fisher Scientific. Buffers and other solutions were prepared with highly pure deionized water from a Milli-Q Plus System (Millipore). All schematics were created with BioRender (www.Biorender.com). Figures were generated with CorelDraw 2021.

4.2 Cloning

4.2.1 Basic cloning techniques

Cloning strategies were planned and designed *in silico* using the benchling.com open-source online software (www.Benchling.com).

4.2.1.1 Restriction Digest

For linearization of plasmids or cutting a desired sequence from a plasmid a restriction digest was performed using the Fast Digest enzymes from Thermo Fisher Scientific. Per reaction between 500-1000 ng of plasmid DNA (if applicable) was incubated at 37°C for 1-1.5 h in a reaction mix according to the manufacturer protocol.

4.2.1.2 Polymerase chain reaction (PCR)

PCR was performed using the Q5 high fidelity DNA polymerase (M0491, NEB) according to the manufacturer protocol. Respective primer pairs were ordered as cloning oligos from Eurofins Genomics. Lyophilized primers were reconstituted in Milli-Q water and further diluted up to a 10 mM working concentration. The template DNA was used at a total concentration of 10 ng per reaction. For Gibson Assembly, primers with a non-annealing overhang were ordered and PCR was performed as "touch-up" starting from 60°C up to the Q5 elongation temperature of 72°C for 30-35 cycles.

4.2.1.3 Site-directed mutagenesis

For incorporation of single point mutations or small insertions within the capsid-encoding sequence of the AAV9 plasmid (pAAV2/9\-sw-SEED) primer pairs were designed carrying the desired sequence modification in the center and 10-15 bp annealing to the template upstream and downstream (cloning oligos, EurofinsGenomics). Q5 high-fidelity DNA polymerase was used in a conventional PCR as stated in 4.2.1.2 amplifying the whole AAV9 plasmid. After

41

completion the template DNA was digested with DpnI (FD1704, Thermo Fisher Scientific) for 2 h at 37°C following a 5 min heat inactivation step at 80°C.

4.2.1.4 Gel electrophoresis and DNA purification

Following PCR or restriction digest the resulting DNA fragments were separated via conventional gel electrophoresis in TBE-buffer (Tris/Borate/EDTA) using agarose concentrations between 0.7 - 2.5 % depending on the desired sequences length. For visualization of DNA the liquid agarose gel was supplemented with peqGREEN (732-3196, VWR) following the manufacturer specifications. The gel was run for 20-30 min at 170-190 V before extraction of desired DNA bands under the UV light (GelDoc 2000 imaging system, Bio-Rad Laboratories). Following band excision, the DNA was purified using the the Qiaquick Gel Extraction Kit (28706, Qiagen) according to the manufacturer instructions.

1 x TBE buffer	Volume
Boric acid	27.5 g
Tris	54.0 g
0.5 M EDTA (pH 8.0)	20 mL
H_2O	*ad* 5 L

4.2.1.5 Gibson assembly

A one-step-isothermal assembly was performed after the touch-up PCR (described in 4.2.1.2) performed with Gibson assembly primers introducing desired overhangs to the desired fragments. Purified DNA sequences were used at a molar ratio of 1:3 backbone to insert as published before [220], [221]. The purified DNA fragments were added to a Gibson assembly master mix containing T5 Exonuclease (T5E4111K, Epicentre), Taq DNA Ligase (M0208L, NEB) and Phusion High-Fidelity DNA Polymerase (F-530S, NEB) in Isothermal buffer and incubated for 1h at 50°C.

4.2.1.6 Ligation

Conventional ligation of fragments was performed for all plasmids after restriction digest as described in 4.2.1.1. Therefore, the T4 ligase (EL0014, Thermo Fisher Scientific) was used following the manufacturer instructions. Small inserts were used at a molar ratio of 1:3 or 1:5 backbone to insert. Incubation was performed for 1 h at room temperature or at 16°C overnight for ligations with a low efficiency.

4.2.1.7 Bacterial transformation and DNA extraction

After Gibson assembly or conventional ligation 2-4 μL of the reaction mix were transferred to chemically competent Stbl3 *Escherichia coli* bacteria on ice (C854003, Thermo Fisher Scientific). After 30 min of incubation on ice a 45 sec heat shock at 42°C was performed, followed by 2 min incubation on ice. Bacteria were plated on 100 μg/mL ampicillin-containing LB+ agar plates and incubated over night at 37°C. The following day single bacteria colonies were picked and incubated for 14-16 h in a shaking incubator at 225 rpm with 100-250 mL LB+ medium containing 1 μg/μL ampicillin as described before. Subsequently, DNA extraction was performed using the PureLink HiPure Plasmid-Midiprep or Maxiprep Kit (K210004 or K210007, Thermo Fisher Scientific) following the manufacturer instructions.

LB(+) medium	Volume
Peptone	10 g
Yeast extract	5 g
NaCl	5 g
D-(+)-glucose	1 g
H_2O	*ad* 1 L

pH was adjusted to 7.2-7.5 before autoclaving

LB(+) agar plates	Volume
Agar	15 g
LB(+) medium	*ad* 1 L

100 mg ampicillin was added after cooling the solution to 50°C before pouring in petri dishes

4.2.1.8 RNA isolation and cDNA synthesis

24 hours prior to RNA extraction ACE2-OE-HEK293T cells were seeded as triplicates at a count of 5×10^6 cells/well into a 6well-plate and incubated at 37°C and 10% CO_2. Cells were PBS-washed and harvested with 350 μL RLTplus buffer (1053393, Qiagen) supplemented with 1% β-mercapto-ethanol (ME). RNA was further processed with the RNeasy plus Mini Kit (74034, Qiagen) following the manufacturer instructions. Final concentration was measured at the NanoDrop 2000 spectrophotometer (ND-2000, Thermo Fisher) prior to reverse transcription. For cDNA synthesis 700 μg RNA was used as template with the RevertAid First Strand cDNA Synthesis Kit (K1621, Thermo Fisher). A non-transfected control (NTC) as well as a water control and a -RT control was carried in each step to assess potential contaminations.

4.2.1.9 Quantitative real-time PCR (qRT-PCR)

Primer-pairs for qRT-PCR were designed with NCBI Primer Blast within a range of T_A between 59°C and 64°C. β-Actin was carried as the housekeeping gene for assessing the expression of ACE2 in HEK293T cells. qRT-PCR was performed with the PowerUp SYBR Green Master Mix (A25742, Thermo Fisher) on the QuantStudio 5 Real-Time PCR system. Each sample condition

was assessed with three technical as well as three biological replicates also including -RT and water controls.

4.2.2 Cloning of immunogenic AAV capsids

The generation of three highly immunogenic capsid versions was conducted by previously described Gibson assembly (see 4.2.1.5). Therefore, parts of the receptor-binding domain (RBD) of SARS-CoV-2 from the plasmid pcDNA3.1-SARS2-Spike (#145032, Addgene) were amplified with primers manufactured by EurofinsGenomics (Table 2) introducing overlaps to the linearized backbone plasmid pRC'99 [222], [223] for AAV2 or the pAAV2/9\-sw-SEED for AAV9. Both plasmids are encoding the *Rep* and *Cap* ORF and further contain an ampicillin resistance gene (*AmpR)*. Parts of the RBD were inserted at position N587 for AAV2 or position Q588 for AAV9. 197 amino acids from the RBD sequence (position 333 to 529) were introduced into both serotypes, resulting in the plasmids termed HtW2_S1.1 and HtW9_S1.1 for AAV2 and AAV9. Additionally, an extended RBD sequence of 206 amino acids (position 300 to 505) was inserted within the AAV2 capsid sequence incorporating more immunogenic motifs of the SARS-CoV-2 RBD [224].

Table 2: List of primers for cloning of HtW capsid variants Lowercase indicates the part annealing to the desired insert; uppercase represents the overhang to the backbone. fw = forward primer, rv = reverse primer.

Primer name	Sequence 5'-3'
pHtW2_S1.1_fw	CTA CCA ACC TCC AGA GAG GCA ACG CGG CCG CAa cta atc ttt gtc cgt tcg gtg agg ttt
pHtW2_S1.1_rv	TGA CAT CTG CGG TAG CTG CTT GGC GCG CcG Ctc cct ttt tgg gcc cac aaa ctg t
pHtW9_S1.1_fw	CCA CAA ACC ACC AGA GTG CCC AAG CGG CCG CAa cta atc ttt gtc cgt tc ggt gag gtt t
pHtW9_S1.1_rv	TTT GAA CCC AAC CGG TCT GCG CCT GTG CCG Cct ttt tgg gcc cac aaa ctg tag c
pHtW_S1.2_fw	TAT CTA CCA ACC TCC AGA GAG GCA ACG CGG CgG CGa agt gca ccc tga aga gct tca cc
pHtW_S1.2_rv	TTG ACA TCT GCG GTA GCT GCT TGG CGC GCC GCg tat ccc act ccg ttg gtt ggc t

4.2.3 Cloning of novel engineered AAV9 capsids

The previously described AAV2.NN and AAV2.GL insertion modifying the naturally occurring heparan-sulfate proteoglycan (HSPG) binding site [225] was introduced in the context of AAV9 by linearizing the AAV9-*cap*-encoding plasmid pAAV2/9\-sw-SEED within the surface-exposed flexible region of loop IV at position Q588 using cloning oligos purchased from Eurofins Genomics (Table 3). The primers introduced the desired NN- or GL-insertion flanked by three

alanines prior to the insertion and two alanines downstream as flexible linkers [226]. A touch-up PCR amplifying the entire plasmid (see 4.2.1.2) followed by DpnI digestion of the template DNA and T4 ligation over night at 16°C was performed. Subsequently, plasmid DNA was transformed into chemically competent Stbl3 *E.coli* bacteria and further processed as described above (4.2.1). Starting from the resulting parental plasmids AAV9.NN and AAV9.GL a site-directed mutagenesis (see 4.2.1.3) with 5'-phosphorylated primers was conducted to introduce single point mutation A589R resulting in respective plasmids AAV9.NNR and AAV9.GLR. For an additional point-mutation A589K double-stranded gene fragments were ordered from Eurofins Genomics (see 7.2). AAV9.NNR was cut with previously introduced cutting sites NdeI and Eco47III (FD0583 and FD0324, Thermo Fisher Scientific). Together with the reconstituted gene fragments a Gibson assembly as described above (4.2.1.5) was performed resulting in the plasmids AAV9.NNK, AAV9.GLK and AAV9.RAAK.

For generation of reference plasmids introducing potential alternative HSPG-binding motifs without extension of loop IV through NN- or GL-insertion the AAV9.NNR plasmid was used as a template introducing only short modifications via site-directed mutagenesis (4.2.1.3). Resulting in the following three plasmids: AAV9.R carrying a single point mutation A589R, AAV9.AAR with an additional insertion of two alanines at pos 589 and AAV9.RAAR with an additional arginine introduced at pos 589.

Table 3: Primer list introducing AAV9 cap modifications Lowercase indicates the part annealing to the template plasmid; uppercase represents the novel introduced sequences or modified base pairs. fw = forward primer, rv = reverse primer, seq = sequencing primers.

Primer name	Sequence 5'-3'
AAV9.NN_fw	CAA ACA ACC CCA CCC CCT CCC GGG CCG CGG CAC AGG CGC AGA CCG GCT G
AAV9.NN_rv	GCC CGG GAG GGG GTG GGG TTG TTT GCG GCC GCT TGG GCA CTC TGG TGG TTT G
AAV9.NNR_fw	aac aac ccc acc ccc tcc cgg gcc gcg CGa cag gcg cag acc ggT tgg gtt caa aac caa gga ata ctt ccg
AAV9.NNR_rv	tgc ggc cgc ttg ggc act ctg gtg gtt tgt ggc cac ttg tcc ata Tga ctc cgt tgc tac cgg gt t
AAV9.GL_fw	CAG GCC TGT CCC CCC CCA CCC GGG CCG CGG CAC AGG CGC AGA CCG GCT G
AAV9.GL_rv	GCC CGG GTG GGG GGG GAC AGG CCT GCG GCC GCT TGG GCA CTC TGG TGG TTT G
AAV9.GLR_fw	Ggc ctg tcc ccc ccc acc cgg gcc gcg CGa cag gcg cag acc ggT tgg gtt caa aac caa gga ata ctt ccg
AAV9.GLR_rv	see AAV9.NNR_rv
AAV9.R_fw	CGA cag gcg cag acc GGT tgg gtt caa aa
AAV9.R_rv	ttg Agc Gct ctg gtg gtt tgt ggc cac ttg tcc
AAV9.AAR_fw	gcc gcg CGA cag gcg cag acc GGT t
AAV9.AAR_rv	see AAV9.R_rv

AAV9.RAAR_fw	cgg gcc gcg CGA cag gcg cag ac
AAV9.RAAR_rv	see AAV9.R_rv
AAV9mut_seq_fw	ggc tgt cca ggg aag aaa ct
AAV9mut_seq_rv	ctc gat ctc cac gct gac tt

4.3 Cell culture

4.3.1 Cultivation and maintenance of eukaryotic cells

Evaluation of novel AAV vector variants was performed in immortalized HEK293T cells or HeLa cells. Prior to vector evaluation both cell lines were recovered from cryopreservation and cultured following standard protocols. HEK293-derived Lenti-X 293T (HEK293T) cells (Clontech) were maintained with 4.5g/L high glucose Dulbecco's Modified Eagle Medium DMEM + GlutaMAX (61965059, Gibco™, Thermo Fisher) which was supplemented with 10% FBS (S0615-500ML, Sigma Aldrich) and 1% Pen/Strep (P0781-100ML, Sigma Aldrich) in T-75 flasks at 37°C and 10% CO_2. HeLa cells were maintained with 1.0 g/L low glucose DMEM with GlutaMAX™ and pyruvate (21885025, Gibco™, Thermo Fisher) supplemented with 10% FBS and 1% Pen/Strep in T-75 flasks at 37°C and 5% CO_2. At 80-90% confluency cells were passed twice a week by aspiring the culture medium, washing with warm 1 x PBS (pH 7.4) and trypsinization using 0.05% Trypsin-EDTA with phenol red (25300054, Thermo Fisher). For *in vitro* assays prior to seeding cells were counted using 0.4% Typan blue (T10282, Thermo Fisher) and the Countess 3 FL Automated Cell Counter (Thermo Fisher).

HEK293T medium	Volume
DMEM	450 mL
+ GlutaMAX	5 g
+ L(+)D-glucose	4.5 g/L
FBS	50 mL
Pen/Strep	5 mL
	500 mL

HeLa medium	Volume
DMEM	450 mL
+ GlutaMAX	5 g
+ L(+)D-glucose	1.0 g/L
+ pyruvate	
FBS	50 mL
Pen/Strep	5 mL
	500 mL

4.3.2 Generation of ACE2-overexpressing HEK293T cells

The desired ACE2-sequence was PCR-amplified from the pCEP4-myc-ACE2 plasmid (#141185, Addgene) and cloned into the linearized piggyBac vector PB_CMV-GPR108-SV40pA_MCS/EF1-HygroR. Linearization was performed via enzymatic digestion with Fast Digest (FD) NheI and KspAI (FD0974 and FD1034, Thermo Fisher). Backbone and insert were cut from an 1% agarose

46

gel and purified using the QIAquick Gel Extraction Kit (28706, Qiagen). Both fragments were ligated using the T4 ligase (EL0011, Thermo fisher) following the manufacturer protocol. The resulting plasmid was termed PB_CMV-ACE2-SV40pA_MCS/EF1-Hygro. Immortalized HEK293T cells were transfected with the resulting plasmid using the Xfect™ Transfection Reagent (631318, Takara) and cultivated side by side with a non-transfected HEK293T well serving as negative control. Both wells were exposed to 1 mg/mL hygromycin B treatment (10687010, Thermo Fisher) for 14 days. Negative control showed no remaining cell growth after 11 days. 1 μL of the transfected HEK293T cells was seeded into a 15 cm with fresh media (see above) and incubated over night at 37°C and 10% CO_2. The following day attached single cells were trypsinized from the dish and transferred into a 96well plate with fresh media and further cultivated. New medium was supplied every second day. The ACE2-gene expression was assessed using quantitative real-time PCR (qRT-PCR). The clone with the highest gene overexpression was used for further experiments.

Table 4: qRT-PCR primers for assessing ACE2-overexpression in transfected HEK293T cells

Primer name	Sequence 5'-3'	T_A [°C]
ACE2_qPCR_fw	TCG CCC TGA GCT ACA TCT TC	60
ACE2_qPCR_rv	GAA CAG GTC TTC GGC TTC GT	
β-Actin_qPCR_fw	CAC CAT TGG CAA TGA GCG GTT C	60
β-Actin_qPCR_rv	AGG TCT TTG CGG ATG TCC ACG T	

4.3.3 *In vitro* transduction assays

Transduction assays to evaluate infectivity of AAV vectors was assessed either in HEK293T cells and ACE2-OE-HEK293T cells (see 5.2.3) or HeLa cells (see 5.1.3). Immortalized cells were cultivated up until 80-90% confluency in T-75 flasks, PBS-washed, trypsinized and counted as described above and then seeded at a count of 50 000 cells/well into 24well plates. Cells were provided with a total of 500 μL medium and incubated with 5-10 % CO_2 at 37°C. 24 hours later cells were transduced with viral vectors at different MOIs (multiplicity of infections, vg/cell). Viral vectors were prediluted in 500 μL fresh medium which was applied on cells (n = 3) and then incubated for 48 hours. Cells were monitored daily, and representative fluorescence pictures were taken after 24 hours and 48 hours post transduction with the EVOS fluorescence microscope (EVOS® FL Cell Imaging System, Thermo fisher) at a magnification of 10x and 20x

at 60% GFP intensity. Quantification of GFP-positive cells was conducted after 48 hours with the Countess 3 FL Automated Cell Counter (Thermo Fisher).

4.3.4 *In vitro* neutralization assays

Neutralization assays were performed in HEK293T cells and ACE2-OE-HEK293T cells. Therefore, cells were seeded at 50 000 cells/well in 24well plates as described in 4.3.3 and incubated for 24 hours at 37°C and 10 % CO_2. Viral vectors were prediluted in fresh medium at an MOI of 250 vg/cell and incubated with serum of either AAV vector immunized rabbits or blood plasma of mRNA-vaccinated human donors at different dilutions for 1 hour at 37°C. Rabbit sera were tested at final dilutions of 1:1 000, 1:2 500, 1:5 000 and 1:10 000. Peripheral blood from three Comirnaty®-vaccinated human donors (#1, #6, #7) was collected by Prof. Dr. Gerhild Wildner (LMU Munich, University Hospital, Department of Ophthalmology). The use of human blood plasma for scientific purposes was approved by the ethics committee of the University Hospital LMU Munich (project number 227/03). Written informed consent was obtained from all donors before blood was collected. Human blood plasma was assessed for neutralization properties at a final dilution of 1:50, 1:250; 1:500 and 1:1 000. A non-transfected control without blood plasma was treated equally. After incubation old medium was removed and AAV vector/blood plasma-mixture was directly applied on the cells. Incubation was carried out for 48 hours monitoring and evaluating each well as described in 4.3.3.

4.3.5 Maintenance and transduction of human retinal explants

The use of human retinal tissue for scientific purposes was approved by the institutional review board of the LMU Munich (project-number 17-531) and conformed to the principles set out in the WMA Declaration of Helsinki and the Department of Health and Human Services Belmont Report. Written informed consent was obtained from all patients before tissue collection. After enucleation surgery the eyes from human donors were transferred into CO_2-independent medium (18045-054, Thermo Fisher) and transported or stored on ice until further processing. The tissue was cleaned of any residual vitreous fluids and carefully separated from the remaining retinal pigment epithelium (RPE) under a stereomicroscope on a 2% agar plate. The retina was cut into several pieces of 7-10 mm diameter depending on the

size of the received tissue and carefully placed on a cell culture filter of 30 mm diameter and a pore size of 0.4 µm (PICMORG50, Millipore). Orientation was maintained with the outer nuclear layer (ONL) being placed on the filter photoreceptors facing down towards the medium and the vitreous side facing up. In addition, a part of the RPE was cultivated alongside the retina on the same filter. Retinal tissue was maintained on the filters in 6well plates with 2 mL Neurobasal A medium (10888022, Thermo Fisher) supplemented with 1:100 Antibiotic/Antimycotic (15240062, Thermo Fisher), 1:100 2 mM GlutaMAX (25030024, Thermo Fisher), and 1:50 B27 supplement (17504044, Thermo Fisher) for 9 days at 37°C and 5% CO_2. A total of 1×10^{11} vg novel AAV vector packaged with an scCMV-eGFP reporter cassette was applied in a total volume of 40 µL on the retinae from the vitreal side directly after tissue preparation. Every day 50-60% of the cultivation medium was carefully removed and replaced by fresh medium. Representative brightfield (4/10 PH, 60-75%) and fluorescence images (50% GFP intensity) were acquired from day 0 until day 9 using the EVOS FL cell imaging system (Thermo Fisher) at 10x and 20x magnification. Each day the same area from the peripheral part and the central part of each tissue was captured to see the eGFP expression develop over time.

On day 9 the tissue was fixed by removing the old cultivation medium and adding 1 mL of sterile 4% PFA in 0.1 M PB next to the filter as well as on top of the tissue. After 2 hours of incubation at room temperature the tissue was washed on the filter three times with fresh 0.1M PB for 5 min each. Lastly, 1 mL of 30% sucrose in 0.1 M PB was added to the well and onto the tissue. 6-well plates were sealed with parafilm and incubated over night at 4°C on a shaker. On day 10 retinal explants were embedded by carefully cutting the filter around the cultivated retinae and RPE tissue with a scalpel and transferring the tissues on previously prepared aluminum foil molds filled with liquid O.C.T Tissue Tek (4583, Science Services) medium. The tissue was then frozen within the molds on dry ice until the Tissue Tek solidified and further stored at -80°C until further processing.

CO₂-independent medium	Volume		Neurobasal A medium	Volume
CO₂-independent medium + pyruvate	100 mL		Neurobasal A medium	48.85 mL
			+ Antibiotic/Antimycotic	500 µL
			+ GlutaMAX	500 µL
	100 mL		+ B27 supplement	100 µL
				50 mL

4.3.6 Maintenance and transduction of human retinal organoids (hROs)

4.3.6.1 Generation and maintenance of hROs (Dr. Grazia Giorgio)

Human retinal organoids (hROs) were derived from human induced pluripotent stem cells (iPSCs), namely PGPs #1, CRTD and B7 cells and further maintained up until viral transduction by a lab group member (Dr. Grazia Giorgio) as described before [227]. The protocol was followed with small alterations. Colony bonds were weakened using 1U/mL of dispase (#07923, Stem Cell Technologies) following 7 min of incubation at 37°C. Wells were washed with warm medium and afterwards filled with 2 mL of warm mTESR1 medium. Colonies were detached and further transferred into 35 mm dishes (#38069, Stem Cell Technologies). Medium was slowly changed over into Neuronal Induction Medium (NIM) consisting of DMEM/F12 + Glutamax (#31331-028, Gibco), 1% MEM-NEAA (#11140-035, Gibco, and 1% N-2 supplement (#17502048, Gibco). Once matured embryonic bodies (EBs) were developed they were transferred onto a 6-well plate coated with Matrigel and cultured until day 15. Next, the medium was switched to Retinal Differentiation Medium (RDM-A) containing DMEM + Glutamax mixed with F12 + Glutamax (#31765-027, Gibco) in a ratio of 3:1, supplemented with 1% MEM-NEAA, 2% B27 w/o vitamin A (#A3353501, Gibco) and 1% Antimycotic/Antibiotic (A/A). From here on the iPSCs start to differentiate and form optic vesicles (OVs) with neural retina and premature RPE. When OVs are fully formed, the culture was broken up by p200 pipette tip and resulting pieces were transferred to TPP® culture dishes (#Z707651) and cultivated as a suspension culture in RDM-A media until day 41. Until then, a medium change was performed every two days. On day 42 the medium was again switched to Retinal Maturation Medium 1 (RMM-1) which consists of RDM-A supplemented with 10% FBS and 100 µM taurine (#T8691, Sigma) until day 69. From day 70 on 10 µM retinoic acid was added to the RMM-1 which was further decreased to 5 µM on day 100 and completely removed after day 130 allowing for proper formation of outer segments. Starting at day 130 the medium was switched to Retinal Maturation Medium 2 (RMM-2) for which 2% B27 w/o vitamin A was replaced by 1% N2 supplement (#17502048, Thermo Fisher). From day 70 on medium was only changed twice per week. hROs were kept in culture until the point of transduction. For further details see dissertation of Dr. Grazia Giorgio (not yet published).

4.3.6.2 Transduction of mature hROs

Transduction of organoids was performed at day 220 in two separately derived batches of hROs. Prior to transduction organoids were separated and carefully transferred into an Ultra-low attachment Cluster 96well plate with round bottoms (Costar #7007, Corning Incorporate). A total of 1×10^{10} vg was prediluted in RMM-2 medium and applied in a total volume of 150 µL per organoid. HROs were incubated at 37°C and 5% CO_2 and further cultivated for 8 days. Each day the condition of the organoids was monitored and representative brightfield (20/40 PH, 35-45%) and fluorescence pictures (60% GFP intensity) were taken with the EVOS FL cell imaging system (Thermo Fisher) at a 2.5x magnification. Starting 48 hours post-transduction every second day a medium change was performed by removing 50-60% of the current medium and adding fresh medium. After 8 days post-transduction the organoids were washed with 0.1 M PBS followed by PFA-fixing with 4% PFA in 0.1 M PBS over night at 4°C. Following PFA-fixing the organoids were washed in 0.1 M PBS three times for 5 min each followed by overnight incubation in 30% sucrose in 0.1 M PBS at 4°C. Human retinal organoids were embedded vertically in plastic molds filled with liquid O.C.T. Tissue-Tek embedding medium (#4583, Science Services) and frozen over dry ice. Up until further use the hROs were stored at -80°C.

RMM-1 medium	Volume
DMEM medium	35 mL
F12 medium	12 mL
+ FBS	5 mL
+ MEM-NEAA	500 µL
+ Antibiotic/Antimycotic	500 µL
+ 100 µM Taurine	50 µL
+ B27 supplement	500 µL
	50 mL

RMM-2 medium	Volume
DMEM medium	35 mL
F12 medium	12 mL
+ FBS	5 mL
+ MEM-NEAA	500 µL
+ Antibiotic/Antimycotic	500 µL
+ 100 µM Taurine	50 µL
+ N2	500 µL
	50 mL

4.4 Production and purification of AAV vectors

Production of adeno-associated virus (AAV) vectors was performed as previously described [228]. Since some details were changed for optimization of the original protocol an overview of each individual step is described below.

4.4.1 Triple transfection of HEK293T cells

HEK293T cells were cultivated in T-75 flasks until 80-90% confluency as described in 4.3.1. In preparation of transfection cells were PBS-washed, trypsinized and seeded in 15x15 cm plates and incubated at 37°C with 10% CO_2 until confluent. Prior to triple transfection medium was changed to FBS-free DMEM high-glucose culturing medium.

Starving HEK293T medium	Volume
DMEM	450 mL
GlutaMAX	5 g
L(+)D-glucose	4.5 g/L
+ Pen/Strep	5 mL
	500 mL

Cells were transfected using polyethyleneimine (PEI) 20 as a complex builder and three separate plasmids: The pTransgene plasmid containing the desired transgene cassette flanked by inverted terminal repeats (ITRs), the pRep/Cap plasmid containing the *Rep/Cap*-ORF encoding for the AAV vector capsid and four nonstructural viral proteins and the pAdHelper plasmid encoding for genes derived from adenovirus 2 necessary for AAV vector processing. For this study modified AAV2 or AAV9 vectors carrying a transgene were generated by transfection with a self-complementary (sc) plasmid with an eGFP-reporter cassette controlled by a CMV-promoter and flanked by AAV2 ITRs termed pAAV2.1_scCMV-eGFP [229].

The DNA master mix containing all three plasmids in serum-free HEK293T medium was prepared separately from the PEI-20 master mix. For calculation of the appropriate amounts of plasmid DNA and PEI-20 the following formulae were used:

$$\text{pAdHelper } [\mu g] = \frac{90 \text{ } \mu g \text{ *MM pAdHelper [kDa]}}{\text{MM pTransgene [kDa]}} = X$$

$$\text{pRep/Cap } [\mu g] = \frac{90 \text{ } \mu g \text{ *MM pRep/Cap [kDa]}}{\text{MM pTransgene [kDa]}} = Y$$

The amount of PEI-20 was calculated as follows:

$$\text{PEI-20 [µL]} = (\text{pTransgene[µg]} + \text{pAdHelper [µg]} + \text{pRep/Cap [µL]})*2 = Z$$

DNA-master mix	Volume
pTransgene	90 µg
pAdHelper	X µg
pRep/Cap	Y µg
serum-free medium	*ad* 7 500 µL

PEI-master mix	Volume
PEI-20*	Z µL
serum-free medium	*ad* 7 500 µL

*pH 7.05, 1 mg/mL in dH$_2$O, sterile filtered

Both master mixes were prepared separately and briefly vortexed before transferring the DNA-master mix to the PEI-master mix following 10 sec or vortex. After 15 min of incubation at room temperature (RT) 1 mL of the reaction mixture was pipetted on each 15 cm plate. Plates were gently tilted to evenly distribute the plasmid mixture and then incubated for 72 hours at 37°C and 10 % CO$_2$. Cells were briefly monitored each day under the EVOS FL cell imaging system (Thermo Fisher).

For virus-like particles (VLPs) not carrying a transgene cassette the transfection protocol was adapted accordingly. Instead of pTransgene the corresponding volume of serum-free medium was added. This applies for the "empty vectors" HtW2_S1.1, HtW2_S1.2 and HtW9_S1.1 described in 4.2.2.

4.4.2 Cell harvesting and DNA digestion

After 72 hours of incubation cells were harvested by using a cell scraper to remove the attached cells from the 15 cm plates and transfer them together with the supernatant into an autoclaved centrifuge bottle (Ref31400-500, Thermo Fisher). After centrifugation at 4 000 rpm and 4°C for 15 min supernatant and cell pellet were processed separately. Supernatant was filtered with a 0.45 µm pore size filter and mixed with 40% polyethylene glycol 8 000 (PEG) to a final concentration of 8% of PEG and stored at 4°C for 48 hours. For calculating the amount of PEG 40% to be added the following formula was used:

$$\text{40\% PEG [mL]} = \frac{\text{supernatant [mL] * 0.08}}{0.32}$$

After 48 hours of incubation the mixture was centrifuged at 4 000 rpm and 4°C for 15 min resulting in a white PEG-pellet containing the AAV vectors. The supernatant was autoclaved and discarded. The PEG-pellet was frozen at -20°C or directly processed with the cell pellet.

The cell pellet remaining in the original bottle was resuspended with 7.5 mL Lysis buffer and transferred into a 50 mL Falcon tube. The cells were frozen in liquid nitrogen followed by immediate thawing at 37°C. These freeze/thaw-cycle was performed three times in total.

The warmed cell pellet was used to resuspend the PEG-pellet after the last thawing step. For digestion of remaining free DNA 2 µL 50U/mL benzonase (1.01695.0001, Merck) was added to the mixture and incubated at 37°C for 30 min in the water bath. Subsequently the mixture was centrifuged twice for 20 min at 4 000 rpm and 4°C. Between centrifugation steps the mix was transferred into a fresh tube.

Lysis buffer	Volume
5 M NaCl	150 mM
1 M Tris-HCl (pH 8.5)	50 mM
H_2O	*ad* 50 mL

buffer was sterile filtered

4.4.3 Iodixanol density gradient purification

The centrifugated AAV vector-containing supernatant from 4.4.2 was transferred into a 39 mL Quick-Seal polyallomer tube (#342414, Beckmann Coulter). A density gradient was established by sublayering iodixanol solutions at different percentages using a Pasteur glass pipette and a peristaltic pump (Mini Plus 3, Gilson). Iodixanol was added in layers as follows: 7 mL of 15%, 5 mL of 25%, 5 mL of 40% and 6 mL of 60% iodixanol. Phases can be visually divided through the addition of different phenol red concentrations, creating a change in color for every sublayer. Tubes were sealed with the Beckman Tube Topper and centrifuged at 70 000 rpm and 18 °C for 1 h 45 min in an Optima L-80K ultracentrifuge (70 Ti rotor, Beckman Coulter). Subsequently, the centrifugal tube was perforated with a cannula to allow pressure release. The clear 40% iodixanol phase containing the viral particles was collected by inserting a 20 G cannula between the 40% and the 60% phase and removing 2-5 mL of the upper phase. The solution was either stored at -80°C or directly proceeded with the chromatography-based purification.

15% iodixanol solution	Volume
10x PBS	5 mL
1 M MgCl$_2$	50 µL
2.5 M KCl	50 µL
Optiprep*	12.5 mL
1% phenol red	37.5 µL
5 M NaCl	10 mL
dH$_2$O	*ad* 50 mL

25% iodixanol solution	Volume
10x PBS	5 mL
1 M MgCl$_2$	50 µL
2.5 M KCl	50 µL
Optiprep*	20.9 mL
1% phenol red	50 µL
5 M NaCl	10 mL
dH$_2$O	*ad* 50 mL

40% iodixanol solution	Volume
10x PBS	5 mL
1 M MgCl$_2$	50 µL
2.5 M KCl	50 µL
Optiprep*	33.3 mL
dH$_2$O	*ad* 50 mL

60% iodixanol solution	Volume
1 M MgCl$_2$	50 µL
2.5 M KCl	50 µL
Optiprep*	50 mL
1% phenol red	37.5 µL

*protect from direct light (#1114542, Progen)

4.4.4 Chromatography-based purification

4.4.4.1 Anion exchange chromatography (AEX)

Conventional chromatography-based purification following iodixanol gradient centrifugation was implemented using the ÄKTA^{TM} prime plus system from GE Healthcare via anion exchange chromatography (AEX). Therefore the 40% iodixanol phase containing the AAV vectors was diluted 1:1 with ÄKTA buffer and run over a 5mL HiTrap Q FF Sepharose column (17-5156-01, Cytiva). UV-absorbance and conductivity was assessed with the PrimeView 5.31 software (GE Healthcare) from the manufacturer. Fractions showing high UV-absorbance indicating iodixanol were collected for further processing. The chromatography columns were regenerated with high salt buffer containing 2.5 M NaCl (pH 8.4) and reused up to 12 times. Columns and superloop were stored in 20% ethanol at 4°C up until further use.

ÄKTA buffer	Volume
Tris	20 mM
NaCl	15 mM
dH$_2$O	*ad* 500 mL

pH was adjusted to 8.5

4.4.4.2 Cation exchange chromatography (CEX)

For AAV vectors described in 4.2.2 with immunogenic potential the CIMmultus SO_3 column (1 mL, 2 μm pore width, BIA separations) was used for CEX chromatography to avoid potential immunogenic reactions towards the X-ray contrast medium iodixanol. Cell lysate and PEG precipitate were pooled and processed as described in 4.2.2 and afterwards directly diluted 1:10 with a 25 mM sodium acetate ($C_2H_3NaO_2$) and 50 mM sodium chloride (NaCl) buffer resulting in a desired conductivity span between 15 and 20 mS/cm and a pH of 4.0. After column equilibration with a high-salt buffer containing 50 mM sodium acetate and 100 mM NaCl (pH = 4.0) the sample was loaded at a medium flow rate of 5mL/min. During the elution a buffer gradient from 0-100% 50 mM sodium acetate and 2 mM NaCl (pH = 4.0) was developed over 20 column volumes (CV). Regeneration of the column was conducted with a buffer containing 1 M NaOH and 2 M NaCl. The column was stored at 4°C in 20% ethanol until further use.

4.4.4.3 Affinity chromatography (AC)

To verify capsid identity after introducing large insertions on the AAV2 and AAV9 capsid surface (as described in 4.2.2) affinity chromatography (AC) was performed using a Poros capture select AAVx column (POROS™ GoPure™ AAVX Pre-packed Column, 0.8 x 10 cm, 5 mL, Cat. No. A36651, Thermo Fisher). The column is packaged with AAV capsid specific exposed epitope antibodies resulting in a purification based on capsid identity and integrity. Loading of samples was implemented at pH 7.4 with a constant flow rate of 0.3mL/min. The elution was performed at a lower pH of 3.0 with 100mM citric acid (8.18707.1000, VWR) at a flow rate of 0.7 mL/min followed by immediate AAV neutralization in 1 M Tris at pH 8.7. The AAVx column was cleaned in place using 100 mM phosphoric acid (1005730510, Merck) at pH 2.0, and 6 M guanidine HCl (G3272-100G, Sigma-Aldrich).

4.4.5 Amicon concentration

Directly after chromatography-based purification samples were supplemented with 1% PBS-MK + 0.014% Tween-20 and then sterile filtered using a 0.2 μm pore filter (514-0061, VWR) and further concentrated using Amicon Ultra-4, PLHK Ultracel-PL membrane filters (UFC810096, Sigma Aldrich). After each loading step Amicon tubes were centrifugated at 2000 rpm for 2 min at room temperature. At a final volume of 500μL AAV vector suspension 1 mL

of wash buffer (PBS-MK with 0.014% Tween-20 or 0.001% PX-188) was added. The mix was concentrated to a final volume of 50 to 100μL which was separated in 10μL aliquots and stored at -80°C until further use.

Phosphate-buffered saline (PBS)	Volume
NaCl	40 g
KCl	1 g
$Na_2HPO_4*2H_2O$	7.2 g
KH_2PO_4	1.2 g
dH_2O	*ad* 5 L

pH adjusted to 7.4, aliquot into 500 mL bottles, autoclaved

PBS-MK	Volume
10 x PBS	50 mL
1 M $MgCl_2$	500 μL
2.5 M KCl	500 μL
dH_2O	*ad* 500 mL

sterile filtration, storage at 4°C

PBS-MK + 0.014% Tween	Volume
PBS-MK	49.93 mL
Tween-20	70 μL
	50 mL

PBS-MK + 0.001% PX-188	Volume
PBS-MK	49.95 mL
1% PX-188 solution	50 μL
	50 mL

4.4.6 Genomic titer determination

Transgene expression was assessed by qRT-PCR with ITR-specific primers on a StepOnePlus Real-Time PCR system (Applied Biosystems, Thermo Fisher Scientific). Standard curves were established using ITR-specific primers as described before [230], [231].

Table 5: qRT-PCR primers for genomic titer determination of AAV vectors

Primer name	Sequence 5'-3'
ITR2_forward	GGA ACC CCT AGT GAT GGA GTT
ITR2_reverse	CGG CCT CAG TGA GCG A

A reference ITR standard was generated by purifying the resulting ITR fragment after PCR amplification with the ITR-specific primers. DNA concentration was measured with the Nanodrop™ 2000c spectrophotometer (Thermo Fisher Scientific). The resulting ITR standard was diluted to a final concentration c of 10^{10} copies in 5 μL using the following formula:

$$\text{concentration c} \left(\frac{\text{pg}}{\text{μL}}\right) = \frac{10^{10} * 660 * 10^{12} \text{ pg mol}^{-1} * \text{fragment size}}{6.022 * 10^{23} \text{ mol}^{-1} * 5 \text{ μL}}$$

The final standard solution was frozen at -20°C until further use. For genomic titer determination a dilution series, up to a final range from 10^9 to 10^5 ITR copies was prepared in ddH_2O. The AAV samples were prediluted (1:10 000 or 1:100 000) in double-deionized water

(ddH$_2$O) and assessed side by side with the diluted standard series on a MicroAmp^{TM} Fast Optical 96well Reaction Plate (Applied Biosystems, Thermo Fisher) as three technical replicates. Therefore, the PowerUp^{TM} SYBR Green master mix (A25742, Thermo Fisher) was used according to the manufacturers protocol. The standard curve was generated by plotting the resulting cycle threshold (C$_t$) values against the logarithm of the dilution. The resulting genomic titer [vg/µL] of the produced AAVs vectors could be interfered from corresponding C$_t$ values of the standard curve.

4.4.7 Stunner measurements

The Stunner from Unchained Labs (Boston, USA) was used for additional characterization of novel AAV capsid candidates. It combines UV/Vis spectroscopy and dynamic light scattering (DLS) as well as static light scattering (SLS) which allows for detailed characterization of AAV capsids especially in regards of capsid and genomic titer, full/empty capsid ratio, aggregate formation or quantification of residual iodixanol in AAV preparations. For measurements 2 µL sample was directly applied on the stunner 96well plate. In the corresponding Stunner Client software version 8.0 the "AAV Quant" application was selected and AAV profiles containing specific information such as genome sequence, capsid proteins, buffer formulation were created. Excitation coefficients were calculated with the software, based on DNA length and serotype information. Data analyses was automatically conducted by the stunner software. Each sample was measured at n = 4 for 5 sec each and automatically evaluated by the Stunner Analysis tool (Version 8.0 Lunatic&Stunner Analysis 2021).

4.4.8 Thermal stability assay

The thermal stability of the novel AAV vector capsid candidates was measured by intrinsic differential scanning fluorimetry (iDSF). Therefore, the Prometheus NT.48 (NanoTemper Technologies, Munich, Germany) was used to evaluate the melting temperature T$_m$ of AAV capsids. This system measures the intrinsic fluorescence of tryptophan residues at 330 and 350 nm after excitation at 280 nm [232]. To evaluate their thermal stability AAV capsids were diluted in PBS (10 mM Na2PO4, 1.8 mM KH2PO4, 4.27 mM KCl, and 137 mM NaCl, pH 7.4). 10 µL sample was filled in capillaries and run with a temperature gradient from 20 - 100°C in a linear ramp of 1°C/min. Samples were run with three replicates per condition. Fluorescence

signal of tryptophan residues facing the capsid cargo was measured against temperature. The final melting temperature T_m was determined with the PR. ThermControl software V2.1 (NanoTemper Technologies, Munich, Germany). Once starting to unfold a peak in fluorescence can be measured. The T_m results from the maximum of the first derivatives from both thermal curves at 330 and 350 nm [233], [234]. All AAV samples were adjusted to the same capsid titer and measured as n = 3.

4.4.9 Dot blot assay of HtW vectors

The condition of characteristic AAV capsid surface epitopes as well as neutralizing antibodies (NAbs) in different sera or blood plasma was assessed by dot blot assays. HtW vectors were applied at different concentrations on an activated polyvinylidene difluoride (PVDF) membrane (T831.1, Roth) and later incubated with specific primary and secondary antibodies. The PVDF membrane was activated for 2 min in 100% methanol followed by incubation in dH_2O and TBS-T buffer for 5 min each. The wet membrane was spotted with 1 µL of 3×10^9 capsid proteins (cp) AAV vector sample diluted in PBS up to 1:100 per spot and left to dry for 1 hour. Afterwards the membrane was blocked with 5% dried milk powder (A0830-1000, AppliChem) in TBS-T for another hour followed by direct incubation with a commercially available primary antibody targeting the desired region of interest such as the RBD of SARS-CoV-2 on the vector capsid. Alternatively, a dilution of sera from HtW-immunized rabbits or blood plasma of Comirnaty®-vaccinated human donors containing potentially RBD-specific IgG antibodies was used for membrane incubation. After overnight incubation at 4°C or 1 hour incubation at room temperature the membrane was washed in TBS-T and incubated for another hour with a species-specific secondary antibody coupled with a horseradish peroxidase (HRP) at room temperature. Table 6 provides an overview of the antibodies used for dot blot analysis. Detection with the western blotting luminol reagent (sc-2048, Santa Cruz) was monitored under the GelDoc 2000 imaging system (Bio-Rad Laboratories). Membranes were stored at 4°C in TBS-T with 0.02% sodium azide (NaN_3). For re-using the PVDF membranes were stripped in the microwave three times for 45 sec each in fresh TBS-T buffer.

TBS-T buffer	Volume
Tris	1.2 g
NaCl	8.0 g
Tween-20*	1 mL
dH$_2$O	*ad* 1 L

*protect from direct light!

Table 6: Overview of antibodies used for dot blot analysis

Anti-	Host	Catalog no.	Supplier	Working dilution
Primary antibodies				
α-SARS-CoV-2/ α-RBD	rabbit	40592-T62	Sino Biological	1:500
α-HtW2_S1.1	rabbit	-	LMU Department of Veterinary Sciences, Prof. Dr. H. Ammer	1:10 000
α-HtW2_S1.2	rabbit	-		
α-HtW9_S1.1	rabbit	-		
α-AAV9	rabbit	-		
α-AAV2	rabbit	-		
α-SARS-CoV-2 spike	human	-	LMU Munich, University Hospital, donor #1, #6, #7	1:500
Secondary antibodies				
α-rabbit-IgG-HRP	donkey	NA934-1ML	GE Healthcare	1:2 000
α-human-IgG-HRP	goat	#31410	Thermo Fisher	1:2 000
α-human-IgM-HRP	rabbit	ab97195	Abcam	1:2 000

4.5 Animals

All *in vivo* animal experiments were conducted strictly as approved by the local authorities (Government of Upper Bavaria) and in accordance with the German laws on animal welfare (Tierschutzgesetz, TierSchG).

4.5.1 C57BL6/J mice

Evaluation of novel AAV vectors was assessed in adult male and female C57BL6/J mice at and age of 2 to 4 months. Mice were kept at 12-hour light/dark conditions with food and water *ad libitum* following local regulations and legal guidelines. All *in vivo* experiments were performed under anesthesia delivered via intraperitoneal injection of 100mg/kg ketamine (Medistar GmbH) and 10 mg/kg xylazine (Xylariem®; Ecuphar GmbH) in 0.9% sodium chloride (NaCl 0.9 %, B. Braun).

4.5.2 ZIKA rabbits

Immunogenic potential of HtW-vectors and AAV2 and AAV9 wildtype vector variants was assessed in adult male and female ZIKA rabbits ("Zimmermann-Kaninchen"). Experiments were conducted at the LMU Department of Veterinary Sciences (Prof. Dr. Hermann Ammer) by an external company in accordance with the German law for animal protection and the European Directive, 2010/63/EU. All immunization and bleeding procedures were approved by the government of Upper Bavaria (Munich, Germany, license number ROB-55.2-2532.Vet_03-17-110). All animal experiments were handled in compliance with the european and national regulations for animal experimentation (European Directive 2010/63/EU; Animal Welfare Acts in Germany)

4.6 *In vivo* experiments

4.6.1 Immunization of adult rabbits

Rabbits were immunized with CEX-purified empty VLPs of AAV2 WT, AAV9 WT, HtW2_S1.1, HtW2_S1.2 and HtW9_S1.1. For each capsid variant, two female ZIKA hybrid rabbits (Dr. Zimmermann GbR, Abtsgmünd, Germany; 2.8 kg body weight) were immunized using standard procedures. In brief, primary immunizations were attempted with 100 µg virus particles emulsified in Freund´s complete adjuvant (Sigma-Aldrich, # 344289) subcutaneously (s.c.) applied to 10 different injection sites (100 µl each) at the lower back of the animals. Booster injections were conducted with 50 µg virus particles at 4-week intervals with Freund´s incomplete adjuvant (Sigma-Aldrich, # F5506), applied to 10 different injection sites (100 µL each) at the upper back of the animals. Blood samples were taken under acepromazine sedation (Tranquisol P 10 mg/ml Injektionslösung für Pferde; CP Pharma GmbH; 0.1 mg/kg body weight intravenously into the lateral ear vein) 10 days after the first, second and third booster injection by puncture of the central ear arteria (30 mL volume). Blood was allowed to clot for 1 h at 37°C in a water bath and sera were separated subsequently by centrifugation at 1,200 × g for 20 min at 4°C (Mega Star 600 R; VWR GmbH). Sera were stored in aliquots at -20°C until use. Control sera (5 mL) were taken from each animal 1 week before primary immunization. Final blood collection was performed on day 150 via heart puncture.

4.6.2 Intravitreal injection of novel AAV9 capsid mutants

Adult mice of at least 4 weeks of age were anaesthetized intraperitoneally (i.p.) according to their body weight with ketamine/xylazine in NaCl as described in 4.5.1. The body temperature of mice was maintained on heating plates at 37°C. 5g/mL tropicamide eye drops (Mydriaticum Stulln ATR, PZN 05520023, Pharma Stulln) were applied on the mice eyes for 15-30 min. Once pupils were fully dilated mydriaticum was removed and replaced with 2% methylcellulose eye drops (2% Methocel ATR, PZN 04781081, OmniVision GmbH) to keep the eyes from drying during the procedure. Mice were then placed under an Opmi 1 FR pro surgical microscope (Carl Zeiss) and positioned sideways for clear vision into the eye via the pupil. 1 µL of novel AAV vectors packaged with a pAAV2.1_scCMV-eGFP reporter cassette were injected intravitreally with a Nanofil Sub-Microliter Injection System (World Precision Instruments) equipped with a 34-gauge beveled needle (NF34BV-2, WPI). Novel vector variants were injected at three different doses of 1×10^9, 5×10^9 or 1×10^{10} total vg (respectively low, middle and high dose). AAV vectors were released once the needle was positioned under the lens of the mouse with the opening of the needle towards the optic nerve. After vector release the position was maintained for 10 sec to avoid backflow of sample with the removal of the needle. Directly after the injection eyes were treated with 0.3 mg/g dexamethasone and 5mg/g gentamycin sulfate containing eye cream (Dexamytrex SAL, PZN 02747789, Bausch&Lomb). Mice were kept on the heating plate until fully awake. Condition of mice was evaluated for the following three weeks including confocal scanning laser ophthalmoscopy (cSLO) once a week (see 4.6.3).

4.6.3 Confocal scanning laser ophthalmoscopy (cSLO)

Fundus images were taken after 7, 14 and 21 days respectively 1-, 2- and 3-weeks post injection (WPI). Prior to imaging mice were anaesthetized i.p. as described above and treated with tropicamide to dilate the pupils and placed on a heating plate to maintain body temperature during sedation. Subsequently, methylcellulose was applied on the eyes. Custom made optic lenses were placed on both eyes for improved imaging and maintaining moisture on the cornea during acquisition [235]. Mice were placed in a custom-made holder allowing precise positioning of sedated mice in front of the camera during measurements. The examination of mouse retinae was performed using a modified Spectralis HRA + OCT system

(Heidelberg Engineering). Fundus images were acquired in a high-resolution mode with an infrared laser at 820 nm and 30° field of view. Excitation of eGFP fluorophore was examined at a laser wavelength of 488 nm and an integrated set of emission filters (LP 458 nm for 820 nm, BP 550/49 nm for 488 nm) as previously described [236].

4.7 Enzyme-linked immunosorbent assay (ELISA)

Serum of immunized rabbits (see 4.6.1) was evaluated for expression of RBD-specific IgM and IgG antibodies using a custom-made ELISA. Plates (#442404, Nunc-Immuno plate F96 Maxisorp, Thermo Fisher Scientific) were coated with 100 ng of SARS-Cov-2 wildtype RBD (#SPD-C52H2, Acro Biosystems) in carbonate buffer for 1 hour (0.2 M sodium carbonate; pH 9.4). Plates were blocked with 3 % (m/v) sodium caseinate (#9005-46-3, Sigma Aldrich) in phosphate-buffered saline (pH 7.4) for 30 min before plates were washed and - 3log dilutions of the antisera were applied to the plates in phosphate-buffered saline containing 0.1 % (m/v) sodium caseinate. Plates were incubated for 2 hours at room temperature, washed, and incubated for 1 hour with horseradish labelled goat anti-rabbit IgG (#ab6721, Abcam) and goat anti-rabbit IgM (#ab9167, Abcam) each diluted 1:5 000 in phosphate-buffered saline for 30 min. After final washes, antibody titers were read out using TMB substrate solution (#N301, Sigma Aldrich) in an EPOCH/2 plate reader from BioTEK at λ = 450 nM. Assays were performed in quadruplicate determination and titers were defined as the dilution showing a signal above 2 standard deviations (SD) above background. ELISA was kindly performed by Prof. Dr. Hermann Ammer at the Department of Veterinary Sciences (LMU Munich).

4.8 Tissue preparation

All tissue preparations in C57BL6/J mice were performed at day 22 or day 23 after three weeks post injection (WPI) monitoring via cSLO. After isoflurane inhalation mice were immediately euthanized via cervical dislocation. The working bench was cleaned with bacillol and dissection tools (World Precision Instruments) were bacillol-washed and further heat-sterilized accordingly prior to use.

4.8.1 Eyecup preparation

Eyes were removed and transferred into cold 0.1 M phosphate buffer (PB). Afterwards eyes were carefully punctured at the *ora serrata* using a 20 G cannula (PZN 02050798, Sterican)

and fixed for 10 min in 4% paraformaldehyde (PFA) at pH = 7.4 (158127-100G, Sigma Aldrich) in 0.1 M PB on ice. Next, eyes were transferred to a 3.5 cm petri dish and dissected on a PB-moistened qualitative filter paper (516-0814, VWR) under a stereomicroscope (Stemi 2000, Zeiss). Eyes were cut with 2.5 mm curved micro scissors (Vannas Spring Scissors, Fine Science Tools) along the *ora serrata.* For special protection of the ciliary body only the cornea was cut while maintaining the iris. Two opposing incisions were made into the iris to flip the structure to the side for lens removal. Prior to removal of the lens the eyes were transferred into another 3.5 mm petri dish filled with cold 0.1 M PB to avoid collapsing of the empty eyecup. Lens, vitreous and cornea was carefully removed with micro forceps (Dumont #55, Fine Science Tools) and eyecup was transferred into could 4% PFA again for 45 min for final tissue fixation. Afterwards the eyecup was washed three times in cold 0.1 M PB for 10 min each and incubated overnight at 4°C in 30% sucrose. The following day eyecups were embedded with tissue freezing medium (Tissue-Tek® O.C.T.™ Compound, Sakura Finetek™) in prepared aluminum foil cups and frozen on dry ice. Temporal side was marked on the outside of the aluminum foil for orientation purposes. Frozen eyecups were stored at -80 °C until further processing and cryo-sectioning.

4.8.2 Brain preparation

Dissection of the brain was performed simultaneously to eyecup preparation by Dr. Verena Mehlfeld or Philipp Lorenz (both LMU Munich, Pharmacology for Natural Sciences, Department of Chemistry and Pharmacy). After enucleation the fur and skin of the head was cut with Iris scissors (500216, WPI) and the scull was carefully opened with a scalpel (233-5323, VWR). The bone carefully was shifted to the side with a small, curved spatula (WPI) and meninges were removed using Dumont Titanium forceps (14187, WPI). Brain was extracted from the scull with a spatula and flipped upside down on a moistened Whatman filter paper with 0.1 M PB. Optic nerve and chiasm were carefully removed with the forceps and transferred to cold 0.1 M PB. The brain was immediately fixed free floating in 4% PFA in 0.1 M PB on a shaker at 4°C for 5 hours. Afterwards the brain was transferred to a small glass beaker containing 30% sucrose in 0.1 M PB and incubated on a shaker over night at 4°C. The consecutive day the brain was transferred to a piece of aluminum foil and frozen on dry ice and kept at -80°C up until further use.

4.8.3 Optic nerve and chiasm

The optic nerve and chiasm were removed from the brain using forceps and transferred into cold 0.1 M PB as described in 4.8.2. Next, the tissue was carefully transferred into 4% PFA in 0.1 PB and fixed for 45 min free floating on a shaker at 4°C. Afterwards the tissue was washed three times for 5 min each in 0.1 M cold PB and finally incubated overnight in 30% sucrose in 0.1 M PB at 4°C. The following day optic nerve and chiasm were carefully placed on a Whatman filter paper, transferred into prepared aluminum foil molds, and covered with tissue freezing medium. The tissue was then frozen on dry ice in the aluminum molds and stored at -80°C until further processing.

4.9 Cryo-sectioning

All tissues were cryo-sectioned at the CryoStar^{TM} NX70 cryostat (Epredia^{TM}, Thermo Fisher Scientific). The tissue was transferred from its -80°C storage to the cryostat and tempered for 10 to 45 min depending on the size of the tissue prior to attaching the tissue in the desired orientation on a cryostat cutting plate with Neg-50^{TM} freezing medium (84000-154, VWR). Each tissue was processed at slightly different setting regarding temperature and thickness of slices (see Table 7). Eyecups were cut along the naso-temporal axis from temporal to the nasal side, brains were cut sagittal and upside down, human retinal organoids (hROs) were positioned upright and cut radial, human retinal explants were cut vertical and optic nerve and chiasm was also put in an upright position and cut radial. Tissue slices were collected on Epredia™ SuperFrost Plus™ microscope slides (Epredia™ J1800AMNZ, Thermo Fisher Scientific) and stored at -20°C until further processing. Prior to storage optic nerve, chiasm and brain slices were checked for autofluorescence at the Keyence Compact Fluorescence Microscope BZ-X800 (see 4.11.1).

Table 7: Cryostat settings for each tissue type

Tissue type	Object temperature	Blade temperature	Slice thickness
Eyecups	- 13°C	- 9°C	12 - 14 µm
Human retinal explants	- 16°C	- 12°C	16 µm
Human retinal organoids	-15°C	- 13°C	12 µm
Brains	- 14°C	- 12°C	14 - 16 µm
Optic nerve and chiasm	- 11°C	- 8°C	12 -14 µm

4.10 Immunohistochemistry (IHC)

Frozen tissue slices were thawed at room temperature. Slices were outlined with a liquid blocker PAP pen (N71312, Science Services) and rehydrated with 0.1 M PB for 10 min at room temperature (RT). PB was removed, slices were fixed with 4% PFA in 0.1 PB for 15 min followed by three 5 min washing steps with 0.1 M PB. A master mix containing 5% ChemiBlocker (2170, Merck), 0.03% Triton™-X100 (X100-100ML, Sigma Aldrich) and the primary antibodies in their working dilution (see Table 8) in 0.1 M PB was applied on the samples. Incubation was performed either at RT for 3 hours or overnight at 4°C.

Table 8: Primary antibodies for immunohistochemistry

Anti-	Host	Catalog no.	Supplier	Working dilution
α-Cacna1s	mouse	MAB427	Millipore	1:500
α-Calbindin-D28-K	mouse	C9848	Sigma Aldrich	1:500
α-Cd11b	rat	101202	Biolegend	1:500
α-Cone Arrestin	Rabbit	AB15282	Sigma Aldrich	1:500
α-Cone Arrestin	goat	sc-34547	Santa Cruz	1:500
α-GFAP	mouse	644701	Biolegend	1:400
α-eGFP	chicken	GFP-1020	Aves Labs	1:500
α-eGFP	rat	sc-101536	Santa Cruz	1:300
α-Iba1	guinea pig	234 308	SySy	1:400
α-MAP2	rabbit	840601	Bioloegend	1:300
α-Pcp2	mouse	137064	Santa Cruz	1:500
α-PECAM (cd31)	rat	553370	BD Pharmingen™	1:100
α-Recoverin	rabbit	AB5585	Millipore	1:500
α-Rhodopsin	mouse	MA1-722	Invitrogen	1:400
α-Rhodopsin	mouse	MAB5356	Sigma Aldrich	1:1000

After incubation with the primary antibodies the slices were again washed three times with 0.1 M PB for 5 min each and directly incubated with the second master mix containing 3% ChemiBlocker and the secondary antibodies in their working dilution (see Table 9) in 0.1 M PB for 1.5 hours at room temperature.

Table 9: Secondary antibodies for immunohistochemistry

Anti-	Host	Catalog no.	Supplier	Working dilution
α-chicken-Alexa488	goat	A-11039	Invitrogen	1:500
α-goat-Cy3	bovine	805-165-180	Jackson	1:300
α-guinea pig-Cy3	donkey	706-165-148	Jackson	1:400
α-Lectin-PNA-A594	*Arachis hypogaea*	L32459	Invitrogen	1:300
α-mouse-Cy3	donkey	715-165-150	Jackson	1:400
α-rabbit-Cy3	donkey	AP182C	Millipore	1:400
α-rat-Cy3	donkey	712-165-153	Jackson	1:200
α-rat-A488	donkey	A-21208	Invitrogen	1:500

Samples were washed three times in 0.1 M PB. Nuclei were stained with a 1:1 000 dilution of DAPI (62248, Thermo Fisher) in 0.1 M PB for 10 min at RT. After a final PB-wash the slices were mounted with Aqua-Poly/Mount mounting medium (18606-5, Polysciences) and covered with 24x60 mm glass coverslips (630-2108, VWR). Slides were dried under exclusion of light overnight.

4.11 Imaging

4.11.1 Keyence microscopy

Overview pictures of retinae or other tissues were acquired with the Compact Fluorescence Microscope BZ-X800 (Keyence Corporation) at a 10x or 20x magnification using multiple z-stacks and the stitching tool. Pictures were further processed using the Keyence BZ-X800 analyzer software.

4.11.2 Confocal microscopy

Confocal images were acquired with Leica SP8 inverted or Leica SP8 upright microscopes with lasers emitting at 405, 488, 552 and 638 nm. For signal multiplication a PMT detector was used. Pictures were acquired as multiple z-stacks with a line average of 2 at a 20x or 40x magnification using the LAS X software V3.5.1.18803 (Leica). Further processing of confocal images was conducted with the open-source software Fiji ImageJ Version 1.53t [237].

4.12 Modeling of AAV capsids

In silico modeling was performed with the open-source RoseTTAfold algorithm from the BakerLab (https://robetta.bakerlab.org/). This structure prediction tool enables for accurate protein structure modeling while it does not rely on the input of a template sequence [238]. From the five received *de novo* models the protein structure with the lowest angstrom error and the least errors in the Ramachandran plot regarding amino acid angles and protein folding was further evaluated with the python-based Chimera software (Chimera 14.1, UCSF).

4.13 Statistics

If not mentioned otherwise n = 3 biological and/or technical replicates were performed. Statistical significance was evaluated using GraphPad Prism 9.1 (Graph-Pad, San Diego). Either paired or unpaired two-way analysis of variance was performed following Sidak's or Tuckey's post-hoc multiple comparisons test. The results are shown as mean ± standard error of the mean (SEM). Only values of $p \leq 0.05$ were accepted and considered significant. Levels of significance: $*p \leq 0.05$, $**p < 0.01$, $***p < 0.001$.

5 Results

5.1 Novel capsid mutants for retinal gene therapy based on AAV9 serotype

For the purpose of treating IRDs via AAV-based gene supplementation, AAV2 has been widely explored and proven to be a potent vector for long-term gene expression in various pre-clinical animal models, with sustained expression levels over at least 4-5 years after administration in canines [6], [239]. However, challenges like pre-existing immunity and low efficiency of target cell transduction often lead to insufficient therapeutic results [240], [241]. Therefore, the exploration of novel AAV capsids tailored towards more efficient photoreceptor transduction is crucial. Additionally, patient safety is one of the top priorities during human ocular gene therapy. Thus, less invasive pathways of vector delivery like intravitreal (IVT) injections need to be further explored. To address this, our lab engineered AAV2 capsid variants with modified heparan-sulfate proteoglycan (HSPG) binding motifs using a directed evolution approach. This resulted in vectors that can efficiently target photoreceptors through the less invasive IVT administration route [225]. To further enhance our toolbox with additional capsid variants that have favorable properties in the retina, we considered AAV9 as a capsid candidate for subsequent engineering and characterization. AAV9 was originally isolated from human liver tissue [242], [243] and has been shown to have low pre-existing immunity [244], [245] as well as strong neuronal transduction in the central nervous system (CNS) as it efficiently crosses the blood-brain barrier (BBB) [246], [247]. As such, the AAV9 serotype poses a good candidate for modification that will enhance its potency in the retina and extend our ability to transduce photoreceptors through alternative injection routes.

5.1.1 Strategy for modifying the HSPG-binding properties of AAV9

HSPG residues are unbranched and strongly negative charged heparan sulfate (HS) polysaccharides found on matrix proteins and cell surfaces serving as primary receptors for AAV2 [29], [51] by interacting with positively charged residues R585 and R588 exposed on the AAV2 capsid surface [53]. Although important for viral cell entry after IVT administration AAV2 strongly accumulates to HSPG residues at the inner limiting membrane (ILM) which results in low transduction efficiency in the retina [141], [248]. Editing the HSPG-binding affinity of AAV2 significantly improved penetration of vectors into all layers of the retina after IVT injection [225]. The two superior capsid variants, termed AAV2.NN and AAV2.GL, carry a small peptide insertion of seven amino acids (NNPTPSR = "NN" or GLSPPTR = "GL") and five additional

alanine residues between position R587 and R588. Three alanines upstream and two alanines downstream were introduced as flexible linkers flanking the NN- or GL-peptide insertion. These 12-mers disrupted the natural HSPG-binding motif and changed the native tropism of AAV2 WT [249], [250]. It is believed that these small peptide insertions confer an enhanced transduction ability to these capsids. We therefore hypothesized that superimposing the same modification in the context of AAV9 capsids could result in additional variants with high penetrance in the retina.

In this study, alternative HSPG-binding motifs are explored in the context of AAV9 utilizing advantages of this serotype like lower pre-existing immunity and strong neuronal tropism. AAV9 WT is known to primarily bind to glycans with terminal galactose residues [28], [251]. Here we explore the efficiency of introducing the 12-mer insertions "NN" or "GL" at selected residues on the AAV9 capsid. Therefore, a small peptide insertion was added at the top of loop IV displayed on the AAV9 capsid surface. In this serotype the top position of this loop is slightly shifted downstream between Q588 and A589 (Figure 16A, magenta). The insertion is located within the common VP3 part of the Cap-sequence resulting in a display in all 60 subunits comprising the final AAV9 capsid mutant (Figure 16C).
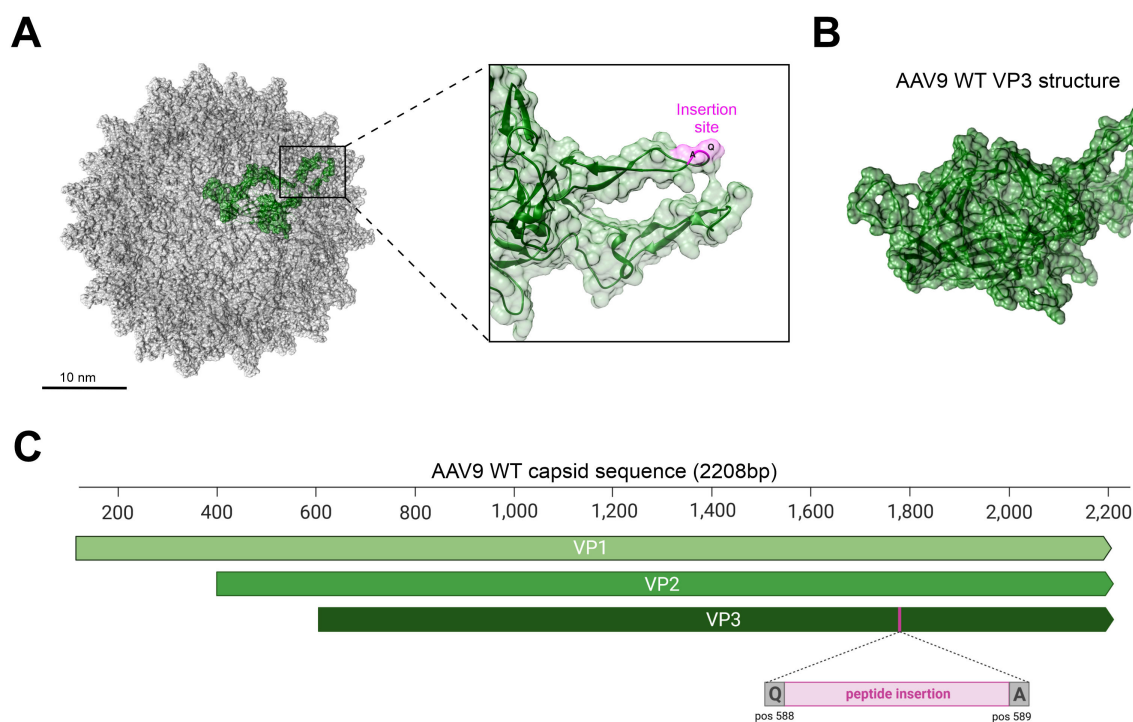
Figure 16 Generation of novel AAV9 capsid mutants (A) Biological assembly of AAV9 capsid (PDB: 3ux1) showing the location of the insertion site (magenta) in loop IV on the capsid surface. (B) Single VP3 monomer comprising the AAV capsid. (C) Location of the peptide insertion (magenta) in the AAV9 Cap-sequence between Q588 and A589. Scale bar marks 10 nm.

A total of ten novel AAV9 capsid mutants were generated: Six variants displaying either the NN- or GL-insertion flanked by alanine linkers to allow for a more sterically flexible extension of loop IV (Figure 17A). Additionally, four capsid mutants were generated with only small amino acid substitutions and/or insertions without the additional NN- or GL-insertion (Figure 17C). AAV9 WT does not bind to HSPG per se. We hypothesized that in AAV2.NN and AAV2.GL an alternative HSPG-binding motif is generated by the positively charged arginine residue at the end of the NN- or GL-insertion and a naturally occurring second arginine at position R588 following the insertion. Incorporation of the NN or GL peptides into the AAV9 WT capsid would not produce this motif because AAV9 has an alanine instead of an arginine at the position that follows the insertion site (A589 instead of R588 in AAV2). However, the two neutrally charged amino acids (such as alanines) need to be flanked by two positively charged amino acids for efficient HSPG-binding [53], [252]. To explore if this binding motif can be generated and result in improved transduction properties of AAV9, single amino acid substitutions were established at position A589 changing this amino acid into a positively charged arginine (Arg, R) or lysine (Lys, K). These modifications resulted in the R- and K-mutants termed AAV9.NNR, AAV9.NNK, AAV9.GLR, and AAV9.GLK (Figure 17B). Histidine as a positively charged amino acid was not tested due to its low pK$_A$ of 6.04 [53].

Capsid	*Q588	Linker	Insertion	Linker	*A589
AAV9 WT	Q	-	-	-	A
AAV9.R	Q	-	-	-	R
AAV9.AAR	Q	-	-	AA	R
AAV9.RAAR	Q	-	R	AA	R
AAV9.RAAK	Q	-	R	AA	K
AAV9.NN	Q	AAA	NNPTPSR	AA	A
AAV9.NNR	Q	AAA	NNPTPSR	AA	R
AAV9.NNK	Q	AAA	NNPTPSR	AA	K
AAV9.GL	Q	AAA	GLSPPTR	AA	A
AAV9.GLR	Q	AAA	GLSPPTR	AA	R
AAV9.GLK	Q	AAA	GLSPPTR	AA	K
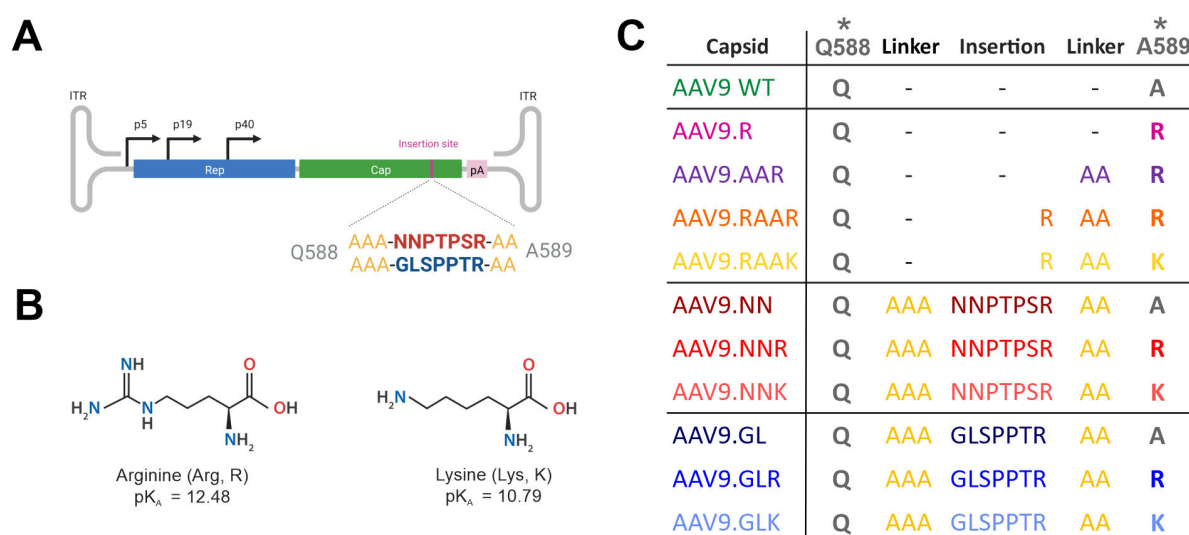
Figure 17 Overview of capsid mutants and their corresponding insertion sequences Shown are the amino acid sequences of all ten novel AAV9 capsid mutants between Q588 and A589 (gray). (A) shows the NN- and GL-insertion flanked by three alanines upstream and two alanines downstream as linkers (yellow). (B) Table provides a detailed overview of the amino acid sequences for all novel capsid mutants in comparison to AAV9 WT (first row; green).

Additionally, the potential alternative HSPG-binding motif was explored in four novel capsid variants without the NN or GL peptide by insertion of an arginine (R) at position 589 followed by two alanines (AA) and substitution of A589 to R (= "AAV9.RAAR") or K (= "AAV9.RAAK"). Moreover, variants with double alanine insertion and A589R substitution (= "AAV9.AAR") or a single A589R substitution (= "AAV9.R") were generated. All mutants are listed in Figure 17C.

The novel capsid mutants were modelled *in silico* using the RoseTTAfold tool from the BakerLab (https://robetta.bakerlab.org/). This structure prediction tool enables for accurate protein structure modeling while it does not rely on the input of a template sequence [238]. RoseTTAfold results were further processed with the UCSF Chimera open-source software. For detailed analysis the model with the lowest angstrom error and the least amino acids outside the border limits in their respective Ramachandran plots were used. Figure 18 shows the surface exposed loop III and loop IV region of one VP3 subunit of each mutant at its most probable structural conformation after the insertion or substitution. Due to the small size of modifications in each novel vector variant the overall capsid structure is maintained while only minor changes are visible at the insertion point and the adjacent loops on the capsid surface (Figure 18B-L) in comparison to the AAV9 WT (Figure 18A) in one single VP3 monomer. For AAV9.R, AAV9.RAAR, AAV9.RAAK, AAV9.NN, AAV9.NNR and AAV9.GL (Figure 18B, D-G, J) the modifications result in an extension of loop IV without an additional tertiary structure. On the other hand, AAV9.AAR, AAV9.NNK, AAV9.GLR and AAV9.GLK (Figure 18C, H, K, L) show the formation of α-helices within the loop IV region due to the inserted amino acid sequences and their residues interacting with each other. The whole capsid assembly of each mutant (Figure 19) shows all 60 subunits assembled to a full icosahedral AAV capsid with the corresponding-colored sequence modifications. Each variant shows three VP3 subunits converging on the 3-fold symmetry axis with their corresponding insertion or substitution presented on the capsid surface.
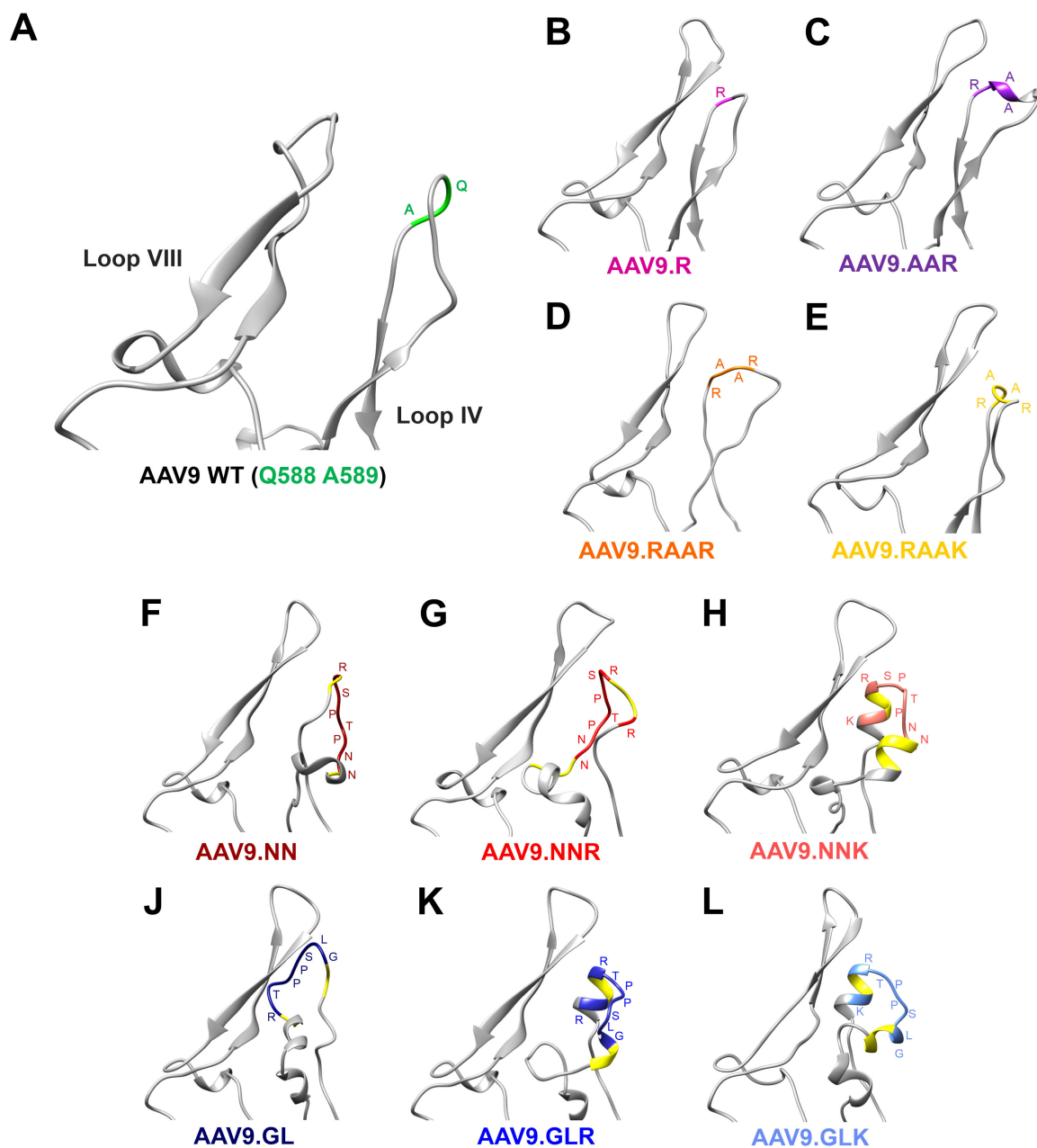
Figure 18 Detailed overview of AAV9 capsid mutant insertions Single loops showing the insertions or substitutions for each novel capsid mutant in one VP3 monomer. (A) AAV9 WT monomer with the insertion site marked (green) in loop IV. (B-E) Capsid mutants carrying small insertions and substitutions without the NN- or GL-insertion. (F-H) AAV9 capsid mutants with the NN- or the GL-insertion (J-L) followed by a single amino acid substitution.
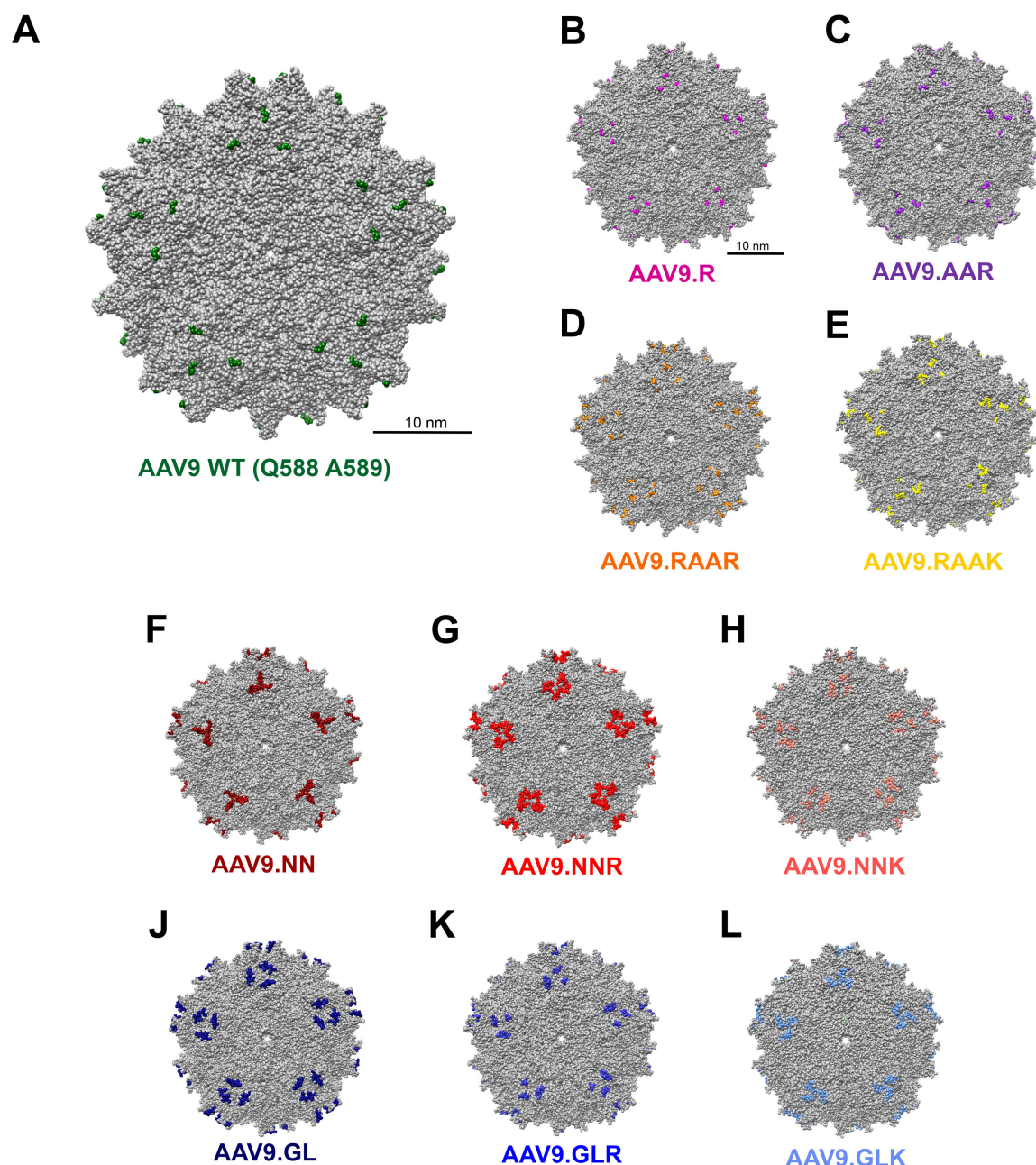
Figure 19 Overview of assembled AAV9 mutant capsids shown from the 5-fold axis (A) AAV9 WT capsid with insertion site marked (green). (B-E) Capsid mutants carrying small insertions and substitutions without the NN- or GL-peptide. (F-H) AAV9 capsid mutants with the NN- or the GL-insertion (J-L) followed by a single amino acid substitution. Respective insertions or substitutions on the capsid surface are colored. Scale bar marks 10 nm.

5.1.2 Characterization of AAV9 capsid variants

5.1.2.1 Production yields of novel AAV9 capsid mutants

For initial characterization we first assessed whether the AAV9 capsid mutants can support the production of AAV vectors using a standard production process. To this end, we assessed both the genomic titer and the capsid titer of AAV9 WT and mutant vector preparations to gain a first impression of potential differences between AAV9 WT and capsid mutant. The

genomic titer was determined by qRT-PCR using primers that bind at the ITR-sequence of the pAAV2.1_sc_CMV-eGFP transgene cassette. Typically, genomic titers between 1×10^{10} vg/µL and 5×10^{11} vg/µL can be generated with AAV9 in our facility, which is higher than what we obtain from AAV2-based viral preparations. For AAV9 WT we obtained a mean genomic titer of 3.3×10^{11} vg/µL ± 1.9 x 1011 vg/µL SEM and then compared all mutants to that baseline, while also comparing between the mutants. The capsid variants AAV9.R and AAV9.AAR showed the most comparable genomic titers to AAV9 WT. In contrast, the mutants AAV9.RAAR and AAV9.RAAK resulted in the lowest titers between 2×10^7 vg/µL and 8×10^8 vg/µL (Figure 20A). The AAV9.NN capsid mutant reaches the highest genomic titer out of all 11 evaluated capsid variants with a mean genomic titer of 3.4×10^{11} vg/µL. Further NN-carrying variants showed slightly decreased genomic titers for AAV9.NNR (4.3×10^{10} vg/µL) and AAV9.NNK (3.1×10^{10} vg/µL), but well within the AAV9 WT range. AAV9.GL-based capsids showed a similar trend with AAV9.GL generating the highest genomic titer (5.5×10^{10} vg/µL) and AAV9.GLR (2×10^{10} vg/µL) and AAV9.GLK (1×10^{10} vg/µL) with slightly reduced genomic titers. However, looking at the capsid titers determined by static light scattering (SLS) measurement (Figure 20B) AAV9.RAAK shows the highest discrepancy between genomic and capsid titer (yellow). While AAV9 WT shows 54% full capsids, AAV9.RAAK with a capsid titer of 3.4×10^8 cp/µL leads to only 0.5% full AAV capsids due to its low genomic titers. This suggests that although the capsid seems to be assembled correctly, the capability of genome packaging is highly decreased for this vector. In comparison, AAV9.R shows 80.3% full capsids which is the highest percentage of full capsids within the investigated AAV9 mutants. Across the remaining AAV9 mutants a range of full capsids from 22% up to 59% was measured (Table 10).
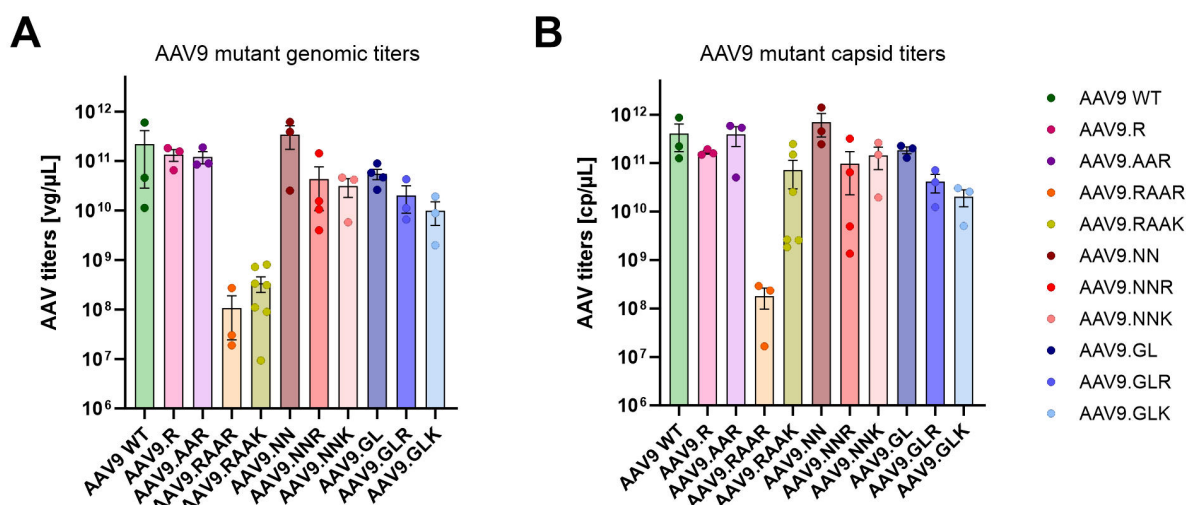
Figure 20 Overview of AAV9 capsid mutant production yields (A) Genomic titer of capsid variants determined via ITR-binding qRT-PCR. (B) Capsid titer in final AAV sample measured by SLS. n = 3, error bars indicating ± SEM.

Table 10: Full capsid ratio of novel AAV9 mutants

AAV capsid	AAV9 WT	AAV9.R	AAV9.AAR	AAV9.RAAR	AAV9.RAAK	AAV9.NN	AAV9.NNR	AAV9.NNK	AAV9.GL	AAV9.GLR	AAV9.GLK
full capsid Mean [%]	54	80.3	30.9	59.1	0.5	48.9	44.4	21.8	29.7	48.6	48.8

5.1.2.2 Evaluation of thermal stability of AAV9 capsid variants

Another characteristic property of AAV capsids is their melting temperature T_m which was analyzed in a thermal stability assay by intrinsic differential scanning fluorimetry (iDSF) [232]. With this method the absorbance of tryptophan residues facing the capsid cargo is assessed during exposure to a temperature gradient. A peak in fluorescence signal determines the unfolding temperature of the capsid where these residues can be detected. All AAV9 mutants were adjusted to the same capsid titer for measurements. Due to low genomic and capsid titers, AAV9.RAAR and AAV9.RAAK were measured as undiluted samples. AAV9 WT is known to have a comparably high T_m of 78°C, which is 10°C higher than other naturally occurring serotypes like AAV2 WT with T_m = 68°C [253]. Since the melting temperatures differ characteristically among AAV serotypes, the T_m value can be used to confirm the identity of AAV capsids [232], [254]. In our measurements, AAV9.WT shows T_m of 77.6°C, which is in the expected range from literature. While AAV9.R matches the AAV9 WT, AAV9.AAR (66.5°C), AAV9.RAAR (63°C) and AAV9.RAAK (57.5°C) show a strongly decreased T_m (Figure 21A-B). For AAV9.RAAR and AAV9.RAAK measurements were unprecise due to the low sample titers. All AAV9.NN-based mutants showed a similar decrease in T_m to 61-62°C (Figure 21C-D), which is also the T_m of AAV2.NN and AAV2.GL carrying the same insertion [225]. AAV9.GL-based variants showed T_m of 59-62°C (Figure 21E-F). For AAV9.GLR and AAV9.GLK the lower sample titers indicated by peak heights in (Figure 21E) could also affect the T_m to be lower than 60°C. Overall these results illustrate how strongly the T_m can be influenced by minor changes in the capsid sequence leading to drastic decreases in thermal capsid stability.
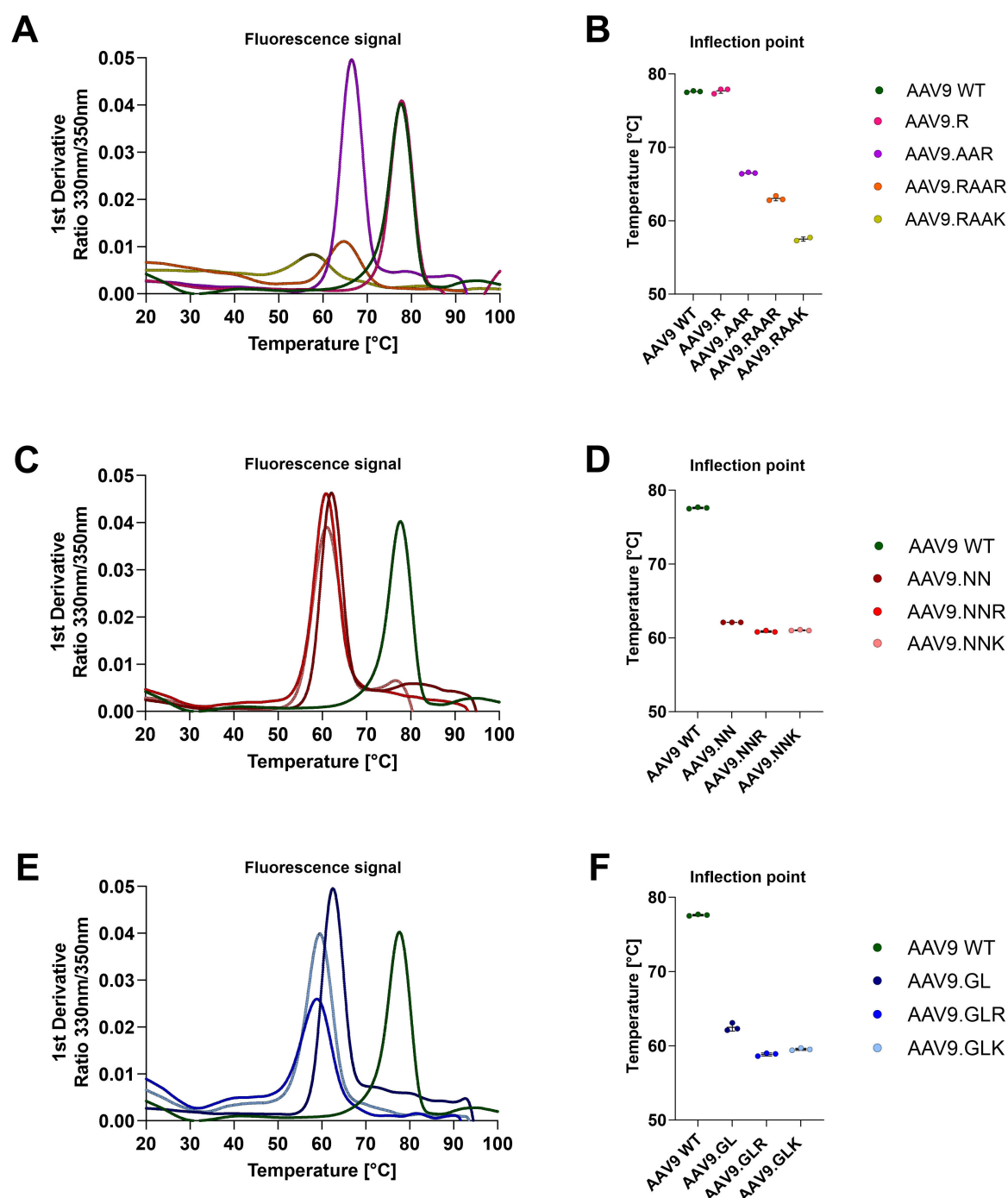
Figure 21 Thermal stability analysis of AAV9 capsid mutants (A) T_m of AAV9 WT-based variants with corresponding Inflection point (B) indicating the temperature at which the AAV capsid unfolds measured via iDSF. T_m of mutants carrying the NN- (C-D) or the GL-insertion (E-F) with the AAV9 WT (green) as reference. Error bars indicating ± SEM, n = 3.

5.1.3 Evaluation of AAV9 mutants in HeLa cells

Transduction properties of novel AAV9 mutants were first assessed in HeLa cells. AAVs have been evaluated extensively in HeLa cells showing higher transduction properties than in other immortalized cell lines [255]. Cells were seeded in 24well plates as described in 4.3.3 and

transduced the following day with AAV9 capsid mutants carrying an ITR-flanked scCMV-eGFP reporter cassette at a multiplicity of infections (MOI) of 5 000, 10 000 and 100 000 vg/cell.

All ten AAV9 capsid mutants were tested with the AAV9 WT as a reference. Cells were incubated for 48 hours at 37°C following imaging at the EVOS fluorescence microscope (BF; 60% GFP λ_{ex} 488) and quantification of eGFP-positive cells at the Countess 3 FL Automated Cell Counter. AAV9 WT and AAV9.RAAK show modest transduction of HeLa cells at 5 000 vg/cell, and a dose dependent increase (Figure 22). Although at 10 000 vg/cell AAV9.RAAK significantly outperforms the WT, at 100 000 vg/cell the maximum saturation is reached, resulting in comparable transduction rates. In contrast, AAV9.R, AAV9.AAR and AAV9.RAAR show almost no transduction in HeLa cells.
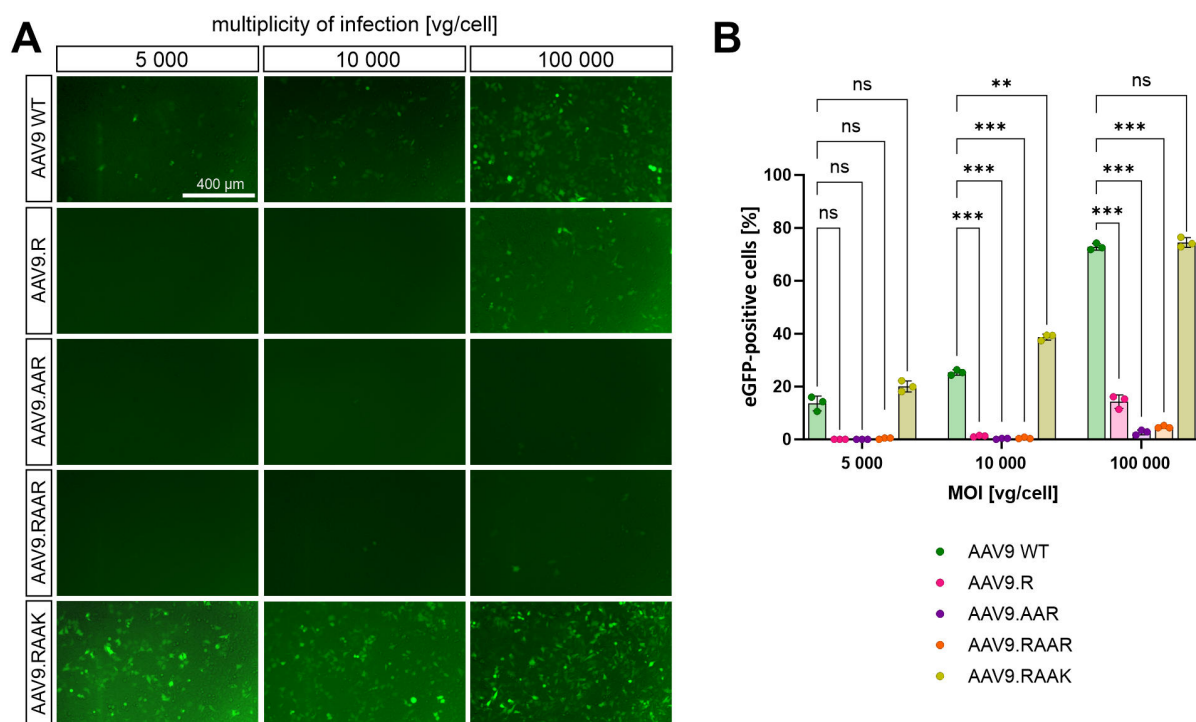
Figure 22 Transduction properties of AAV9 WT, AAV9.R, AAV9.AAR, AAV9.RAAR and AAV9.RAAK in HeLa cells
(A) Representative epifluorescence images taken 48 hours after transduction at 60% GFP intensity and 10x magnification. Cells were transduced with eGFP-expressing AAV9 capsid mutants at MOI 5 000, 10 000 and 100 000 [vg/cell]. Scale bar marks 400 µm. (B) Quantification of eGFP-positive HeLa cells. Two-way ANOVA with Tuckey's post-hoc test. * $p < 0.05$, ** $p < 0.01$, *** $p < 0.001$, n = 3.

AAV9 capsid mutants carrying the NN-insertion significantly decreased the transduction efficiency compared to AAV9 WT. However, substitution of A589 with R or K (AAV9.NNR and AAV9.NNK) strongly increased transduction efficiency and outperformed the AAV9 WT (Figure 23). This suggests, that the artificial "RAAR" or "RAAK" HSPG-binding motif increases the functionality of AAV9.NN, probably by increasing cell entry.
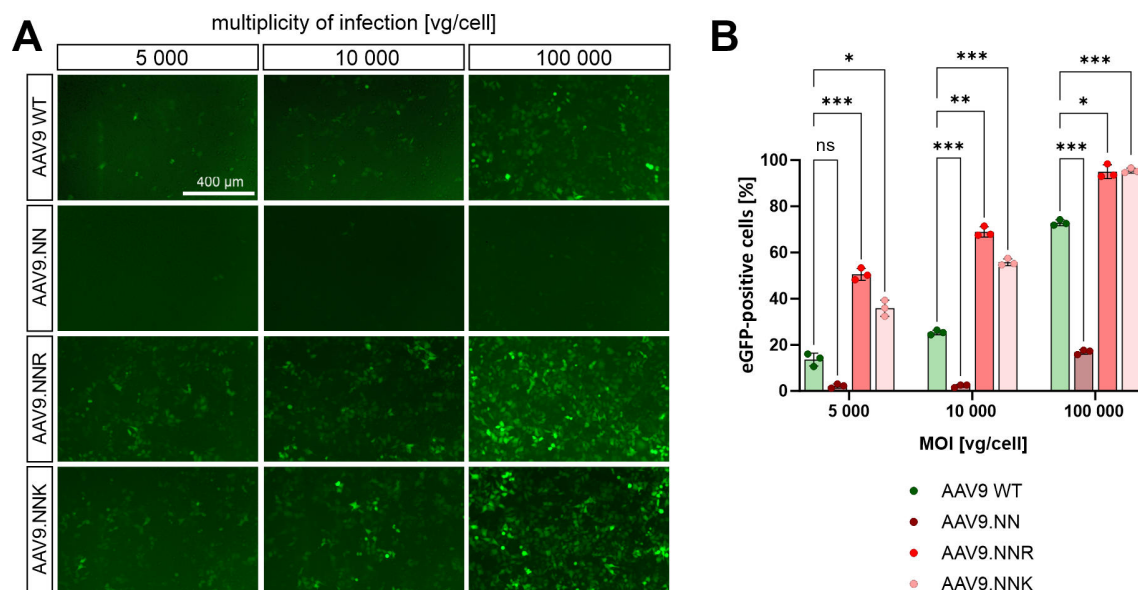
Figure 23 Transduction properties of AAV9.NN, AAV9.NNR and AAV9.NNK in HeLa cells (A) Representative epifluorescence images taken 48 hours after transduction at 60% GFP intensity and 10x magnification. Cells were transduced with eGFP-expressing AAV9 capsid mutants at MOI 5 000, 10 000 and 100 000 [vg/cell]. Scale bar marks 400 µm. (B) Quantification of eGFP-positive HeLa cells. Two-way ANOVA with Tuckey's post-hoc test. * $p < 0.05$, ** $p < 0.01$, *** $p < 0.001$, n = 3.

This mechanism can also be observed with the AAV9.GL mutant (Figure 24). Transduction rates are decreased with the GL-insertion compared to the AAV9 WT but can be restored and even significantly improved with single amino acid substitutions (A589R or A589K) as in AAV9.GLR and AAV9.GLK.
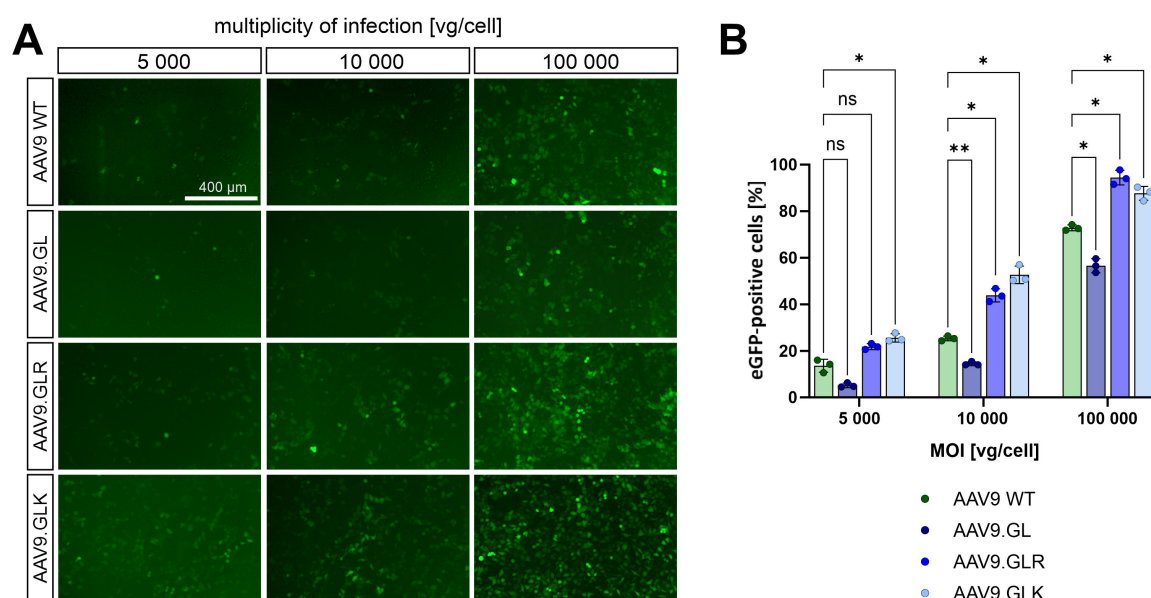
Figure 24 Transduction properties of AAV9.GL, AAV9.GLR and AAV9.GLK in HeLa cells (A) Representative epifluorescence images taken 48 hours after transduction at 60% GFP intensity and 10x magnification. Cells were transduced with eGFP-expressing AAV9 capsid mutants at MOI 5 000, 10 000 and 100 000 [vg/cell]. Scale bar marks 400 µm. (B) Quantification of eGFP-positive HeLa cells. Two-way ANOVA with Tuckey's post-hoc test. * $p < 0.05$, ** $p < 0.01$, *** $p < 0.001$, n = 3.

5.1.4 *In vivo* evaluation of IVT vector administration in C57BL6/J mice

For *in vivo* vector evaluation a dose escalation study was conducted by IVT administration of 1-1.5 µL of 1 x 10^9 total vg (low dose), 5 x 10^9 total vg (medium dose) and 1 x 10^{10} total vg (high dose) in adult C57BL6/J mice. Each vector was packaged with an ITR-flanked scCMV-eGFP reporter cassette. Transgene expression was monitored for three weeks by confocal scanning laser ophthalmoscopy (cSLO). After 3 WPI eyes were removed, dissected, and further processed for cryo-sectioning and immunohistochemistry (IHC).

5.1.4.1 Evaluation of 1 x 10^9 total vg low dose vector administration

AAV9 WT shows promising widespread eGFP expression in the cSLO measurements after 1 µL IVT low dose vector administration, which stays constant during the three weeks of *in vivo* monitoring while AAV9.R, AAV9.AAR and AAV9.RAAR show no or only weak eGFP signal (Figure 25, row 1-4). In contrast, AAV9.RAAK shows eGFP expression around the optic nerve (ON) where the vector was released during IVT injection (Figure 25, row 5). Note that due to low production titers for this vector exclusively 1.5 µL were injected to achieve the desired 1 x 10^9 total vg (low dose). For this reason, *in vivo* vector evaluation of AAV9.RAAK is limited to low dose administration only.

AAV9.NN-based vector variants show the strongest *in vivo* performance with AAV9.NN (Figure 26A, upper row). Transgene expression stays constant during the period of monitoring across the whole fundus. In contrast, AAV9.NNR (Figure 26A, middle row) shows strong eGFP signal around the ON and blood vessels which increases from 1 WPI to 2 WPI but then stays constant while AAV9.NNK (Figure 26A, bottom row) shows almost no signal. AAV9.GL-based variants reveal AAV9.GL as the strongest performing vector at 1 x 10^9 total vg also showing strong transduction around the blood vessels and the ON (Figure 26B, upper row), while AAV9.GLR and AAV9.GLK show only peripheral eGFP expression (Figure 26B, middle and bottom row).

Further, cell type specific transduction by novel vector variants was evaluated via IHC (Figure 27). For antibody staining cryo-sections located close to the ON were chosen and stained for eGFP (green), since AAV vectors were released at this position during IVT administration. Transduction of cone photoreceptors was confirmed by staining for cone arrestin (Arr3, magenta). Side-by-side comparison of all eleven tested vectors after low dose AAV

administration reveals low levels of ONL and photoreceptor transduction for AAV9 WT (Figure 27A) with co-localization at the synaptic terminals of the photoreceptors.
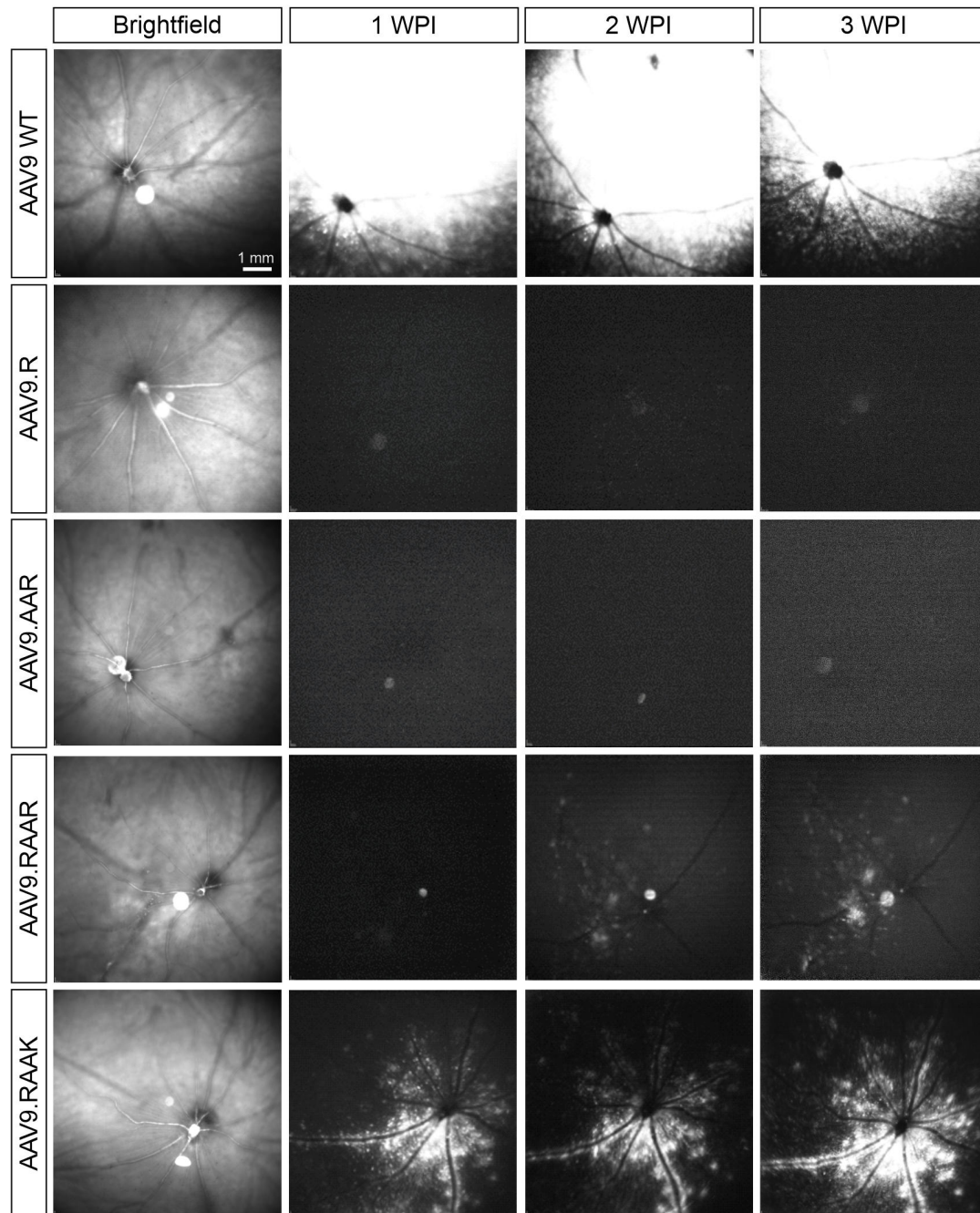
Figure 25 *In vivo* **cSLO fundus imaging after IVT low dose administration of AAV9 WT and AAV9 WT-based variants** A low dose of AAV9 mutants (1 µL, 1 x 10^9 vg total) carrying an scCMV-eGFP reporter cassette was injected IVT. Mice were monitored and imaged for three consecutive weeks. cSLO images show brightfield fundus (first column) and epifluorescence signal for 1 WPI, 2 WPI and 3 WPI. Scale bar marks 1 mm. WPI weeks post injection.

AAV9.R and AAV9.AAR (Figure 27B-C) show intact retinal cell layers but no transduction while AAV9.RAAR (Figure 27D) shows only few transduced photoreceptors. In contrast, AAV9.RAAK (Figure 27E) shows stronger ONL and photoreceptor transduction than AAV9 WT.
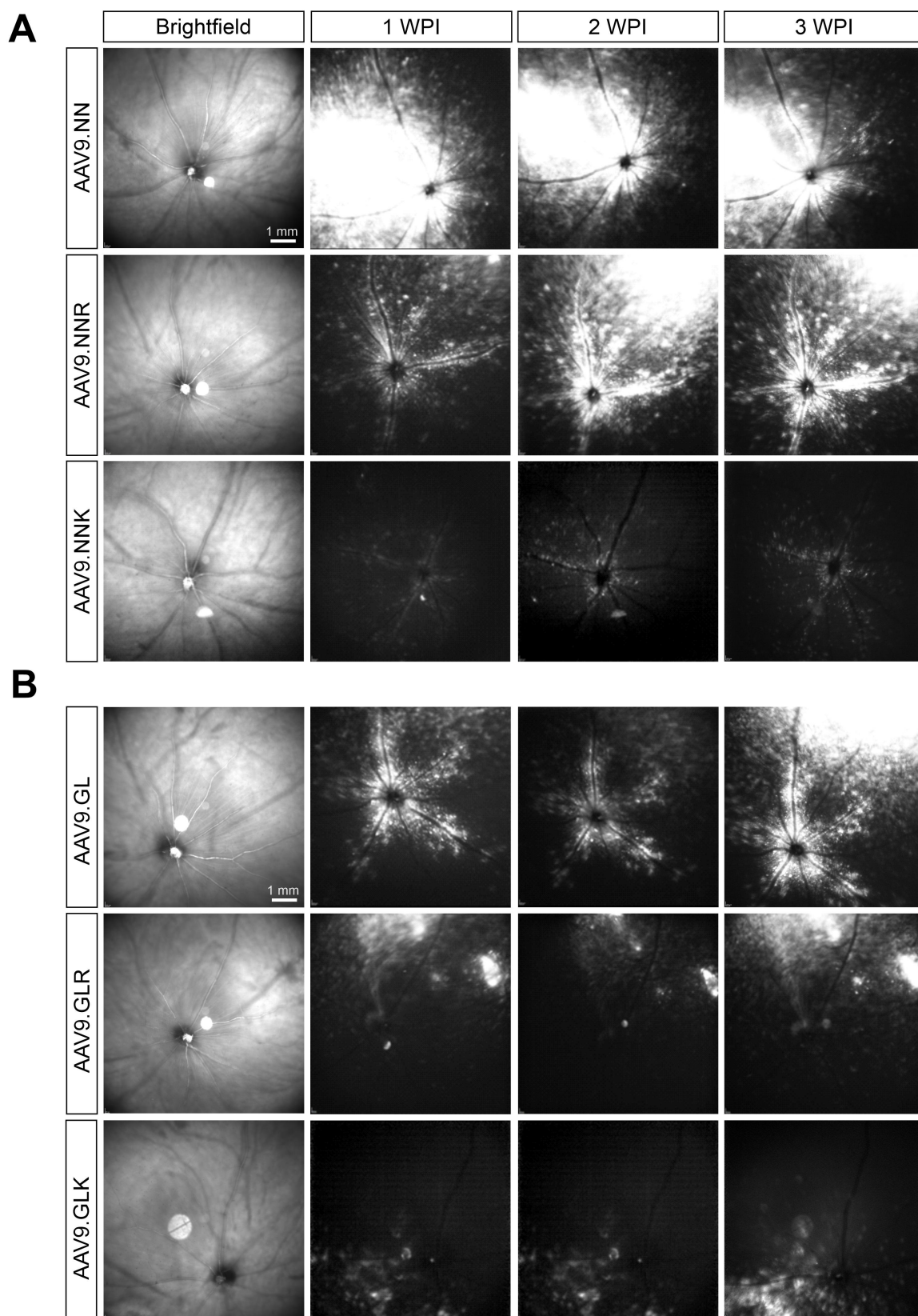
Figure 26 *In vivo* cSLO fundus imaging after IVT low dose administration of AAV9.NN- and AAV9.GL-based capsid variants A low dose of (A) AAV9.NN- or (B) AAV9.GL-based capsid mutants (1 µL, 1 x 10^9 vg total) carrying an scCMV-eGFP reporter cassette was injected IVT. Mice were monitored and imaged for three consecutive weeks. cSLO images show brightfield fundus (first column) and epifluorescence signal for 1 WPI, 2 WPI and 3 WPI. Scale bar marks 1 mm. WPI weeks post injection.

The NN-based variants (Figure 27F-H) show the strongest ONL transduction for AAV9.NN followed by AAV9.NNR and only low transduction levels for AAV9.NNK. Further, the variants carrying the GL-insertion (Figure 27J-L) show the highest transduction levels for AAV9.GLR, followed by AAV9.GL and almost no transduction with AAV9.GLK. Overall, the IHC results match the cSLO impressions although transduction levels for some variants are higher in the stained cross-sections than shown by fundus fluorescence (Figure 27E, K). This effect most likely depends on the cross-sections chosen for IHC.
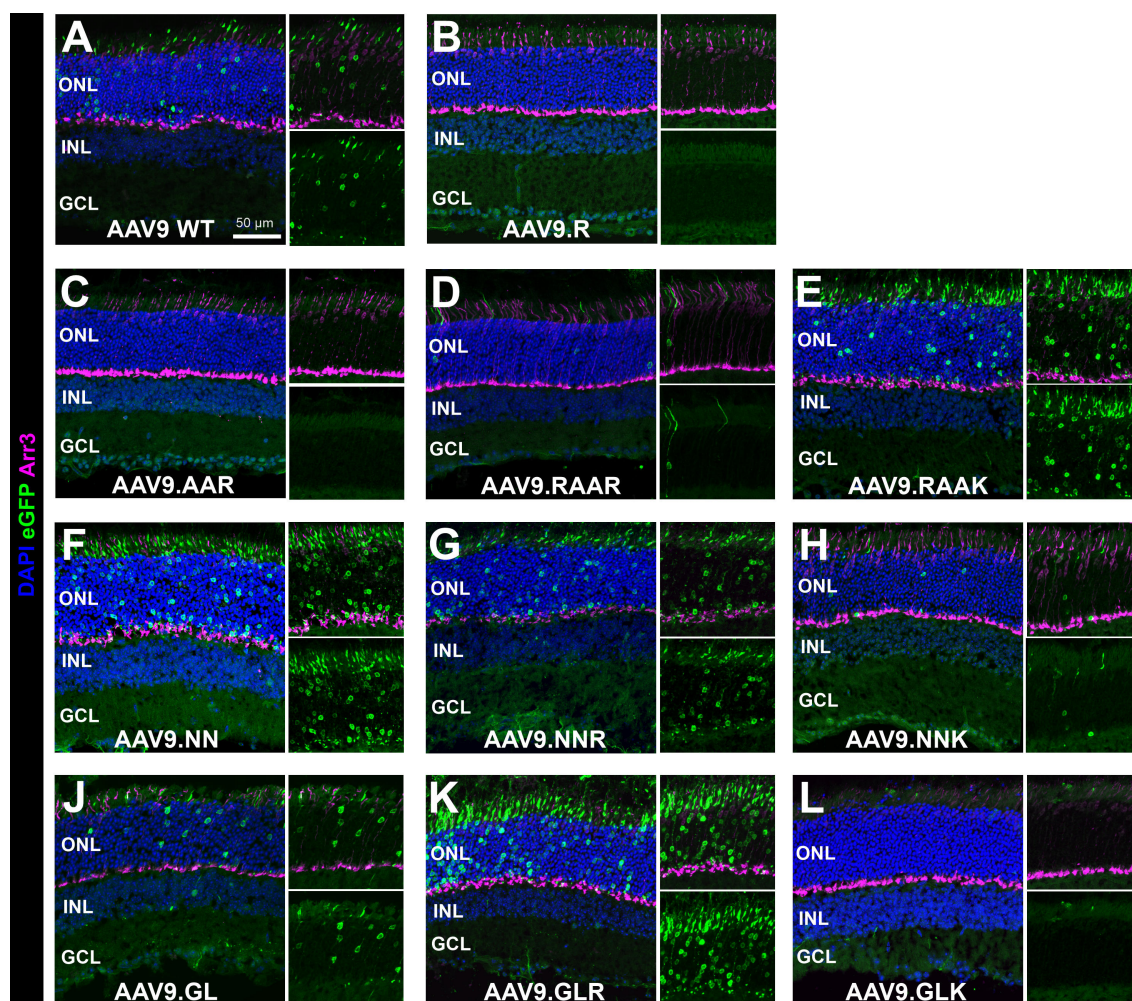
Figure 27 IHC of retinal cross-sections after IVT administration of low dose AAV9 capsid mutants Representative retinal cross-sections showing transduction of retinal cell layers after injection of 1×10^9 total vg three weeks after IVT administration. eGFP-positive cells are shown in green; cone photoreceptors were stained for cone arrestin (CAR, Arr3, magenta). Cell nuclei were stained with DAPI (blue). Small images show focus on ONL transduction. Scale bar marks 50 μm. ONL outer nuclear layer, INL inner nuclear layer, GCL ganglion cell layer.

5.1.4.2 Evaluation of 5 x 10^9 total vg medium dose vector administration

To further explore the full potential of the AAV9 variants two higher viral vector doses were injected intravitreally. A medium dose of 5 x 10^9 total vg carrying an eGFP expression cassette was injected with a total volume of 1 µL in adult C57BL6/J mice. Mice were monitored over three weeks as described in 5.1.4.1. cSLO fundus images show a dose-dependent increase in eGFP signal compared to the low dose study (Figure 28). While AAV9 WT shows whole fundus fluorescence already at 1 WPI (Figure 28A) the eGFP expression of AAV9.NNR (Figure 28B, middle row) increases most during the monitoring period. It is also noticeable that AAV9.GL (Figure 28C, upper row) shows an irregular pattern of transduction throughout the fundus with several concentrated spots of eGFP expression around large retinal blood vessels. Moreover, with the medium vector dose both K-mutants (Figure 28B, C; bottom row) show increased transduction.

This increase in transduction also translates to the confocal images after IHC (Figure 29). AAV9 WT (Figure 29A) shows transduction localized mainly in the ONL and the photoreceptor (inner) segments with only few co-localized cones at the synaptic terminal in the outer plexiform layer (OPL). AAV9.NN, AAV9.NNK and AAV9.GLK (Figure 29B, D, G) show elevated eGFP expression in photoreceptors while AAV9.GL (Figure 29E) performs just slightly better than in the low dose study (5.1.4.1). Remarkable is the performance of both R-mutants (Figure 29C, F), which show the highest photoreceptor transduction across all vector variants at this dose.

Figure 28 *In vivo* **cSLO fundus imaging after IVT medium dose administration of AAV9 WT, AAV9.NN- and AAV9.GL-based capsid variants** Medium dose of AAV9 capsid mutants (1 μL, 5 x 10^9 vg total) carrying an scCMV-eGFP reporter cassette was injected IVT. Mice were monitored and imaged for three consecutive weeks. cSLO images show brightfield fundus (first column) and epifluorescence signal for 1 WPI, 2 WPI and 3 WPI for (A) AAV9 WT (B) AAV9.NN-based variants and (C) AAV9.GL-based variants. Scale bar marks 1 mm. WPI weeks post injection.
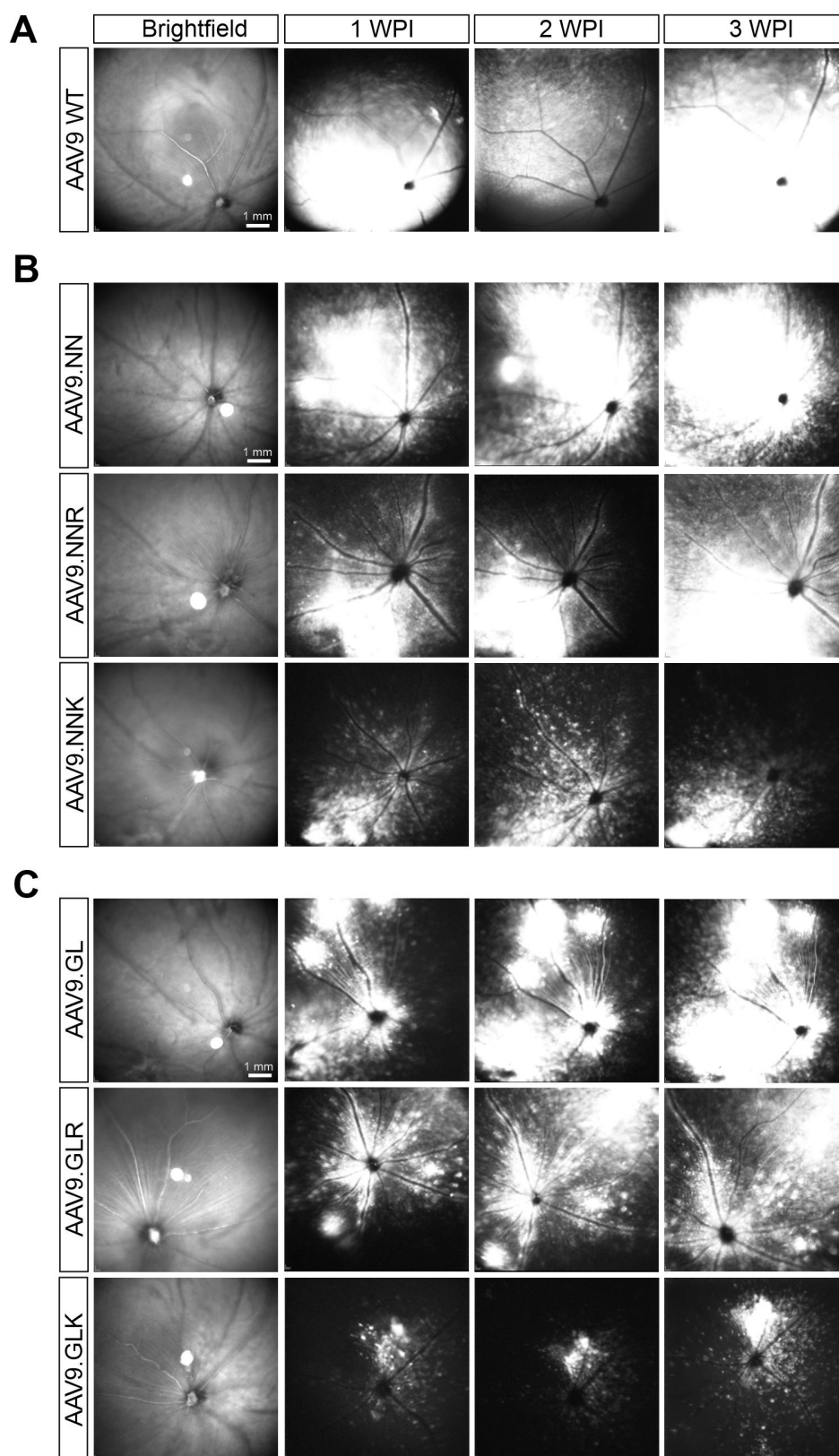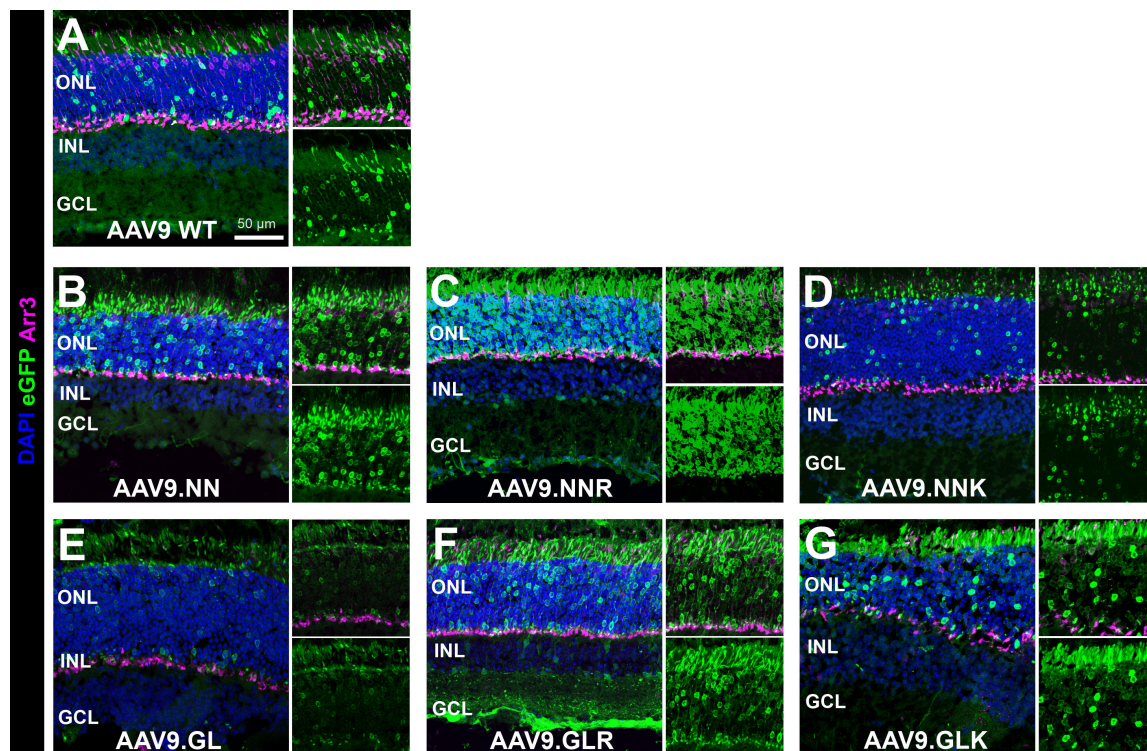
Figure 29 IHC of retinal cross-sections after IVT administration of medium dose AAV9 capsid mutants
Representative retinal cross-sections showing transduction of retinal cell layers after injection of 5 x 10^9 total vg three weeks after IVT administration. eGFP-positive cells are shown in green; cone photoreceptors were stained for cone arrestin (CAR, Arr3, magenta). Cell nuclei were stained with DAPI (blue). Small images show focus on ONL transduction. Scale bar marks 50 µm. ONL outer nuclear layer, INL inner nuclear layer, GCL ganglion cell layer.

5.1.4.3 Evaluation of 1 x 10^{10} total vg high dose AAV administration

Lastly, the dose dependency of AAV9 mutant capsid-mediated transduction efficiency was investigated with a high dose IVT injection of 1 x 10^{10} total vg in 1 µL. The vector administration and monitoring were performed as described for the low and middle dose study. This dose escalation study was performed specially to investigate any structural changes and the degree of reactive gliosis after high dose vector administration. Comparing medium dose cSLO images (Figure 28) to the dose escalation study (Figure 30) its recognizable that the eGFP signal across the fundus for AAV9 WT (Figure 30A) and AAV9.GL (Figure 30C, upper row) did not further increase substantially. AAV9.GL (Figure 30C, upper row) shows a different eGFP expression pattern than at the medium dose, however, the signal is still concentrated at the central retinal area. For all NN-based variants (Figure 30B) as well as AAV9.GLR and AAV9.GLK (Figure 30C, middle and bottom row) there is a clear increase in fluorescence signal compared to the medium dose.
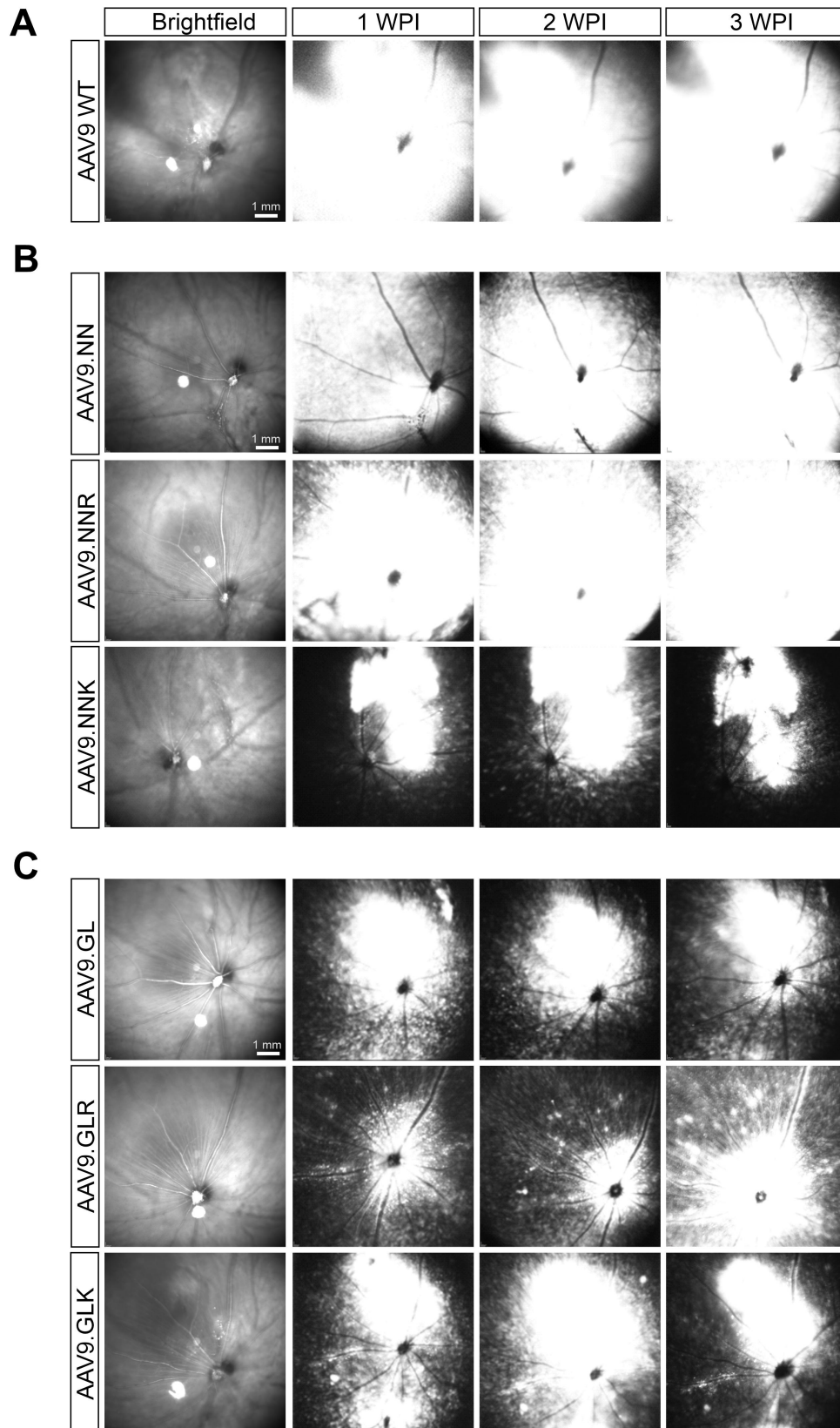
Figure 30 *In vivo* **cSLO fundus imaging after IVT high dose administration of AAV9 WT, AAV9.NN- and AAV9.GL-based capsid variants** High dose of AAV9 capsid mutants (1 µL, 1 x 10^{10} vg total) carrying an scCMV-eGFP reporter cassette was injected IVT. Mice were monitored and imaged for three consecutive weeks. cSLO images show brightfield fundus (first column) and epifluorescence signal for 1 WPI, 2 WPI and 3 WPI for (A) AAV9 WT (B) AAV9.NN-based variants and (C) AAV9.GL-based variants. Scale bar marks 1 mm. WPI weeks post injection.
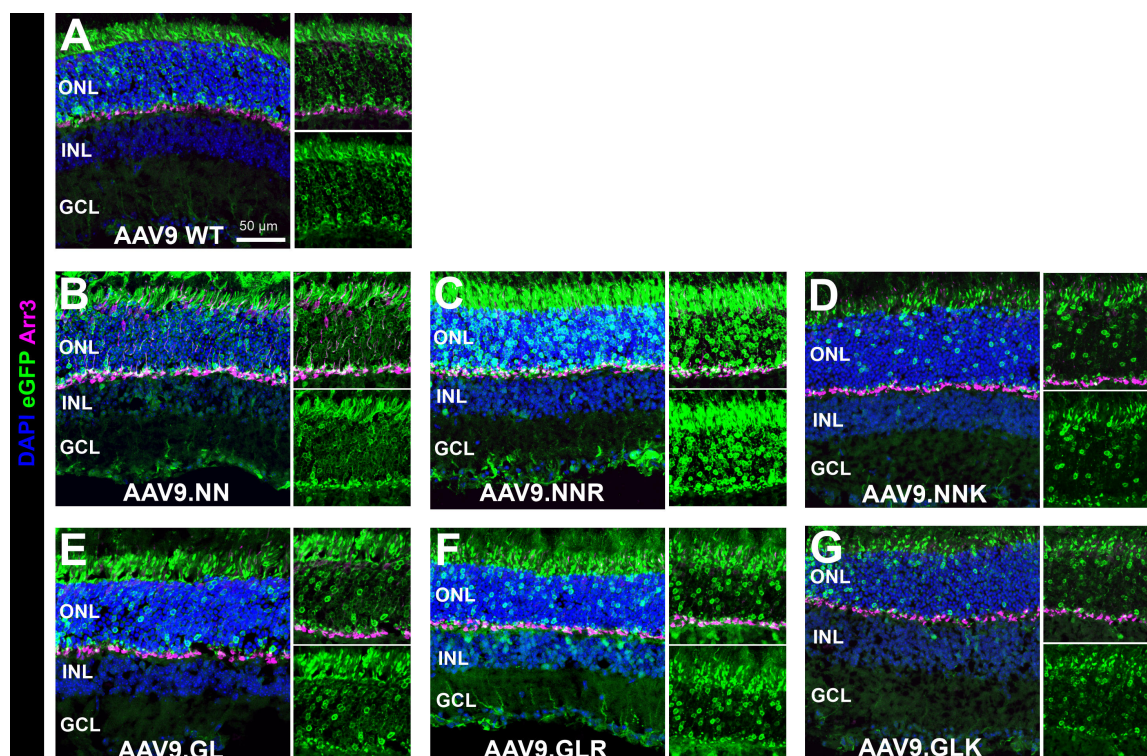
Figure 31 IHC of retinal cross-sections after IVT administration of high dose AAV9 capsid mutants
Representative retinal cross-sections showing transduction of retinal cell layers after injection of 1 x 10^{10} total vg three weeks after IVT administration. eGFP-positive cells are shown in green; cone photoreceptors were stained for cone arrestin (CAR, Arr3, magenta). Cell nuclei were stained with DAPI (blue). Small images show focus on ONL transduction. Scale bar marks 50 µm. ONL outer nuclear layer, INL inner nuclear layer, GCL ganglion cell layer.

The IHC images of the high dose group show an increase in eGFP-positive photoreceptors for all vector mutants except AAV9.GLK (Figure 31G). Although cSLO images showed high eGFP signal, the cross-sections revealed transduction levels of ONL and photoreceptor segments comparable to or slightly lower than the medium dose study. With a vector dose of 1 x 10^{10} total vg the AAV9.NNR mutant (Figure 31C) shows the highest transduction rate across all tested variants. Co-localization of eGFP signal at the synaptic terminal of photoreceptors can be observed at the OPL.

5.1.4.4 Müller glia activation after IVT administration of AAV9 mutants

Animal studies as well as clinical trials have shown that intraocular application of AAV vectors can result in retinal stress, inflammation and surgery-related collateral damage which impact on the gene therapy outcome [95], [256], [257]. In this study, the degree of morphological changes in the retina due to "retinal stress" after vector administration was evaluated by immunostaining for glial fibrillar acidic protein (GFAP), which indicates activation of Müller glia cells (Figure 42F-K, magenta) [258]–[260]. Upon activation intermediate fibers of Müller glia cells are induced and extend into the ONL. This process is termed "Müller cell gliosis"

[259], [261]. Such gliosis can be seen as an early reaction to inflammatory processes [262], mechanical trauma [263] or retinal degeneration [264]. We hereby assess if activation of Müller glia cells is triggered by a specific vector or can be expected to correlate with the amount of administered vector dose while being less dependent on the AAV capsid. The following figures show mice retinal cross-sections stained for GFAP at 3 WPI after IVT low, medium, or high dose administration of novel AAV9 capsid mutants.

For AAV9 WT and capsid variants without the NN- or GL-insertion the GFAP signal is located almost exclusively in astrocytes in the nerve fiber layer below the ganglion cells (Figure 32, magenta). Low dose vector administration resulted in some degree of Müller cell gliosis into the inner plexiform layer (IPL) for AAV9.AAR (Figure 32G) and AAV9.RAAK (Figure 32N). With the medium dose of 5×10^9 total vg expression levels of GFAP were increased in Müller glia across all five vector variants. AAV9 WT (Figure 32B) and AAV9.R (Figure 32E) show enhanced signals for GFAP in Müller glia end-feet and processes into the IPL and the INL. The high dose group showed comparable GFAP expression levels for novel vector mutants than the medium dose. AAV9 WT however showed an increase in Müller gliosis with end-feet reaching into the ONL (Figure 32C).

All novel AAV9 variants carrying the NN-insertion showed some level of reactive gliosis with intermediate processes reaching through the IPL after low dose vector administration (Figure 33, left column). With IVT application of 5×10^9 total vg the Müller cell gliosis was enhanced for AAV9.NNR (Figure 33E) and AAV9.NNK (Figure 33H). The high-dose study showed constant GFAP signal for AAV9.NN (Figure 33C) and even decreased Müller cell gliosis for AAV9.NNK (Figure 33J). Interestingly, AAV9.NNR (Figure 33F) exhibited a disruption of Müller glia fibers across the IPL. AAV9.GL (Figure 34A) and AAV9.GLK (Figure 34G) showed moderate GFAP signal, mostly limited to the GCL and the NFL at 1×10^9 total vg while AAV9.GLR displayed Müller glia processes into the INL (Figure 34D). With 5×10^9 total vg gliosis in AAV9.GLR and AAV9.GLK increased in comparison to low dose vector administration (Figure 34E, H). However, GFAP signal again decreased after escalation of the dose to 1×10^{10} total vg (Figure 34F, J). With this dose AAV9.GL showed moderate Müller cell gliosis in the IPL (Figure 34C).
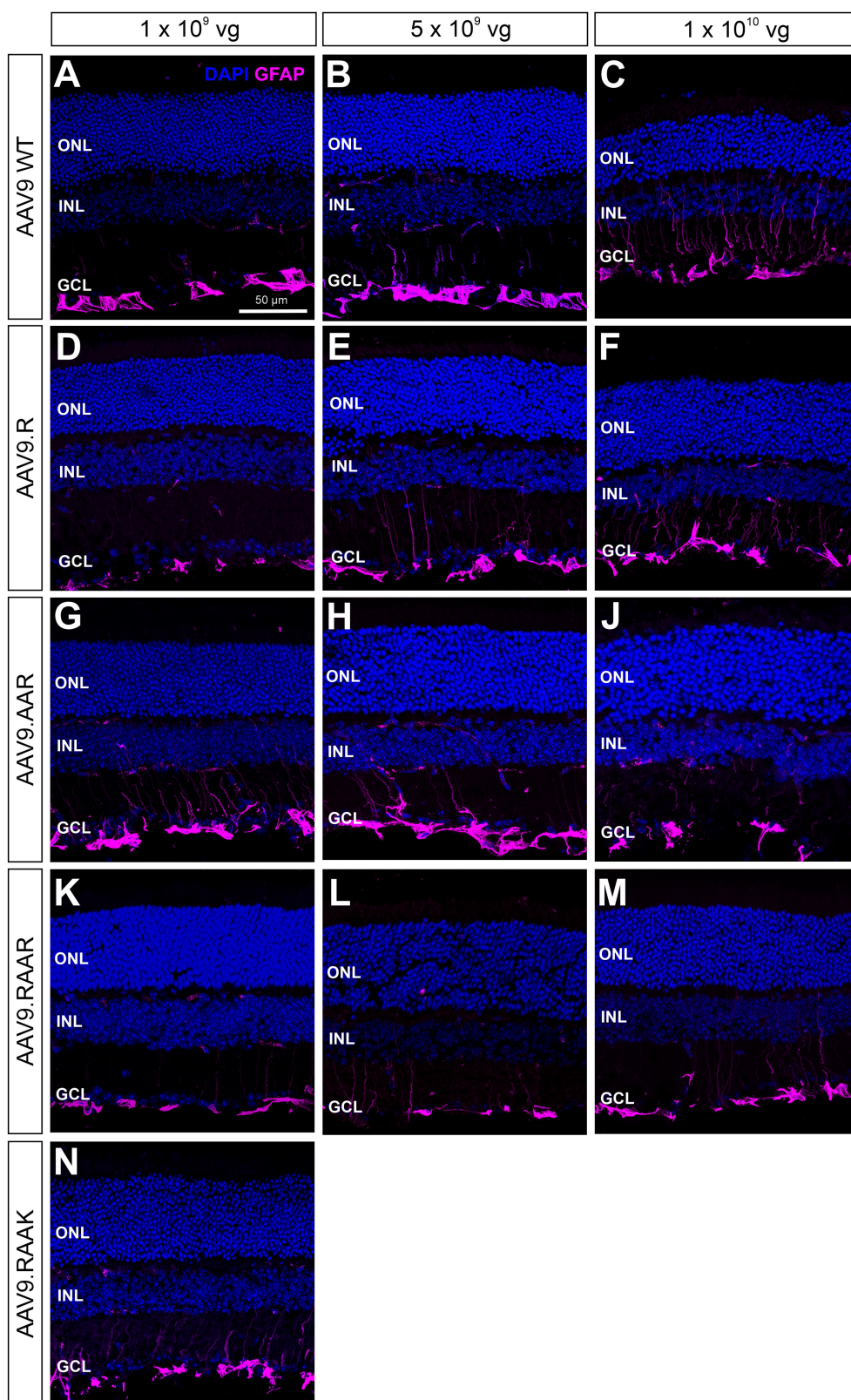
Figure 32 Activation of Müller glia after IVT administration of AAV9 WT-based variants Representative cross-sections of retinae three weeks post injection. Stainings show Müller glia migrating the retinal cell layers indicated by expression of glial fibrillar acidic protein (GFAP, magenta, A-N) after administration of 1×10^9, 5×10^9 or 1×10^{10} total vg IVT. Cell nuclei were stained with DAPI (blue). Scale bar marks 50 µm. ONL outer nuclear layer, INL inner nuclear layer, GCL ganglion cell layer.
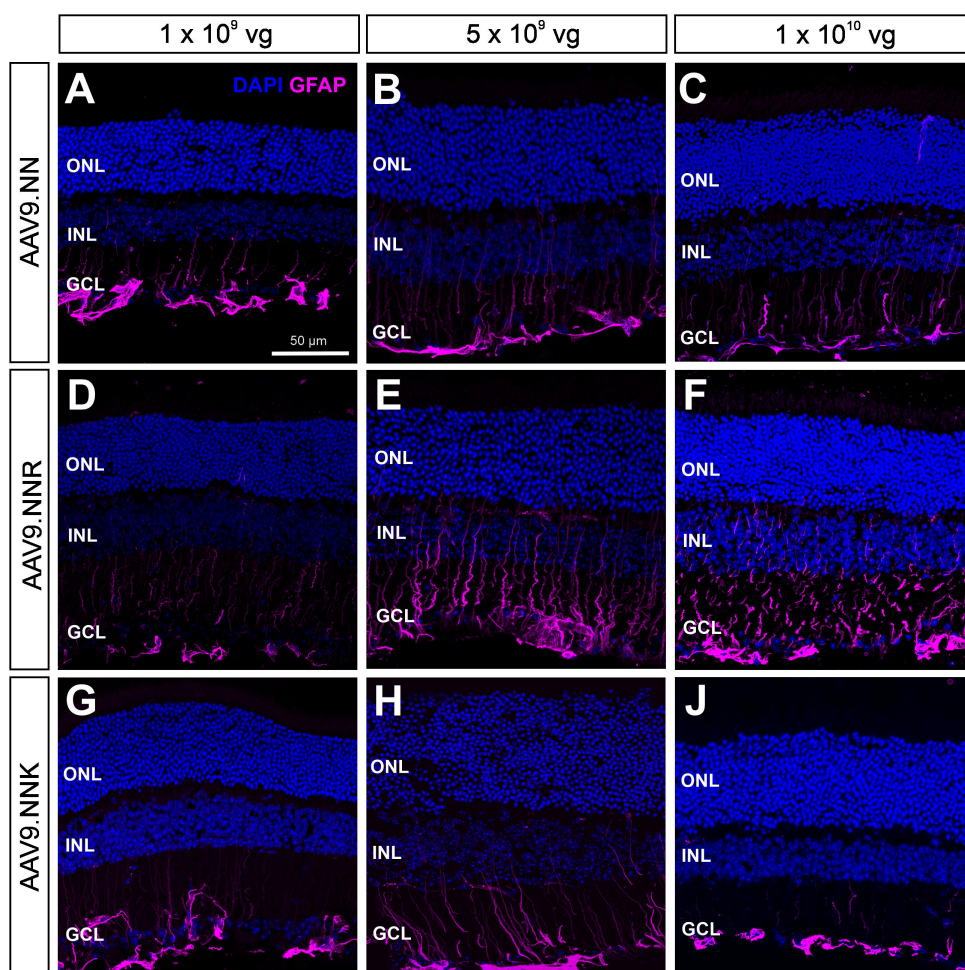
Figure 33 Activation of Müller glia after IVT administration of AAV9.NN-based variants Representative cross-sections of retinae after AAV9.NN-based vector administration three weeks post injection. Stainings show microglia migrating the retinal cell layers indicated by expression of glial fibrillar acidic protein (GFAP, magenta, A-N) after administration of 1×10^9, 5×10^9 or 1×10^{10} total vg IVT. Cell nuclei were stained with DAPI (blue). Scale bar marks 50 µm. ONL outer nuclear layer, INL inner nuclear layer, GCL ganglion cell layer.

Taken together it can be concluded that the activation of Müller glia is for the most part dependent on the applied vector dose and not necessarily the specific capsid mutant. Between the low dose and the medium dose, an increase in GFAP signal is observed for each variant. In comparison, the differences between the medium and the high dose are mostly small. For some vectors, such as AAV9.NNK, AAV9.GLR and AAV9.GLK, the Müller glia activation was reduced with the high vector dose. AAV9.NNR, which showed the strongest eGFP expression in the photoreceptors and the ONL (5.1.4.3) also results in the strongest Müller glia activation. Overall, the extent of GFAP signal for all AAV9 capsid mutants indicates only mild to moderate Müller glia activation.
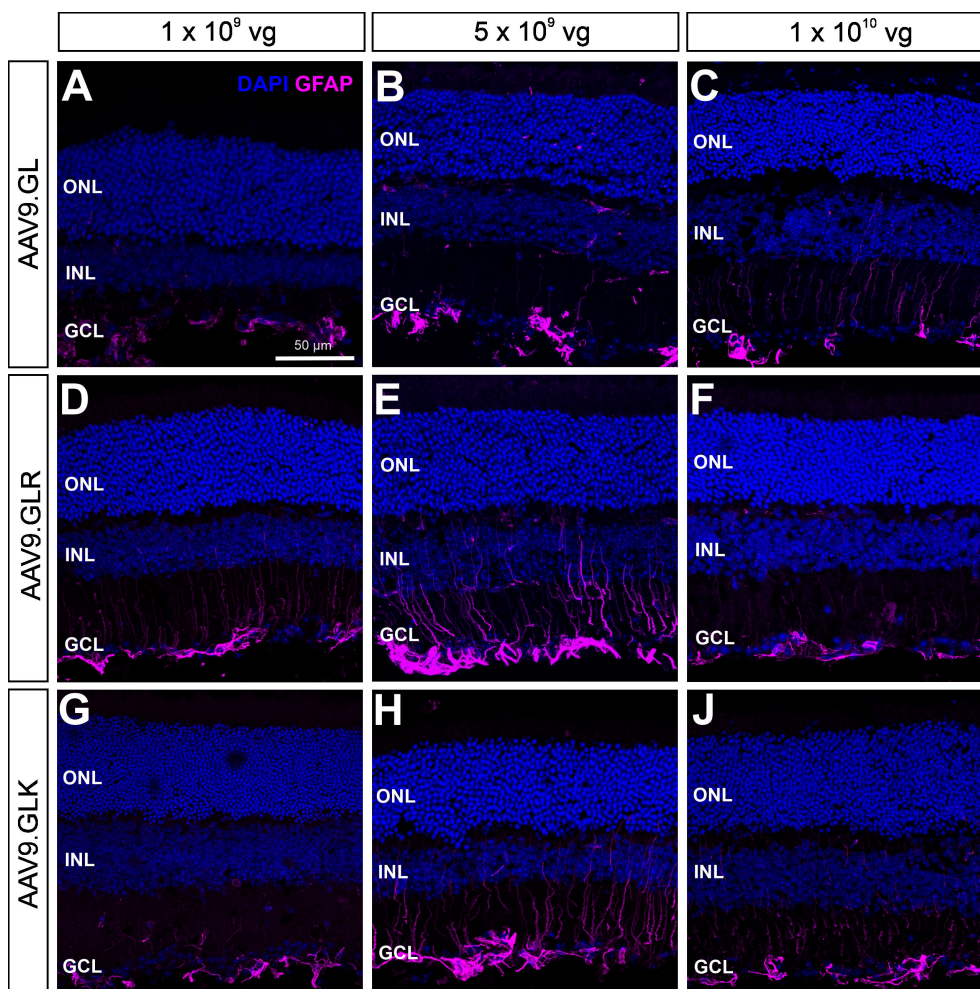
Figure 34 Activation of Müller glia after IVT administration of AAV9.GL-based variants Representative cross-sections of retinae after AAV9.GL-based vector administration three weeks post injection. Stainings show microglia migrating the retinal cell layers indicated by expression of glial fibrillar acidic protein (GFAP, magenta, A-N) after administration of 1 x 10^9, 5 x 10^9 or 1 x 10^{10} total vg IVT. Cell nuclei were stained with DAPI (blue). Scale bar marks 50 µm. ONL outer nuclear layer, INL inner nuclear layer, GCL ganglion cell layer.

5.1.4.5 Comparison of eGFP-immunosignal in whole fundus cross-sections

It was noticeable that the level of eGFP expression during close-up confocal imaging of the retinal cross-sections differs depending on the imaged region of the tissue. Therefore, entire cross-sections of each novel vector variant were examined to characterize different transduction patterns of eGFP expression among the variants. The images were acquired at the Keyence Compact Fluorescence Microscope BZ-X800 using the stitching function and z-stacks of several focus points to capture the whole tissue. For comparison, cross-sections of eyes injected with 5 x 10^9 total vg of AAV9 WT and AAV9 variants carrying the NN- or GL-insertion were evaluated (Figure 35). With AAV9 WT (Figure 35A) the fundus shows a broadly transduced area while for AAV9.NN, AAV9.NNK and AAV9.GL (Figure 35B, D, E) the transduced area is smaller and shows lower transduction levels. AAV9.NNR and AAV9.GLR (Figure 35C, F) show eGFP-expressing areas limited to the ventral (v) side of the eye where eGFP is expressed

strongly in all retinal cell layers. These overall impressions give merely an outlook to further aspects of characterization. The patterns of localization lead to the conclusion that the HSPG-binding motif in the R-mutants is potent enough to keep the virus from spreading through the vitreous while AAV9 WT, AAV9.NN and AAV9.GL lack this binding mechanism and therefore have a more widespread transduction area although lower transduction in the detailed confocal images.
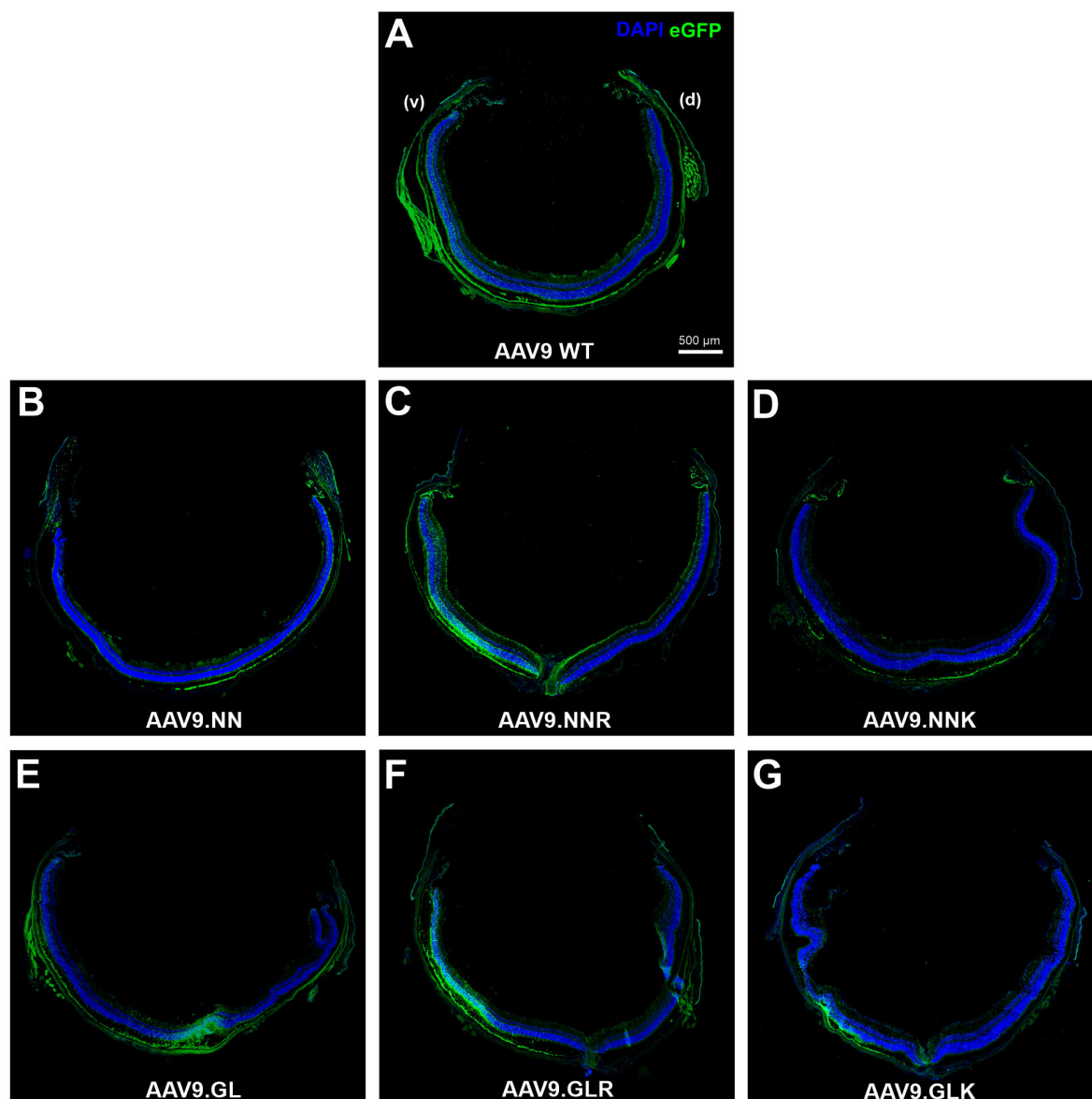
Figure 35 Whole fundus cross-sections after IVT administration of AAV9 capsid mutants Representative Keyence microscope images of whole cross-sections three weeks after IVT injection of 5 x 10^9 total vg (medium dose). Images show distribution of eGFP signal (green) within the eye from sections taken at the median close to the optic nerve. Eyecup orientation: Left side marks the ventral (v) and right side the dorsal (d) part. Cell nuclei were stained with DAPI (blue). Scale bar marks 500 µm.

5.1.4.6 Transduction of the ciliary body by novel AAV9 capsid variants

During *in vivo* characterization of the novel AAV9 capsid mutants it could be observed that some of the novel capsids, namely the R- and the K-mutants, show increased tropism for the ciliary body in the mouse eye. For closer evaluation of the ciliary body the eyecup dissection technique was adjusted adequately to ensure preservation of this fragile structure located on the inside of the eyecup close to the *ora serrata*, which would be removed during standard eye cup dissection for preparation of retinal cross-sections. Figure 36A shows a radial cut through the eye of an adult C57BL6/J mouse. The anterior part of the ciliary body, namely the *pars plicata* is characterized by a fluted, tubular structure [265], [266] while the posterior part, the *pars plana,* is the adjacent unfolded region which then continues with the neural retina at the *ora serrata* [80], [267]. The cross-section (Figure 36B) illustrates the two different cell layers, namely the pigmented ciliary epithelium (PCE) and the non-pigmented ciliary epithelium (NPCE) with the iris maintained after the modified dissection technique.
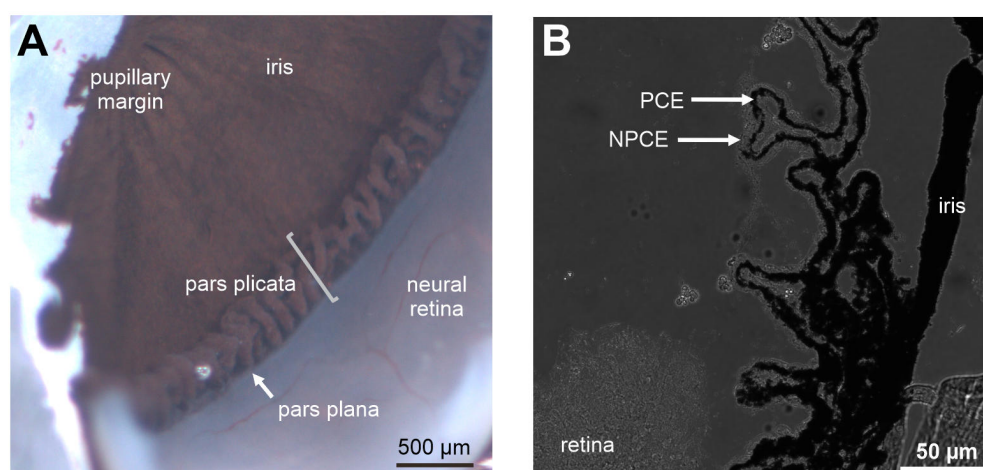
Figure 36 Ciliary body of adult C57BL6/J mice (A) Whole cross-section of the eye at the median, anatomic structures are named. Scale bar marks 500 µm. (B) IHC of AAV9.GLR (see also Figure 37K). Scale bar marks 50 µm. PCE pigmented ciliary epithelium, NPCE non pigmented ciliary epithelium.

For IHC the tissue was co-stained for the platelet endothelial cell adhesion molecule (PECAM1 or CD31, magenta), which marks the endothelial blood vessels responsible for oxygen and nutrient delivery to the ciliary body and eGFP (green). The close-up confocal images were acquired at a 40x magnification including a brightfield channel to distinguish the pigmented ciliary epithelium (PCE) from the black background. Figure 37 illustrates the ciliary body transduction achieved with each of the AAV9 capsid mutants after IVT low dose administration of 1 x 10^9 total vg. The brightfield channel shows the PCE and the tubular ciliary processes in black and a thin outer monolayer of cells, namely the NPCE around them. The iris was also

attempted to be preserved (see pigmented structure behind the PCE in Figure 37B, H, K. AAV9 WT (Figure 37A) shows strong transduction of the peripheral part of the retina but not within the ciliary body. The strongest transduction of the ciliary body can be observed for AAV9.NNR and AAV9.GLR (Figure 37G, K). The K-mutants, namely AAV9.RAAK, AAV9.NNK and AAV9.GLK (Figure 37E, H, L) show a similar pattern as observed for the R-mutants, albeit at overall lower eGFP signal intensity. Across all other tested vector variants, no ciliary body transduction was observed. The eGFP-positive cells transduced by the R- and K-mutants are the NPCE cells which play a crucial rule for secretion of fluids into the posterior chamber and maintenance of the intraocular pressure (IOP) [268].
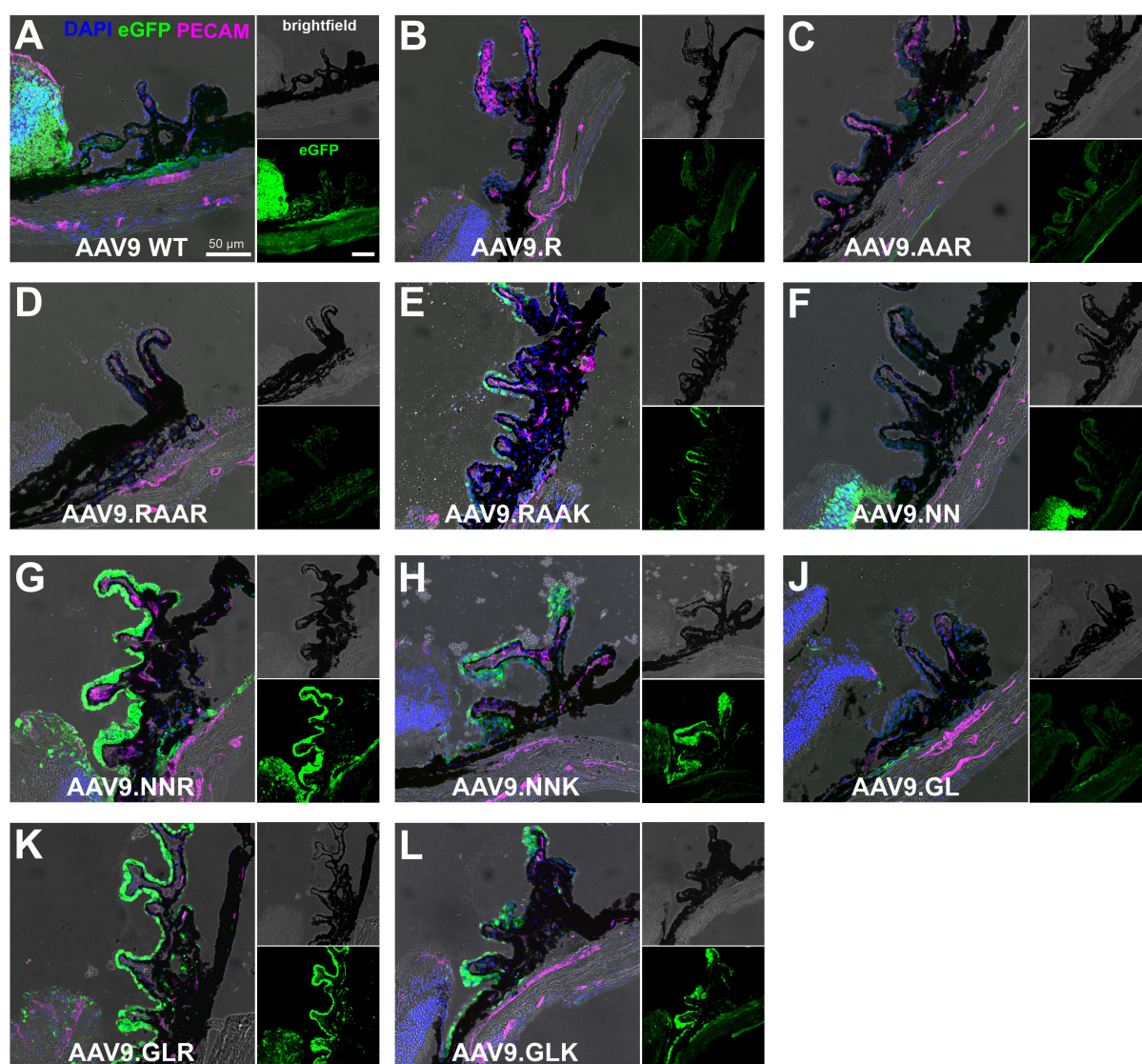
Figure 37 Transduction properties in the ciliary body after IVT injection of AAV9 capsid mutants Representative confocal images showing the ciliary body of injected eyes at 40x magnification. Capsid mutants were injected at 1×10^9 total vg (low dose) expressing eGFP. Blood vessels were stained for platelet endothelial cell adhesion molecule (PECAM1, CD31, magenta). Cell nuclei were stained with DAPI (blue). Transduction of non-pigmented ciliary epithelium cells (NPCE) can be seen in R- and K-mutants (G, H, K, L). Small images show brightfield (BF) channel and eGFP signal. Scale bar marks 50 µm.

To further evaluate the extend of NPCE transduction cross-sections from the periphery of the eyecup, namely the temporal or the dorsal side were stained for eGFP. While cross-sections from the median axis of the eye around the optic nerve (ON) show only a single cross-sectional plane of the ciliary body at the dorsal and the ventral side of the eyecup, cross-sections from the temporal and the nasal periphery allow visualization of a larger area of the ciliary body. In Figure 38 the three most promising vector variants AAV9.RAAK, AAV9.NNR and AAV9.GLR are shown. AAV9.RAAK after low dose administration of 1×10^9 total vg shows a limited area of retinal transduction (Figure 38A, white arrow) and at the opposite site of the eyecup a strong transduction of the NPCE (Figure 38D). AAV9.NNR and AAV9.GLR are shown at 5×10^9 total vg injection.
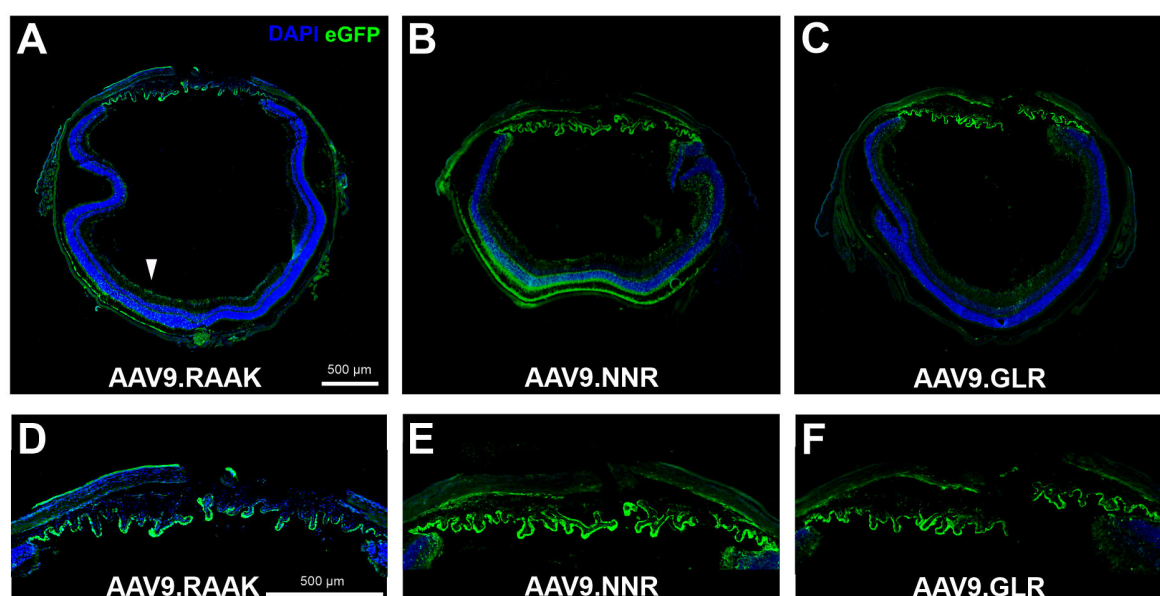
Figure 38 Ciliary body transduction in temporal retinal cross-sections Representative confocal images of cross-sections after IVT administration of low dose AAV9.RAAK (1×10^9 total vg; A, D) or medium dose of AAV9.NNR (5×10^9 total vg; B, E) or AAV9.GL (5×10^9 total vg; C, F). Images show the transduction across the temporal side of the ciliary body after 3 WPI (eGFP, green). (A) White arrow marks the transduced retina at the point of vector release during IVT injection. Cell nuclei were stained with DAPI (blue). Scale bar marks 500 µm.

AAV9.NNR as the strongest performing vector variant shows strong transduction across retinal cell layers as well as potent eGFP expression in the NPCE (Figure 38B, E). AAV9.GLR does not show as highly transduced retinal cells as AAV9.NNR in the peripheral area of the eyecup but also shows high ciliary body transduction (Figure 38C, F). These results suggest that the HSPG-binding motif generated in R- and K-mutants also plays an important role for transduction of parts of ciliary body NPCEs.

5.1.5 Neuronal transduction properties of AAV9 capsid mutants

AAV9 has been intensively studied in the context of cardiac or CNS gene delivery after systemic, e.g. intravenous (i.v.) application [247], [269], [270]. Some studies also show retinal transduction after i.v. administration leading to the conclusion that AAV9 is also capable of passing the blood-retina-barrier (BRB) [271], [272]. We therefore aimed to investigate the extent of neuronal transduction along the visual pathway after IVT injection. In particular, optic nerve (ON), optic tract and brain of IVT injected mice were removed after 3 WPI and co-stained for eGFP expression. First, the retinal cross-sections containing the base of the ON were examined more detailed for all tested AAV9 capsid mutants. Confocal images were acquired at 20x magnification with multiple z-stacks for all vectors after low dose (1×10^9 total vg) IVT administration. AAV9 WT (Figure 39A) shows, as expected, the highest transduction at the optic nerve directly adjacent to the retina, while AAV9.NN, AAV9.NNR, AAV9.NNK, AAV.GLR and AAV9.GLK (Figure 39F-H, K, L) show visibly lower eGFP expression in the ON in the retina. AAV9.R, AAV9.AAR and AAV9.RAAR (Figure 39B-D) show almost no transduction of the ON.
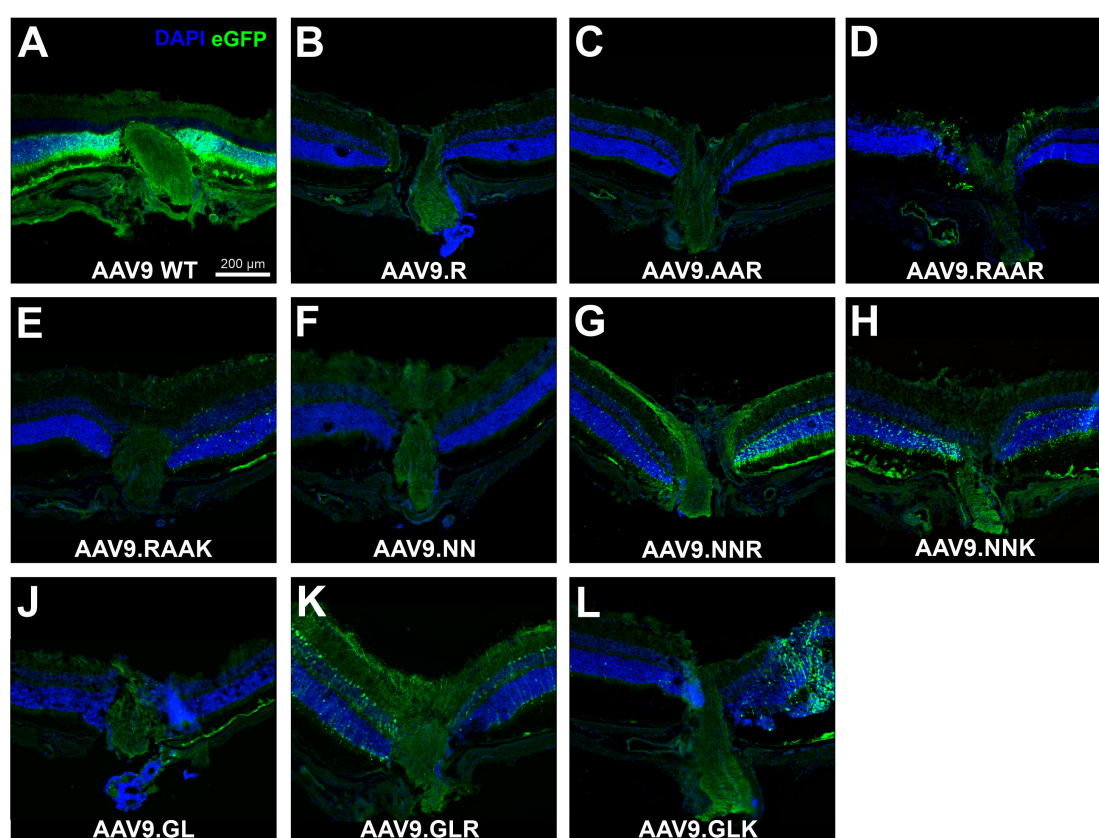
Figure 39 Transduction of the optic nerve in retinal cross-sections Representative confocal images of cross-sections from the median of the eye at the optic nerve. AAV9 mutants were IVT administered at 1×10^9 total vg low dose expressing an scCMV-eGFP reporter cassette (green). Images were captured at 20x magnification. Cell nuclei were stained with DAPI (blue). Scale bar marks 200 μm.

Next, the whole ON with the connecting chiasm was carefully removed during brain dissection and immediately washed and PFA fixed. Prior to further processing, the ON was checked under the epifluorescence microscope for native fluorescence. The structure was embedded on a filter in a V-like shape with optic nerves from both eyes on the side and the chiasm in front. Cryosectioning and IHC were performed as described above. Imaging was conducted at the Keyence Compact Fluorescence Microscope BZ-X800 using the stitching function and z-stacks of several focus points to capture the whole tissue. Notice that because of the fragility of this structure for some samples only part of one ON could be preserved. As a control ON and brain from non-injected C57BL6/J mice were processed similarly but showed no eGFP signal (Figure 40, first panel). AAV9 WT shows the highest eGFP expression throughout the chiasm and the whole ON (Figure 40A). This was also observed during initial control of native eGFP expression directly after cryo-sectioning (data not shown). The AAV9.R, AAV9.AAR and AAV9.RAAR capsid mutants (Figure 40B-D) show only background signal but no eGFP expression. For all remaining vector variants (Figure 40E-L) eGFP signal could be observed but to a strongly decreased extent than shown in the AAV9 WT.
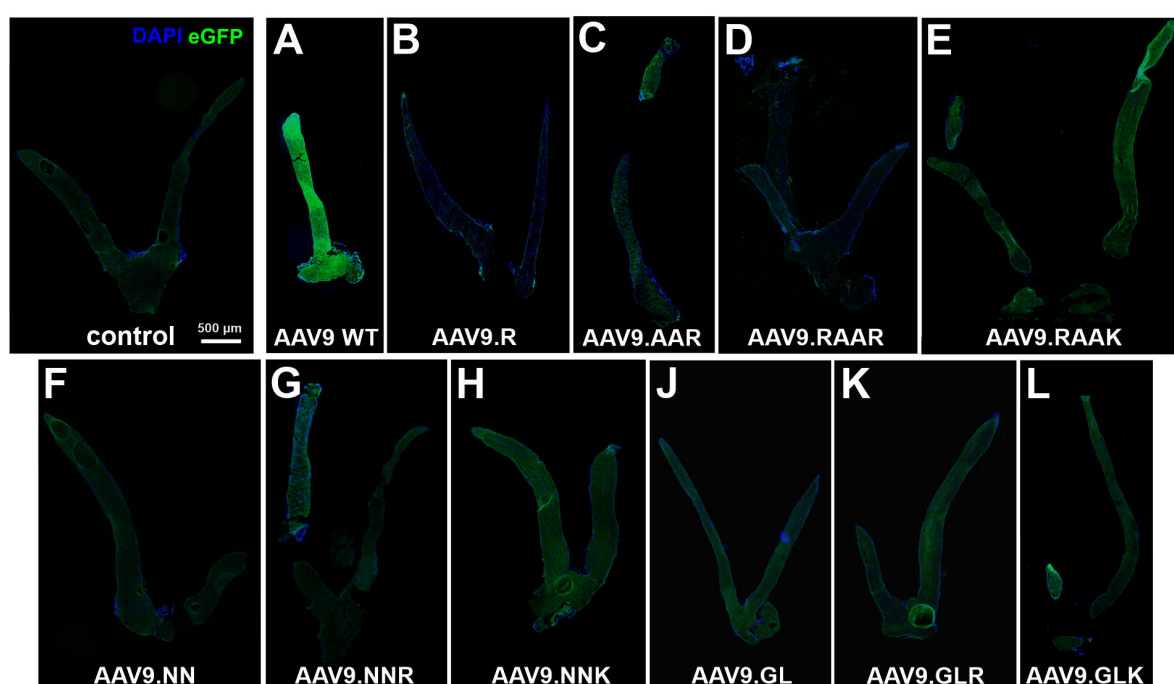
Figure 40 Transduction of optic nerves and chiasm after IVT administration of AAV9 capsid mutants Representative fluorescence images of optic nerves after IVT high dose injection of AAV9 mutants (1×10^{10} total vg) expressing an scCMV-eGFP reporter cassette (green). Control images were taken from ON of a non-treated mouse. Cell nuclei were stained with DAPI (blue). For some capsid mutants only one ON could be preserved during dissection (A, C, L). Images were acquired at the Keyence microscope using the stitching function for large area imaging. Scale bar marks 500 µm, n = 2, ON optic nerve.

Lastly, the eGFP signal in the brain regions was investigated. Therefore, brains were cut sagittal followed by IHC of cross-sections from the optical tract and the Dorsal Lateral Geniculate (DLG). Both regions were co-stained for eGFP and microtubule-associated protein 2 (MAP2) as a neuronal marker. However, no eGFP expression could be observed in the brain for all vector variants (data not shown). These results suggest, that despite potent neuronal transduction of the retina after IVT delivery of 1 x 10^{10} total vg (high dose) of the AAV9 variants, only limited transduction of the ON and chiasm, and no transduction of the brain can be observed.

5.1.6 Evaluation of AAV9 mutants on human retinal explants

As a next step *ex vivo* vector evaluation on human retinal tissues was performed for AAV9 WT, AAV9.NN, AAV9.NNR, AAV9.GL and AAV9.GLR due to the limited amounts of human donor tissue. Donor tissue was checked by the pathology department (LMU Munich, University Hospital, Department of Ophthalmology) after surgical removal and immediately picked up for further processing. Tissues were carefully cut to a size of 10 x 10 mm and cultivated side by side with a piece of RPE for co-expression of important nutrients on a filter. The photoreceptors were facing down into the culturing medium. AAV vectors packaged with a scCMV-eGFP reporter cassette were applied at 1 x 10^{11} total vg from the vitreal side on the tissue. Retinal explants were cultured for 9 days while monitoring eGFP expression at the EVOS fluorescence microscope. Images were taken each day from the same position of the thinner peripheral area (Figure 41A) as well as the central part of the tissue (Figure 41B). AAV9 WT showed increasing transduction levels from day 3 on, while AAV9.NN expressed only weak eGFP signal. AAV9.NNR showed only few transduced cells at the peripheral area around day 9 while in the central area due to the thickness of the tissue no eGFP expression could be observed. In contrast, AAV9.GL and AAV9.GLR showed high tissue transduction from day 3 on increasing over the monitoring period across the whole retinal explant.
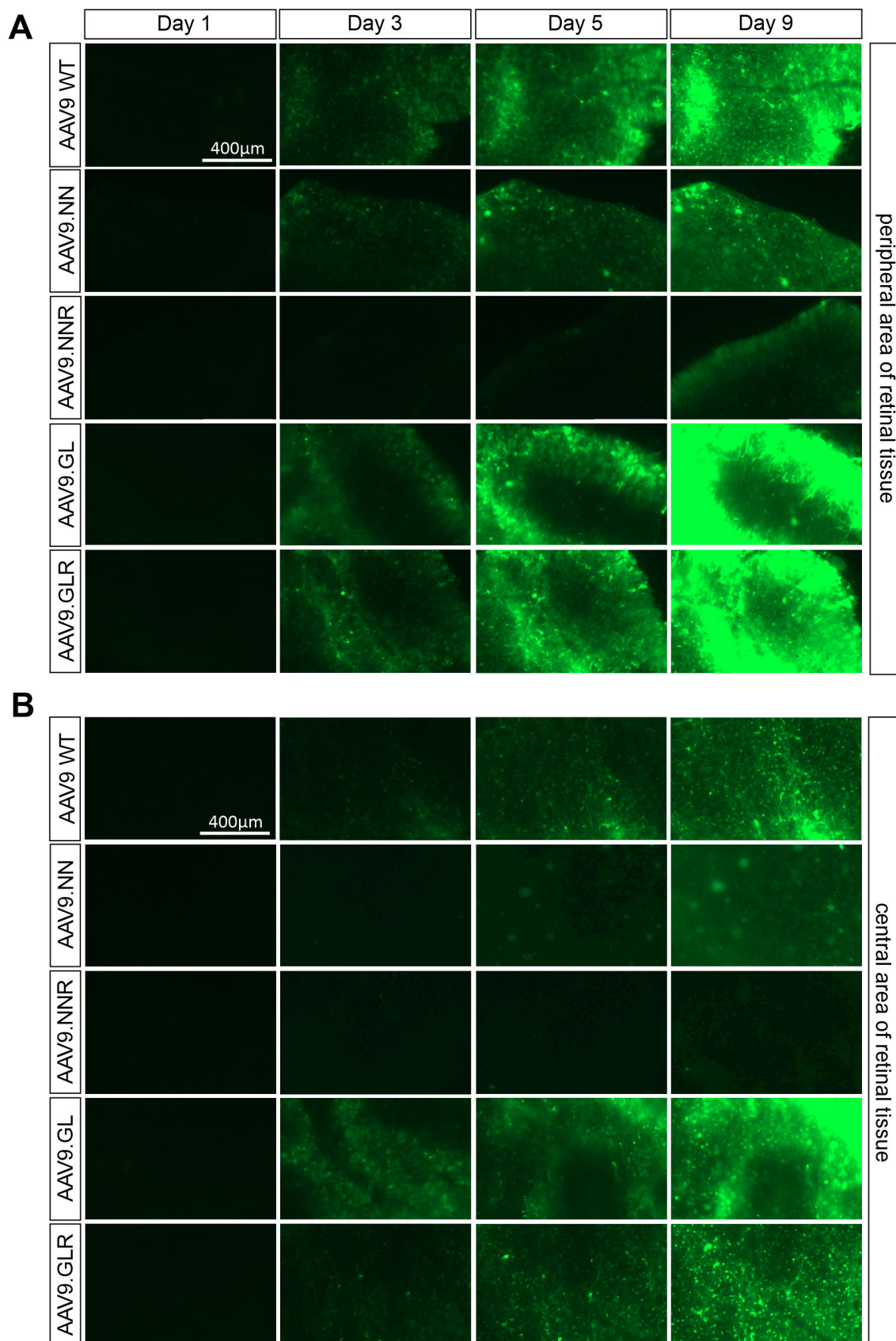
Figure 41 Transduction of AAV9 capsid mutants on human retinal explant culture Retinal tissues were transduced with 1 x 10^{11} vg novel AAV9 capsid mutants carrying an scCMV-eGFP reporter cassette. Explants were monitored for 9 days at 50% GFP intensity. Representative epifluorescence pictures were taken from the edge (A) and the center of the tissue (B) for 9 consecutive days. Scale bar marks 400 μm. n = 3 for AAV9 WT, n = 2 for AAV9.NN, AAV9.NNR, AAV9.GL and AAV9.GLR.

After 9 days the retinal explants were further prepared for cryo-sectioning following IHC. While several cell-type specific antibody markers were tested, only few worked properly on human retinal tissue. The condition of the retina varied across the samples due to the advanced age of the donors and already ongoing retinal degeneration within the tissue which can also be seen in the decreased retinal thickness in some of the cross-sections (Figure 42). Antibody staining for rhodopsin (Rho, magenta) as a marker for rods (Figure 42, left panels) emphasizes the quality differences across the retinal tissues. While all tested vectors show low eGFP expression in the photoreceptors (Figure 42A-E) only AAV9.NNR shows minor co-localization (white) with rhodopsin (Figure 42C). AAV9.GLR shows strong eGFP expression in the ONL and the GCL. Moreover, both R-mutants AAV9.NNR and AAV9.GLR show astrocyte transduction in the GCL. AAV9.GL (Figure 42D) also expresses eGFP signal accumulating at the position of the INL which explains the strong fluorescence signal observed in Figure 41. The degree of Müller glia activation was investigated by GFAP staining (Figure 42F-K) [260]. While the strongest GFAP signal is limited to the GCL, AAV9.NN and AAV9.GLR show first microglia fibers migrating into the INL (Figure 42H, K).

Overall, the evaluation of novel vectors on human tissue serves as a valuable first indicator on how possible capsid mutants perform on human tissue. However, the age of the donors as well as the condition of the tissue needs to be considered before drawing conclusions.
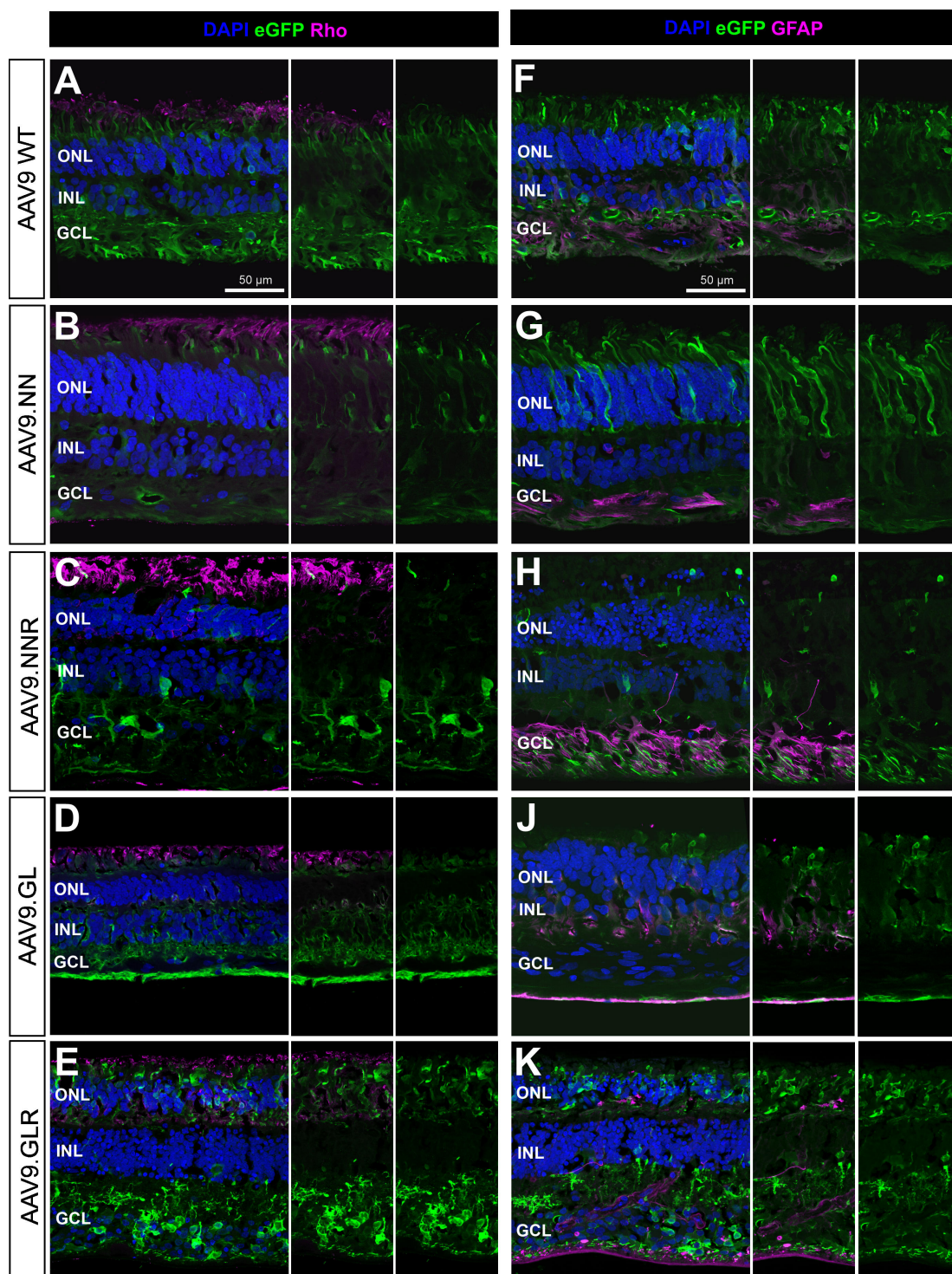
Figure 42 IHC of human retinal explants transduced with AAV9 capsid mutants Representative confocal images showing the transduction of rods (rhodopsin, Rho) in magenta for AAV9 WT, AAV9.NN, AAV9.NNR, AAV9.GL and AAV9.GLR (A-E, left column) in retinal cross-sections. Reactive gliosis is shown in the right column by glial fibrillar acidic protein staining (GFAP, magenta, F-K). Cell nuclei were stained with DAPI (blue). Scale bar marks 50 μm. ONL outer nuclear layer, INL inner nuclear layer, GCL ganglion cell layer.

5.1.7 Evaluation of novel AAV9 capsid mutants on human retinal organoids

After extensive characterization of the novel AAV9 vectors *in vitro*, *ex vivo* and *in vivo* in the mouse model the next step towards clinical application is evaluation of transduction properties in a more complex humanized model such as human retinal organoids (hROs) derived from induced pluripotent stem cells (iPSCs). The hROs were developed and provided by Dr. Grazia Giorgio according to previously published protocols [227]. Mature 220 days old hROs were transduced with 1×10^{10} total vg. Due to limited amounts of organoids only the most promising vectors were tested with the respective n-numbers of n = 1 for AAV9.NN and AAV9.GL, n = 2 for AAV9.NNK and AAV9.GLK, n = 3 for AAV9.NNR and AAV9.GLR. The development of eGFP expression was monitored over 8 days at the EVOS fluorescence microscope. From day 3 on fluorescence signal was visible and slowly increasing up until the final day of the experiment. AAV9.NN, AAV9.NNK and AAV9.GLK (Figure 43) showed only faint eGFP expression limited to a very small area across the organoid while AAV9.NNR, AAV9.GL and AAV9.GLR show stronger signals developing from the central area of the organoid. The peripheral regions of the hROs where the ONL can be expected however are mostly not transduced across all samples.

After day 8 the organoids were PFA-fixed and embedded for cryo-sectioning and IHC. Unfortunately, due to bacterial contamination co-stainings with cell-type specific markers such as rhodopsin (Rho) and cone arrestin (Arr3) showed only unspecific signal. However, the detailed confocal images are still shown in Figure 44 to assess the fluorescence signals observed.

Confocal images of the whole organoid after IHC showed, as expected from the EVOS images, only limited eGFP signal. Representative close-up images from intact ONL areas were acquired at 40x magnification to allow for a more detailed evaluation of transduced cell types. Figure 44 illustrates the eGFP expression in the peripheral area of each organoid. Mostly activation and transduction of Müller glia (white arrows) can be observed across the organoids which is particularly evident from the strong processes within the retinal cell layers and suggests that the structural organization is already affected. However, some isolated photoreceptor transduction could be observed for some variants (Figure 44C-F, yellow arrows). Overall, the potential of novel AAV9 capsid mutants needs to be further explored in hROs to be able to characterize their transduction properties in a 3D *in vitro* model such as hROs.

Additionally, the previously established vector dose of 1 x 10^{10} total vg [226] needs to be adapted accordingly to generate a transient eGFP expression.
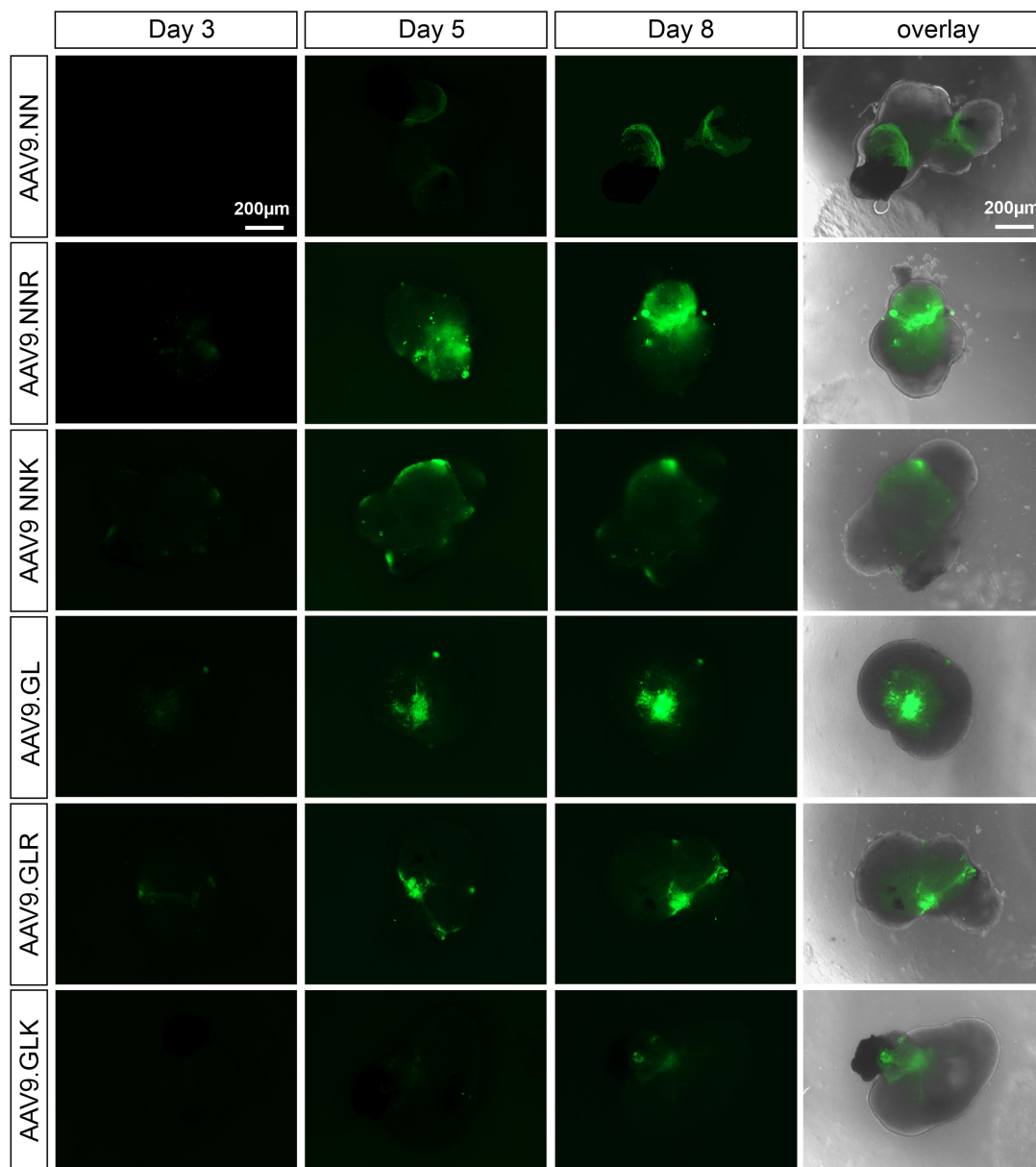
Figure 43 Transduction of human retinal organoids iPSC-derived hROs (*courtesy of Dr. Grazia Giorgio, AG Michalakis*) were transduced at day 220 with 1 x 10^{10} total vg carrying a scCMV-eGFP reporter cassette. hROs were cultured and monitored for 8 days. Representative epifluorescence pictures were acquired each day at 4/10 PH brightfield, 50% GFP intensity and 2.5x magnification. Scale bar marks 200 μm. n = 1 for AAV9.NN and AAV9.GL, n = 2 for AAV9.NNK and AAV9.GLK, n = 3 for AAV9.NNR and AAV9.GLR.
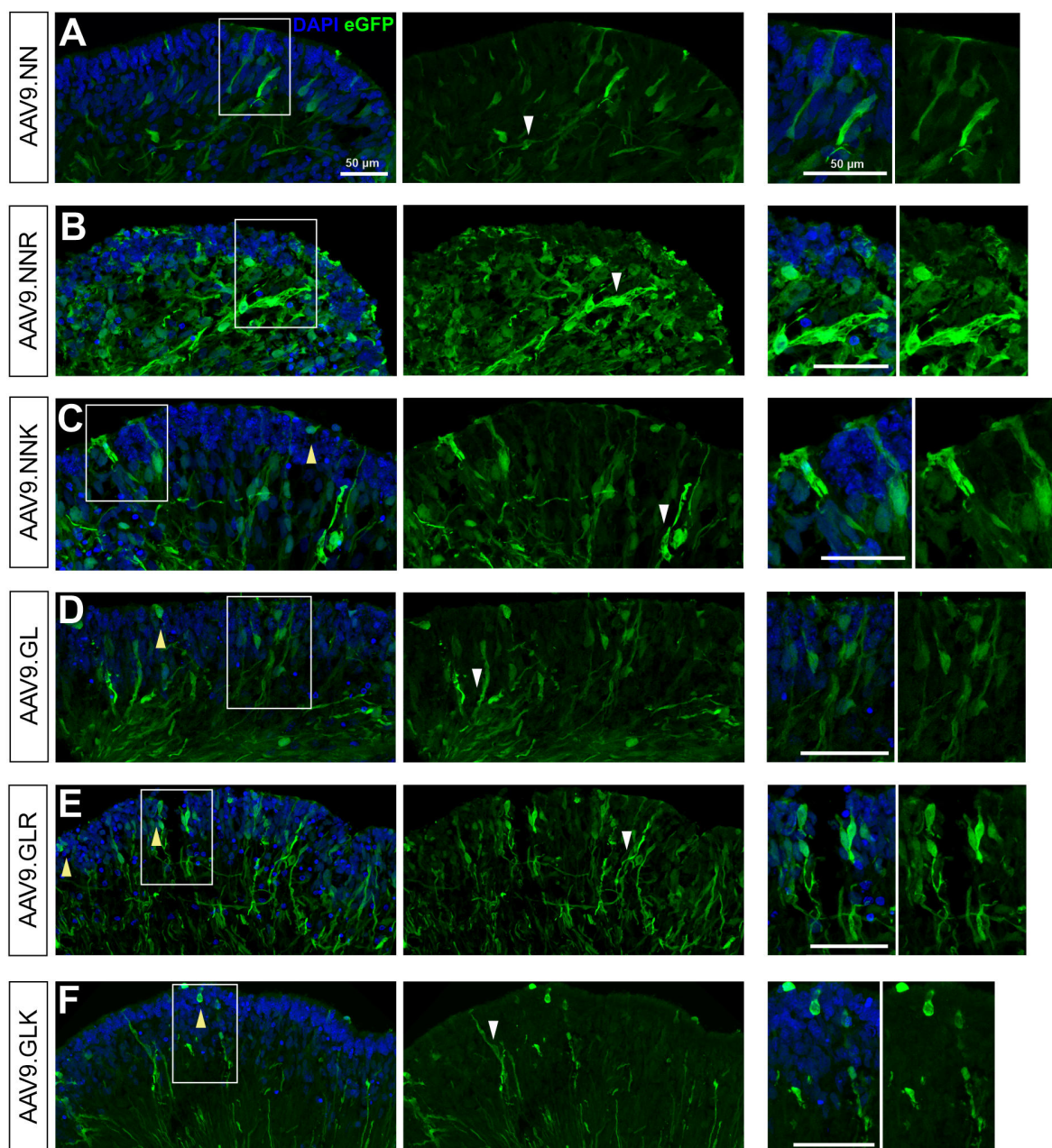
Figure 44 IHC of human retinal organoids Representative confocal images were acquired at 40x magnification for AAV9.NN, AAV9.NNR, AAV9.NNK, AAV9.GL, AAV9.GLR and AAV9.GLK (A-F). Cross-sections show different patterns of transduction of Müller glia (white arrows) and photoreceptors (yellow arrows). Close-up images show detailed cell transduction. Cell nuclei were stained with DAPI (blue). Scalebar marks 50 µm.

5.2 A novel platform for engineered AAV-based vaccines

During the COVID-19 pandemic extensive studies have shown that the human angiotensin-converting enzyme 2 receptor (ACE2) serves as the primary receptor for SARS-CoV-2-mediated viral cell entry [273]–[276]. The receptor-binding domain (RBD) is a 197 amino acid long protein in the S1 subunit of the spike glycoprotein which interacts with the ACE2-receptor and mediates internalization of SARS-CoV-2 (Figure 45A). In this study, the potential of utilizing said receptor-ligand-interaction as a trigger for RBD-specific immune responses is explored by delivery of parts of the SARS-CoV-2 RBD on the capsid surface of AAV2 and AAV9 (Figure 45B).
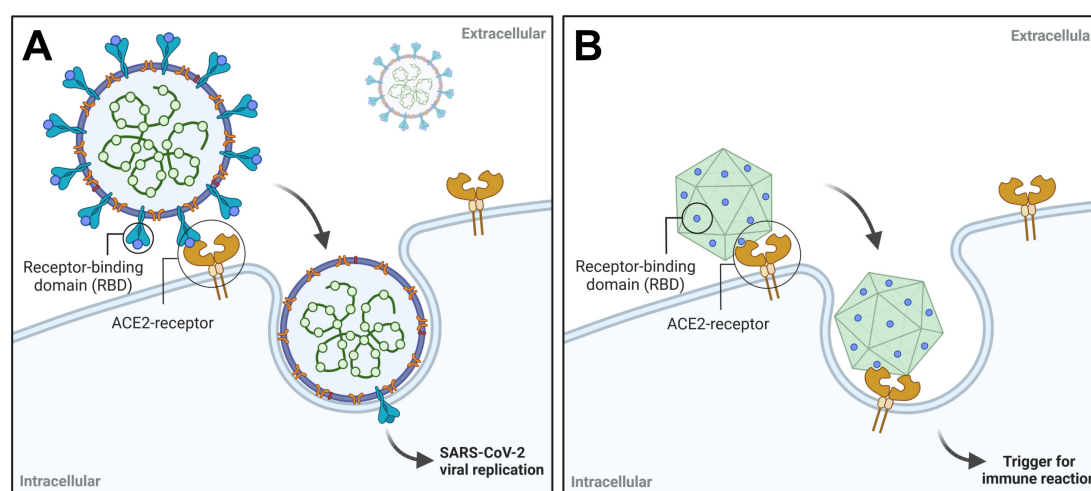
Figure 45 SARS-CoV-2 receptor-ligand interactions for viral cell entry (A) Interaction between SARS-CoV-2 viral particle and ACE2-receptor on human cells (B) Modified AAV capsid presenting the RBD of SARS-CoV-2 on the capsid surface. ACE2 angiotensin-converting enzyme, RBD receptor-binding domain.

5.2.1 Virus-like particles (VLPs) for presenting immunogens - Concept overview

Three novel capsid variants were generated by introducing parts of the SARS-CoV-2 RBD at the top of loop IV on the AAV capsid. This position has previously been reported to be essential for the HSPG-binding of AAV2 [53] and has been shown to tolerate small peptide insertions [225]. Moreover, an analogous position has been utilized for establishing the AAV9 capsid mutants described above (5.1). For AAV2 the insertion was made between position N587 and R588 within the VP3 region (Figure 46A, orange) while the corresponding insertion site for AAV9 is between position N588 and A589. In both AAV WT capsids the full length RBD of 197 amino acids plus flanking alanine linkers was inserted resulting in the respective capsids termed HtW2_S1.1 for AAV2 and HtW9_S1.1 for AAV9 carrying the same RBD-insertion. Since the insertion is established within the VP3 region of the Cap-sequence (Figure 46C) the large

peptide is presented 60x on the HtW capsid surface. Additionally, another capsid variant was created, which has a slightly shifted 206 amino acid insertion that includes additional RBD-adjacent amino acids reported to contain immunogenic T-cell epitopes [224]. This insertion was introduced in the AAV2 context only, resulting in the capsid mutant HtW2_S1.2.
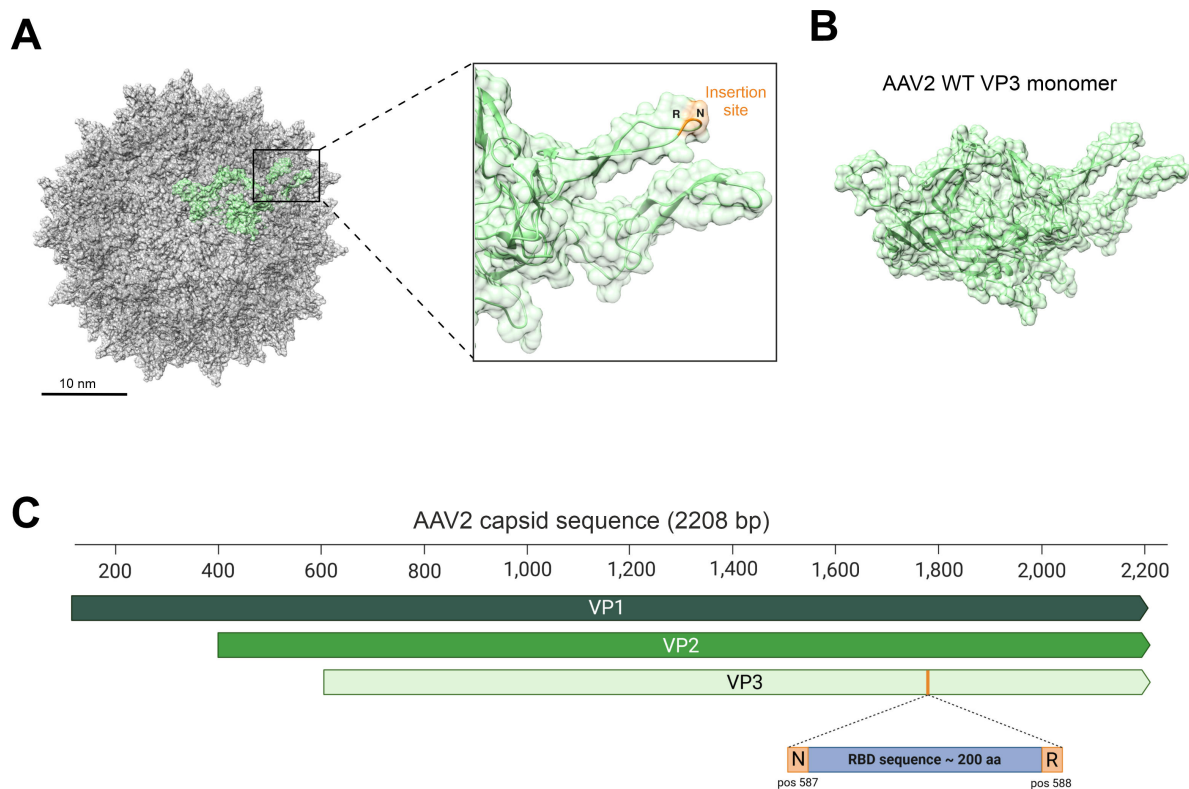
Figure 46 Generation of HtW capsid mutants (A) Biological assembly of the AAV2 WT capsid (PDB: 6ih9) showing the location of the insertion site in loop IV on the capsid surface. (B) Single VP3 monomer comprising the AAV capsid (green). (C) Location of the peptide insertion (blue) in the AAV2 cap sequence between N587 and R588. Scale bar marks 10 nm.

To get a general idea of what these novel capsid mutants with larger insertions could potentially look like, we used the RoseTTAfold algorithm for *in silico* protein modeling. For detailed analysis the model with the lowest angstrom error and the least amino acids outside the border limits in their respective Ramachandran plots was used. Results were further processed with the python-based UCSF Chimera open-source software. Single VP3 monomers of HtW2_S1.1 and HtW9_S1.1 show the 197 amino acid RBD-insertion and the 206 amino acid RBD-insertion in HtW2_S1.2 (Figure 47A-C, blue) in their energetically and sterically most favorable conformation. For HtW2_S1.1 and HtW9_S1.1 the modeled RBD-sequence is facing the same direction but shows variations in tertiary structure folding (Figure 47A, C), while the larger RBD-sequence in HtW2_S1.2 results not only in another protein structure but also a 90° bend of the whole insertion towards the capsid cargo (Figure 47B).
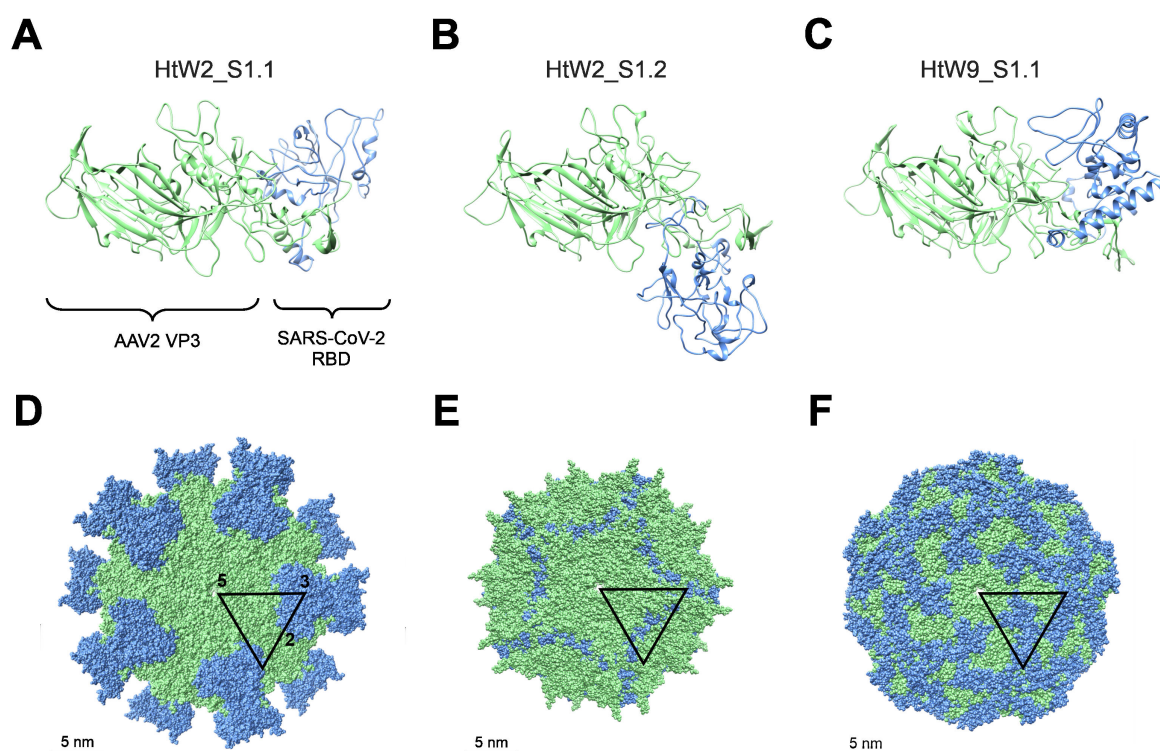
Figure 47 Overview of novel HtW capsid mutants Single VP3 monomers of (A) HtW2_S1.1, (B) HtW2_S1.2, and (C) HtW9_S1.1 and their whole capsid assembly from the 5-fold axis (D-F). Single VP3 monomer structures were obtained from the RoseTTAfold *in silico* modeling algorithm by the BakerLab and further processed using UCSF Chimera. The AAV2 and AAV9 WT sequence is portrayed in light green, SARS-CoV-2 RBD-insertions are shown in blue. Black triangle marks one icosahedral plane to illustrate the 5-fold (5), 3-fold (3) and 2-fold (2) symmetry axis (D). Scale bar marks 5 nm. RBD receptor-binding domain.

The assembled capsid of HtW2_S1.1 shows the RBD-insertion structurally exposed at the capsid surface, reminiscent of the structure of the spike glycoprotein of SARS-CoV-2 (Figure 47D). HtW9_S1.1 presents the insertion more incorporated on the capsid surface which results in a larger capsid size according to this *in silico* model (Figure 47E). For HtW2_S1.2 only a minor part of the insertion can be seen on the assembled capsid surface (Figure 47F). The black triangle marks the 5-fold (5), 3-fold (3) and 2-fold (2) symmetry axes across the novel capsid mutants for better orientation.

To illustrate the localization of the RBD on the capsid surface Figure 48 shows the full capsids from the 5-fold and the 3-fold symmetry axis. The VP3 monomers at each axis are colored to better display how they interact with one another and how the RBD-insertions of each VP3 monomer interact. For HtW2_S1.1 the spike glycoprotein-like RBD structure is generated by assembly of RBD-insertions from three subunits exclusively at the 3-fold symmetry axis (Figure 48A, D). For HtW2_S1.2 minor parts of the insertion are incorporated in the 3-fold, but also the 2-fold symmetry axis (Figure 48B, E) with the largest part facing the inside of the capsid.

HtW9_S1.1 shows diffuse distribution of the insertion across the capsid surface at each symmetry axis (Figure 48C, F).
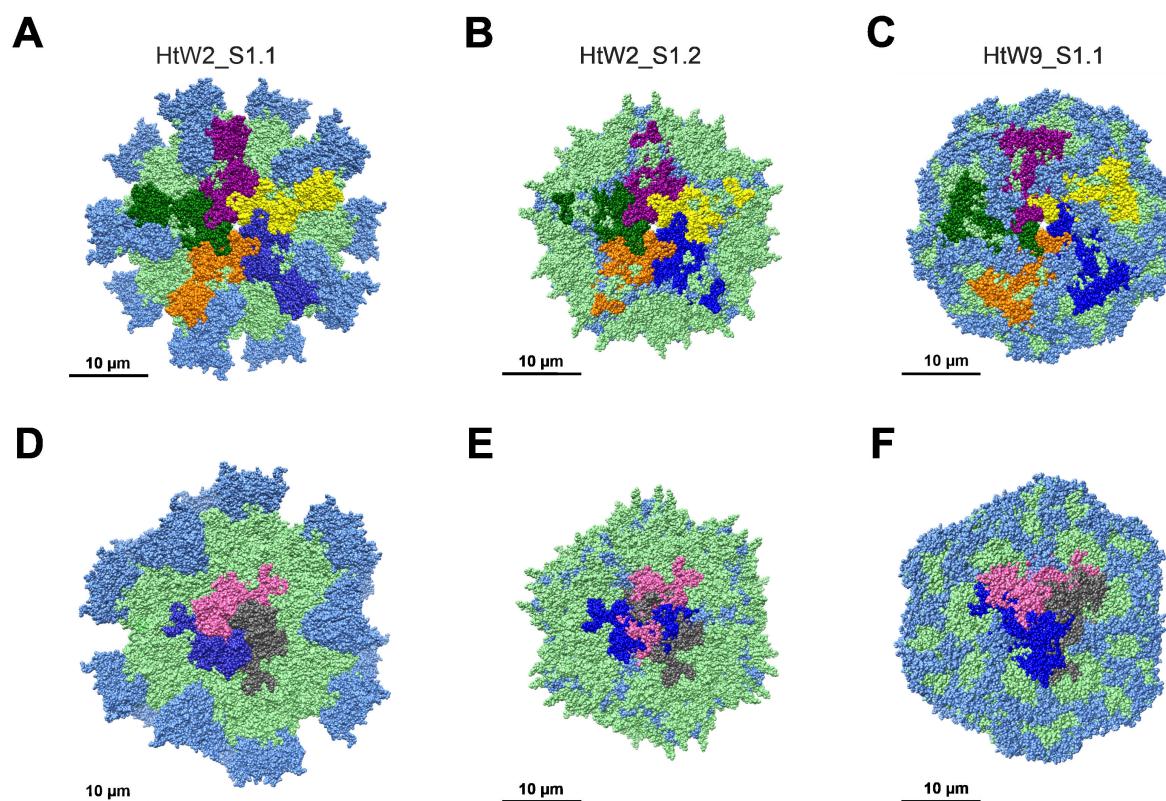
Figure 48 Orientation of the SARS-CoV-2 RBD-insertion on the HtW capsid surface Detailed overview of RBD (blue) displayed on the whole capsid of HtW2_S1.1, HtW2_S1.2 and HtW9_S1.1. (A-C) show the RBD-insertion (blue) from the 5-fold axis view with all five interacting subunits colored. (D-E) shows the 3-fold axis view with three interacting subunits. Scale bar marks 10 nm. RBD receptor-binding domain.

5.2.2 Evaluation of production yields for HtW vectors and VLPs

5.2.2.1 HtW capsids carrying large peptide insertions support production of genome-containing and empty virus-like particles

To test whether the novel HtW capsids can be used to produce infectious particles, we aimed to produce them as AAV vectors and test their transduction properties in HEK293T cells. To produce HtW vectors, we used standard triple-transfection in HEK293T cells of a pAdHelper plasmid, the AAV2-Rep/HtW-Cap plasmid, and a pTransgene plasmid that carries an ITR-flanked scCMV-eGFP expression cassette (see 4.4 for more details). In addition, we performed productions with double-transfection of pAdHelper plasmid and the AAV2-Rep/HtW-Cap only, without a pTransgene plasmid to manufacture "empty" virus-like particles (VLPs) without a vector genome. Purification of HtW vectors and VLPs was done using standard protocols as

described in 4.4. Interestingly, HtW particles could be affinity-purified using AAVx affinity chromatography confirming the AAV-like nature of genome-containing and empty HtW particles. While not fully disclosed by the manufacturer, AAVx columns are thought to be coated with multiple anti-AAV capsid antibodies directed against specific conformational epitopes on the surface of intact capsids of different AAV serotypes, such as AAV2 or AAV9. These surface epitopes only form in completely and correctly assembled AAV capsids which enables for an in-process quality control of AAV batches. The chromatograms obtained for genome containing HtW2_S1.1 showed a similar shape, binding, and elution profile as conventional AAV2 WT vectors with only a slight shift towards later elution volume (Figure 49A, B). Empty HtW1_S1.1 VLPs could also be purified with AAVx, but the chromatogram is further shifted towards higher elution volumes (between 21 and 22 mL) (Figure 49C).
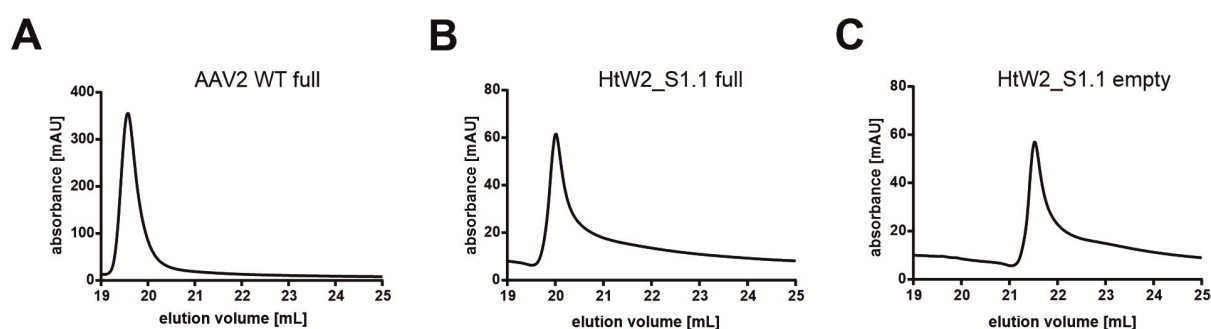
Figure 49 AAVx affinity purification chromatography of AAV vectors Chromatograms show the elution of (A) AAV2 WT full capsids compared to (B) HtW2_S1.1 full capsids and (C) HtW2_S1.1 empty virus-like particles. AAV2 WT and HtW2_S1.1 were conventionally produced by a triple transfection carrying an ITR-flanked scCMV-eGFP reporter cassette. (C) HtW2_S1.1 empty VLPs were produced in the absence of a pTransgene plasmid.

However, the titers were strongly decreased for HtW variants compared to the AAV2 WT as indicated by the absorbance peak height and reduced AUC for HtW2_S1.1 batches. Comparable results were seen for HtW2_S1.2 and HtW9_S1.1 affinity-based purification. This suggests that HtW capsids carrying large peptide insertions are still able to express specific conformational wildtype epitopes to a certain extend retaining "AAV capsid characteristics".

For further experiments and HtW characterization vectors were purified using anion exchange chromatography (AEX) or cation exchange chromatography (CEX) to avoid harsh elution conditions at pH 3.0 needed for AAVx affinity-based purification.

5.2.2.2 Production yields of HtW vectors displaying large peptide insertions

Following chromatographic purification and size-exclusion filtration (Amicon) HtW preparations were evaluated by static light scattering (SLS) measurement of capsid titers and if produced with vector genomes by ITR-based genomic titer determination via qRT-PCR. HtW vectors could be produced at genomic titers with a mean of 8.8×10^7 vg/µL for HtW2_S1.1, 6.7×10^7 vg/µL for HtW2_S1.2 and 5.5×10^7 vg/µL for HtW9_S1.1 (Figure 50A). This is several log units lower than for AAV2 WT and AAV9 WT vectors, which could be routinely produced at high titers with mean values of 1.4×10^{10} vg/µL (AAV2 WT) and 2.2×10^{11} vg/µL (AAV9 WT). However, the capsid titers of HtW variants were rather high and ranged between 8.9×10^9 cp/µL and 2.2×10^{10} cp/µL (Figure 50B), which corresponds in ratios of only 0.5-1% full capsid proteins for each HtW variant. Capsid titers of AAV2 WT and AAV9 WT were 8.8×10^{10} cp/µL and 5.7×10^{11} cp/µL, respectively. These results suggest that the ability to package the vector genome appears to be lower for all three HtW capsid variants, although capsid assembly is reasonably good.
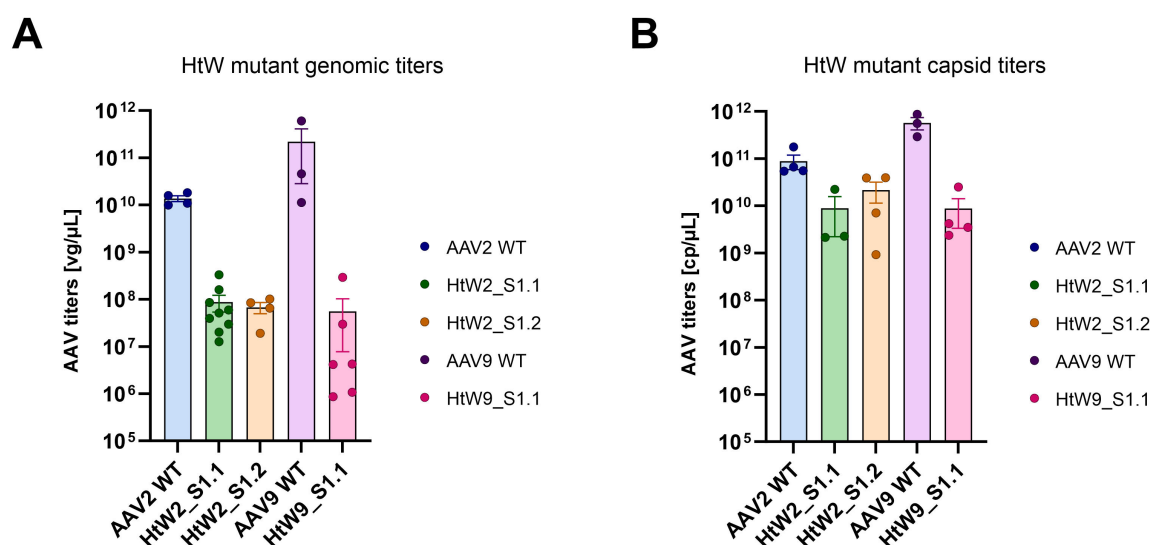
Figure 50 Overview of HtW mutant production yields (A) Genomic titer of capsid variants determined via ITR-directed qRT-PCR. (B) Capsid titer in final AAV sample measured by SLS. Error bars indicating ± SEM.

5.2.3 Transduction properties of HtW vectors carrying large peptide insertions

Next, the transduction efficiency of HtW vector variants was evaluated in HEK293T cells at three different MOIs of 250, 500 and 1000 vg/cell. Due to the overall low genomic titers of HtW vectors and the low *in vitro* infectivity of AAV9-based vectors, only AAV2-based HtW were further investigated *in vitro*. HEK293T cells were seeded 24 hours prior to transduction.

Expression of eGFP was monitored over 48 hours at the EVOS fluorescence microscope followed by quantification of eGFP-positive cells using the Countess 3 FL Automated Cell Counter.
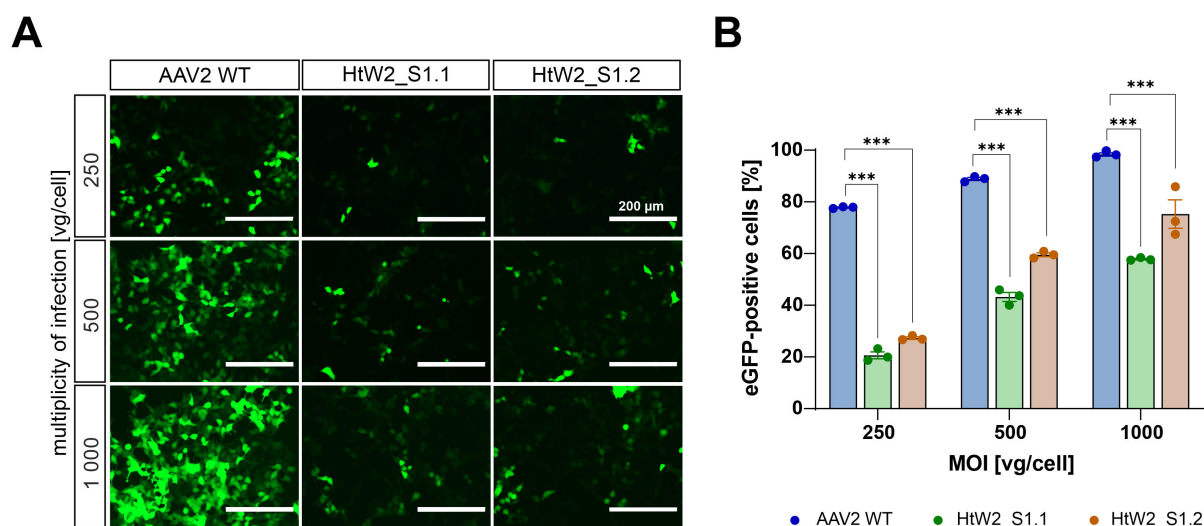
Figure 51 Transduction properties of AAV2 WT, HtW2_S1.1 and HtW2_S1.2 in HEK293T cells (A) Representative epifluorescence images acquired 48 hours after transduction at 60% GFP intensity and 20x magnification. Cells were transduced with AAV2 WT, HtW2_S1.1 or HtW2_S1.2 expressing eGFP at three different MOIs (Multiplicity of infections, vg/cell): 250, 500 and 1 000 vg/cell. Scale bar marks 200 µm. (B) Quantification of eGFP-positive cells in HEK293T cells 48 hours post transduction. 1-way ANOVA, Šídák's multiple comparisons test: * $p < 0.05$, ** $p < 0.01$, *** $p < 0.001$, error bars indicating ± SEM, n = 3.

Note that the cell counter quantifies only GFP expression but not GFP intensity of individual transduced cells. Therefore, comparable quantification levels can result in differences of intensity shown in fluorescence images. HtW2_S1.1 and HtW2_S1.2 show significantly lower transduction rates compared to AAV2 WT (Figure 51) especially at an MOI of 250 vg/cell. The difference in transduction efficiency decreases with higher MOIs but remains significant.

The RBD of SARS-CoV-2 is known to bind to ACE2 and this interaction contributes to cell infectivity [273], [277]. To test whether the RBD at the capsid surface of HtW is presented in a functional conformation that is still capable of engaging in this characteristic receptor-ligand interaction, we generated an ACE2-overexpressing HEK293T cell line (ACE2-OE-HEK293T) using the PiggyBac transposon system [278]. We hypothesized that if functional, the RBD should facilitate the infection and transduction of HEK293T cells in a ACE2 dose-dependent manner. In support of the presence of a functional RBD, HtW2_S1.2 showed significantly increased transduction of ACE2-OE-HEK293T cells across all three MOIs tested (Figure 52), whereas AAV2 WT showed no difference in transduction between the two cell lines (data not shown).
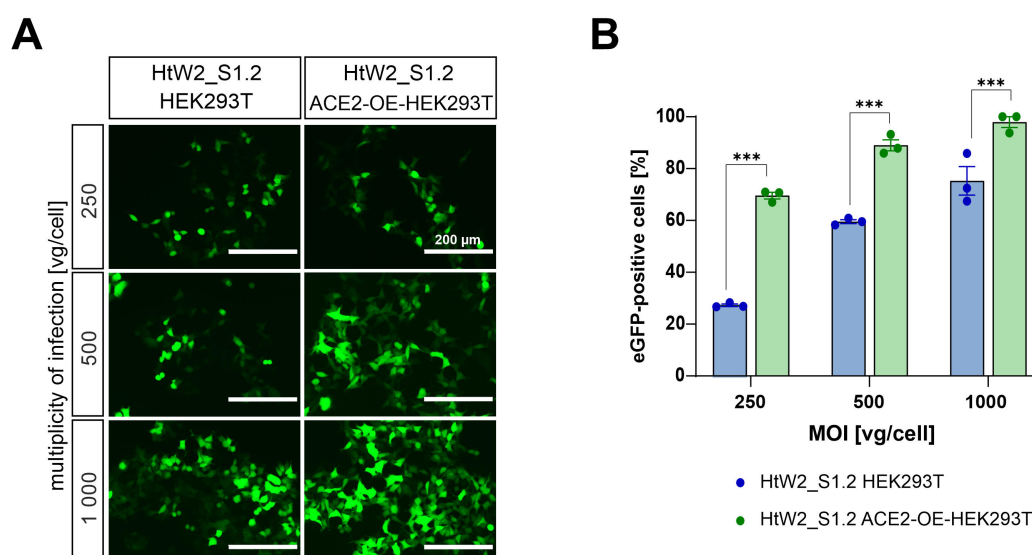
Figure 52 Capability for viral cell entry of HtW2_S1.2 (A) Transduction of HtW2_S1.2 in native HEK293T cells (left) compared to a stable ACE2-overexpressing HEK293T cell line (ACE2-OE-HEK293T, right) at three different MOIs: 250, 500 and 1 000 vg/cell. Vector is carrying a scCMV-eGFP reporter cassette. (B) Quantification of eGFP-positive cells 48 hours after transduction. 1-way ANOVA, Šídák's multiple comparisons test: * $p < 0.05$, ** $p < 0.01$, *** $p < 0.001$. Error bars indicating ± SEM, n = 3. Scale bar marks 200 µm.

These results suggest that HtW vectors are still capable of transducing cells *in vitro* and with a relatively low MOI despite the large peptide insertions in all 60 VPs of the capsid. Moreover, the transduction rate can be increased by overexpression of ACE2, which confirms proper folding and exposure of the RBD sequence on the HtW capsid surface.

5.2.4 Evaluation of the immunogenic potential of HtW VLPs in rabbits

5.2.4.1 Immunization of adult rabbits with HtW VLPs

To evaluate the immunogenic potential of HtW capsids *in vivo* we immunized adult ZIKA hybrid rabbits. This breed of rabbits is approved and widely used for antibody production since they do not produce different IgG isotypes while mice or humans show four isotypes each [279]. Instead rabbits show potent immune responses after subcutaneous (s.c.) administration of antigens [280]. Note that for rabbit-related experiments HtW and control AAVs were produced as VLPs without transgene and were purified via CEX using a SO_3-column without prior iodixanol gradient centrifugation to avoid potential immunogenic reactions to either the genome, the transgene or iodixanol. Animals were immunized with VLPs according to the immunization scheme depicted in Figure 53A. The initial immunization was performed with 100 µg of VLPs via s.c. administration. Every 30 days a booster injection of 50 µg VLPs was performed, followed by collection of 30 mL serum 10 days after each booster injection. The

final serum collection was performed at day 150. Control sera (5 mL) were taken from each animal 1 week before primary immunization. Note that all *in vivo* rabbit experiments were kindly performed by Prof. Dr. Hermann Ammer at the Department of Veterinary Sciences (LMU Munich).

5.2.4.2 Evaluation of antibody titers in sera of immunized rabbits

The serum collected at each timepoint was tested for RBD-specific IgG titers from rabbits immunized with HtW2_S1.1, HtW2_S1.2, HtW9_S1.1 or with AAV2 WT and AAV9 WT control vectors. For evaluation via self-made enzyme-linked immunosorbent assay (ELISA) a commercially available RBD protein was immobilized on a plate and probed with serial dilutions of rabbit sera in -3 log dilutions. Antisera titers were determined as described before [281]. All three HtW variants show IgG antibody titers detectable up until a dilution between 3.9 and 4.5 (values indicated as 1/log 10 dilution steps) while the sera of AAV2 and AAV9 wildtype immunized rabbits show no RBD-specific IgG antibody production (Figure 53B).
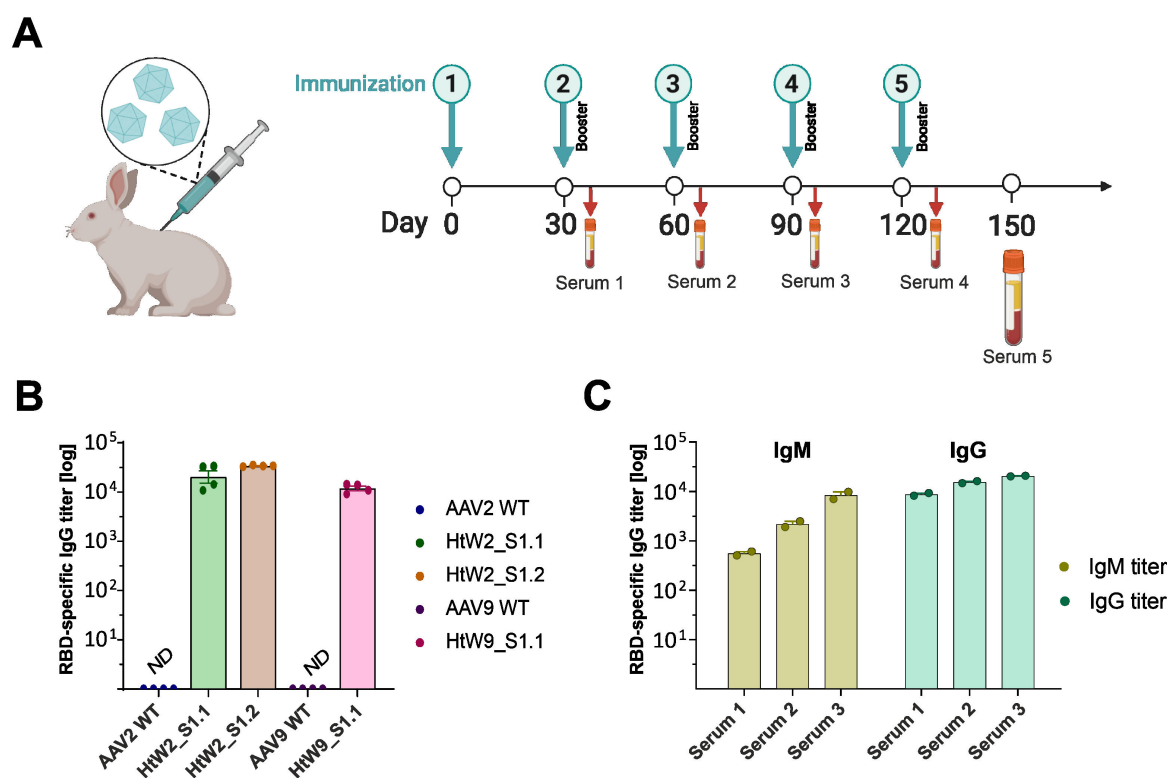
Figure 53 Immunization of ZiKa rabbits with HtW capsid mutants and antibody titer evaluation (A) Schematic of immunization strategy for adult rabbits *(performed by Prof. H. Ammer, LMU Department of Veterinary Sciences):* Initial s.c. administration of HtW VLPs followed by booster injections every 30 days. Blood was collected 10 days after each booster injection until day 150. Rabbits were immunized with wildtype AAV capsids (AAV2 WT; AAV9 WT) or HtW capsids (HtW2_S1.1, HtW2_S1.2 or HtW9_S1.1). (B) RBD-specific IgG titers in serum of immunized rabbits. (C) IgG (blue) and IgM (yellow) antibody titers in HtW2_S1.2-immunized rabbit sera 10 days after the first three serum collections. Shown are the endpoint titers of SARS-CoV-2 RBD specific IgG and IgM antibodies. Values are indicated as 1/log 10 dilution steps. (A) n = 3, (B) n = 4, (C) n = 2, ± SD.

114

Additionally, the sera of HtW2_S1.2 immunized rabbits was collected 10 days after the immunizations 2-4, respectively serum 1-3 were tested for the RBD-specific IgG and IgM titers (Figure 53C). While the IgG titers between each serum stay at comparable levels over the evaluated 90 days the IgM titer increases after each VLP administration from 2.7 up to 3.9. This suggests a strong T-cell response to HtW VLPs after each booster immunization resulting in high IgM production to the antigen which ultimately leads to high IgG titers detectable in a range between 3.9 up to 4.3.

5.2.4.3 Evaluation of cross-reactivity of anti-HtW rabbit sera

The ELISA experiments showed that HtW VLPs induced RBD-specific IgGs, but the specificity of each serum towards the immunized capsid variant remained unclear. Because HtW2_S1.1, HtW2_S1.2, and HtW9_S1.1 carry similar RBD-insertions, we hypothesized that antibodies raised against one of the HtWs should also cross-react with the other HtWs. To evaluate the cross-reactivity of RBD-specific IgG antibodies in sera of immunized rabbits, we performed dot blot experiments.

Serial dilutions of HtWs and AAV WT were spotted and immobilized on a PVDF membranes for immunodetection. First, the dot blots were incubated with a commercially available anti-SARS-CoV-2 Spike S1-specific antibody. The dot blot showed a concentration-dependent RBD-specific signal for all three HtWs, but not for the AAV2 and AAV9 WT controls (Figure 54A). This confirmed that the RBD sequence is present in all three HtW variants. Moreover, since the dot blot protocol does not contain any denaturation step, this result also suggests that the RBD sequence is exposed at the capsid surface and has a conformation that allows for binding of anti-SARS-CoV-2 Spike S1-specific antibody. The dot blot signal was strongest with HtW9_S1.1, followed by HtW2_S1.2, suggesting differences in the exposure and/or presentation of the RBD sequence on the capsid surface among the three HtWs.

Next, dot blots were incubated with serum of rabbits immunized with one of the HtWs or one of the two wildtype AAV serotypes. Incubation with HtW9_S1.1-immunized rabbit serum at a dilution of 1:10 000 resulted in a strong immunosignal with all HtW variants and even at the lowest dilution tested (8×10^7 cp per dot) (Figure 54B). The serum also showed a weak signal with the high AAV2 capsid concentrations, suggesting the presence of some antibodies directed against the AAV capsid part. Similar results were obtained with sera from HtW2_S1.2 and HtW2_S1.1 immunized rabbits (data not shown).

A

B
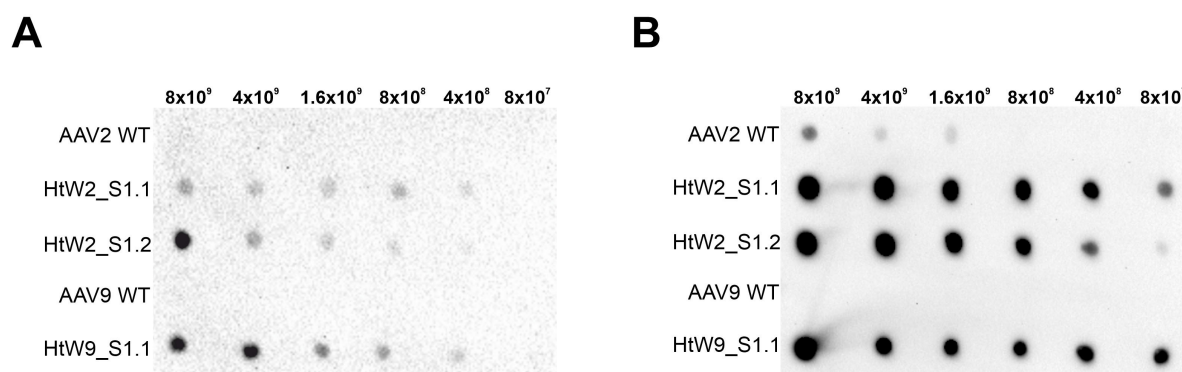
Figure 54 Evaluation of RBD-binding properties (A) Dot blot of HtW and AAV WT capsids immobilized on a PVDF mebrane at a titer of 8×10^9 cp up to a 1:100 dilution. Incubation with commercially available rabbit monoclonal anti-SARS-CoV-2 Spike S1 antibody (1:500). Only HtW capsids show a signal against the SARS-CoV-2 antibody. (B) Dot blot with HtW and AAV WT capsid variants after incubation with serum of HtW9_S1.1-immunized rabbits after final heart puncture (1:10 000). The blot shows a strong cross-reaction between HtW variants.

5.2.4.4 *In vitro* neutralization efficacy of rabbit anti-HtW sera

Binding of antibodies to a specific immunogen does not necessarily lead to neutralization of that antigen. Having established the binding affinity of the rabbit anti-HtW sera, we set out to characterize their ability to neutralize the HtWs. For evaluation of neutralization of HtWs by the rabbit sera obtained via HtW-immunization, we used the ACE2-OE-HEK293T cell line introduced in 5.2.3. Cells were seeded 24 hours prior to transduction. AAV2 WT and HtW2_S1.2 were compared in this experiment. Each capsid was produced as genome-containing vector carrying a scCMV-eGFP expression cassette. Dilutions of vectors were prepared at an MOI of 250 vg/cell, pre-incubated with a dilution of anti-HtW2_S1.2 serum for 1 hour at 37°C and then applied to the cells for infection. eGFP fluorescence was imaged for 48 hours at the EVOS fluorescence microscope followed by quantification with the Countess 3 FL Automated Cell Counter. A total of four different dilutions (1:1 000, 1:2 500, 1:5 000 and 1:10 000) of rabbit anti-HtW2_S1.2 serum were tested. At the highest serum concentration (1:1 000 dilution) both vectors, AAV2 WT and HtW2_S1.2, were neutralized (Figure 55A, top row). At higher dilutions, transduction by AAV2 WT increased. However, transduction efficiency of HtW2_S1.2 remained very low even at the highest serum dilution, suggesting the presence of high levels of HtW2_S1.2-specific neutralizing antibodies in the serum of immunized rabbits (Figure 55A, right column).

A

B

C
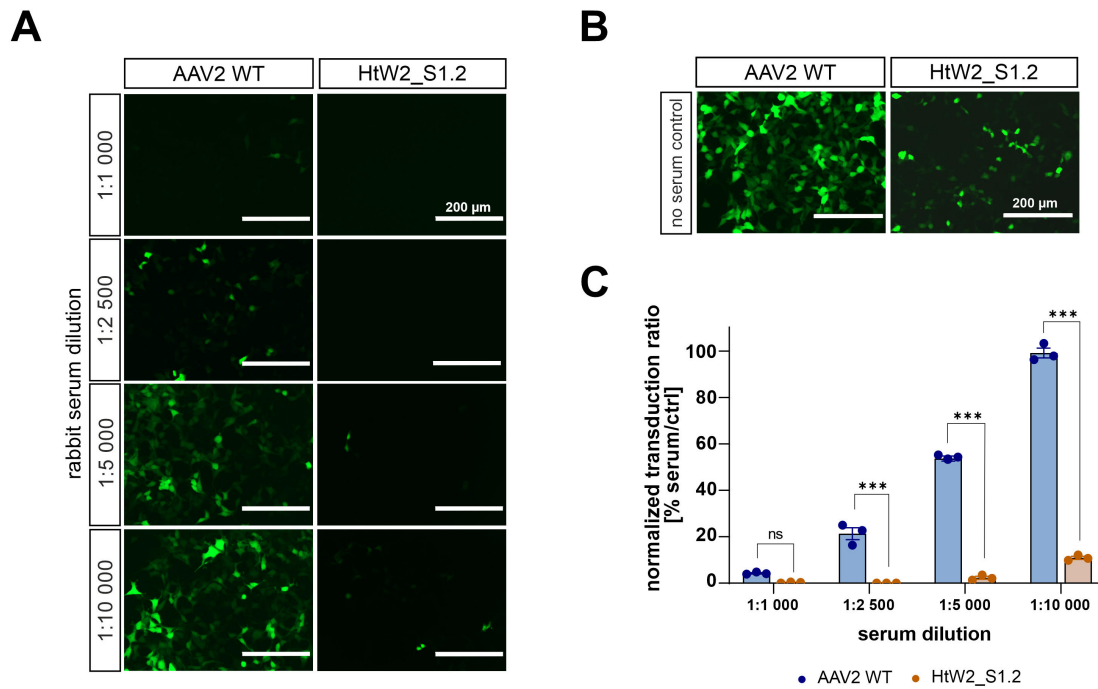
Figure 55 Evaluation of neutralization efficacy of immunized rabbit sera (A) Representative fluorescence images of stable ACE2-OE-HEK293T cells after transduction with AAV2 WT and HtW2_S1.2 vectors carrying an scCMV-eGFP reporter cassette. Vectors were preincubated at an MOI of 250 vg/cell with four different dilutions of HtW2_S1.2-immunized rabbit sera for 1 hour at 37°C (1:1 000, 1:2 500, 1:5 000, 1:10 000). No serum control (B) shows transduction properties of capsid variants after preincubation without serum. Images were acquired 48 hours post transduction at 60% GFP intensity and 20x magnification. Scale bar marks 200µm. (C) Quantification of eGFP-positive cells 48 hours post transduction normalized to the respective no serum controls. 1-way ANOVA, Šídák's multiple comparisons test: * $p < 0.05$, ** $p < 0.01$, *** $p < 0.001$. Error bars indicating ± SEM, n = 3.

5.2.5 Neutralization of HtW vectors by human blood plasma of individuals vaccinated with Comirnaty®

Given the availability of blood plasma from human donors after mRNA-based SARS-CoV-2 vaccination, we expanded this study to investigate the neutralization of HtWs by such plasma. Due to the ongoing vaccination during the pandemic, we were able to collect blood samples from three individual donors prior to vaccination and after each of the first two recommended vaccinations with the mRNA-based vaccine Comirnaty® (see scheme in Figure 56).
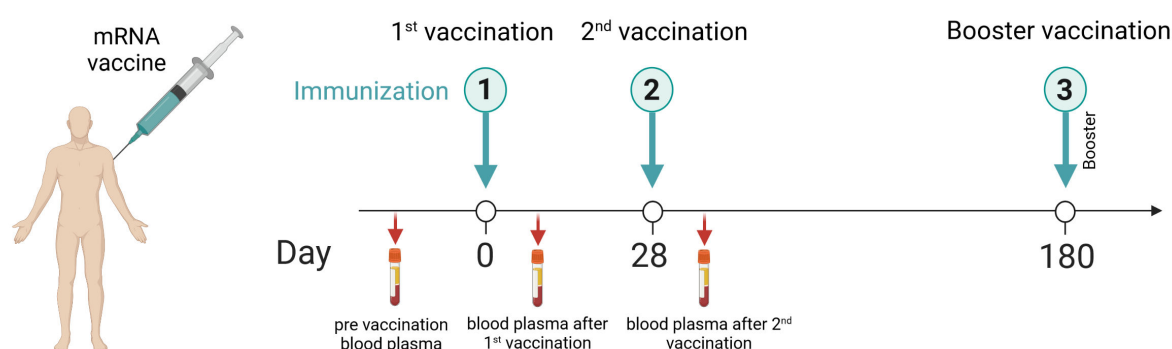
Figure 56 Immunization scheme with mRNA-based vaccine against SARS-CoV-2 Immunization was performed according to the valid STIKO recommendation in early 2021 with mRNA-based vaccines against the SARS-CoV-2 spike protein. Pre-vaccination blood plasma was collected before vaccination, blood plasma 1 was collected 2 weeks after the first vaccination and blood plasma 2 was collected one week after the second vaccination.

Blood plasma of three human donors were then analyzed for their HtW vector neutralization efficiency. Due to low production titers only HtW2_S1.2 and AAV2 WT were evaluated. In detail, ACE2-OE-HEK293T cells were seeded one day prior to transduction. Vectors were diluted to an MOI of 250 vg/cell as in 5.2.4.4 and preincubated with four different dilutions of human blood plasma (1:50, 1:250, 1:500 and 1:1 000) for 1 hour at 37°C. Again, eGFP fluorescence was monitored for 48 hours followed by quantification as described above for the rabbit sera. Quantification results were normalized to the transduction rates observed in the respective "no plasma"-control. The blood plasma prior to vaccination had almost no effect on HtW2_S1.2 showing a transduction rate, which ranged between 89% and 96% of the no plasma control level (Figure 57B). The blood plasma collected after the first and the second vaccination showed strong neutralization effects especially at 1:50 and 1:250 dilution. Interestingly, the blood plasma obtained after the first vaccination reduced the transduction rate to 4% (1:50) and 28% (1:250), whereas the blood plasma collected after the second vaccination lowered the transduction rate to only 14% (1:50) and 44% (1:250) of the no plasma control of HtW2_S1.2, respectively (Figure 57). Nevertheless, these experiments show that

HtW can be efficiently neutralized by blood plasma from Comirnaty®-immunized individuals, thereby confirming proper exposure of the SARS-CoV-2 RBD sequence at the capsid surface of HtW allowing for binding of human neutralizing anti-SARS-CoV-2 Spike S1-specific antibodies.
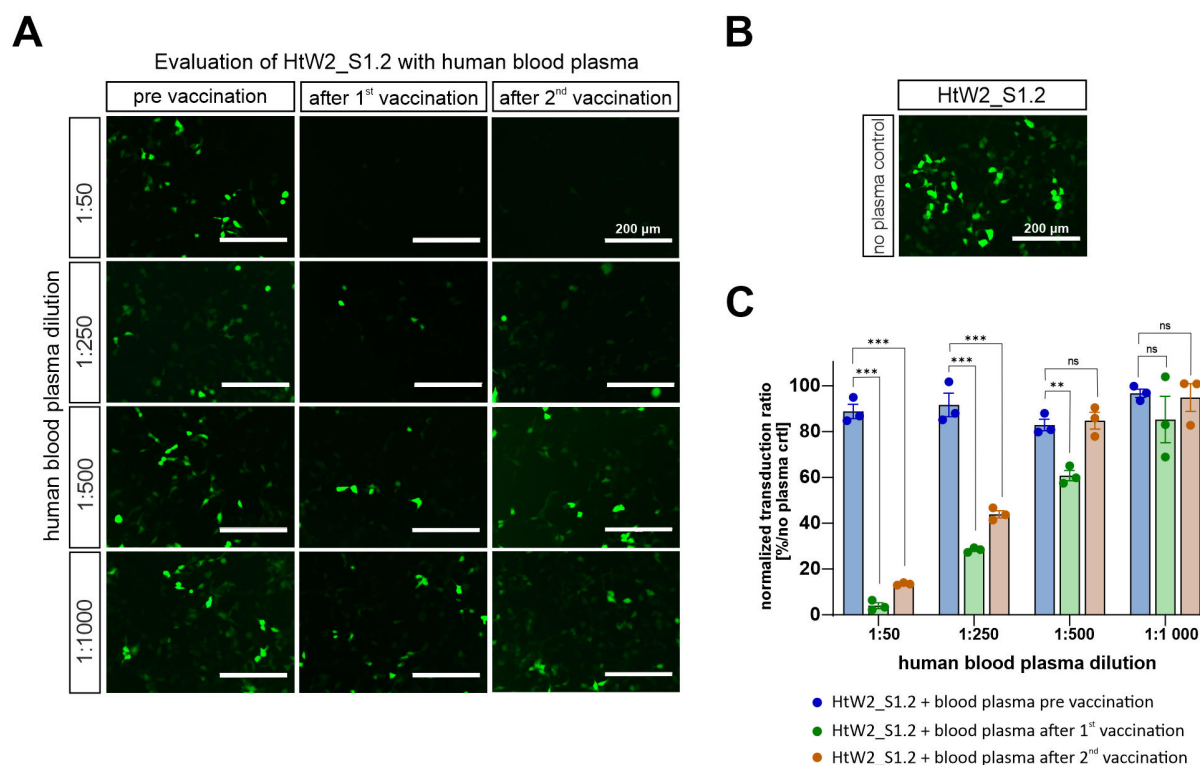
Figure 57 Neutralization of HtW2_S1.2 by human blood plasma obtained after mRNA-based immunization (A) Representative fluorescence images showing transduction of HtW2_S1.2 expressing eGFP in stable ACE2-overexpressing HEK293T cells at 250 MOI. Vectors were preincubated for 1 hour at 37°C with four different dilutions (1:50, 1:250, 1:500, 1:1000) of human blood plasma from individuals that had been vaccinated with Comirnaty®. Images were taken 48 hours post infection with 60% GFP intensity at 20x magnification. (B) Control transduction in the absence of blood plasma (no plasma control). Scale bar marks 200 μm. (C) Quantification of eGFP-positive cells 48 hours post transduction normalized to no plasma control. 1-way ANOVA, Šídák's multiple comparisons test: * $p < 0.05$, ** $p < 0.01$, *** $p < 0.001$. Error bars indicating ± SEM, n = 3.

5.2.6 Dot blot analysis comparing rabbit serum with human blood plasma

Lastly, the binding affinity of anti-RBD antibodies in the human blood plasma was tested on dot blots and compared to the affinity of a rabbit serum. All three HtW variants as well as AAV2 WT and AAV9 WT were immobilized on a PVDF membrane in a serial dilution as described above. The membrane was first incubated with the blood plasma of Comirnaty®-vaccinated human donors at a dilution of 1:500. As shown in Figure 58A, antibodies of the human blood plasma cross-reacted with all three HtW variants. The signal was strongest with HtW9_S1.1 showing a signal up to the 8×10^8 cp dot.

The AAV2 and AAV9 wildtype controls showed no signal, confirming that the blood plasma was negative for anti-AAV antibodies and that the signal obtained for the HtWs resulted from an RBD-specific antibody binding (Figure 58A).
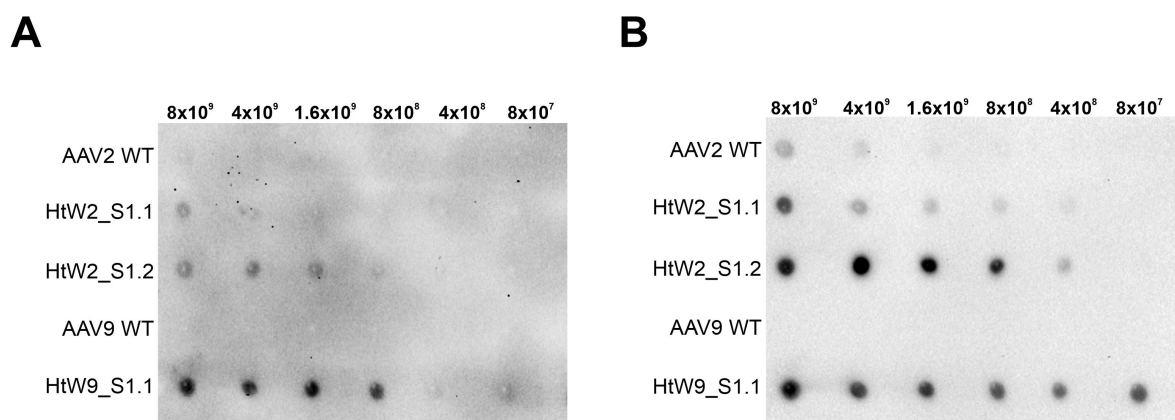
Figure 58 Testing HtW binding affinity of human blood plasma and rabbit sera (A) Dot blot of HtW and AAV WT vectors after incubation with Comirnaty®-vaccinated human blood plasma (1:500) collected one week after the second vaccination. HtW and AAV WT capsid variants were spotted on the PVDF membrane at 8×10^9 cp on the first dot and at up to a 1:100 dilution on the following dots. (B) The membrane from (A) was stripped and re-incubated with HtW9_S1.1-immunized rabbit serum at a 1:10 000 dilution.

The PVDF membrane was stripped to remove bound antibodies and re-incubated with serum from HtW9_S1.1-immunized rabbits at a dilution of 1:10 000. The membrane now showed strong signals across all three HtW vector (Figure 58B), similar to the results obtained previously (Figure 54B).

These results indicate that the Comirnaty® vaccine, which delivers a modified mRNA-sequence that encodes for the entire SARS-CoV-2 spike protein induces antibodies targeting the RBD region of SARS-CoV-2 that can bind to HtWs immobilized on a PVDF membrane. The titer of these HtW-binding antibodies in the human blood plasma must be lower than the respective titer in the serum of rabbits immunized with HtW.

6 Discussion

6.1 Novel engineered AAV9 capsid mutants with tailored tropism for intravitreal gene therapy

AAVs are small, non-pathogenic virus vectors that have become a popular tool for episomal gene delivery. They combine broad tissue tropism, with other advantages such as low immunogenicity and the potential for long-term gene expression [5], [6], [240], [282]. For inherited retinal dystrophies (IRDs) so far only Luxturna® (voretigene neparvovec-rzyl), an AAV2-based gene therapy for Leber congenital amaurosis, was granted FDA/EMA-approval [283]. Currently, there are almost 100 ongoing clinical studies showing promising therapeutic effects for AAV-based gene therapy of ocular diseases, such as retinitis pigmentosa [284], achromatopsia [285] and age-related macular degeneration [283]. Most of them rely on well-characterized natural serotypes such as AAV2, AAV5 and AAV8. However, novel engineered AAV capsid variants are explored in preclinical animal models such as rodents as well as large animals, namely canine, pig and NHP [286]–[288]. This allows for vectors to be tailored to tissue- and cell-type specific needs and moreover the exploration of alternative less-invasive pathways of delivery. Ideally novel capsid mutants should be suitable for intravenous administration while providing efficient transduction of the desired target cells. In this context, the AAV-PHP.B mutant initially provided high levels of CNS transduction after intravenous injection in mice [289] but failed to transduce marmoset brain [161] while furthermore causing severe toxicity in NHPs [162].

In the context of ocular gene therapy, a less invasive but nonetheless challenging alternative to subretinal (SR) vector administration is intravitreal (IVT) AAV delivery. Application into the vitreous fluid allows for a wider spreading of the therapeutic vector without damaging the retina at the injection site following retinal detachment [225]. However, when delivered via IVT injection, the vector needs to overcome biological barriers such as the inner limiting membrane (ILM), which separates the vitreous fluid from the retina. This thin monolayer has been reported to cause HSPG-dependent accumulation of AAV vectors resulting in decreased retinal transduction and insufficient therapeutic effects [141], [248]. Subsequently, higher vector doses need to be administered to reach therapeutic concentrations, e.g. at photoreceptors, which increases the risk of potential immune reactions and the production of capsid specific neutralizing antibodies (NAbs) [290]–[292].

To allow for efficient retinal transduction after IVT injection, various approaches of modifying the HSPG-binding motif have been investigated. Previous studies have shown that efficient HSPG-binding relies on a motif created by two neutrally charged amino acids, such as glycine or alanine, flanked by two positively charged amino acids such as R585 and R588 in the AAV2 WT capsid. This binding motif results in efficient binding of negatively charged heparan sulfate (HS) residues [53]. In the context of AAV1 and AAV8, Woodard et al. in 2016 substituted crucial positions in the Cap-sequence with a positively charged lysine (AAV1-E531K and AAV8-E533K), resulting in enhanced HSPG-binding and increased *in vitro* transduction efficiency but also accumulation at the ILM after IVT administration [248], [293].

In our previous directed evolution approach, AAV2-based libraries with small peptide insertions disrupting characteristic HSPG-binding sites were administered intravenously and selected for enriched capsid mutants in the eye. The stringent *in vivo* selection process resulted in two superior capsid variants, termed AAV2.NN and AAV2.GL. Both variants show decreased accumulation at the ILM and efficient photoreceptor transduction after IVT administration compared to AAV2 WT. Both peptide insertions (NNPTPSR = "NN" or GLSPPTR = "GL") are flanked by linkers of three alanines upstream and two alanines downstream [225].

In this study, these small peptide insertions were further modified and introduced into AAV9 WT to explore alternative HSPG-binding motifs for efficient targeting of photoreceptors after less invasive IVT administration in C57BL6/J mice.

6.1.1 Characterization of AAV9 capsid mutants

Prior to administration in animals or humans, characterization of novel AAV vectors is crucial. While *in vitro* or *ex vivo* experiments provide valuable first impressions on vector properties, such as infectious potential, transduction capabilities and cell tropism, initial characterization should not be limited to biological aspects but also include technical aspects. To that end three important attributes were evaluated in this study: Genomic titer, capsid titer and melting temperature T_m of the novel AAV9 capsid mutants. These three characteristics can further be used to maintain constant quality levels and avoid experimental bias through fluctuations in the manufacturing process.

AAV production is a time-consuming process involving initial production of plasmids, HEK293T cell transfection, harvesting, cell lysis, ultracentrifugation or chromatographic purification and size-exclusion filtration [228]. Variations introduced at each step of the production can result in fluctuations of quality, purity, stability, and titers of the final product [165]. Therefore, it is paramount to implement the measurement of these parameters to guarantee a constant quality of the products and early detection of problems in the production process.

In this study, capsid and genomic titers revealed full/empty ratios between 20% to 50% of full capsids (Figure 20; Table 10) except for AAV9.RAAR and AAV9.RAAK which showed highly decreased genomic titers (Figure 20A, orange, yellow). Since AAV9.RAAR also resulted in low capsid titers (Figure 20B, orange), it can be assumed that the incorporation of the two positively charged arginines into the AAV9 capsid without additional extension of loop IV by small peptide insertions may cause inefficient capsid assembly and subsequently lower amounts of full AAV capsids. For AAV9.RAAK, the capsid titers are comparable to AAV9.NNR and AAV9.GLR however low genomic titers indicate less efficient genome packaging. Possible reasons for this discrepancy could be differences in post-translational modifications (PTMs) between the AAV9 capsid mutants. In AAV9 capsid proteins several PTMs such as ubiquitination (K105 and K650) or SUMOylation (small ubiquitin related modifier) (K84, K316, K557) of lysine residues were identified [294]. Both types of PTMs were first discovered to modify intracellular trafficking by directly helping to shuttle protein complexes from the cytosol to the nucleus [295]. Furthermore, ubiquitination can also result in lysosomal or proteasomal degradation [296] or activation of intracellular immune reaction pathways [297]. Some studies have shown that SUMO-inhibition leads to an increase in viral transduction rates [298]. Furthermore, modifications of residues prone to PTMs decreased the genome packaging ability of AAVs [294]. These findings could explain the differences in capsid and genomic titers amongst the novel AAV9 capsid mutants. As a possible consequence, large amounts of empty VLPs not only lack a therapeutic effect but further significantly decrease the transduction efficiency of AAVs carrying a transgene in mice [299]. Additionally, high titers of empty VLPs enhance the amount of antigens presented to the cell, increasing the risk of immune responses to the capsid protein *in vivo* [300]. Lastly, previous studies have identified several regions within the VPs responsible for correct capsid assembly. Modifications at the 5-fold and 2-fold symmetry axes especially interfered in the process of capsid assembly while alterations within secondary structures such as α-helices often lead to incorrect folding of VP

monomers and subsequently proteasomal degradation [18], [301]. Overall, the process of capsid assembly, as well as the full range of effects of PTMs during capsid assembly and viral performance are not fully understood to date.

Additionally, AAV capsid characterization was performed via thermal stability assessment. Since the melting temperature T_m of AAVs varies a lot across serotypes ranging from 66-90°C, a thermal stability assay can be used for the determination of capsid identity [253]. The characterization of AAV9 vector variants via iDSF (Figure 21C-F) revealed a decrease of ~15°C in melting temperature T_m after the insertion of the NN- or GL-peptide resulting in a T_m comparable to AAV2.NN and AAV9.GL [225]. Considering that AAV9 WT shows a comparably high T_m of approximately 78°C [253] it is surprising to see that similar insertions in different AAV serotypes result in a comparable T_m. This phenomenon has been shown in 2017 by Bennett et al. with single amino acid substitutions in AAV1 and AAV6 WT resulting in destabilization or stabilization of the capsid. Both modified capsids, namely AAV1-E531K and AAV6-K531E, showed the T_m of the respective other WT capsid [253], [254]. Single amino acid substitutions however not necessarily affect the T_m as shown for AAV9.R (Figure 21A, B) depending on the position on the capsid and potential interaction partners of this residue. While all vectors carrying the NN- or GL-insertion differ in one amino acid position, they overall showed comparable T_m (Figure 21C-F). Differences in T_m can affect factors such as genome release or storage stability at non-optimal pH or temperature. High T_m results in stable capsids tolerating non-optimal storage conditions while also leading to inefficient capsid degradation following decreased levels of DNA release. On the other side lower T_m allows for easy intracellular genome unpacking but may result in fragile capsids degrading faster under non-optimized storage conditions [302].

Overall, determination of these properties generates valuable data and helps initial characterization of novel AAV capsid mutants. In addition, this data also raises awareness to manufacturing problems like scale-up possibilities of promising vectors that can only be produced at low genomic titers such as AAV9.RAAK (Figure 20; Table 10).

Moreover, conventional purification via ultracentrifugation impedes proper full/empty capsid characterization since iodixanol elicits a strong UV signal, which prevents simultaneous UV/Vis and SLS/DLS measurements. Alternative gradient-ultracentrifugation media such as cesium chloride (CsCl) are known to be toxic and further can alter the tropism of purified vectors

[303]. Additionally, combination of several consecutive columns with different binding properties further improves full/empty ratio and purity of AAV vectors but also leads to an increase in manufacturing costs [304]. Ultimately, there are still many challenges in AAV production and technical characterization that need to be addressed in the future.

6.1.2 *In vitro* and *in vivo* evaluation of AAV9 capsid mutants

To assess their transduction properties, the novel AAV9 capsid mutants were evaluated *in vitro* in immortalized HeLa cells (5.1.3). AAV9.NN and AAV9.GL showed significantly decreased transduction rates in HeLa cells, which can be explained by the different natural tropism of AAV9 WT and its primary receptor N-linked galactose (GAL) instead of HSPG [28], [251]. In AAV9.NN and AAV9.GL the peptide insertions are followed by an alanine instead of a positively charged amino acid. Thus, other than in the AAV2 context, no additional HSPG-binding motif, such as RAAR is generated, which could have contributed to increase *in vitro* transduction efficiency [53]. To generate this binding motif a single amino acid substitution of A589R or A589K after the NN- or GL-insertion was established. The resulting R- and K-mutants showed increased transduction properties in HeLa cells (Figure 23; Figure 24), hereby supporting the hypothesis of generating an artificial HSPG-binding motif in AAV9. Indeed, combination of capsid properties of AAV serotypes has already been explored, by the generation of capsid chimeras, such as AAV2G9 which combines AAV9-based galactose and AAV2-based HSPG-binding properties [305]. Overall, our approach of generating artificial HSPG-binding motifs shows promising results *in vitro* by increasing the transduction efficiencies of R- and K-mutants compared to their parental AAV9.NN or AAV9.GL variant.

In vivo evaluation after IVT administration of AAV9 capsid mutants in adult C57BL6/J mice resulted in AAV9.NNR and AAV9.GLR showing the highest transduction properties in the ONL and the photoreceptors (5.1.4). However, AAV9.NN also showed high ONL transduction rates after administration of a 5×10^9 vg/cell medium dose (Figure 29B), while both AAV9.NN and AAV9.GL revealed strong eGFP expression in the photoreceptors after dose escalation to 1×10^{10} vg/cell (Figure 31B, E). Both vectors outperform the transduction levels of high-dose AAV9.NNK and AAV9.GLK (Figure 31D, G).

These *in vivo* results partially contradict the effects observed in HeLa cells raising an issue that has been observed in preclinical gene therapy for many years: AAV vector evaluation *in vitro*

125

does not necessarily predict efficacy in a living organism [306]. The evaluation of *ex vivo* human retinal explants showed auspicious performances for AAV9 WT, AAV9.GL and AAV9.GLR mutants while AAV9.NN and AAV9.NNR performed less promising (Figure 41; Figure 42). In contrast, both NN-variants clearly outperform the corresponding GL-versions in mice especially after 1 x 10^9 vg/cell low dose vector administration (Figure 26A, B, first and middle row). Note that due to limited availability of human retinal tissue, the vectors were evaluated at small n-numbers which limits the significance of these results.

The eye is considered immune privileged which limits inflammatory processes due to natural barriers such as the blood-retina-barrier and the blood-aqueous-barrier [68], [86], [307], [308]. However, clinical and preclinical studies report moderate to severe inflammatory events which often require anti-inflammatory corticosteroid treatment in patients [137], [285], [309], [310]. In this study, the degree of "retinal stress" induced by vector administration was evaluated by GFAP-staining indicating activation of Müller glia in transduced retinal cross-sections. However, IHCs revealed no AAV9 capsid variant-specific reactive gliosis (5.1.4.4). Instead there was a moderate dose-dependent Müller glia activation, which could be observed especially by comparison of low dose and medium dose vector administration (Figure 32; Figure 33; Figure 34). Additionally, AAV9.NNR with the highest transduction rates in the mouse retina resulted in the highest GFAP signal (Figure 33D-F) which indicates a correlation between the activation of Müller glia cells and eGFP expression levels. These dose-dependent effects have been observed in clinical trials but also in large animal models [311], [312]. However, the degree of reactive gliosis observed in 5.1.4.4 remains moderate compared to degenerative knock-out mouse models [313].

Additionally, the application route of AAV vectors needs to be taken into consideration. Although less invasive and technically easier as the SR vector administration the IVT injection is associated with an overall higher immunogenic potential through the vitreous fluid. In comparison, SR vector administration poses a lower immunogenic risk due to the natural barrier of the tight junctions between RPE and blood vessels which are considered responsible for the immune privileged status of the eye [314]. Studies have reported increased immune responses and elevated titers of NAbs against the vector capsid mediated by IVT injection which poses challenges if a re-administration of the vector is needed [290], [291].

AAV9 WT has been reported to pass the BBB, efficiently transduce the CNS [247], [269] and achieve retinal transduction [271], [272] after systemic application. Furthermore, Dudes et al. (1999) showed eGFP expression in the optic nerve (ON) and the lateral geniculate nucleus after IVT injection of AAV vectors in mice and dogs up to 6 months after vector administration [315]. We therefore investigated the extent of neuronal transduction along the visual pathway after IVT injection of AAV9 capsid mutants (5.1.5). In our evaluation of potential transduction in the ON after high dose IVT administration AAV9 WT has shown the strongest transduction (Figure 40A). For all AAV9 capsid mutants the eGFP expression in the ON is decreased compared to the wildtype (Figure 40B-L). Moreover, we observed no tansduction of the optic tract and directly adjacent brain areas after IVT administration of 1×10^{10} total vg. These results lead to the conclusion that although AAV9-based neuronal transduction properties remain in most of the AAV9 capsid mutants no potent distribution into the brain can be expected.

6.1.3 Evaluation of AAV9 capsid mutants on human retinal explants and humanized 3D models

The problem of AAV vector properties such as tissue targeting, transduction efficiency and dose-dependent immunogenicity not translating across different has been extensively studied before [162], [289], [316]. Since initial characterization and evaluation of novel vectors cannot be implemented in patients, current translational approaches rely on humanized animals [317], *ex vivo* evaluation on human retinal tissue or complex humanized models such as human retinal organoids (hROs) [227], [318]. While AAV capsids tested in humanized animal models such as chimeric mice with human liver xenografts show immune escape from NAbs in human serum, these results can only be translated to a limited extend into human patients [319], [320]. Donated human retinal tissue allows for a valuable preclinical evaluation of novel vectors. However, the tissue often shows poor condition since surgical removal is mostly performed in older patients with severely damaged retinae or tumorous tissue which limits its scientific use [321]. As IHC has shown (Figure 42) the human retina is reduced in thickness and often already underwent degradation of cell layers, in these patients, which complicates the interpretiation of results due to the non-optimal quality of the tissue. Therefore, selected AAV9 capsid mutants were additionally evaluated in iPSC-derived hROs (5.1.7). 3D tissue

cultures are widely used as *in vitro* models for vector characterization to evaluate AAV capsid mutants in a more complex humanized model [226], [322], [323]. Since AAV9 WT has previously shown efficient transduction of cones in NHP [59], in 2020 Garita-Hernandez et al. evaluated AAV9 WT on cone-enriched hROs showing only poor transduction levels. This was explained by the absence of cone outer segments and therefore undetectable GAL-levels at the timepoint of transduction, which serves as primary receptor for AAV9-mediated cell entry [322]. In 2021 Völkner et al. evaluated AAV2 and AAV9 carrying the NN- or GL-insertion in iPSC-derived hROs which resulted in high eGFP expression levels for AAV2.NN and AAV2.GL after transduction at day 200. In comparison, only AAV9.NN after high-dose transduction (5 x 10^{10} total vg) showed strong eGFP expression [226]. To investigate if our artificial HSPG-binding motif increases transduction levels, hROs were transduced at day 220 with 1 x 10^{10} total vg of AAV9.NN or AAV9.GL and their respective R- and K-mutants (5.1.7). Transduction levels across all hROs were considerably low (Figure 43; Figure 44), leading to the conclusion that further experiments with higher vector doses are needed to allow for interpretation of potential differences between the novel AAV9 vectors and their respective transduction properties in humanized 3D cultures.

6.1.4 The ciliary body as a therapeutic target

Apart from gene therapy of IRDs targeting the retina, another potentially interesting target for a different subset of ocular diseases is the ciliary body. This delicate ring-like structure at the periphery of the eye is responsible for production and secretion of ocular fluids [324] and maintenance of the intraocular pressure (IOP). Imbalances in the production and recycling of ocular fluids can increase the IOP which is the most common risk for developing a primary open-angle glaucoma (POAG) or a primary angle-closure glaucoma (PACG) [325], the leading cause of irreversible blindness worldwide. This disease is characterized by progressive optic neuropathy eventually leading to complete loss of vision [326]–[330]. Over 70 % of POAG patients have a genetic predisposition [331], [332]. So far, 16 genes have been discovered to be associated with POAG. Two of these genes, namely *GAS7* and *TMCO1,* are highly expressed in the ciliary body [333]*.*

During *in vivo* evaluation of the novel AAV9 capsid mutants we discovered five vectors with tropism favorable for targeting the non-pigmented ciliary epithelium (NPCE). Those vectors,

namely AAV9.RAAK, AAV9.NNR, AAV9.NNK, AAV9.GLR and AAV9.GLK showed strong transduction of the NPCE after IVT low dose administration of 1×10^9 total vg in mice (Figure 37E, G, H, K, L). Full cross-sections from the periphery of the eyecup confirmed strong transduction rates of the NPCE for AAV9.NNR, AAV9.GLR and AAV9.RAAK (Figure 38). Since only AAV9 capsid mutants with artificial HSPG-binding motif showed NPCE transduction, these results suggest that HSPG-binding is crucial for ciliary body targeting. Recently, two studies focusing on the distribution of different HSPG-classes in the mouse and rat eye showed that especially syndecan-1, -2 and -4 are highly enriched in NPCE. Furthermore, syndecan-3, glypican-2, and agrin are more present in the endothelial cells of the ciliary processes [334], [335]. For a more detailed analysis of the exact binding properties, the five AAV9 capsid mutants with NPCE tropism should be further evaluated to discriminate which HSPG subclass is involved in capsid-binding. In 2013, Bemelmans et al. evaluated the ciliary body transduction of AAV9 WT with a comparable scCMV-GFP transgene after i.v. high dose (1×10^{12} total vg) vector administration [272]. Here, they show transduction of retinal cells and high eGFP expression in the pigmented ciliary epithelium (PCE). Considering these results, the i.v. administration of AAV9.NNR and AAV9.GLR can be tested to assess whether this application route also results in high NPCE transduction with capsid mutants optimized for artificial HSPG-binding. Moreover, the NPCE is known to play a major role in the production and secretion of aqueous humor [82], therefore various options could be further explored from a therapeutic point of view. A gene supplementation strategy delivering the defective transgene (e.g. *GAS7* or *TMCO1*) or small antibodies such as anti-VEGF bevacizumab via IVT administration of AAV9.NNR or AAV9.GLR may be worth considering.

Even though glaucoma is the most common cause of blindness with a highly genetic prevalence, there is currently no available gene therapy. Some preclinical studies have investigated the potential of CRISPR/Cas9 strategies of reducing the IOP in mice by disrupting water-transporting transmembrane proteins such as Aquaporin-1 [336] or knockdown of an overactive myocilin gene (*MYOC*) [337]. The promising tropism for the NPCE observed with AAV9.NNR, AAV9.GLR and AAV9.RAAK in this study might facilitate the development of such treatment approaches in the future. Using these AAV9 capsid variants to directly target the NPCE and control the fluid production and IOP can be considered as a possible alternative therapeutic approach in the context of glaucoma-related applications.

6.2 Exploring the potential beyond gene therapy - AAV capsid mutants as vaccines

During the COVID-19 pandemic various strategies using AAVs for delivery of immunogens were explored. The characteristic features of AAVs such long-term gene expression and high transduction properties provided advantages for potential vaccination strategies. However, long before the pandemic, there were some initial studies using AAVs to induce potent immune responses against various diseases:

The first attempt to use AAV vectors for delivering vector-encoded immunization sequences was already made in 1997 by Manning et al. [338]. They explored the potential of AAV2 WT expressing the glycoproteins B and D of Herpes Simplex Virus Type 2 (HSV-2) after intramuscular administration in mice [338]. Furthermore, evaluation of an engineered AAV hybrid, namely AAVrh32.33, for vaccination against HIV-1 and Influenza Type A showed promising CD8$^+$ T-cell levels in macaques [339], leading to the discovery of VP3 regions responsible for immune responses [340], [341]. Additionally, several groups successfully investigated AAV5 and AAV9 for intranasal immunization against Human Papilloma Virus Type 16 (HPV16) in mice and rhesus macaques [7], [342], [343]. During the pandemic, numerous vaccination approaches against SARS-CoV-2 were explored using AAV vectors for transgene delivery. Some groups evaluated the transgene expression of the entire spike glycoprotein or exclusively the S1 subunit in NHPs [8], [344], while other groups focused on AAV5- or AAV9-based delivery of parts of the receptor-binding domain (RBD) into mice and NHP [345]–[347].

Overall, investigating immunization strategies for different diseases, routes of application and AAV serotypes show promising results for AAV vectors as a vaccination platform. However, all of these approaches rely on the expression of an immunogenic transgene. Therefore, a considerable amount of time elapses between vector application and elicitation of the desired immune response.

6.2.1 Engineering AAV capsid mutants with large peptide insertions

In this study, we investigated the introduction of large immunogenic peptide insertions of approximately 200 amino acids at the capsid surface of AAV2 and AAV9. This novel

immunization platform does not rely on transgene expression but presents the desired antigen directly on the capsid surface of engineered AAV-based virus-like particles (VLPs).

Three novel capsid mutants were generated exposing the RBD of SARS-CoV-2 at the top of loop IV on the AAV capsid. The novel capsid mutants, termed HtW2_S1.1, HtW2_S1.2 and HtW9_S1.1, could be produced, but resulted in low genomic titers compared to their parental AAV2 or AAV9 capsids (Figure 50A). The chromatograms obtained during affinity-based chromatography (Figure 49B) showed elution timepoints comparable to AAV2 with a decreased AUC which also suggests lower capsid titers for HtW2_S1.1 (Figure 49B, C). It is tempting to speculate that the incorporation of approximately 200 additional amino acids displayed 60x on the capsid surface impairs the complex process of AAV capsid assembly as previously described [348]. However, capsid titers determined by SLS were considerably high and ranged between 9×10^9 cp/μL and 2×10^{10} cp/μL (Figure 50B). Genomic titers of vector variants carrying an eGFP-transgene cassette were low and ranged between 9×10^5 vg/μL and 3×10^8 vg/μL (Figure 50A).

Potentially essential proteins for the correct capsid assembly, such as the assembly-activating protein (AAP) [349], are not disrupted by the RBD-insertion and should be intact during HtW capsid assembly. These observations suggest the assembly of potentially leaky capsids which cannot efficiently carry a transgene. One reason can be that AAV capsids are known to destabilize and release DNA under thermal stress, such as extensive freeze/thaw cycles [350] or increased temperature [302]. Another possible explanation could be differences in capsid modifications or steric hindrance around the pore at the 5-fold symmetry axis, which is the entry point for the vector genome into fully assembled AAV capsids [18]. In addition, it is possible that large parts of the RBD-insertion face the capsid cargo, resulting in a confined space inside the AAV capsid, which cannot sufficiently carry the transgene (Figure 47B, E). The RoseTTAfold *in silico* modeling (Figure 47) shows highly variable RBD-conformations in the single VP3 monomers and in the assembled capsids across the three HtW capsids. For HtW2_S1.1 the RBD-insertion is structurally exposed on the capsid surface (Figure 47D), while the HtW2_S1.2 *in silico* model shows major parts of the RBD-insertion facing the inside of the capsid (Figure 47E) which could explain the low genomic titers due to low cargo capacity. For HtW9_S1.1 the RBD-insertion is incorporated on the capsid surface which results in a larger capsid size compared to HtW2_S1.1 according to the *in silico* model. SLS measurement using

the Stunner revealed aggregation, which could be caused by the large RBD-insertion and further complicated the accurate measurement of capsid titers.

Ultimately, *in silico* modeling by RoseTTAfold provides an idea on how the most energetically and sterically favorable protein conformation could be displayed. The process of AAV capsid assembly is not fully understood to date and *in silico* modeling does not necessarily accurately predict complex higher order structures. Thus, for determination of exact protein structures, Cryo-EM-based experiments need to be considered in the future.

6.2.2 *In vitro* evaluation of receptor-ligand interactions

Next, the infectious potential of the novel vector variants HtW2_S1.1 und HtW2_S1.2 was assessed. Both vectors, were able to transduce HEK293T cells, albeit with significantly decreased efficiency compared to AAV2 WT (Figure 51). Transduction rates were increased in HEK293T cells overexpressing the natural ACE2-receptor (ACE2-OE-HEK293T), which mediates viral entry of SARS-CoV-2 after RBD-binding (Figure 52). These results suggest that HtW vectors remain infectious despite large peptide insertions on the capsid surface. Moreover, increased transduction rates in ACE2-overexpressing HEK293T cells confirm the correct folding and exposure of the RBD-insertion mediating viral cell entry. Ensuring that the immunogenic region is exposed in a functional conformation on the capsid surface is not only crucial for receptor-interactions but also promotes the production of antigen-specific neutralizing antibodies (NAbs) that ultimately lead to the desired protective immunity [351]. Vaccination strategies based on transgene expression often require sequence modifications to stabilize the desired protein in a conformation that exposes immunogenic epitopes for NAbs to be produced. This has been observed in mRNA-based vaccination strategies against SARS-CoV-2 [352]–[354]. In these studies, the S2 subunit was adapted by two proline substitutions at K986P and V987P, resulting in higher stability of the prefusion conformation that exposes the immunogenic residues of the RBD (Figure 15B,C) and enables a stronger immune response [277], [355]. Moreover, in SARS-COV-2, the S2 subunit of the spike-protein controls the fusion between virus and host cell membrane [356]. The furin-cleavage site of the S2 subunit further promotes fusion between S1 subunit and host cell [357]. Since the HtW capsid variants do not carry this protein sequence, viral internalization relies exclusively on endogenous endocytosis by HEK293T cells. This poses an additional challenge for viral cell entry.

6.2.3 Neutralization of HtW variants in rabbit sera and human blood plasma

To evaluate the immunogenic potential of the HtW capsid mutants in terms of their ability to induce the production of RBD-specific NAbs, adult rabbits were immunized with empty virus-like particles (VLPs) of HtW2_S1.1, HtW2_S1.2, HtW9_S1.1 or their parental serotypes AAV2 and AAV9 WT (Figure 53A). An ELISA confirmed the production of RBD-specific IgGs in adult rabbits after immunization with HtW VLPs (Figure 53B). Rabbits immunized with HtW2_S1.2 VLPs showed comparable IgG levels in the first three sera collected, whereas IgM titers increased with each VLP administration (Figure 53C). This is consistent with clinical trials showing an initial increase in IgM titers after each immunization but overall constant IgG levels after each booster vaccination [358], [359]. Elevated IgM titers indicate a currently ongoing infection that triggers a strong T-cell response and induces immature B-cells to produce IgM antibodies that switch subclasses after maturation into an IgG response [360]. In the absence of T-cells, humoral B-cells continue to secrete IgM antibodies [361]–[363]. However, the overall high IgG titers (Figure 53C) indicate a strong IgG switch. After re-administration, the T-cell response and subsequently the IgM titer increases with every booster injection, indicating a rapid and strong immune response. With mRNA-based SARS-COV-2 vaccination initial high IgG and IgM titers are observed, peaking 4-8 weeks after the second vaccination were reported [364]. However, in human patients, increased IgM titers have been reported to result in higher NAbs levels and thus increased immunity against potential SARS-CoV-2 infections [365].

Furthermore, after incubation with serum of immunized rabbits, HtW variants showed RBD-specific cross-reactivity in dot blots, indicating an RBD-conformation that allows for antibody production against similarly exposed immunogenic epitopes in all three vector variants (Figure 54B). Serum from HtW9_S1.1 immunized rabbits showed a weak signal with AAV2 capsids in dot blots, indicating much weaker antibody production directed against the AAV2 capsid part compared with the RBD-insertion. The dot blots show the strongest immunosignal for HtW9_S1.1 and HtW2_S1.1. This experimental data is in contrast with the RoseTTAFold *in silico* modelling data, which suggested differences in the surface exposure of the RBD in the three variants. In both capsid variants the RBD-sequence is either strongly incorporated (HtW9_S1.1) or exposed (HtW2_S1.1) on the capsid surface (Figure 47A, C, D, F) according to *in silico* modeling. In comparison, HtW2_S1.2 shows a strong but ultimately weaker signal which is consistent with the in silico modeling,

displaying large parts of the RBD-insertion facing the capsid cargo (Figure 47B, E). To evaluate whether the anti-RBD antibodies also have the potential to inactivate HtW vectors expressing eGFP, a neutralization assay was performed in ACE2-OE-HEK293T cells (5.2.4.4). Quantification of eGFP-positive cells showed that pre-incubation with rabbit anti-HtW2_S1.2 serum resulted in significantly decreased transduction efficiency for HtW2_S1.2, whereas AAV2 WT was only neutralized by high amounts of serum (Figure 55). These results indicate an RBD-specific neutralization process.

Lastly, we investigated the neutralization of HtW variants by blood plasma from Comirnaty®-vaccinated human donors (5.2.5). While human blood plasma prior to vaccination had little effect on transduction rates, HtW2_S1.2 was strongly neutralized by plasma collected after the first and the second vaccination (Figure 57). Notably, the blood plasma after the initial vaccination had stronger neutralization capability than the blood plasma collected after the second vaccination. The effect of NAb titers peaking after initial antigen contact has been observed previously in the context of mRNA-based vaccination [366], [367]. Dot blots also showed cross-reactivity for all HtW variants with human blood plasma (Figure 58A), complementing the results observed with the rabbit serum (Figure 54B). Notably, in this experiment the immunosignal was stronger after incubation with the blood plasma after the second vaccination. This could indicate a higher amount of total IgG antibodies in the human blood plasma after the second vaccination but a lower amount of RBD-specific NAbs compared to the blood plasma after the initial vaccination [368], [369]. Re-incubation of the dot blot with the corresponding HtW9_S1.1-immunized rabbit serum showed the same results, but with an overall stronger immunosignal. Given that rabbits were only immunized with capsids displaying the RBD-insertion and Comirnaty®-vaccination elicits immune responses to the whole spike protein, the total amount of RBD-specific NAbs produced in rabbits is expected to be higher than in Comirnaty®-vaccinated humans.

In conclusion, this data provides a promising first evaluation of an innovative and sustainable next generation AAV-based platform to overcome shortcomings occurring in traditional vaccine production as well as introducing a new strategy for broad applications of antigen delivery. Recently a study showed that the development of immunogenic AAV capsid mutants can also be implemented as immunotherapy for cancer applications such as melanoma and thymoma [370]. Additionally, possible applications in the context of cystic fibrosis may be

worth evaluating as some serotypes such as AAV9 showed promising immunization effects after re-administration in the presence of high amounts of NAbs [160].

Overall, our platform enables strong and specific immune responses without the need for genetically encoded immunogens, thus reducing the risk of potentially pathogenic intracellular processes associated with viral vector genomes and prolonged transgene expression. Moreover, this next-generation vaccination platform provides the flexibility to easily adjust the size of the antigen to be presented on the AAV capsid surface to target new epitopes of emerging variants or other diseases.

6.3 Summary

AAVs are the current gold standard in gene therapy as promising vectors for the delivery of small to medium size genes. Since the first AAV-based gene therapy was granted market access in 2012, six additional gene therapies have received FDA or EMA approval. However, there is currently no gene therapy for many inherited diseases.

The first part of this thesis investigated a previously discovered artificial HSPG-binding motif from AAV2 peptide libraries in the context of AAV9 hereby combining a directed evolution approach with rational design to generate novel AAV capsid mutants. In addition, this study emphasized the challenges in assessing AAV properties across different cell types or model species, which needs to be taken into account throughout the *in vitro* and *in vivo* characterization process. Three promising novel capsid variants, namely AAV9.RAAK, AAV9.NNR and AAV9.GLR, exhibit a strong tropism for the NPCE of the ciliary body. This tropism can be exploited for novel gene therapy approaches targeting inherited POAG.

The second study explored the potential of AAV-based therapeutic applications beyond gene supplementation therapy. We showed that engineered AAV capsids tolerate large immunogenic peptide insertions exposed on the capsid surface in a conformation that still allows for natural receptor-ligand-interactions. These variants termed HtW2_S1.1, HtW2_S1.2 and HtW9_S1.1 elicit potent IgG and IgM responses in rabbits specific to the immunogenic RBD-insertion. Moreover, HtW2_S1.2 was strongly neutralized with serum of HtW2_S1.2-immunized rabbits and with human blood plasma after vaccination with the mRNA-based vaccine Comirnaty®. These encouraging results allow for further exploration of this approach of presenting antigens on AAV capsids, which represents a promising strategy for the development of vaccines against diseases where conventional vaccination attempts have failed so far.

Taken together, this thesis highlights the potential of AAV capsid engineering to generate optimized AAV variants tailored to future therapeutic needs for a wide range of applications within and outside of ocular gene therapy through modification and adaptation of the AAV capsid sequence.

7 Appendix

7.1 Plasmid maps
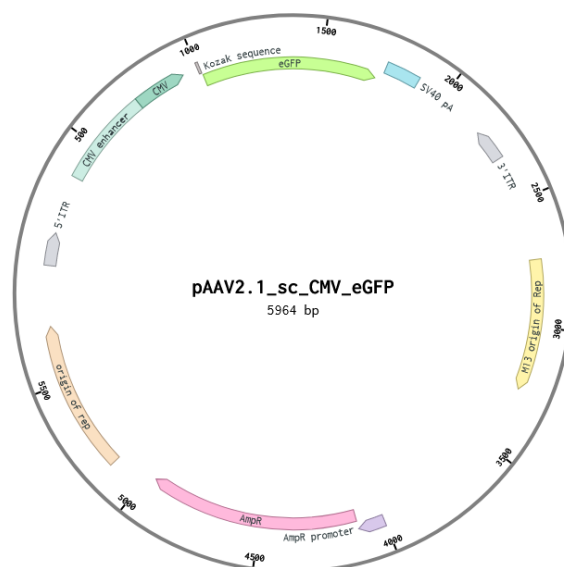
Figure 59 Plasmid map pAAV2.1_scCMV-eGFP transgene
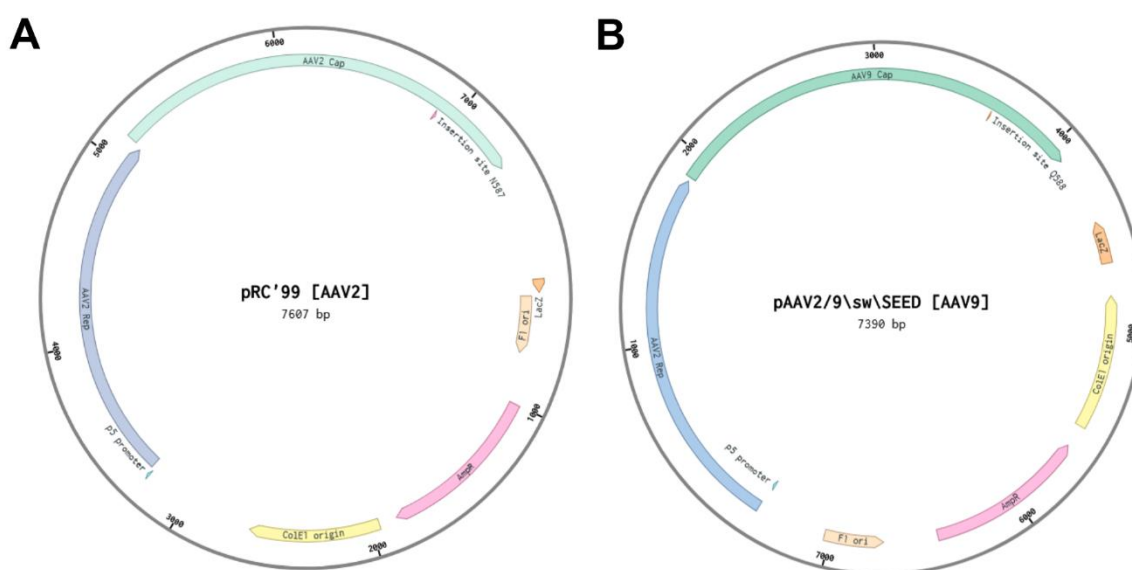
Figure 60 Plasmid maps from AAV2 and AAV9 backbone

7.2 Gene Fragments

AAV9.NNK	AAAACTACTAACCCGGTAGCAACGGAGTCATATGGACAAGTGGCCACAAACCACCAGAGTGCCCAAGCGGCCGCAA ACAACCCCACCCCCTCCCGGGCCGCGAAACAGGCGCAGACCGGTTGGGTTCAAAACCAAGGAATACTTCCGGGTATG GTTTGGCAGGACAGAGATGTGTACCTGCAAGGACCCATTTGGGCCAAAATTCCTCACACGGACGGCAACTTTCACCCT TCTCCGCTGATGGGAGGGTTTGGAATGAAGCACCCGCCTCCTCAGATCCTCATCAAAAACACACCTGTACCTGCGGAT CCTCCAACGGCCTTCAACAAGGACAAGCTTAACTCTTTCATCACCCAGTATTCTACTGGCCAAGTCAGCGTGGAGATC GAGTGGGAGCTGCAGAAGGAAAACAGCAAGCGCTGGAACCCGGAGATCCAGTACACTTCC
AAV9.GLK	AAAACTACTAACCCGGTAGCAACGGAGTCATATGGACAAGTGGCCACAAACCACCAGAGTGCCCAAGCGGCCGCAG GCCTGTCCCCCCCCACCCGGGCCGCGAAACAGGCGCAGACCGGTTGGGTTCAAAACCAAGGAATACTTCCGGGTATG GTTTGGCAGGACAGAGATGTGTACCTGCAAGGACCCATTTGGGCCAAAATTCCTCACACGGACGGCAACTTTCACCCT TCTCCGCTGATGGGAGGGTTTGGAATGAAGCACCCGCCTCCTCAGATCCTCATCAAAAACACACCTGTACCTGCGGAT CCTCCAACGGCCTTCAACAAGGACAAGCTTAACTCTTTCATCACCCAGTATTCTACTGGCCAAGTCAGCGTGGAGATC GAGTGGGAGCTGCAGAAGGAAAACAGCAAGCGCTGGAACCCGGAGATCCAGTACACTTCC
AAV9.RAAK	AAAACTACTAACCCGGTAGCAACGGAGTCATATGGACAAGTGGCCACAAACCACCAGAGCGCTCAACGGGCCGCGA AACAGGCGCAGACCGGTTGGGTTCAAAACCAAGGAATACTTCCGGGTATGGTTTGGCAGGACAGAGATGTGTACCT GCAAGGACCCATTTGGGCCAAAATTCCTCACACGGACGGCAACTTTCACCCTTCTCCGCTGATGGGAGGGTTTGGAAT GAAGCACCCGCCTCCTCAGATCCTCATCAAAAACACACCTGTACCTGCGGATCCTCCAACGGCCTTCAACAAGGACAA GCTTAACTCTTTCATCACCCAGTATTCTACTGGCCAAGTCAGCGTGGAGATCGAGTGGGAGCTGCAGAAGGAAAACA GCAAGCGCTGGAACCCGGAGATCCAGTACACTTCC

7.3 RBD sequences

S1.1_RBD	ACTAATCTTTGTCCGTTCGGTGAGGTTTTTAACGCGACAAGGTTCGCTAGTGTATATGCTTGGAACCGAAAGAGAATC TCCAATTGCGTAGCTGATTACTCCGTTCTCTATAACAGTGCGTCCTTTTCAACCTTTAAGTGTTACGGCGTTTCTCCAAC GAAGCTGAATGATCTCTGTTTTACGAACGTGTATGCTGACTCTTTCGTTATACGGGGGGACGAAGTGAGACAGATAG CACCAGGTCAGACTGGGAAGATAGCGGATTACAACTATAAGTTGCCCGATGATTTTACGGGGTGCGTAATCGCATGG AACTCAAACAACCTCGACTCCAAAGTAGGTGGTAATTATAATTACTTGTATCGCCTGTTTCGAAAGAGCAATTTGAAG CCTTTTGAGCGGGATATTTCAACCGAAATTTACCAAGCAGGCAGTACGCCATGTAACGGAGTAGAGGGATTTAATTGC TACTTTCCTCTTCAATCTTATGGCTTTCAACCAACAAACGGAGTGGGGTATCAACCTTATAGAGTGGTAGTATTGTCCT TTGAGCTCCTCCACGCCCCGGCTACAGTTTGTGGGCCCAAAAAGGGA
S1.2_RBD	AAGTGCACCCTGAAGAGCTTCACCGTGGAGAAGGGCATCTACCAGACCTCCAATTTCCGCGTGCAGCCAACCGAGAG CATCGTGCGCTTCCCCAATATCACCAACCTGTGCCCATTCGGCGAGGTGTTCAACGCTACCAGGTTCGCCAGCGTGTA CGCTTGGAATCGCAAGCGCATCTCCAACTGCGTGGCCGACTACAGCGTGCTGTACAACTCCGCCAGCTTCTCCACCTTC AAGTGCTACGGCGTGTCCCCCACCAAGCTGAATGATCTGTGCTTCACCAACGTGTACGCCGATAGCTTCGTGATCAGG GGCGACGAGGTGCGCCAGATCGCTCCAGGACAGACCGGCAAGATCGCTGACTACAATTACAAGCTGCCCGACGATTT CACCGGCTGCGTGATCGCCTGGAACTCCAACAATCTGGATAGCAAAGTGGGCGGCAACTACAATTACCTGTACCGCCT GTTCCGCAAGTCCAATCTGAAGCCATTCGAGCGCGACATCTCCACCGAGATCTACCAGGCTGGAAGCACCCCATGCAA TGGAGTGGAGGGCTTCAACTGCTACTTCCCCCTGCAGAGCTACGGCTTCCAGCCAACCAACGGAGTGGGGATAC

Bibliography

[1]   R. W. Atchison, B. C. Casto, and W. M. D. Hammon, "Adenovirus-associated defective virus particles," *Science (80-.).*, 1965, doi: 10.1126/science.149.3685.754.

[2]   M. D. Hoggan, N. R. Blacklow, and W. P. Rowe, "Studies of small DNA viruses found in various adenovirus preparations: physical, biological, and immunological characteristics.," *Proc. Natl. Acad. Sci. U. S. A.*, 1966, doi: 10.1073/pnas.55.6.1467.

[3]   A. Pupo, A. Fernández, S. H. Low, A. François, L. Suárez-Amarán, and R. J. Samulski, "AAV vectors: The Rubik's cube of human gene therapy," *Mol. Ther.*, vol. 30, no. 12, pp. 3515–3541, 2022, doi: 10.1016/j.ymthe.2022.09.015.

[4]   S. Pillay and J. E. Carette, "Host determinants of adeno-associated viral vector entry," *Current Opinion in Virology*. 2017. doi: 10.1016/j.coviro.2017.06.003.

[5]   M. Penaud-Budloo *et al.*, "Adeno-Associated Virus Vector Genomes Persist as Episomal Chromatin in Primate Muscle," *J. Virol.*, 2008, doi: 10.1128/jvi.00649-08.

[6]   G. M. Acland *et al.*, "Long-term restoration of rod and cone vision by single dose rAAV-mediated gene transfer to the retina in a canine model of childhood blindness," *Mol. Ther.*, 2005, doi: 10.1016/j.ymthe.2005.08.008.

[7]   D. Kuck *et al.*, "Intranasal Vaccination with Recombinant Adeno-Associated Virus Type 5 against Human Papillomavirus Type 16 L1," *J. Virol.*, 2006, doi: 10.1128/jvi.80.6.2621-2630.2006.

[8]   N. Zabaleta *et al.*, "An AAV-based, room-temperature-stable, single-dose COVID-19 vaccine provides durable immunogenicity and protection in non-human primates," *Cell Host Microbe*, vol. 29, no. 9, pp. 1437-1453.e8, 2021, doi: 10.1016/j.chom.2021.08.002.

[9]   L. V. Crawford, E. A. Follett, M. G. Burdon, and D. J. McGeoch, "The DNA of a minute virus of mice.," *J. Gen. Virol.*, 1969, doi: 10.1099/0022-1317-4-1-37.

[10]   J. A. Rose, K. I. Berns, M. D. Hoggan, and F. J. Koczot, "Evidence for a single-stranded adenovirus-associated virus genome: formation of a DNA density hybrid on release of viral DNA.," *Proc. Natl. Acad. Sci. U. S. A.*, 1969, doi: 10.1073/pnas.64.3.863.

[11]   S. E. Straus, E. D. Sebring, and J. A. Rose, "Concatemers of alternating plus and minus strands are intermediates in adenovirus associated virus DNA synthesis," *Proc. Natl. Acad. Sci. U. S. A.*, 1976, doi: 10.1073/pnas.73.3.742.

[12]   B. J. Carter, G. Khoury, and J. A. Rose, "Adenovirus-Associated Virus Multiplication IX. Extent of Transcription of the Viral Genome In Vivo," *J. Virol.*, 1972, doi: 10.1128/jvi.10.6.1118-1125.1972.

[13]   E. Hastie and R. J. Samulski, "Adeno-Associated Virus at 50: A Golden Anniversary of Discovery, Research, and Gene Therapy Success - A Personal Perspective," *Hum. Gene Ther.*, vol. 26, no. 5, pp. 257–265, 2015, doi: 10.1089/hum.2015.025.

[14]   D. S. Im and N. Muzyczka, "The AAV origin binding protein Rep68 is an ATP-dependent site-specific endonuclease with DNA helicase activity," *Cell*, 1990, doi: 10.1016/0092-8674(90)90526-K.

[15]   D. S. Im and N. Muzyczka, "Partial purification of adeno-associated virus Rep78, Rep52, and Rep40 and their biochemical characterization," *J. Virol.*, vol. 66, no. 2, pp. 1119–1128, 1992, doi: 10.1128/jvi.66.2.1119-1128.1992.

[16]   M. S. Chapman and M. Agbandje-Mckenna, "Atomic structure of viral particles," in *Parvoviruses*, 2005. doi: 10.1201/b13393-13.

[17]   Q. Xie *et al.*, "The atomic structure of adeno-associated virus (AAV-2), a vector for human gene therapy," *Proc. Natl. Acad. Sci. U. S. A.*, 2002, doi: 10.1073/pnas.162250899.

[18]   S. Bleker, F. Sonntag, and J. A. Kleinschmidt, "Mutational Analysis of Narrow Pores at the Fivefold Symmetry Axes of Adeno-Associated Virus Type 2 Capsids Reveals a Dual Role in Genome Packaging and Activation of Phospholipase A2 Activity," *J. Virol.*, 2005, doi: 10.1128/jvi.79.4.2528-2540.2005.

[19]   A. Girod *et al.*, "The VP1 capsid protein of adeno-associated virus type 2 is carrying a phospholipase A2 domain required for virus infectivity," *J. Gen. Virol.*, 2002, doi: 10.1099/0022-1317-83-5-973.

[20]   J. C. Grieger, J. S. Johnson, B. Gurda-Whitaker, M. Agbandje-McKenna, and R. J. Samulski, "Surface-Exposed Adeno-Associated Virus Vp1-NLS Capsid Fusion Protein Rescues Infectivity of Noninfectious Wild-Type Vp2/Vp3 and Vp3-Only Capsids but Not That of Fivefold Pore Mutant Virions," *J. Virol.*, 2007, doi: 10.1128/jvi.00580-07.

[21]   J. A. Rose, J. V. Maizel, J. K. Inman, and A. J. Shatkin, "Structural Proteins of Adenovirus-Associated Viruses," *J. Virol.*, 1971, doi: 10.1128/jvi.8.5.766-770.1971.

[22]   F. Sonntag, K. Schmidt, and J. A. Kleinschmidt, "A viral assembly factor promotes AAV2 capsid formation in the nucleolus," *Proc. Natl. Acad. Sci. U. S. A.*, vol. 107, no. 22, pp. 10220–10225, 2010, doi:

10.1073/pnas.1001673107.

[23]   P. J. Ogden, E. D. Kelsic, S. Sinai, and G. M. Church, "Comprehensive AAV capsid fitness landscape reveals a viral gene and enables machine-guided design," *Science (80-.).*, 2019, doi: 10.1126/science.aaw2900.

[24]   Z. C. Elmore *et al.*, "The membrane associated accessory protein is an adeno-associated viral egress factor," *Nat. Commun.*, 2021, doi: 10.1038/s41467-021-26485-4.

[25]   M. Cao, H. You, and P. L. Hermonat, "The X gene of Adeno-Associated Virus 2 (AAV2) is involved in viral DNA replication," *PLoS One*, 2014, doi: 10.1371/journal.pone.0104596.

[26]   L. M. Drouin and M. Agbandje-Mckenna, "Adeno-associated virus structural biology as a tool in vector development," *Future Virology*. 2013. doi: 10.2217/fvl.13.112.

[27]   L. Poudel, "Deciphering of Packing Signal Hypothesis in Bacterophage RNA Recognition by the MS2 Capsid Protein in Virus Assembly," University of Missouri, Kansas City, 2018.

[28]   S. Shen, K. D. Bryant, S. M. Brown, S. H. Randell, and A. Asokan, "Terminal n-linked galactose is the primary receptor for adeno-associated virus," *J. Biol. Chem.*, 2011, doi: 10.1074/jbc.M110.210922.

[29]   C. Summerford and R. J. Samulski, "Membrane-Associated Heparan Sulfate Proteoglycan Is a Receptor for Adeno-Associated Virus Type 2 Virions," *J. Virol.*, 1998, doi: 10.1128/jvi.72.2.1438-1445.1998.

[30]   C. Summerford, J. S. Bartlett, and R. J. Samulski, "αVβ5 integrin: A co-receptor for adeno-associated virus type 2 infection," *Nat. Med.*, 1999, doi: 10.1038/4768.

[31]   Y. Kashiwakura *et al.*, "Hepatocyte Growth Factor Receptor Is a Coreceptor for Adeno-Associated Virus Type 2 Infection," *J. Virol.*, 2005, doi: 10.1128/jvi.79.1.609-614.2005.

[32]   A.-M. Douar, K. Poulard, D. Stockholm, and O. Danos, "Intracellular Trafficking of Adeno-Associated Virus Vectors: Routing to the Late Endosomal Compartment and Proteasome Degradation," *J. Virol.*, 2001, doi: 10.1128/jvi.75.4.1824-1833.2001.

[33]   P.-J. Xiao and R. J. Samulski, "Cytoplasmic Trafficking, Endosomal Escape, and Perinuclear Accumulation of Adeno-Associated Virus Type 2 Particles Are Facilitated by Microtubule Network," *J. Virol.*, 2012, doi: 10.1128/jvi.00935-12.

[34]   J. S. Bartlett, R. Wilcher, and R. J. Samulski, "Infectious Entry Pathway of Adeno-Associated Virus and Adeno-Associated Virus Vectors," *J. Virol.*, 2000, doi: 10.1128/jvi.74.6.2777-2785.2000.

[35]   S. Cohen, S. Au, and N. Panté, "How viruses access the nucleus," *Biochimica et Biophysica Acta - Molecular Cell Research*. 2011. doi: 10.1016/j.bbamcr.2010.12.009.

[36]   F. K. Ferrari, T. Samulski, T. Shenk, and R. J. Samulski, "Second-strand synthesis is a rate-limiting step for efficient transduction by recombinant adeno-associated virus vectors," *J. Virol.*, 1996, doi: 10.1128/jvi.70.5.3227-3234.1996.

[37]   A. Ehrhardt, H. Xu, and M. A. Kay, "Episomal Persistence of Recombinant Adenoviral Vector Genomes during the Cell Cycle In Vivo," *J. Virol.*, 2003, doi: 10.1128/jvi.77.13.7689-7695.2003.

[38]   R. M. L. Buller, J. E. Janik, E. D. Sebring, and J. A. Rose, "Herpes Simplex Virus Types 1 and 2 Completely Help Adenovirus-Associated Virus Replication," *J. Virol.*, 1981, doi: 10.1128/jvi.40.1.241-247.1981.

[39]   M.-C. Geoffroy and A. Salvetti, "Helper Functions Required for Wild Type and Recombinant Adeno-Associated Virus Growth," *Curr. Gene Ther.*, 2005, doi: 10.2174/1566523054064977.

[40]   A. Westhaus *et al.*, "High-Throughput in Vitro, Ex Vivo, and in Vivo Screen of Adeno-Associated Virus Vectors Based on Physical and Functional Transduction," *Hum. Gene Ther.*, 2020, doi: 10.1089/hum.2019.264.

[41]   M. Agbandje-McKenna and J. Kleinschmidt, "AAV Capsid Structure and Cell Interactions Adeno-Associated Virus," in *Methods in Molecular Biology*, 2011.

[42]   M. Nonnenmacher and T. Weber, "Intracellular transport of recombinant adeno-associated virus vectors," *Gene Therapy*. 2012. doi: 10.1038/gt.2012.6.

[43]   A. Asokan, D. V. Schaffer, and R. J. Samulski, "The AAV vector toolkit: Poised at the clinical crossroads," *Molecular Therapy*. 2012. doi: 10.1038/mt.2011.287.

[44]   N. L. Meyer and M. S. Chapman, "Adeno-associated virus (AAV) cell entry: structural insights," *Trends in Microbiology*. 2022. doi: 10.1016/j.tim.2021.09.005.

[45]   A. Srivastava, "In vivo tissue-tropism of adeno-associated viral vectors," *Current Opinion in Virology*. 2016. doi: 10.1016/j.coviro.2016.08.003.

[46]   J. D. Esko, K. Kimata, and U. Lindahl, *Proteoglycans and Sulfated Glucosaminoglycans In: Essentials of Glycobiology*. 2009.

[47]   S. Sarrazin, W. C. Lamanna, and J. D. Esko, "Heparan sulfate proteoglycans," *Cold Spring Harb. Perspect. Biol.*, 2011, doi: 10.1101/cshperspect.a004952.

[48]   M. Götte *et al.*, "Role of syndecan-1 in leukocyte-endothelial interactions in the ocular vasculature,"

Investig. Ophthalmol. Vis. Sci., 2002.

[49]   S. Otsuki *et al.*, "Extracellular sulfatases support cartilage homeostasis by regulating BMP and FGF signaling pathways," *Proc. Natl. Acad. Sci. U. S. A.*, 2010, doi: 10.1073/pnas.0913897107.

[50]   H. Lortat-Jacob, "The molecular basis and functional implications of chemokine interactions with heparan sulphate," *Current Opinion in Structural Biology*. 2009. doi: 10.1016/j.sbi.2009.09.003.

[51]   V. Cagno, E. D. Tseligka, S. T. Jones, and C. Tapparel, "Heparan sulfate proteoglycans and viral attachment: True receptors or adaptation bias?," *Viruses*. 2019. doi: 10.3390/v11070596.

[52]   T. Dierker, R. Dreler, A. Petersen, C. Bordych, and K. Grobe, "Heparan sulfate-modulated, metalloprotease-mediated sonic hedgehog release from producing cells," *J. Biol. Chem.*, 2009, doi: 10.1074/jbc.M806838200.

[53]   L. Perabo *et al.*, "Heparan Sulfate Proteoglycan Binding Properties of Adeno-Associated Virus Retargeting Mutants and Consequences for Their In Vivo Tropism," *J. Virol.*, 2006, doi: 10.1128/jvi.00076-06.

[54]   W. Shi and J. S. Bartlett, "RGD inclusion in VP3 provides adeno-associated virus type 2 (AAV2)-based vectors with a heparan sulfate-independent cell entry mechanism," *Mol. Ther.*, vol. 7, no. 4, pp. 515–525, 2003, doi: 10.1016/S1525-0016(03)00042-X.

[55]   A. Kern *et al.*, "Identification of a Heparin-Binding Motif on Adeno-Associated Virus Type 2 Capsids," *J. Virol.*, 2003, doi: 10.1128/jvi.77.20.11072-11081.2003.

[56]   H. C. Levy *et al.*, "Heparin binding induces conformational changes in Adeno-associated virus serotype 2," *J. Struct. Biol.*, 2009, doi: 10.1016/j.jsb.2008.12.002.

[57]   S. R. Opie, K. H. Warrington, M. Agbandje-McKenna, S. Zolotukhin, and N. Muzyczka, "Identification of Amino Acid Residues in the Capsid Proteins of Adeno-Associated Virus Type 2 That Contribute to Heparan Sulfate Proteoglycan Binding," *J. Virol.*, 2003, doi: 10.1128/jvi.77.12.6995-7006.2003.

[58]   C. L. Bell, B. L. Gurda, K. Van Vliet, M. Agbandje-McKenna, and J. M. Wilson, "Identification of the Galactose Binding Domain of the Adeno-Associated Virus Serotype 9 Capsid," *J. Virol.*, 2012, doi: 10.1128/jvi.00448-12.

[59]   L. H. Vandenberghe *et al.*, "AAV9 Targets Cone Photoreceptors in the Nonhuman Primate Retina," *PLoS One*, 2013, doi: 10.1371/journal.pone.0053463.

[60]   B. Akache, D. Grimm, K. Pandey, S. R. Yant, H. Xu, and M. A. Kay, "The 37/67-Kilodalton Laminin Receptor Is a Receptor for Adeno-Associated Virus Serotypes 8, 2, 3, and 9," *J. Virol.*, 2006, doi: 10.1128/jvi.00878-06.

[61]   Z. Wu, E. Miller, M. Agbandje-McKenna, and R. J. Samulski, "α2,3 and α2,6 N-Linked Sialic Acids Facilitate Efficient Binding and Transduction by Adeno-Associated Virus Types 1 and 6," *J. Virol.*, 2006, doi: 10.1128/jvi.00895-06.

[62]   S. Afione, M. A. DiMattia, S. Halder, G. Di Pasquale, M. Agbandje-McKenna, and J. A. Chiorini, "Identification and Mutagenesis of the Adeno-Associated Virus 5 Sialic Acid Binding Region," *J. Virol.*, 2015, doi: 10.1128/jvi.02503-14.

[63]   H. Wässle, "Parallel processing in the mammalian retina," *Nature Reviews Neuroscience*. 2004. doi: 10.1038/nrn1497.

[64]   M. Ptito, M. Bleau, and J. Bouskila, "The Retina: A Window into the Brain," *Cells*, vol. 10, no. 12, p. 3269, Nov. 2021, doi: 10.3390/cells10123269.

[65]   M. Hoon, H. Okawa, L. Della Santina, and R. O. L. Wong, "Functional architecture of the retina: Development and disease," *Progress in Retinal and Eye Research*. 2014. doi: 10.1016/j.preteyeres.2014.06.003.

[66]   A. Reichenbach and A. Bringmann, "Glia of the human retina," *Glia*, 2020, doi: 10.1002/glia.23727.

[67]   A. P. Sampath and F. Rieke, "Selective Transmission of Single Photon Responses by Saturation at the Rod-to-Rod Bipolar Synapse," *Neuron*, 2004, doi: 10.1016/S0896-6273(04)00005-4.

[68]   R. Zhou and R. R. Caspi, "Ocular immune privilege," *F1000 Biology Reports*. 2010. doi: 10.3410/B2-3.

[69]   F. Mazzoni, H. Safa, and S. C. Finnemann, "Understanding photoreceptor outer segment phagocytosis: Use and utility of RPE cells in culture," *Experimental Eye Research*. 2014. doi: 10.1016/j.exer.2014.01.010.

[70]   J. R. Sparrrow, D. Hicks, and C. P. Hamel, "The Retinal Pigment Epithelium in Health and Disease," *Curr. Mol. Med.*, 2010, doi: 10.2174/156652410793937813.

[71]   T. Euler, S. Haverkamp, T. Schubert, and T. Baden, "Retinal bipolar cells: Elementary building blocks of vision," *Nature Reviews Neuroscience*. 2014. doi: 10.1038/nrn3783.

[72]   R. H. Masland, "The Neuronal Organization of the Retina," *Neuron*. 2012. doi: 10.1016/j.neuron.2012.10.002.

[73]   E. Hartveit and M. L. Veruki, "Electrical synapses between AII amacrine cells in the retina: Function and modulation," *Brain Research*. 2012. doi: 10.1016/j.brainres.2012.05.060.

[74]   J. B. Jonas and A. Dichtl, "Evaluation of the retinal nerve fiber layer," *Survey of Ophthalmology*. 1996. doi: 10.1016/S0039-6257(96)80065-8.

[75]   S. J. Clark *et al.*, "Mapping the differential distribution of glycosaminoglycans in the adult human retina, choroid, and sclera," *Investig. Ophthalmol. Vis. Sci.*, 2011, doi: 10.1167/iovs.11-7909.

[76]   N. A. Delamere, "Ciliary Body and Ciliary Epithelium," *Advances in Organ Biology*. 2005. doi: 10.1016/S1569-2590(05)10005-6.

[77]   E. R. Tamm and E. Lütjen-Drecoll, "Ciliary body," *Microscopy Research and Technique*. 1996. doi: 10.1002/(SICI)1097-0029(19960401)33:5<390::AID-JEMT2>3.0.CO;2-S.

[78]   R. D. Whitley and C. P. Moore, "Ocular diagnostic and therapeutic techniques in food animals.," *Vet. Clin. North Am. Large Anim. Pract.*, 1984, doi: 10.1016/s0196-9846(17)30010-1.

[79]   A. Vaajanen, *Expression and Function of Angiotensins in the Regulation of Intraocular Pressure - an Experimental Study*, no. 2. 2009.

[80]   J. C. Youkilis and S. Bassnett, "Single-cell RNA-sequencing analysis of the ciliary epithelium and contiguous tissues in the mouse eye," *Exp. Eye Res.*, 2021, doi: 10.1016/j.exer.2021.108811.

[81]   M. M. Civan and A. D. C. Macknight, "The ins and outs of aqueous humour secretion," *Exp. Eye Res.*, 2004, doi: 10.1016/j.exer.2003.09.021.

[82]   M. Coca-Prados, J. Escribano, and J. Ortego, "Differential gene expression in the human ciliary epithelium," *Progress in Retinal and Eye Research*. 1999. doi: 10.1016/S1350-9462(98)00026-3.

[83]   P. N. Bishop, M. Takanosu, M. Le Goff, and R. Mayne, "The role of the posterior ciliary body in the biosynthesis of vitreous humour," *Eye*, 2002, doi: 10.1038/sj.eye.6700199.

[84]   W. Jones, J. Rodriguez, and S. Bassnett, "Targeted deletion of fibrillin-1 in the mouse eye results in ectopia lentis and other ocular phenotypes associated with Marfan syndrome," *DMM Dis. Model. Mech.*, 2019, doi: 10.1242/dmm.037283.

[85]   S. Bassnett, "Zinn's zonule," *Progress in Retinal and Eye Research*. 2021. doi: 10.1016/j.preteyeres.2020.100902.

[86]   J. G. Cunha-Vaz, "The blood-ocular barriers: Past, present, and future," *Doc. Ophthalmol.*, 1997, doi: 10.1007/BF02569055.

[87]   E. R. Tamm, "The role of the ciliary body in aqueous humor dynamics structural aspects," in *Encyclopedia of the Eye*, 2010. doi: 10.1016/B978-0-12-374203-2.00085-3.

[88]   A. Aspelund *et al.*, "The Schlemm's canal develops from venous endothelium into a VEGF-C / VEGFR-3 responsive lymphatic vessel," *J. Clin. Invest.*, 2014.

[89]   J. Buffault, A. Labbé, P. Hamard, F. Brignole-Baudouin, and C. Baudouin, "The trabecular meshwork: Structure, function and clinical implications. A review of the literature," *Journal francais d'ophtalmologie*. 2020. doi: 10.1016/j.jfo.2020.05.002.

[90]   D. K. Sunderland and A. Sapra, *Physiology, Aqueous Humor Circulation*. 2020.

[91]   S. Veleri, C. H. Lazar, B. Chang, P. A. Sieving, E. Banin, and A. Swaroop, "Biology and therapy of inherited retinal degenerative disease: Insights from mouse models," *DMM Disease Models and Mechanisms*. 2015. doi: 10.1242/dmm.017913.

[92]   E. L. Fletcher, A. I. Jobling, K. A. Vessey, C. Luu, R. H. Guymer, and P. N. Baird, "Animal models of retinal disease," in *Progress in Molecular Biology and Translational Science*, 2011. doi: 10.1016/B978-0-12-384878-9.00006-6.

[93]   G. B. Collin *et al.*, "Mouse models of inherited retinal degeneration with photoreceptor cell loss," *Cells*. 2020. doi: 10.3390/cells9040931.

[94]   A. Moshiri, "Animals Models of Inherited Retinal Disease," *Int. Ophthalmol. Clin.*, 2021, doi: 10.1097/IIO.0000000000000368.

[95]   L. H. Vandenberghe *et al.*, "Dosage thresholds for AAV2 and AAV8 photoreceptor gene therapy in monkey," *Sci. Transl. Med.*, 2011, doi: 10.1126/scitranslmed.3002103.

[96]   J. Gordon, G. Grafton, P. M. Wood, M. Larché, and R. J. Armitage, "Modelling the human immune response: Can mice be trusted?," *Current Opinion in Pharmacology*. 2001. doi: 10.1016/S1471-4892(01)00074-1.

[97]   X. Zhou *et al.*, "A comparative gene expression profile of the whole eye from human, mouse, and guinea pig," *Mol. Vis.*, 2007.

[98]   J. M. Skeie, S. H. Tsang, and V. B. Mahajan, "Evisceration of mouse vitreous and retina for proteomic analyses," *J. Vis. Exp.*, 2011, doi: 10.3791/2795.

[99]   A. Hendrickson, "Organization of the adult primate fovea," in *Macular Degeneration*, 2005. doi:

10.1007/3-540-26977-0_1.

[100]   C. A. Curcio, K. R. Sloan, R. E. Kalina, and A. E. Hendrickson, "Human photoreceptor topography," *J. Comp. Neurol.*, 1990, doi: 10.1002/cne.902920402.

[101]   E. van Beest *et al.*, "A Fovea-Like Representation of Space in Mouse Visual Cortex," *SSRN Electron. J.*, 2019, doi: 10.2139/ssrn.3441090.

[102]   R. S. Molday and O. L. Moritz, "Photoreceptors at a glance," *J. Cell Sci.*, 2015, doi: 10.1242/jcs.175687.

[103]   S. Van Soest, A. Westerveld, P. T. V. M. De Jong, E. M. Bleeker-Wagemakers, and A. A. B. Bergen, "Retinitis pigmentosa: Defined from a molecular point of view," *Surv. Ophthalmol.*, 1999, doi: 10.1016/S0039-6257(98)00046-0.

[104]   S. Nickell, P. S. H. Park, W. Baumeister, and K. Palczewski, "Three-dimensional architecture of murine rod outer segments determined by cryoelectron tomography," *J. Cell Biol.*, 2007, doi: 10.1083/jcb.200612010.

[105]   G. G. Lin and J. G. Scott, *Structure of cone Photoreceptores*, vol. 100, no. 2. 2012. doi: 10.1016/j.preteyeres.2009.05.003.Structure.

[106]   M. M. Giarmarco *et al.*, "Daily mitochondrial dynamics in cone photoreceptors," *Proc. Natl. Acad. Sci. U. S. A.*, 2020, doi: 10.1073/pnas.2007827117.

[107]   J. C. Gilliam *et al.*, "Three-dimensional architecture of the rod sensory cilium and its disruption in retinal neurodegeneration," *Cell*, 2012, doi: 10.1016/j.cell.2012.10.038.

[108]   J. L. Schnapf, T. W. Kraft, and D. A. Baylor, "Spectral sensitivity of human cone photoreceptors," *Nature*, 1987, doi: 10.1038/325439a0.

[109]   T. W. Kraft, D. M. Schneeweis, and J. L. Schnapf, "Visual transduction in human rod photoreceptors.," *J. Physiol.*, 1993, doi: 10.1113/jphysiol.1993.sp019661.

[110]   D. M. Hunt, L. S. Carvalho, J. A. Cowing, and W. L. Davies, "Evolution and spectral tuning of visual pigments in birds and mammals," *Philosophical Transactions of the Royal Society B: Biological Sciences*. 2009. doi: 10.1098/rstb.2009.0044.

[111]   S. S. Nikonov, R. Kholodenko, J. Lem, and E. N. Pugh, "Physiological features of the S- and M-cone photoreceptors of wild-type mice from single-cell recordings," *J. Gen. Physiol.*, 2006, doi: 10.1085/jgp.200609490.

[112]   M. L. Applebury *et al.*, "The murine cone photoreceptor: A single cone type expresses both S and M opsins with retinal spatial patterning," *Neuron*, 2000, doi: 10.1016/S0896-6273(00)00062-3.

[113]   A. Moriondo and G. Rispoli, "A step-by-step model of phototransduction cascade shows that Ca 2+ regulation of guanylate cyclase accounts only for short-term changes of photoresponse," *Photochem. Photobiol. Sci.*, 2003, doi: 10.1039/b303871h.

[114]   S. Michalakis, E. Becirovic, and M. Biel, "Retinal cyclic nucleotide-gated channels: From pathophysiology to therapy," *International Journal of Molecular Sciences*. 2018. doi: 10.3390/ijms19030749.

[115]   K. Palczewski, "Chemistry and biology of the initial steps in vision: the Friedenwald lecture," *Invest. Ophthalmol. Vis. Sci.*, 2014, doi: 10.1167/iovs.14-15502.

[116]   J. B. Hurley, "Phototransduction," in *Encyclopedia of Neuroscience*, 2009. doi: 10.1016/B978-008045046-9.00914-1.

[117]   J. Enoch, L. McDonald, L. Jones, P. R. Jones, and D. P. Crabb, "Evaluating Whether Sight Is the Most Valued Sense," *JAMA Ophthalmol.*, 2019, doi: 10.1001/jamaophthalmol.2019.3537.

[118]   J. H. Lee *et al.*, "Gene therapy for visual loss: Opportunities and concerns," *Progress in Retinal and Eye Research*. 2019. doi: 10.1016/j.preteyeres.2018.08.003.

[119]   M. Hanany, C. Rivolta, and D. Sharon, "Worldwide carrier frequency and genetic prevalence of autosomal recessive inherited retinal diseases," *Proc. Natl. Acad. Sci. U. S. A.*, 2020, doi: 10.1073/pnas.1913179117.

[120]   A. Fahim, "Retinitis pigmentosa: Recent advances and future directions in diagnosis and management," *Current Opinion in Pediatrics*. 2018. doi: 10.1097/MOP.0000000000000690.

[121]   D. T. Hartong, E. L. Berson, and T. P. Dryja, "Retinitis pigmentosa," *Lancet*. 2006. doi: 10.1016/S0140-6736(06)69740-7.

[122]   S. Ferrari, E. Di Iorio, V. Barbaro, D. Ponzin, F. S. Sorrentino, and F. Parmeggiani, "Retinitis Pigmentosa : Genes and Disease Mechanisms," *Curr. Genomics*, 2011.

[123]   N. Hirji, J. Aboshiha, M. Georgiou, J. Bainbridge, and M. Michaelides, "Achromatopsia: clinical features, molecular genetics, animal models and therapeutic options," *Ophthalmic Genetics*. 2018. doi: 10.1080/13816810.2017.1418389.

[124]   S. Kohl *et al.*, "CNGB3 mutations account for 50% of all cases with autosomal recessive achromatopsia," *Eur. J. Hum. Genet.*, 2005, doi: 10.1038/sj.ejhg.5201269.

[125] N. Kumaran *et al.*, "Retinal structure in RPE65-associated retinal dystrophy," *Investig. Ophthalmol. Vis. Sci.*, 2020, doi: 10.1167/iovs.61.4.47.

[126] G. A. R. Gonçalves and R. de M. A. Paiva, "Gene therapy: advances, challenges and perspectives," *Einstein (Sao Paulo, Brazil)*. 2017. doi: 10.1590/S1679-45082017RB4024.

[127] L. M. Occelli *et al.*, "Gene Supplementation Rescues Rod Function and Preserves Photoreceptor and Retinal Morphology in Dogs, Leading the Way Toward Treating Human PDE6A-Retinitis Pigmentosa," *Hum. Gene Ther.*, 2017, doi: 10.1089/hum.2017.155.

[128] W. L. Chew *et al.*, "A multifunctional AAV-CRISPR-Cas9 and its host response," *Nat. Methods*, 2016, doi: 10.1038/nmeth.3993.

[129] N. A. Moore, P. Bracha, R. M. Hussain, N. Morral, and T. A. Ciulla, "Gene therapy for age-related macular degeneration," *Expert Opinion on Biological Therapy*. 2017. doi: 10.1080/14712598.2017.1356817.

[130] J. M. Martinez-Navio *et al.*, "Adeno-Associated Virus Delivery of Anti-HIV Monoclonal Antibodies Can Drive Long-Term Virologic Suppression," *Immunity*, 2019, doi: 10.1016/j.immuni.2019.02.005.

[131] F. Conroy *et al.*, "Chemical engineering of therapeutic siRNAs for allele-specific gene silencing in Huntington's disease models," *Nat. Commun.*, 2022, doi: 10.1038/s41467-022-33061-x.

[132] B. L. Ellis, M. L. Hirsch, J. C. Barker, J. P. Connelly, R. J. Steininger, and M. H. Porteus, "A survey of ex vivo/in vitro transduction efficiency of mammalian primary cells and cell lines with Nine natural adeno-associated virus (AAV1-9) and one engineered adeno-associated virus serotype," *Virology Journal*. 2013. doi: 10.1186/1743-422X-10-74.

[133] J. A. Greig *et al.*, "Determining the Minimally Effective Dose of a Clinical Candidate AAV Vector in a Mouse Model of Crigler-Najjar Syndrome," *Mol. Ther. - Methods Clin. Dev.*, 2018, doi: 10.1016/j.omtm.2018.07.008.

[134] G. S. Omenn, "The proteomes of the human eye, a highly compartmentalized organ," *Proteomics*. 2017. doi: 10.1002/pmic.201600340.

[135] S. Mookherjee *et al.*, "714. Gene Therapy Rescues Cone Function and Viability in an Rp2 Knockout Mouse Model for X-Linked Retinitis Pigmentosa Over a Wide Dose Range and a Broad Therapeutic Time Window," *Mol. Ther.*, 2015, doi: 10.1016/s1525-0016(16)34323-4.

[136] V. Anand, B. Duffy, Z. Yang, N. S. Dejneka, A. M. Maguire, and J. Bennett, "A deviant immune response to viral proteins and transgene product is generated on subretinal administration of adenovirus and adeno-associated virus," *Mol. Ther.*, 2002, doi: 10.1006/mthe.2002.0525.

[137] J. S. Heier *et al.*, "Intravitreous injection of AAV2-sFLT01 in patients with advanced neovascular age-related macular degeneration: a phase 1, open-label trial," *Lancet*, 2017, doi: 10.1016/S0140-6736(17)30979-0.

[138] M. P. Simunovic, K. Xue, J. K. Jolly, and R. E. MacLaren, "Structural and functional recovery following limited iatrogenic macular detachment for retinal gene therapy," *JAMA Ophthalmol.*, 2017, doi: 10.1001/jamaophthalmol.2016.5630.

[139] K. Xue, M. Groppe, A. P. Salvetti, and R. E. MacLaren, "Technique of retinal gene therapy: Delivery of viral vector into the subretinal space," *Eye*, 2017, doi: 10.1038/eye.2017.158.

[140] I. P. Seitz *et al.*, "Superior retinal gene transfer and biodistribution profile of subretinal versus intravitreal delivery of AAV8 in nonhuman primates," *Investig. Ophthalmol. Vis. Sci.*, 2017, doi: 10.1167/iovs.17-22473.

[141] D. Dalkara *et al.*, "Inner limiting membrane barriers to aav-mediated retinal transduction from the vitreous," *Mol. Ther.*, 2009, doi: 10.1038/mt.2009.181.

[142] A. Mullard, "Gene therapies advance towards finish line," *Nat. Rev. Drug Discov.*, vol. 10, no. 10, pp. 719–720, 2011, doi: 10.1038/nrd3572.

[143] F. Salmon, K. Grosios, and H. Petry, "Safety profile of recombinant adeno-associated viral vectors: Focus on alipogene tiparvovec (Glybera®)," *Expert Review of Clinical Pharmacology*. 2014. doi: 10.1586/17512433.2014.852065.

[144] M. Senior, "After Glybera's withdrawal, what's next for gene therapy?," *Nat. Biotechnol.*, vol. 35, no. 6, pp. 491–492, 2017, doi: 10.1038/nbt0617-491.

[145] R. Goswami *et al.*, "Gene therapy leaves a vicious cycle," *Frontiers in Oncology*. 2019. doi: 10.3389/fonc.2019.00297.

[146] C. E. Dunbar, K. A. High, J. K. Joung, D. B. Kohn, K. Ozawa, and M. Sadelain, "Gene therapy comes of age," *Science*. 2018. doi: 10.1126/science.aan4672.

[147] R. S. Anderton and F. L. Mastaglia, "Advances and challenges in developing a therapy for spinal muscular atrophy," *Expert Review of Neurotherapeutics*. 2015. doi: 10.1586/14737175.2015.1059757.

[148] S. Ogino, D. G. B. Leonard, H. Rennert, W. J. Ewens, and R. B. Wilson, "Genetic risk assessment in carrier testing for spinal muscular atrophy," *Am. J. Med. Genet.*, 2002, doi: 10.1002/ajmg.10425.

[149] M. R. Lunn and C. H. Wang, "Spinal muscular atrophy," *The Lancet*. 2008. doi: 10.1016/S0140-6736(08)60921-6.

[150] N. L. Goedeker *et al.*, "Evaluation of rAAVrh74 gene therapy vector seroprevalence by measurement of total binding antibodies in patients with Duchenne muscular dystrophy," *Ther. Adv. Neurol. Disord.*, 2023, doi: 10.1177/17562864221149781.

[151] B. Monteleone and K. Hyland, "Case report: Discovery of 2 gene variants for aromatic L-amino acid decarboxylase deficiency in 2 African American siblings," *BMC Neurol.*, 2020, doi: 10.1186/s12883-019-1596-8.

[152] S. J. Keam, "Eladocagene Exuparvovec: First Approval," *Drugs*, 2022, doi: 10.1007/s40265-022-01775-3.

[153] Y. A. Heo, "Etranacogene Dezaparvovec: First Approval," *Drugs*, 2023, doi: 10.1007/s40265-023-01845-0.

[154] H. A. Blair, "Valoctocogene Roxaparvovec: First Approval," *Drugs*, 2022, doi: 10.1007/s40265-022-01788-y.

[155] L. H. Vandenberghe, J. M. Wilson, and G. Gao, "Tailoring the AAV vector capsid for gene therapy," *Gene Therapy*. 2009. doi: 10.1038/gt.2008.170.

[156] S. J. Chen *et al.*, "Enhancing the utility of adeno-associated virus gene transfer through inducible tissue-specific expression," *Hum. Gene Ther. Methods*, 2013, doi: 10.1089/hgtb.2012.129.

[157] R. Lin *et al.*, "Directed evolution of adeno-associated virus for efficient gene delivery to microglia," *Nat. Methods*, 2022, doi: 10.1038/s41592-022-01547-7.

[158] H. C. Verdera, K. Kuranda, and F. Mingozzi, "AAV Vector Immunogenicity in Humans: A Long Journey to Successful Gene Transfer," *Molecular Therapy*. 2020. doi: 10.1016/j.ymthe.2019.12.010.

[159] D. Wang *et al.*, "A Rationally Engineered Capsid Variant of AAV9 for Systemic CNS-Directed and Peripheral Tissue-Detargeted Gene Delivery in Neonates," *Mol. Ther. - Methods Clin. Dev.*, 2018, doi: 10.1016/j.omtm.2018.03.004.

[160] M. P. Limberis and J. M. Wilson, "Adeno-associated virus serotype 9 vectors transduce murine alveolar and nasal epithelia and can be readministered," *Proc. Natl. Acad. Sci. U. S. A.*, 2006, doi: 10.1073/pnas.0601433103.

[161] Y. Matsuzaki *et al.*, "Intravenous administration of the adeno-associated virus-PHP.B capsid fails to upregulate transduction efficiency in the marmoset brain," *Neurosci. Lett.*, 2018, doi: 10.1016/j.neulet.2017.11.049.

[162] J. Hordeaux, Q. Wang, N. Katz, E. L. Buza, P. Bell, and J. M. Wilson, "The Neurotropic Properties of AAV-PHP.B Are Limited to C57BL/6J Mice," *Molecular Therapy*. 2018. doi: 10.1016/j.ymthe.2018.01.018.

[163] J. E. Hunter, L. Ramos, and J. H. Wolfe, "Viral vectors in the CNS," in *The Curated Reference Collection in Neuroscience and Biobehavioral Psychology*, 2016. doi: 10.1016/B978-0-12-809324-5.02446-9.

[164] P. L. Hermonat, J. G. Quirk, B. M. Bishop, and L. Han, "The packaging capacity of adeno-associated virus (AAV) and the potential for wild-type-plus AAV gene therapy vectors," *FEBS Lett.*, 1997, doi: 10.1016/S0014-5793(97)00311-6.

[165] Z. Jiang and P. A. Dalby, "Challenges in scaling up AAV-based gene therapy manufacturing," *Trends Biotechnol.*, vol. xx, no. xx, pp. 1–14, 2023, doi: 10.1016/j.tibtech.2023.04.002.

[166] A. Iwasaki and R. Medzhitov, "Toll-like receptor control of the adaptive immune responses," *Nature Immunology*. 2004. doi: 10.1038/ni1112.

[167] C. A. Janeway, "Approaching the asymptote? Evolution and revolution in immunology," in *Cold Spring Harbor Symposia on Quantitative Biology*, 1989. doi: 10.1101/sqb.1989.054.01.003.

[168] S. Akira, S. Uematsu, and O. Takeuchi, "Pathogen recognition and innate immunity," *Cell*. 2006. doi: 10.1016/j.cell.2006.02.015.

[169] A. J. Pollard and E. M. Bijker, "A guide to vaccinology: from basic principles to new developments," *Nature Reviews Immunology*. 2021. doi: 10.1038/s41577-020-00479-7.

[170] M. Ghattas, G. Dwivedi, M. Lavertu, and M. G. Alameh, "Vaccine technologies and platforms for infectious diseases: Current progress, challenges, and opportunities," *Vaccines*. 2021. doi: 10.3390/vaccines9121490.

[171] A. Chauveau *et al.*, "Visualization of T Cell Migration in the Spleen Reveals a Network of Perivascular Pathways that Guide Entry into T Zones," *Immunity*, 2020, doi: 10.1016/j.immuni.2020.03.010.

[172] C. G. Vinuesa, M. A. Linterman, D. Yu, and I. C. M. Maclennan, "Follicular Helper T Cells," *Annu. Rev. Immunol.*, 2016, doi: 10.1146/annurev-immunol-041015-055605.

[173] W. Ratajczak, P. Niedźwiedzka-Rystwej, B. Tokarz-Deptuła, and W. Deptuła, "Immunological memory

cells," *Central European Journal of Immunology*. 2018. doi: 10.5114/ceji.2018.77390.

[174] P. Mistry *et al.*, "SARS-CoV-2 Variants, Vaccines, and Host Immunity," *Frontiers in Immunology*. 2022. doi: 10.3389/fimmu.2021.809244.

[175] CDC, "From the Centers for Disease Control and Prevention. Ten great public health achievements--United States, 1900-1999.," *JAMA*, 1999.

[176] I. J. Amanna and M. K. Slifka, "Successful vaccines," in *Current Topics in Microbiology and Immunology*, 2020. doi: 10.1007/82_2018_102.

[177] N. J. Willis, "Edward Jenner and the eradication of smallpox," *Scottish Medical Journal*. 1997. doi: 10.1177/003693309704200407.

[178] T. D. Baker, "W.H.O., The Global Eradication of Smallpox. Final Report of The Global Commission for the Certification of Smallpox Eradication. Geneva, World Health Organization, 1980, 122 pp., Sfr. 11,-.," in *Clio Medica. Acta Academiae Internationalis Historiae Medicinae, Vol. 17*, 1980. doi: 10.1163/9789004418677_071.

[179] M. A. Strassburg, "The global eradication of smallpox," *AJIC Am. J. Infect. Control*, 1982, doi: 10.1016/0196-6553(82)90003-7.

[180] T. W. Mak and M. E. Saunders, "Vaccines and Clinical Immunization," in *The Immune Response*, 2006. doi: 10.1016/b978-012088451-3.50025-9.

[181] World Health Organization, "WHO position on the use of fractional doses – June 2017, addendum to vaccines and vaccination against yellow fever WHO: Position paper – June 2013," *Vaccine*. 2017. doi: 10.1016/j.vaccine.2017.06.087.

[182] B. Sanders, M. Koldijk, and H. Schuitemaker, "Inactivated viral vaccines," in *Vaccine Analysis: Strategies, Principles, and Control*, 2015. doi: 10.1007/978-3-662-45024-6_2.

[183] J. S. Yum *et al.*, "Use of pre-S protein-containing hepatitis B virus surface antigens and a powerful adjuvant to develop an immune therapy for chronic hepatitis B virus infection," *Clin. Vaccine Immunol.*, 2012, doi: 10.1128/CVI.05355-11.

[184] M. E. Pichichero, "Protein carriers of conjugate vaccines," *Hum. Vaccin. Immunother.*, 2013.

[185] WHO, "Diphtheria vaccine: WHO position paper, August 2017 – Recommendations," *Vaccine*. 2018. doi: 10.1016/j.vaccine.2017.08.024.

[186] WHO, "Tetanus vaccines: WHO position paper," *World Heal. Organ.*, 2017.

[187] C. S. Rollier, A. Reyes-Sandoval, M. G. Cottingham, K. Ewer, and A. V. S. Hill, "Viral vectors as vaccine platforms: Deployment in sight," *Curr. Opin. Immunol.*, 2011, doi: 10.1016/j.coi.2011.03.006.

[188] V. Cimica and J. M. Galarza, "Adjuvant formulations for virus-like particle (VLP) based vaccines," *Clinical Immunology*. 2017. doi: 10.1016/j.clim.2017.08.004.

[189] M. O. Mohsen, L. Zha, G. Cabral-Miranda, and M. F. Bachmann, "Major findings and recent advances in virus–like particle (VLP)-based vaccines," *Seminars in Immunology*. 2017. doi: 10.1016/j.smim.2017.08.014.

[190] R. Xu, M. Shi, J. Li, P. Song, and N. Li, "Construction of SARS-CoV-2 Virus-Like Particles by Mammalian Expression System," *Front. Bioeng. Biotechnol.*, 2020, doi: 10.3389/fbioe.2020.00862.

[191] B. Huber, J. W. Wang, R. B. S. Roden, and R. Kirnbauer, "Rg1-vlp and other l2-based, broad-spectrum hpv vaccine candidates," *Journal of Clinical Medicine*. 2021. doi: 10.3390/jcm10051044.

[192] K. S. Corbett *et al.*, "SARS-CoV-2 mRNA vaccine design enabled by prototype pathogen preparedness," *Nature*, 2020, doi: 10.1038/s41586-020-2622-0.

[193] M. N. Uddin and M. A. Roni, "Challenges of storage and stability of mrna-based covid-19 vaccines," *Vaccines*. 2021. doi: 10.3390/vaccines9091033.

[194] W. Ho, M. Gao, F. Li, Z. Li, X. Q. Zhang, and X. Xu, "Next-Generation Vaccines: Nanoparticle-Mediated DNA and mRNA Delivery," *Advanced Healthcare Materials*. 2021. doi: 10.1002/adhm.202001812.

[195] H. Tariq, S. Batool, S. Asif, M. Ali, and B. H. Abbasi, "Virus-Like Particles: Revolutionary Platforms for Developing Vaccines Against Emerging Infectious Diseases," *Frontiers in Microbiology*. 2022. doi: 10.3389/fmicb.2021.790121.

[196] S. Rauch, E. Jasny, K. E. Schmidt, and B. Petsch, "New vaccine technologies to combat outbreak situations," *Frontiers in Immunology*. 2018. doi: 10.3389/fimmu.2018.01963.

[197] M. Jeyanathan, S. Afkhami, F. Smaill, M. S. Miller, B. D. Lichty, and Z. Xing, "Immunological considerations for COVID-19 vaccine strategies," *Nature Reviews Immunology*. 2020. doi: 10.1038/s41577-020-00434-6.

[198] W. C. Koff and T. Schenkelberg, "The future of vaccine development," *Vaccine*, 2020, doi: 10.1016/j.vaccine.2019.07.101.

[199] J. Trimpert *et al.*, "Development of safe and highly protective live-attenuated SARS-CoV-2 vaccine

candidates by genome recoding," *Cell Rep.*, 2021, doi: 10.1016/j.celrep.2021.109493.

[200] Y. Wang *et al.*, "Scalable live-attenuated SARS-CoV-2 vaccine candidate demonstrates preclinical safety and efficacy," *Proceedings of the National Academy of Sciences of the United States of America*. 2021. doi: 10.1073/pnas.2102775118.

[201] Y. Zhang *et al.*, "Safety, tolerability, and immunogenicity of an inactivated SARS-CoV-2 vaccine in healthy adults aged 18–59 years: a randomised, double-blind, placebo-controlled, phase 1/2 clinical trial," *Lancet Infect. Dis.*, 2021, doi: 10.1016/S1473-3099(20)30843-4.

[202] S. Xia *et al.*, "Safety and immunogenicity of an inactivated SARS-CoV-2 vaccine, BBIBP-CorV: a randomised, double-blind, placebo-controlled, phase 1/2 trial," *Lancet Infect. Dis.*, 2021, doi: 10.1016/S1473-3099(20)30831-8.

[203] P. M. Folegatti *et al.*, "Safety and immunogenicity of the ChAdOx1 nCoV-19 vaccine against SARS-CoV-2: a preliminary report of a phase 1/2, single-blind, randomised controlled trial," *Lancet*, 2020, doi: 10.1016/S0140-6736(20)31604-4.

[204] J. Sadoff *et al.*, "Interim Results of a Phase 1–2a Trial of Ad26.COV2.S Covid-19 Vaccine," *N. Engl. J. Med.*, 2021, doi: 10.1056/nejmoa2034201.

[205] P. G. Kremsner *et al.*, "Safety and immunogenicity of an mRNA-lipid nanoparticle vaccine candidate against SARS-CoV-2: A phase 1 randomized clinical trial," *Wien. Klin. Wochenschr.*, 2021, doi: 10.1007/s00508-021-01922-y.

[206] F. P. Polack *et al.*, "Safety and Efficacy of the BNT162b2 mRNA Covid-19 Vaccine," *N. Engl. J. Med.*, 2020, doi: 10.1056/nejmoa2034577.

[207] N. Zhu *et al.*, "A Novel Coronavirus from Patients with Pneumonia in China, 2019," *N. Engl. J. Med.*, 2020, doi: 10.1056/nejmoa2001017.

[208] B. Hu, H. Guo, P. Zhou, and Z. L. Shi, "Characteristics of SARS-CoV-2 and COVID-19," *Nature Reviews Microbiology*. 2021. doi: 10.1038/s41579-020-00459-7.

[209] M. K. Looi, "How are covid-19 symptoms changing?," *BMJ*. 2023. doi: 10.1136/bmj.p3.

[210] G. Zhu, C. Zhu, Y. Zhu, and F. Sun, "Minireview of progress in the structural study of SARS-CoV-2 proteins," *Current Research in Microbial Sciences*. 2020. doi: 10.1016/j.crmicr.2020.06.003.

[211] L. Chen *et al.*, "RNA based mNGS approach identifies a novel human coronavirus from two individual pneumonia cases in 2019 Wuhan outbreak," *Emerg. Microbes Infect.*, 2020, doi: 10.1080/22221751.2020.1725399.

[212] T. C. Marcink *et al.*, "Intermediates in SARS-CoV-2 spike-mediated cell entry," *Sci. Adv.*, 2022, doi: 10.1126/sciadv.abo3153.

[213] M. Hoffmann, H. Kleine-Weber, and S. Pöhlmann, "A Multibasic Cleavage Site in the Spike Protein of SARS-CoV-2 Is Essential for Infection of Human Lung Cells," *Mol. Cell*, 2020, doi: 10.1016/j.molcel.2020.04.022.

[214] J. Zhang, T. Xiao, Y. Cai, and B. Chen, "Structure of SARS-CoV-2 spike protein," *Current Opinion in Virology*. 2021. doi: 10.1016/j.coviro.2021.08.010.

[215] A. R. Fehr and S. Perlman, "Coronaviruses: An overview of their replication and pathogenesis," in *Coronaviruses: Methods and Protocols*, 2015. doi: 10.1007/978-1-4939-2438-7_1.

[216] A. Bayati, R. Kumar, V. Francis, and P. S. McPherson, "SARS-CoV-2 infects cells after viral entry via clathrin-mediated endocytosis," *Journal of Biological Chemistry*. 2021. doi: 10.1016/j.jbc.2021.100306.

[217] W. Li *et al.*, "Angiotensin-converting enzyme 2 is a functional receptor for the SARS coronavirus," *Nature*, 2003, doi: 10.1038/nature02145.

[218] L. Piccoli *et al.*, "Mapping Neutralizing and Immunodominant Sites on the SARS-CoV-2 Spike Receptor-Binding Domain by Structure-Guided High-Resolution Serology," *Cell*, 2020, doi: 10.1016/j.cell.2020.09.037.

[219] M. T. Finkelstein, A. G. Mermelstein, E. P. Miller, P. C. Seth, E. S. D. Stancofski, and D. Fera, "Structural analysis of neutralizing epitopes of the sars-cov-2 spike to guide therapy and vaccine design strategies," *Viruses*. 2021. doi: 10.3390/v13010134.

[220] D. G. Gibson, L. Young, R. Y. Chuang, J. C. Venter, C. A. Hutchison, and H. O. Smith, "Enzymatic assembly of DNA molecules up to several hundred kilobases," *Nat. Methods*, 2009, doi: 10.1038/nmeth.1318.

[221] D. G. Gibson, "Enzymatic assembly of overlapping DNA fragments," in *Methods in Enzymology*, 2011. doi: 10.1016/B978-0-12-385120-8.00015-2.

[222] A. Girod *et al.*, "Genetic capsid modifications allow efficient re-targeting of adeno- associated virus type 2," *Nat. Med.*, vol. 5, no. 9, pp. 1052–1056, Sep. 1999, doi: 10.1038/12491.

[223] S. A. Nicklin *et al.*, "Efficient and selective AAV2-mediated gene transfer directed to human vascular endothelial cells," *Mol. Ther.*, 2001, doi: 10.1006/mthe.2001.0424.

[224]   J. Mateus *et al.*, "Selective and cross-reactive SARS-CoV-2 T cell epitopes in unexposed humans," *Science (80-.).*, 2020, doi: 10.1126/science.abd3871.

[225]   M. Pavlou *et al.*, "Novel AAV capsids for intravitreal gene therapy of photoreceptor disorders," *EMBO Mol. Med.*, 2021, doi: 10.15252/emmm.202013392.

[226]   M. Völkner, M. Pavlou, H. Büning, S. Michalakis, and M. O. Karl, "Optimized adeno-associated virus vectors for efficient transduction of human retinal organoids," *Hum. Gene Ther.*, 2021, doi: 10.1089/hum.2020.321.

[227]   E. E. Capowski *et al.*, "Reproducibility and staging of 3D human retinal organoids across multiple pluripotent stem cell lines," *Dev.*, 2019, doi: 10.1242/dev.171686.

[228]   E. Becirovic *et al.*, "AAV vectors for FRET-based analysis of protein-protein interactions in photoreceptor outer segments," *Front. Neurosci.*, 2016, doi: 10.3389/fnins.2016.00356.

[229]   U. T. Hacker *et al.*, "Adeno-associated virus serotypes 1 to 5 mediated tumor cell directed gene transfer and improvement of transduction efficiency," *J. Gene Med.*, 2005, doi: 10.1002/jgm.782.

[230]   C. Aurnhammer *et al.*, "Universal real-time PCR for the detection and quantification of adeno-associated virus serotype 2-derived inverted terminal repeat sequences," *Hum. Gene Ther. Methods*, 2012, doi: 10.1089/hgtb.2011.034.

[231]   S. D'Costa *et al.*, "Practical utilization of recombinant AAV vector reference standards: focus on vector genomes titration by free ITR qPCR," *Mol. Ther. - Methods Clin. Dev.*, vol. 3, no. January, p. 16019, 2016, doi: 10.1038/mtm.2016.19.

[232]   R. Rieser *et al.*, "Intrinsic Differential Scanning Fluorimetry for Fast and Easy Identification of Adeno-Associated Virus Serotypes," *J. Pharm. Sci.*, 2020, doi: 10.1016/j.xphs.2019.10.031.

[233]   D. Breitsprecher, N. Glücklich, A. Hawe, and T. Menzen, "Thermal Unfolding of Antibodies Comparison of nanoDSF and µDSC for Thermal Stability Assessment During Biopharmaceutical Formulation Development," *Nanotemper Appl. Note*, 2016.

[234]   L. Martin, M. Maschberger, and D. Breitsprecher, "Thermal unfolding of antibodies with the Prometheus NT.48," *BioTechniques*. 2015. doi: 10.2144/000114347.

[235]   C. Schön *et al.*, "Long-Term In Vivo Imaging of Fibrillar Tau in the Retina of P301S Transgenic Mice," *PLoS One*, 2012, doi: 10.1371/journal.pone.0053547.

[236]   C. Schön *et al.*, "Loss of HCN1 enhances disease progression in mouse models of CNG channel-linked retinitis pigmentosa and achromatopsia," *Hum. Mol. Genet.*, 2015, doi: 10.1093/hmg/ddv639.

[237]   J. Schindelin *et al.*, "Fiji: An open-source platform for biological-image analysis," *Nature Methods*. 2012. doi: 10.1038/nmeth.2019.

[238]   M. Baek *et al.*, "Accurate prediction of protein structures and interactions using a three-track neural network," *Science (80-.).*, 2021, doi: 10.1126/science.abj8754.

[239]   K. L. Gardiner *et al.*, "Long-Term Structural Outcomes of Late-Stage RPE65 Gene Therapy," *Mol. Ther.*, 2020, doi: 10.1016/j.ymthe.2019.08.013.

[240]   J. W. B. Bainbridge *et al.*, "Long-Term Effect of Gene Therapy on Leber's Congenital Amaurosis," *N. Engl. J. Med.*, vol. 372, no. 20, pp. 1887–1897, 2015, doi: 10.1056/nejmoa1414221.

[241]   R. Calcedo, L. H. Vandenberghe, G. Gao, J. Lin, and J. M. Wilson, "Worldwide epidemiology of neutralizing antibodies to adeno-associated viruses," *J. Infect. Dis.*, 2009, doi: 10.1086/595830.

[242]   G. Gao *et al.*, "Gao et al-2004-J Virol," *J. Virol.*, 2004.

[243]   C. N. Cearley, L. H. Vandenberghe, M. K. Parente, E. R. Carnish, J. M. Wilson, and J. H. Wolfe, "Expanded repertoire of AAV vector serotypes mediate unique patterns of transduction in mouse brain," *Mol. Ther.*, 2008, doi: 10.1038/mt.2008.166.

[244]   S. Boutin *et al.*, "Prevalence of serum IgG and neutralizing factors against adeno-associated virus (AAV) types 1, 2, 5, 6, 8, and 9 in the healthy population: Implications for gene therapy using AAV vectors," *Hum. Gene Ther.*, 2010, doi: 10.1089/hum.2009.182.

[245]   N. Chirmule, K. J. Propert, S. A. Magosin, Y. Qian, R. Qian, and J. M. Wilson, "Immune responses to adenovirus and adeno-associated virus in humans," *Gene Ther.*, 1999, doi: 10.1038/sj.gt.3300994.

[246]   D. Liu, M. Zhu, Y. Zhang, and Y. Diao, "Crossing the blood-brain barrier with AAV vectors," *Metab. Brain Dis.*, vol. 36, no. 1, pp. 45–52, 2021, doi: 10.1007/s11011-020-00630-2.

[247]   K. Bey *et al.*, "Efficient CNS targeting in adult mice by intrathecal infusion of single-stranded AAV9-GFP for gene therapy of neurological disorders," *Gene Ther.*, vol. 24, no. 5, pp. 325–332, 2017, doi: 10.1038/gt.2017.18.

[248]   K. T. Woodard, K. J. Liang, W. C. Bennett, and R. J. Samulski, "Heparan Sulfate Binding Promotes Accumulation of Intravitreally Delivered Adeno-associated Viral Vectors at the Retina for Enhanced Transduction but Weakly Influences Tropism," *J. Virol.*, 2016, doi: 10.1128/jvi.01568-16.

[249]   L. Perabo *et al.*, "In vitro selection of viral vectors with modified tropism: The adeno-associated virus display," *Mol. Ther.*, 2003, doi: 10.1016/S1525-0016(03)00123-0.

[250]   L. Perabo *et al.*, "Combinatorial engineering of a gene therapy vector: Directed evolution of adeno-associated virus," *J. Gene Med.*, 2006, doi: 10.1002/jgm.849.

[251]   C. L. Bell *et al.*, "The AAV9 receptor and its modification to improve in vivo lung gene transfer in mice," *J. Clin. Invest.*, 2011, doi: 10.1172/JCI57367.

[252]   C.-L. Chen *et al.*, "Molecular Characterization of Adeno-Associated Viruses Infecting Children," *J. Virol.*, 2005, doi: 10.1128/jvi.79.23.14781-14792.2005.

[253]   A. Bennett *et al.*, "Thermal Stability as a Determinant of AAV Serotype Identity," *Mol. Ther. - Methods Clin. Dev.*, 2017, doi: 10.1016/j.omtm.2017.07.003.

[254]   S. Pacouret *et al.*, "AAV-ID: A Rapid and Robust Assay for Batch-to-Batch Consistency Evaluation of AAV Preparations," *Mol. Ther.*, 2017, doi: 10.1016/j.ymthe.2017.04.001.

[255]   N. W. Keiser, Z. Yan, Y. Zhang, D. C. M. Lei-Butters, and J. F. Engelhardt, "Unique characteristics of AAV1, 2, and 5 viral entry, intracellular trafficking, and nuclear import define transduction efficiency in HeLa cells," *Hum. Gene Ther.*, 2011, doi: 10.1089/hum.2011.044.

[256]   T. K. MacLachlan *et al.*, "Preclinical safety evaluation of AAV2-sFLT01 a gene therapy for age-related macular degeneration," *Mol. Ther.*, 2011, doi: 10.1038/mt.2010.258.

[257]   C. Cukras *et al.*, "Retinal AAV8-RS1 Gene Therapy for X-Linked Retinoschisis: Initial Findings from a Phase I/IIa Trial by Intravitreal Delivery," *Mol. Ther.*, 2018, doi: 10.1016/j.ymthe.2018.05.025.

[258]   G. P. Lewis and S. K. Fisher, "Up-Regulation of Glial Fibrillary Acidic Protein in Response to Retinal Injury: Its Potential Role in Glial Remodeling and a Comparison to Vimentin Expression," *Int. Rev. Cytol.*, 2003, doi: 10.1016/S0074-7696(03)30005-1.

[259]   A. Bringmann *et al.*, "Cellular signaling and factors involved in Müller cell gliosis: Neuroprotective and detrimental effects," *Progress in Retinal and Eye Research*. 2009. doi: 10.1016/j.preteyeres.2009.07.001.

[260]   P. Ekstrom, S. Sanyal, K. Narfstrom, G. J. Chader, and T. Van Veen, "Accumulation of glial fibrillary acidic protein in Muller radial glia during retinal degeneration," *Investig. Ophthalmol. Vis. Sci.*, 1988.

[261]   A. Bringmann *et al.*, "Müller cells in the healthy and diseased retina," *Progress in Retinal and Eye Research*. 2006. doi: 10.1016/j.preteyeres.2006.05.003.

[262]   V. Dinet *et al.*, "Distinct effects of inflammation on gliosis, osmohomeostasis, and vascular integrity during amyloid beta-induced retinal degeneration," *Aging Cell*, 2012, doi: 10.1111/j.1474-9726.2012.00834.x.

[263]   G. P. Lewis, E. A. Chapin, G. Luna, K. A. Linberg, and S. K. Fisher, "The fate of müller's glia following experimental retinal detachment: Nuclear migration, cell division, and subretinal glial scar formation," *Mol. Vis.*, 2010.

[264]   R. Kinouchi *et al.*, "Robust neural integration from retinal transplants in mice deficient in GFAP and vimentin," *Nat. Neurosci.*, 2003, doi: 10.1038/nn1088.

[265]   F. W. Newell, "Histology of the Human Eye. An Atlas and Textbook," *Am. J. Ophthalmol.*, 1972, doi: 10.1016/0002-9394(72)90324-8.

[266]   G. K. Smelser, "Electron microscopy of a typical epithelial cell and of the normal human ciliary process.," *Trans. - Am. Acad. Ophthalmol. Otolaryngol.*, 1966.

[267]   A. S. Borges- Giampani and J. Giampani, "Anatomy of Ciliary Body, Ciliary Processes, Anterior Chamber Angle and Collector Vessels," in *Glaucoma - Basic and Clinical Aspects*, 2013. doi: 10.5772/52780.

[268]   T. F. Freddo, "Die Rolle des Ziliarkörpers bei der Bildung des Kammerwassers," *Optom. Contact Lenses*, 2022, doi: 10.54352/dozv.wgkr7755.

[269]   B. D. Dufour and J. L. McBride, "Intravascular AAV9 administration for delivering RNA silencing constructs to the CNS and periphery," in *Methods in Molecular Biology*, 2016, pp. 261–275. doi: 10.1007/978-1-4939-3112-5_21.

[270]   K. D. Foust, E. Nurre, C. L. Montgomery, A. Hernandez, C. M. Chan, and B. K. Kaspar, "Intravascular AAV9 preferentially targets neonatal neurons and adult astrocytes," *Nat. Biotechnol.*, vol. 27, no. 1, pp. 59–65, 2009, doi: 10.1038/nbt.1515.

[271]   B. Lei, K. Zhang, Y. Yue, A. Ghosh, and D. Duan, "Adeno-Associated virus serotype-9 mediated retinal outer plexiform layer transduction is mainly through the photoreceptors," in *Advances in Experimental Medicine and Biology*, 2010. doi: 10.1007/978-1-4419-1399-9_77.

[272]   A.-P. Bemelmans, S. Duqué, C. Rivière, S. Astord, and M. Desrosiers, "A Single Intravenous AAV9 Injection Mediates Bilateral Gene Transfer to the Adult Mouse Retina," *PLoS One*, vol. 8, no. 4, p. 61618, 2013, doi: 10.1371/journal.pone.0061618.

[273]   J. Shang *et al.*, "Structural basis of receptor recognition by SARS-CoV-2," *Nature*, 2020, doi: 10.1038/s41586-020-2179-y.

[274]   A. C. Walls, Y. J. Park, M. A. Tortorici, A. Wall, A. T. McGuire, and D. Veesler, "Erratum: Structure, Function, and Antigenicity of the SARS-CoV-2 Spike Glycoprotein (Cell (2020) 181(2) (281–292.e6), (S0092867420302622), (10.1016/j.cell.2020.02.058))," *Cell*. 2020. doi: 10.1016/j.cell.2020.11.032.

[275]   J. Lan *et al.*, "Structure of the SARS-CoV-2 spike receptor-binding domain bound to the ACE2 receptor," *Nature*, 2020, doi: 10.1038/s41586-020-2180-5.

[276]   Q. Wang *et al.*, "Structural and Functional Basis of SARS-CoV-2 Entry by Using Human ACE2," *Cell*, 2020, doi: 10.1016/j.cell.2020.03.045.

[277]   C. B. Jackson, M. Farzan, B. Chen, and H. Choe, "Mechanisms of SARS-CoV-2 entry into cells," *Nat. Rev. Mol. Cell Biol.*, vol. 23, no. 1, pp. 3–20, 2022, doi: 10.1038/s41580-021-00418-x.

[278]   M. H. Wilson, C. J. Coates, and A. L. George, "PiggyBac transposon-mediated gene transfer in human cells," *Mol. Ther.*, 2007, doi: 10.1038/sj.mt.6300028.

[279]   J. Weber, H. Peng, and C. Rader, "From rabbit antibody repertoires to rabbit monoclonal antibodies," *Experimental and Molecular Medicine*. 2017. doi: 10.1038/emm.2017.23.

[280]   B. V. Ayyar, S. Hearty, and R. O'Kennedy, "Facile domain rearrangement abrogates expression recalcitrance in a rabbit scFv," *Appl. Microbiol. Biotechnol.*, 2015, doi: 10.1007/s00253-014-6268-4.

[281]   A. Frey, J. Di Canzio, and D. Zurakowski, "A statistically defined endpoint titer determination method for immunoassays," *J. Immunol. Methods*, 1998, doi: 10.1016/S0022-1759(98)00170-7.

[282]   C. Lebherz, A. Maguire, W. Tang, J. Bennett, and J. M. Wilson, "Novel AAV serotypes for improved ocular gene transfer," *J. Gene Med.*, 2008, doi: 10.1002/jgm.1126.

[283]   S. Russell *et al.*, "Efficacy and safety of voretigene neparvovec (AAV2-hRPE65v2) in patients with RPE65-mediated inherited retinal dystrophy: a randomised, controlled, open-label, phase 3 trial," *Lancet*, 2017, doi: 10.1016/S0140-6736(17)31868-8.

[284]   J. Cehajic-Kapetanovic *et al.*, "Initial results from a first-in-human gene therapy trial on X-linked retinitis pigmentosa caused by mutations in RPGR," *Nature Medicine*. 2020. doi: 10.1038/s41591-020-0763-1.

[285]   M. D. Fischer *et al.*, "Safety and Vision Outcomes of Subretinal Gene Therapy Targeting Cone Photoreceptors in Achromatopsia: A Nonrandomized Controlled Trial," *JAMA Ophthalmol.*, 2020, doi: 10.1001/jamaophthalmol.2020.1032.

[286]   F. M. Mowat *et al.*, "Tyrosine capsid-mutant AAV vectors for gene delivery to the canine retina from a subretinal or intravitreal approach," *Gene Ther.*, 2014, doi: 10.1038/gt.2013.64.

[287]   Y. Mao *et al.*, "Single point mutation in adeno-associated viral vectors -DJ capsid leads to improvement for gene delivery in vivo," *BMC Biotechnol.*, 2016, doi: 10.1186/s12896-015-0230-0.

[288]   G. Yiu *et al.*, "Suprachoroidal and Subretinal Injections of AAV Using Transscleral Microneedles for Retinal Gene Delivery in Nonhuman Primates," *Mol. Ther. - Methods Clin. Dev.*, 2020, doi: 10.1016/j.omtm.2020.01.002.

[289]   B. E. Deverman *et al.*, "Cre-dependent selection yields AAV variants for widespread gene transfer to the adult brain," *Nat. Biotechnol.*, 2016, doi: 10.1038/nbt.3440.

[290]   M. A. Kotterman, L. Yin, J. M. Strazzeri, J. G. Flannery, W. H. Merigan, and D. V. Schaffer, "Antibody neutralization poses a barrier to intravitreal adeno-associated viral vector gene delivery to non-human primates," *Gene Ther.*, 2015, doi: 10.1038/gt.2014.115.

[291]   Q. Li *et al.*, "Intraocular route of AAV2 vector administration defines humoral immune response and therapeutic potential," *Mol. Vis.*, 2008.

[292]   J. W. Miller and L. H. Vandenberghe, "Breaking and Sealing Barriers in Retinal Gene Therapy," *Molecular Therapy*. 2018. doi: 10.1016/j.ymthe.2018.08.003.

[293]   Z. Wu, A. Asokan, J. C. Grieger, L. Govindasamy, M. Agbandje-McKenna, and R. J. Samulski, "Single Amino Acid Changes Can Influence Titer, Heparin Binding, and Tissue Tropism in Different Adeno-Associated Virus Serotypes," *J. Virol.*, 2006, doi: 10.1128/jvi.01288-06.

[294]   B. Mary, S. Maurya, S. Arumugam, V. Kumar, and G. R. Jayandharan, "Post-translational modifications in capsid proteins of recombinant adeno-associated virus (AAV) 1-rh10 serotypes," *FEBS J.*, 2019, doi: 10.1111/febs.15013.

[295]   R. Mahajan, C. Delphin, T. Guan, L. Gerace, and F. Melchior, "A small ubiquitin-related polypeptide involved in targeting RanGAP1 to nuclear pore complex protein RanBP2," *Cell*, 1997, doi: 10.1016/S0092-8674(00)81862-0.

[296]   A. M. Weissman, "Themes and variations on ubiquitylation," *Nature Reviews Molecular Cell Biology*. 2001. doi: 10.1038/35056563.

[297]   I. Lamsoul *et al.*, "Exclusive Ubiquitination and Sumoylation on Overlapping Lysine Residues Mediate

NF-κB Activation by the Human T-Cell Leukemia VirusTax Oncoprotein," *Mol. Cell. Biol.*, 2005, doi: 10.1128/mcb.25.23.10391-10406.2005.

[298] C. Hölscher *et al.*, "The SUMOylation Pathway Restricts Gene Transduction by Adeno-Associated Viruses," *PLoS Pathog.*, 2015, doi: 10.1371/journal.ppat.1005281.

[299] K. Gao *et al.*, "Empty virions in AAV8 vector preparations reduce transduction efficiency and may cause total viral particle dose-limiting side effects," *Mol. Ther. - Methods Clin. Dev.*, 2014, doi: 10.1038/mtm.2013.9.

[300] X. Pei *et al.*, "Efficient capsid antigen presentation from adeno-associated virus empty virions in vivo," *Front. Immunol.*, 2018, doi: 10.3389/fimmu.2018.00844.

[301] A. Bennett, M. Mietzsch, and M. Agbandje-Mckenna, "Understanding capsid assembly and genome packaging for adeno-associated viruses," *Future Virology*. 2017. doi: 10.2217/fvl-2017-0011.

[302] E. D. Horowitz *et al.*, "Biophysical and Ultrastructural Characterization of Adeno-Associated Virus Capsid Uncoating and Genome Release," *J. Virol.*, 2013, doi: 10.1128/jvi.03017-12.

[303] R. L. Klein, R. D. Dayton, J. B. Tatom, K. M. Henderson, and P. P. Henning, "AAV8, 9, Rh10, Rh43 vector gene transfer in the rat brain: Effects of serotype, promoter and purification method," *Mol. Ther.*, 2008, doi: 10.1038/sj.mt.6300331.

[304] S. A. Nass *et al.*, "Universal Method for the Purification of Recombinant AAV Vectors of Differing Serotypes," *Mol. Ther. - Methods Clin. Dev.*, 2018, doi: 10.1016/j.omtm.2017.12.004.

[305] S. Shen *et al.*, "Engraftment of a galactose receptor footprint onto adeno-associated viral capsids improves transduction efficiency," *J. Biol. Chem.*, 2013, doi: 10.1074/jbc.M113.482380.

[306] S. Michelfelder *et al.*, "Successful expansion but not complete restriction of tropism of adeno-associated virus by in vivo biopanning of random virus display peptide libraries," *PLoS One*, 2009, doi: 10.1371/journal.pone.0005122.

[307] E. Simpson, "A historical perspective on immunological privilege," *Immunological Reviews*. 2006. doi: 10.1111/j.1600-065X.2006.00434.x.

[308] J. W. Streilein, "Ocular immune privilege: the eye takes a dim but practical view of immunity and inflammation," *J. Leukoc. Biol.*, 2003, doi: 10.1189/jlb.1102574.

[309] K. Xue *et al.*, "Beneficial effects on vision in patients undergoing retinal gene therapy for choroideremia," *Nat. Med.*, 2018, doi: 10.1038/s41591-018-0185-5.

[310] S. H. Chung *et al.*, "Host immune responses after suprachoroidal delivery of AAV8 in nonhuman primate eyes," *Hum. Gene Ther.*, 2021, doi: 10.1089/hum.2020.281.

[311] Y. K. Chan, A. D. Dick, S. M. Hall, T. Langmann, C. L. Scribner, and B. C. Mansfield, "Inflammation in viral vector-mediated ocular gene therapy: A review and report from a workshop hosted by the foundation fighting blindness, 9/2020," *Transl. Vis. Sci. Technol.*, 2021, doi: 10.1167/tvst.10.4.3.

[312] F. F. Reichel *et al.*, "Humoral immune response after intravitreal but not after subretinal aav8 in primates and patients," *Investig. Ophthalmol. Vis. Sci.*, 2018, doi: 10.1167/iovs.17-22494.

[313] S. Michalakis, H. Geiger, S. Haverkamp, F. Hofmann, A. Gerstner, and M. Biel, "Impaired opsin targeting and cone photoreceptor migration in the retina of mice lacking the cyclic nucleotide-gated channel CNGA3," *Investig. Ophthalmol. Vis. Sci.*, 2005, doi: 10.1167/iovs.04-1503.

[314] H. Wenkel and J. Wayne Streilein, "Analysis of immune deviation elicited by antigens injected into the subretinal space," *Investig. Ophthalmol. Vis. Sci.*, 1998.

[315] L. Dudus *et al.*, "Persistent transgene product in retina, optic nerve and brain after intraocular injection of rAAV," *Vision Res.*, 1999, doi: 10.1016/S0042-6989(98)00308-3.

[316] D. M. Markusic *et al.*, "Evaluation of engineered AAV capsids for hepatic factor IX gene transfer in murine and canine models," *J. Transl. Med.*, 2017, doi: 10.1186/s12967-017-1200-1.

[317] D. Xu *et al.*, "Chimeric TK-NOG mice: A predictive model for cholestatic human liver toxicity," *J. Pharmacol. Exp. Ther.*, 2015, doi: 10.1124/jpet.114.220798.

[318] M. Fradot *et al.*, "Gene therapy in ophthalmology: Validation on cultured retinal cells and explants from postmortem human eyes," *Hum. Gene Ther.*, 2011, doi: 10.1089/hum.2010.157.

[319] N. K. Paulk *et al.*, "Bioengineered AAV Capsids with Combined High Human Liver Transduction In Vivo and Unique Humoral Seroreactivity," *Mol. Ther.*, 2018, doi: 10.1016/j.ymthe.2017.09.021.

[320] L. Lisowski *et al.*, "Selection and evaluation of clinically relevant AAV variants in a xenograft liver model," *Nature*, 2014, doi: 10.1038/nature12875.

[321] A. Farokhfar, A. Ahmadzadeh-Amiri, M. R. Sheikhrezaee, M. A. H. Gorji, and N. Agaei, "Common causes of eye enucleation among patients," *J. Nat. Sci. Biol. Med.*, 2017, doi: 10.4103/0976-9668.210006.

[322] M. Garita-Hernandez *et al.*, "AAV-mediated gene delivery to 3D retinal organoids derived from human induced pluripotent stem cells," *Int. J. Mol. Sci.*, 2020, doi: 10.3390/ijms21030994.

[323] M. E. McClements *et al.*, "Tropism of AAV Vectors in Photoreceptor-Like Cells of Human iPSC-Derived Retinal Organoids," *Transl. Vis. Sci. Technol.*, 2022, doi: 10.1167/tvst.11.4.3.

[324] H. R. L. Napier and S. H. Kidson, "Proliferation and cell shape changes during ciliary body morphogenesis in the mouse," *Dev. Dyn.*, 2005, doi: 10.1002/dvdy.20302.

[325] Y. C. Tham, X. Li, T. Y. Wong, H. A. Quigley, T. Aung, and C. Y. Cheng, "Global Prevalence of Glaucoma and Projections of Glaucoma Burden through 2040: A Systematic Review and Meta-Analysis," *Ophthalmology*, vol. 121, no. 11, pp. 2081–2090, Nov. 2014, doi: 10.1016/J.OPHTHA.2014.05.013.

[326] A. W. Hewitt, J. E. Craig, and D. A. Mackey, "Complex genetics of complex traits: The case of primary open-angle glaucoma," *Clinical and Experimental Ophthalmology*. 2006. doi: 10.1111/j.1442-9071.2006.01268.x.

[327] R. T. Libby, D. B. Gould, M. G. Anderson, and S. W. M. John, "Complex genetics of glaucoma susceptibility," *Annual Review of Genomics and Human Genetics*. 2005. doi: 10.1146/annurev.genom.6.080604.162209.

[328] R. R. Allingham, Y. Liu, and D. J. Rhee, "The genetics of primary open-angle glaucoma: A review," *Experimental Eye Research*. 2009. doi: 10.1016/j.exer.2008.11.003.

[329] B. Thylefors, A. D. Negrel, R. Pararajasegaram, and K. Y. Dadzie, "Global data on blindness," *Bull. World Health Organ.*, 1995.

[330] R. J. Casson, G. Chidlow, J. P. M. Wood, J. G. Crowston, and I. Goldberg, "Definition of glaucoma: Clinical and experimental concepts," *Clinical and Experimental Ophthalmology*. 2012. doi: 10.1111/j.1442-9071.2012.02773.x.

[331] G. Gong, S. Kosoko-Lasaki, G. Haynatzki, H. T. Lynch, J. A. Lynch, and M. R. Wilson, "Inherited, familial and sporadic primary open-angle glaucoma," *J. Natl. Med. Assoc.*, 2007.

[332] J. M. Tielsch, J. Katz, A. Sommer, H. A. Quigley, and J. C. Javitt, "Family History and Risk of Primary Open Angle Glaucoma: The Baltimore Eye Survey," *Arch. Ophthalmol.*, 1994, doi: 10.1001/archopht.1994.01090130079022.

[333] L. M. E. van Koolwijk *et al.*, "Common genetic determinants of intraocular pressure and primary open-angle Glaucoma," *PLoS Genet.*, 2012, doi: 10.1371/journal.pgen.1002611.

[334] T. F. L. Wishart and F. J. Lovicu, "An atlas of heparan sulfate proteoglycans in the postnatal rat lens," *Investigative Ophthalmology and Visual Science*. 2021. doi: 10.1167/iovs.62.14.5.

[335] T. F. L. Wishart and F. J. Lovicu, "Spatiotemporal Localisation of Heparan Sulphate Proteoglycans throughout Mouse Lens Morphogenesis," *Cells*, vol. 12, no. 10, pp. 1–20, 2023, doi: 10.3390/cells12101364.

[336] J. Wu *et al.*, "Gene Therapy for Glaucoma by Ciliary Body Aquaporin 1 Disruption Using CRISPR-Cas9," *Mol. Ther.*, 2020, doi: 10.1016/j.ymthe.2019.12.012.

[337] A. Jain *et al.*, "CRISPR-Cas9–based treatment of myocilin-associated glaucoma," *Proc. Natl. Acad. Sci. U. S. A.*, 2017, doi: 10.1073/pnas.1706193114.

[338] W. C. Manning *et al.*, "Genetic immunization with adeno-associated virus vectors expressing herpes simplex virus type 2 glycoproteins B and D," *J. Virol.*, 1997, doi: 10.1128/jvi.71.10.7960-7962.1997.

[339] J. Lin, R. Calcedo, L. H. Vandenberghe, P. Bell, S. Somanathan, and J. M. Wilson, "A New Genetic Vaccine Platform Based on an Adeno-Associated Virus Isolated from a Rhesus Macaque," *J. Virol.*, 2009, doi: 10.1128/jvi.01441-09.

[340] L. E. Mays *et al.*, "Adeno-Associated Virus Capsid Structure Drives CD4-Dependent CD8+ T Cell Response to Vector Encoded Proteins," *J. Immunol.*, 2009, doi: 10.4049/jimmunol.0803965.

[341] L. E. Mays *et al.*, "Mapping the Structural Determinants Responsible for Enhanced T Cell Activation to the Immunogenic Adeno-Associated Virus Capsid from Isolate Rhesus 32.33," *J. Virol.*, 2013, doi: 10.1128/jvi.00596-13.

[342] K. Nieto, A. Kern, B. Leuchs, L. Gissmann, M. Müller, and J. A. Kleinschmidt, "Combined prophylactic and therapeutic intranasal vaccination against human papillomavirus type-16 using different adeno-associated virus serotype vectors," *Antivir. Ther.*, 2009, doi: 10.3851/IMP1469.

[343] K. Nieto, C. Stahl-Hennig, B. Leuchs, M. Müller, L. Gissmann, and J. A. Kleinschmidt, "Intranasal vaccination with AAV5 and 9 vectors against human papillomavirus type 16 in rhesus macaques," *Hum. Gene Ther.*, 2012, doi: 10.1089/hum.2011.202.

[344] N. Zabaleta *et al.*, "Durable immunogenicity, adaptation to emerging variants, and low-dose efficacy of an AAV-based COVID-19 vaccine platform in macaques," *Mol. Ther.*, 2022, doi: 10.1016/j.ymthe.2022.05.007.

[345] G. Liao *et al.*, "Single-dose rAAV5-based vaccine provides long-term protective immunity against SARS-CoV-2 and its variants," *Virol. J.*, vol. 19, no. 1, pp. 1–11, 2022, doi: 10.1186/s12985-022-01940-w.

[346]   D. Tong *et al.*, "Single-dose AAV-based vaccine induces a high level of neutralizing antibodies against SARS-CoV-2 in rhesus macaques," *Protein Cell*, 2023, doi: 10.1093/procel/pwac020.

[347]   S. Zhao *et al.*, "A protective AAV vaccine for SARS-CoV-2," *Signal Transduct. Target. Ther.*, vol. 7, no. 1, pp. 2–5, 2022, doi: 10.1038/s41392-022-01158-w.

[348]   K. H. Warrington, O. S. Gorbatyuk, J. K. Harrison, S. R. Opie, S. Zolotukhin, and N. Muzyczka, "Adeno-Associated Virus Type 2 VP2 Capsid Protein Is Nonessential and Can Tolerate Large Peptide Insertions at Its N Terminus," *J. Virol.*, 2004, doi: 10.1128/jvi.78.12.6595-6609.2004.

[349]   F. Sonntag *et al.*, "The Assembly-Activating Protein Promotes Capsid Assembly of Different Adeno-Associated Virus Serotypes," *J. Virol.*, 2011, doi: 10.1128/jvi.05359-11.

[350]   Y. Xu, B. Jiang, P. Samai, S. M. Tank, M. Shameem, and D. Liu, "Genome DNA leakage of Adeno–Associated virus under freeze–thaw stress," *Int. J. Pharm.*, 2022, doi: 10.1016/j.ijpharm.2022.121464.

[351]   A. C. Walls, Y. J. Park, M. A. Tortorici, A. Wall, A. T. McGuire, and D. Veesler, "Structure, Function, and Antigenicity of the SARS-CoV-2 Spike Glycoprotein," *Cell*, 2020, doi: 10.1016/j.cell.2020.02.058.

[352]   J. Juraszek *et al.*, "Stabilizing the closed SARS-CoV-2 spike trimer," *Nat. Commun.*, 2021, doi: 10.1038/s41467-020-20321-x.

[353]   R. W. Sanders and J. P. Moore, "Virus vaccines: proteins prefer prolines," *Cell Host and Microbe*. 2021. doi: 10.1016/j.chom.2021.02.002.

[354]   D. Wrapp *et al.*, "Cryo-EM structure of the 2019-nCoV spike in the prefusion conformation," *Science (80-.).*, 2020, doi: 10.1126/science.aax0902.

[355]   J. S. Turner *et al.*, "SARS-CoV-2 mRNA vaccines induce persistent human germinal centre responses," *Nature*, 2021, doi: 10.1038/s41586-021-03738-2.

[356]   Y. Chen, Y. Guo, Y. Pan, and Z. J. Zhao, "Structure analysis of the receptor binding of 2019-nCoV," *Biochem. Biophys. Res. Commun.*, 2020, doi: 10.1016/j.bbrc.2020.02.071.

[357]   G. Papa *et al.*, "Furin cleavage of SARS-CoV-2 Spike promotes but is not essential for infection and cell-cell fusion," *PLoS Pathog.*, 2021, doi: 10.1371/journal.ppat.1009246.

[358]   M. N. Ramasamy *et al.*, "Safety and immunogenicity of ChAdOx1 nCoV-19 vaccine administered in a prime-boost regimen in young and old adults (COV002): a single-blind, randomised, controlled, phase 2/3 trial," *Lancet*, 2020, doi: 10.1016/S0140-6736(20)32466-1.

[359]   J. Fraussen, "IgM responses following SARS-CoV-2 vaccination: insights into protective and pre-existing immunity," *eBioMedicine*. 2022. doi: 10.1016/j.ebiom.2022.103922.

[360]   K. A. Pape *et al.*, "Visualization of the genesis and fate of isotype-switched B cells during a primary immune response," *J. Exp. Med.*, 2003, doi: 10.1084/jem.20012065.

[361]   A. Bortnick, I. Chernova, W. J. Quinn, M. Mugnier, M. P. Cancro, and D. Allman, "Long-Lived Bone Marrow Plasma Cells Are Induced Early in Response to T Cell-Independent or T Cell-Dependent Antigens," *J. Immunol.*, 2012, doi: 10.4049/jimmunol.1102808.

[362]   K. Kinoshita and T. Honjo, "Linking class-switch recombination with somatic hypermutation," *Nature Reviews Molecular Cell Biology*. 2001. doi: 10.1038/35080033.

[363]   M. S. Krangel, "Gene segment selection in V(D)J recombination: Accessibility and beyond," *Nature Immunology*. 2003. doi: 10.1038/ni0703-624.

[364]   Z. Wang *et al.*, "mRNA vaccine-elicited antibodies to SARS-CoV-2 and circulating variants," *Nature*, 2021, doi: 10.1038/s41586-021-03324-6.

[365]   C. Piubelli *et al.*, "Subjects who developed SARS-CoV-2 specific IgM after vaccination show a longer humoral immunity and a lower frequency of infection," *eBioMedicine*, 2023, doi: 10.1016/j.ebiom.2023.104471.

[366]   A. K. Hvidt *et al.*, "Comparison of vaccine-induced antibody neutralization against SARS-CoV-2 variants of concern following primary and booster doses of COVID-19 vaccines," *Front. Med.*, 2022, doi: 10.3389/fmed.2022.994160.

[367]   H. Gruell *et al.*, "mRNA booster immunization elicits potent neutralizing serum activity against the SARS-CoV-2 Omicron variant," *Nat. Med.*, 2022, doi: 10.1038/s41591-021-01676-0.

[368]   W. F. Garcia-Beltran *et al.*, "mRNA-based COVID-19 vaccine boosters induce neutralizing immunity against SARS-CoV-2 Omicron variant," *Cell*, 2022, doi: 10.1016/j.cell.2021.12.033.

[369]   A. Wajnberg *et al.*, "Robust neutralizing antibodies to SARS-CoV-2 infection persist for months," *Science (80-.).*, 2020, doi: 10.1126/science.abd7728.

[370]   A. C. Franke *et al.*, "Capsid-modified adeno-associated virus vectors as novel vaccine platform for cancer immunotherapy," *Mol. Ther. - Methods Clin. Dev.*, vol. 29, no. June, pp. 238–253, 2023, doi: 10.1016/j.omtm.2023.03.010.

List of Publications

Pavlou M, **Babutzka S**, Michalakis S. A Bioengineered In Vitro Model to Assess AAV-Based Gene Therapies for Cyclic GMP-Related Disorders. Int J Mol Sci. 2022 Apr 20;23(9):4538. doi: 10.3390/ijms23094538. PMID: 35562929; PMCID: PMC9101586.

Pavlou M, Schön C, Occelli LM, Rossi A, Meumann N, Boyd RF, Bartoe JT, Siedlecki J, Gerhardt MJ, **Babutzka S**, Bogedein J, Wagner JE, Priglinger SG, Biel M, Petersen-Jones SM, Büning H, Michalakis S. Novel AAV capsids for intravitreal gene therapy of photoreceptor disorders. EMBO Mol Med. 2021 Apr 9;13(4):e13392. doi: 10.15252/emmm.202013392. Epub 2021 Feb 22. PMID: 33616280; PMCID: PMC8033523.

Hiemenz C, Baumeister N, Helbig C, Hawe A, **Babutzka S**, Michalakis S, Friess W, Menzen T. Genome length determination in adeno-associated virus vectors with mass photometry. Mol Ther Methods Clin Dev. 2023 Nov 19;31:101162. doi: 10.1016/j.omtm.2023.101162. PMID: 38094202; PMCID: PMC10716024.

Babutzka S, L Zobel L, Bogedein J, Diedrichs-Möhring M, Gehrke M, Wildner G, Ammer H, Michalakis S, A novel platform for engineered AAV-based vaccines (*manuscript in preparation*)

Babutzka S, Bogedein J, H. Büning H, Michalakis S, Novel AAV9 Peptide Insertion Variants With Improved Tropism Tailored For Effective Retinal Gene Therapy (*manuscript in preparation*)

Acknowledgments

Declaration of Author Contributions - Part I

Novel capsid mutants for retinal gene therapy based on AAV9 serotype

AAV preparation was initially done by myself and, if required, repeated by lab technicians Kerstin Skokann (LMU Munich, Pharmacology for Natural Sciences, Department of Chemistry and Pharmacy) and Johanna Koch (LMU Munich, University Hospital, Department of Ophthalmology). Determination of genomic AAV titers by qRT-PCR was also performed by Kerstin Skokann and Johanna Koch. Mouse brain dissection was performed by Dr. Verena Mehlfeld and Philipp Lorenz (both LMU Munich, Pharmacology for Natural Sciences, Department of Chemistry and Pharmacy). Human retinal organoids were derived from iPSCs and maintained until transduction by Dr. Grazia Giorgio (LMU Munich, University Hospital, Department of Ophthalmology).

<u>My contribution to this work in detail:</u>

For this study, I conducted the initial design and cloning of all vectors, the initial AAV production and their technical analysis. Further, I performed the *in silico* modeling of capsid variants (RoseTTAfold, Bakerlab.org; UCSF Chimera), all *in vitro* experiments and *in vivo* experiments in C57BL6/J mice. Additionally, I designed the experiments and further analyzed and interpreted the data.

Munich, 10.10.2023

_____   _____

   Prof. Dr. Stylianos Michalakis   Sabrina Babutzka

Declaration of Author Contributions - Part II

A novel platform for engineered AAV-based vaccines

AAV preparation was initially done by myself and, if required, repeated by lab technicians Kerstin Skokann (LMU Munich, Pharmacology for Natural Sciences, Department of Chemistry and Pharmacy) and Johanna Koch (LMU Munich, University Hospital, Department of Ophthalmology). Determination of genomic AAV titers by qRT-PCR was also performed by Kerstin Skokann and Johanna Koch. Immunization of ZIKA rabbits and IgM/IgG evaluation via ELISA was performed by Prof. Dr. Hermann Ammer (LMU Munich, Department of Veterinary Sciences). Human blood plasma was collected by Prof. Dr. Gerhild Wildner (LMU Munich, University Hospital, Department of Ophthalmology). HtW2_S1.1 was cloned together with Dr. Lena Zobel (now ViGeneron GmbH).

<u>My contribution to this work in detail:</u>

For this study, I conducted the initial design, cloning of all vectors (except above mentioned), the initial AAV production and their technical analysis. Further, I performed the *in silico* modeling of capsid variants (RoseTTAfold, Bakerlab.org; UCSF Chimera), *in vitro* experiments and all benchwork. Additionally, I designed the experiments and further analyzed and interpreted the data.

Munich, 10.10.2023

_____   _____

Prof. Dr. Stylianos Michalakis   Sabrina Babutzka

Affidavit

Eidesstattliche Versicherung/Affidavit

Sabrina Babutzka

Hiermit versichere ich an Eides statt, dass ich die vorliegende Dissertation „Expanding the scope of adeno-associated-virus vectors: From retinal gene therapy to next generation vaccination platform" selbstständig angefertigt habe, mich außer der angegebenen keiner weiterer Hilfsmittel bedient und alle Erkenntnisse, die aus dem Schrifttum ganz oder annähernd übernommen sind, als solche kenntlich gemacht und nach ihrer Herkunft unter Bezeichnung der Fundstelle einzeln nachgewiesen habe.

I hereby confirm that the dissertation „Expanding the scope of adeno-associated-virus vectors: From retinal gene therapy to next generation vaccination platform" is the result of my own work and that I have only used sources or materials listed and specified in the dissertation.

Munich, 10.10.2023

_____

Sabrina Babutzka